# The Radiation Environment in the Lower Atmosphere
## A Numerical Approach

Dissertation
zur Erlangung des Doktorgrades
der Mathematisch-Naturwissenschaftlichen Fakultät
der Christian-Albrechts-Universität
zu Kiel
vorgelegt von
Daniel Matthiä
Kiel
2009

Referent/in:

Korreferent/in:

Tag der mündlichen Prüfung:

Zum Druck genehmigt: Kiel,

Der Dekan

# Zusammenfassung

Die durch extraterrestrische Quellen verursachte Strahlenexposition in der unteren Atmosphäre steigt mit zunehmender Höhe an. Die Ursache dieses Phänomens sind hochenergetische Teilchen der kosmischen Strahlung, die in die Atmosphäre eindringen und durch Wechselwirkungen mit Atomen in der Atmosphäre eine Sekundärteilchenkaskade erzeugen. Die Primärstrahlung besteht hauptsächlich aus den in der galaktischen Strahlung enthaltenen Atomkernen, die ihren Ursprung außerhalb des Sonnensystems haben und die die Erde nach Durchquerung der Heliosphäre erreichen. Die galaktische Strahlung unterliegt einer quasiperiodischen Modulation die zu einem Intensitätsmaximum während des solaren Minimums und einem Intensitätsminimum während des solaren Maximums führt. Zusätzlich kommt es zu relativ kurzzeitigen am Erdboden mit Neutronenmonitoren messbaren Anstiegen der Teilchenflüsse, so genannten Ground Level Enhancements (GLE). Diese GLEs werden durch solare Ereignisse verursacht bei denen Teilchen auf relativistische Energien beschleunigt werden. Die Untersuchung solcher GLEs auf der Grundlage der Neutronenmonitordaten und die daraus resultierende Erhöhung der Strahlenexposition in der Atmosphäre und im Besonderen in Flughöhe ist das Hauptziel der vorliegenden Arbeit. Hierzu wurden detaillierte Berechnungen des Teilchentransports durch die Magnetosphäre und der Wechselwirkung der Teilchen mit der Atmosphäre auf Grundlage einer Monte-Carlo Technik durchgeführt und die resultierenden sekundären Teilchenflüsse und Strahlenexpositionen bestimmt. Zur Verifizierung der Ergebnisse wurden in einem ersten Schritt die durch die galaktische Strahlung verursachten Teilchenflüsse berechnet und detaillierte Vergleiche mit vorhandenen Messungen durchgeführt.

Im Gegensatz zur galaktischen kosmischen Strahlung, die isotrop auf die Erde einfällt, weist die solare Teilchenstrahlung wechselnde Winkelverteilungen auf. Aufgrund der Ablenkung der geladenen Primärteilchen im Erdmagnetfeld sind die Neutronenmonitore empfindlich auf die Einfallsrichtung der Teilchen und der Vergleich der Zählratenanstiege verschiedener Neutronenmonitore an verschiedenen Orten lässt zudem Rückschlüsse auf das Energiespektrum der solaren Teilchen zu. Diese Eigenschaften wurden ausgenutzt um anhand der Neutronenmonitordaten das Primärspektrum, die Winkelverteilung und die Einfallsrichtung der solaren Teilchen und deren zeitliche Entwicklung zu bestimmen. Dies lieferte wichtige Erkenntnisse über die Anisotropie und die zeitliche Änderung des Einflusses der einfallenden Teilchen auf die Strahlungsumgebung in der Atmosphäre. Auf Basis dieser Ergebnisse wurden die resultierenden Sekundärteilchenflüsse in typischen Flughöhen zwischen 9 km und 12 km über dem Erdboden und die damit verbundene Erhöhung der Strahlenexposition für beliebige Positionen und Zeiten ermittelt. Hierbei hat der in der Anfangsphase der solaren Ereignisse vorhandene anisotrope Teilcheneinfall eine starke Abhängigkeit der Strahlenexposition von der geographischen Lage zur Folge. Des Weiteren wurden effektive Dosen für typische Nordatlantik- und Polarflüge berechnet und je nach Ereignis wurden Erhöhungen der effektiven Dosis von bis zu mehreren hundert Prozent ermittelt.

## Abstract

The radiation exposure in the lower atmosphere caused by extraterrestrial sources is increasing with altitude. The origin of this phenomenon is high energy particles penetrating the atmosphere and producing secondary particles in interactions with atoms in the air. The main sources of the primary radiation are atomic nuclei contained in the galactic cosmic rays arriving at Earth from outside the solar system after traversing the heliosphere. The galactic cosmic rays are subject to a quasi-periodic modulation leading to maximum intensity during solar minimum and minimum intensity during solar maximum. Additionally, during relatively short time periods particles may be accelerated to relativistic energies during solar events causing increases in the particle intensities on ground which are measurable by Neutron Monitor stations in so-called Ground Level Enhancements (GLE). Investigating such GLEs based on Neutron Monitor data and the related increase of the radiation exposure in the atmosphere and especially at aircraft altitudes is the main goal of the present work. For this purpose detailed calculations of the transport of relevant primary particles through the Earth's magnetosphere and their interactions with the atmosphere based on a Monte-Carlo technique were performed, and the resulting secondary particle fluxes and radiation exposures were determined. In order to verify the results of these calculations the secondary particle intensities induced by galactic cosmic rays were calculated and detailed comparisons with existing measurements were performed.

Contrary to the isotropically incident galactic cosmic rays, the solar energetic particles posses variable angular distributions. The deviation of the charged primary particles in the magnetosphere of the Earth leads to a sensitivity of the Neutron Monitors to the incoming direction of the solar particles. Additionally, the comparison of the count rate increases during a GLE of Neutron Monitor stations at different locations provides information about the energy spectrum of the primary particles. These properties were exploited to determine the temporal evolution of the primary particle spectrum, the angular distribution and the incoming direction of the solar particles. This provided important insights into the anisotropy and the temporal variation of the influence of the incoming particles on the radiation environment in the atmosphere. Based on these results the secondary particle fluxes at typical aircraft altitudes at 9 km to 12 km above sea-level and the related increase of the radiation exposure at arbitrary positions and times were determined. The anisotropic angular distribution which is present during the initial phase of the solar events resulted in a strong dependency of the radiation exposure on the geographic position. Additionally, the effective doses for typical north Atlantic and polar flights were calculated and increases of up to several hundred percent depending on the strength of the event were estimated.

# Contents

# Chapter 1

# Introduction

The fact that ionizing radiation has an impact on human tissue and consequently on human health became known shortly after the discovery of X-rays by Konrad Röntgen and radioactivity by Henri Bequerel and the couple Marie and Pierre Curie. Even though little was known about the nature and the effects of radiation at this time impacts on the human body like reddening of the skin and loss of hair could be observed. The awareness of possible threats by ionizing radiation was rising in the following years and decades and for many people it is a major concern in various areas in everyday life. These extend from the application of medical X-ray or nuclear medicine over the exploitation of nuclear power as well as in air travel. It has been known since the first half of the past century that the reduced shielding provided by the atmosphere at higher altitudes from extraterrestrial sources accounts for an increased radiation level compared to the ground.

The harmful effects on humans from X-rays are well known from the utilization in the beginning of the twentieth century when neither patient nor doctor had any protection and very high doses were used. The same is true for the extremely high exposure that can occur during and after accidents in nuclear power plants, during medical radiotherapy or improper handling of radioactive material. On the other hand, in many cases like the radiation exposure in air travel, where the exposure is comparatively small, no evidence for a negative effect on human health has been found yet and the topic remains under discussion. But it is clear that such an effect is small if it exists at all and it is very difficult to find a significant increase in the appearance of cancer or hereditary defects by epidemiological studies. Nevertheless, a possible health threat is of concern for affected persons like airline personnel, and for a reliable estimation of the biological risks arising from the radiation exposure in aviation it is necessary to accurately evaluate the exposure during the flights. This is the topic of the present work and comprises the contributions of galactic cosmic ray particles as well as energetic particles originating at the Sun.

The International Committee on Radiological Protection (ICRP) was founded in 1928 to estimate the risks and possible effects of radiation exposure and to make recommendations on radiological protection. One of the most important policies established by the ICRP is to keep the exposure to radiation "**A**s **L**ow **A**s **R**easonably **A**chievable" (ALARA). The statement of this principle is that

the harm and the benefit of radiation exposure must be balanced against each other. In order to follow this guideline it is absolutely essential to posses detailed knowledge about the composition of the radiation environment, the received doses and the resulting biological effects on human health. This implies that for radiation protection in air traffic a reasonable estimate of the radiation exposure for a given flight route or for an arbitrary point in the atmosphere specified by time, geographic position and altitude must be available and the health risk for this exposure is to be determined. The main reason for the increased radiation level at aircraft cruising altitudes with respect to sea-level is secondary particles produced in interactions of cosmic radiation with the atmosphere. Two kind of particles of extraterrestrial origin are responsible for the increased radiation exposure in air traffic, namely galactic cosmic rays (GCR) originating in the interstellar space in our galaxy and solar cosmic ray which are produced in solar energetic particle (SEP) events on or near the surface of the Sun.

The intensity of galactic cosmic ray particles is comparatively constant and slowly changing with the solar cycle being maximal at solar minimum and minimal during solar maximum. Smaller diurnal and 27-day periodical changes are observed as well as variations related to short duration solar activity and subsequent changes in the geomagnetic field. The GCR, being the dominant component of extraterrestrial particles with respect to radiation exposure in the atmosphere for most of the time, consist of ionized atomic nuclei, mainly hydrogen and helium but also contain heavier elements such as carbon and iron; the also existent electrons, gamma rays and less abundant particles are irrelevant concerning dosimetric questions in aviation. Before reaching the Earth the intensity of the galactic cosmic rays is modulated by the turbulent magnetized solar wind. In addition, the magnetosphere of the Earth acts as a magnetic filter with the strongest reflection at the magnetic equator leading to a characteristic distribution with maxima at the geomagnetic poles and minima at the geomagnetic equator. The resulting secondary particle production and dose rates in the atmosphere were measured and calculated by various authors and will be used in this work for the validation of primary particle models and transport calculations.

In contrast to the continuous nature of GCR, solar energetic particles are only released and accelerated during certain events on the Sun. The frequency of these events strongly depends on the particles' maximum energy and the solar activity ranging from a few events per year during solar minimum and energies above 300 MeV up to tens or hundreds per year for solar maximum counting events containing particles with maximum energies in the MeV region. Due to the attenuation in the atmosphere only solar particles with energies of a few hundred MeV and above have an impact on the radiation environment at aviation altitudes or may even reach the ground. The occurrence of events producing such highly energetic particles is about once a year. If such an increase in particle intensity on the ground caused by solar cosmic rays is detected it is called a Ground Level Enhancement (GLE). During such events information about the solar particles, for example energy spectra and angular distribution, can be derived from Neutron Monitor count rates. These Neutron Monitors are ground based detectors distributed over the whole world recording the hadronic com-

ponent of secondary particles produced by interactions of cosmic radiation with the atmosphere and thereby giving a measure of the primary particles' intensities. In contrast to the GCR particles which have a fairly isotropic distribution and only slowly changing primary spectra, particles accelerated during solar energetic particle events have an anisotropic angular distribution as well as rapidly changing energy spectra which makes it difficult to find a description of the temporal and spatial characteristics of the event. In addition, the radiation exposure during such an event is highly variable in time and in space depending on the incoming direction of the event and the shape of the primary energy spectrum. The Neutron Monitor network provides a tool to determine the spatial and temporal characteristics of solar energetic particle events by exploiting the variations in the sensitivity to primary particle energies and incoming directions of the different detector stations spread over the whole globe.
The main topic of this work is to derive sufficient information about the temporal and spatial evolution as well as the energy distribution of primary particles during Ground Level Enhancements and to estimate arising secondary particle fluences and dose rates at arbitrary points in the atmosphere and flight routes. Therefore it is necessary to incorporate different primary particle models for galactic and solar cosmic particles together with transport models of particles through the Earth's magnetic field and atmosphere into a joint framework. The secondary particle intensities computed with Monte-Carlo simulations can be used both for the estimation of the radiation exposure at aviation altitudes and the determination of Neutron Monitor count rates on the ground. Measurements of a large number of Neutron Monitor stations can then be used to estimate the primary particle intensities during solar energetic particle events, and the dose rates for arbitrary points in the atmosphere can be determined. The necessary steps to reach this goal will be presented in the following chapters of this work together with a few case studies of some of the most important Ground Level Enhancements in the last decades.

# Chapter 2

# Background

The necessary background knowledge to describe, discuss and understand the results of this work is described in this chapter. The cosmic radiation which is the source of the increased radiation levels at higher altitudes has its origin either outside the solar system (galactic cosmic rays; Section 2.1) or at the Sun (Solar Energetic Particles; Section 2.2) and is highly affected on its way through the heliosphere and the magnetosphere (Sec. 2.3) and the subsequent interactions in the Earth's atmosphere (Sec. 2.4). The properties and models for the description of these phenomena are discussed in the corresponding sections. As the main focus of this work is on the radiation exposure at aircraft altitudes, the question of what is radiation and which kind of radiation is important to describe the radiation environment in the atmosphere will be addressed in Section 2.5, and the different kinds of radiation will be summed up with their basic properties such as its interaction with matter. The connection of the physical properties and the effects on tissue and human health is the subject of the field of dosimetry and approached in Section 2.6. In the last part of this chapter (Sec. 2.7) the Neutron Monitor network serving as the primary data source for the analysis of Ground Level Enhancements will be discussed.

## 2.1 Galactic Cosmic Rays

The increased radiation exposure at aircraft altitudes with respect to sea-level conditions is mainly caused by galactic cosmic ray (GCR) nuclei. The galactic cosmic rays have their origin outside the solar system and reach the Earth's atmosphere after traversing the magnetic fields of the heliosphere and the magnetosphere of the Earth. Apart from atomic nuclei which account for 98% of the particle flux the galactic cosmic rays contain a small fraction of electrons ($\approx$2%) (*Amsler et al.*, 2008) and even smaller fractions of anti-protons (*Beach et al.*, 2001) and positrons (*DuVernois et al.*, 2001) produced in interactions of galactic cosmic ray nuclei and electrons with the interstellar gas. Due to their small contribution to the total flux of galactic cosmic ray particles and their short mean free path in the atmosphere the latter particles do not affect the conditions in the lower atmosphere and will not be considered in this work.

The nucleonic component of the galactic cosmic rays in the near Earth interplanetary space contains all stable elements. The dominant particles, however, are hydrogen nuclei which account for approximately 87% of the particles and helium nuclei with a fraction of around 12% (*Simpson*, 1983). Only about one percent of the particles are heavier nuclei. The elemental and isotopic occurrences and abundance in the galactic cosmic ray particles can provide useful information about their origin which is not yet totally clarified but is suspected to be supernovae remnants in the galaxy (see e.g. *Wiedenbeck et al.* (2001)). Moreover, the galactic cosmic ray particles are the only sample of matter from outside the solar system that is directly accessible to measurements.
Contrary to their small number, the heavy nuclei contribute significantly to the radiation exposure in low Earth orbits and near Earth open space (*Cucinotta et al.*, 2003). In the lower atmosphere, on the other hand, heavy ions play a minor role and in this work the focus will be on primary hydrogen and helium nuclei.
Typical energy per nucleon spectra for several galactic cosmic ray ions are illustrated in Fig. 2.1 and Fig. 2.2 for solar minimum and solar maximum conditions. The figures show the results for galactic cosmic ray energy spectra from data recorded by the balloon borne BESS experiment (*Sanuki et al.*, 2000), the AMS experiment performed on a space shuttle flight (*Alcaraz et al.*, 2000b,a) and satellite data from the Cosmic Ray Isotope Spectrometer (CRIS) detector on-board the Advanced Composition Explorer[1] (ACE) (*Stone et al.*, 1998) and the Electron Proton Helium Instrument[2] (EPHIN) (*Müller-Mellin et al.*, 1995) on-board the Solar and Heliospheric Observatory (SOHO). At energies above a few GeV per nucleon the energy spectra of the GCR do not show a solar cycle dependency and for different ion species $i$ they can be described by a power law in energy

$$(dI/dE_k)_i \quad \propto \quad E_k^{-\gamma_i}. \tag{2.1}$$

$E_k$ is the kinetic energy per nucleon and $I$ denotes the intensity, i.e. the number of particles $N$ per area $A$, time $t$ and solid angle $\Omega$: $I = N/At\Omega$. The spectral index $\gamma_i$ is in the order of 2.5–3.0 depending on the ion species. At these high energies the spectrum close to Earth is almost identical to the intergalactic spectra outside the solar system and the particles are unaffected by the solar modulation. At lower energies, however, the particle intensities are modulated by the turbulent magnetic solar wind leading to an anti-correlation with the solar activity. Accordingly, at energies of a few GeV and below the highest GCR intensities are observed during solar minimum whereas the lowest particles fluxes occur during solar maximum. This can be seen in Fig. 2.2 by comparing the particle intensities of the individual ion species in the top panel showing solar minimum with solar maximum conditions in the bottom panel. The processes affecting the charged particle transport in the heliosphere are diffusion among irregularities in the magnetic field, convection with the solar wind, gradient drift in the magnetic field and adiabatic deceleration (see e.g. *Parker* (1965); *Potgieter* (1995) for details). Predictions of various models describing the galactic cosmic ray spectra

[1] http://www.srl.caltech.edu/ACE/
[2] http://www2.physik.uni-kiel.de/SOHO/phpeph/ephin.htm

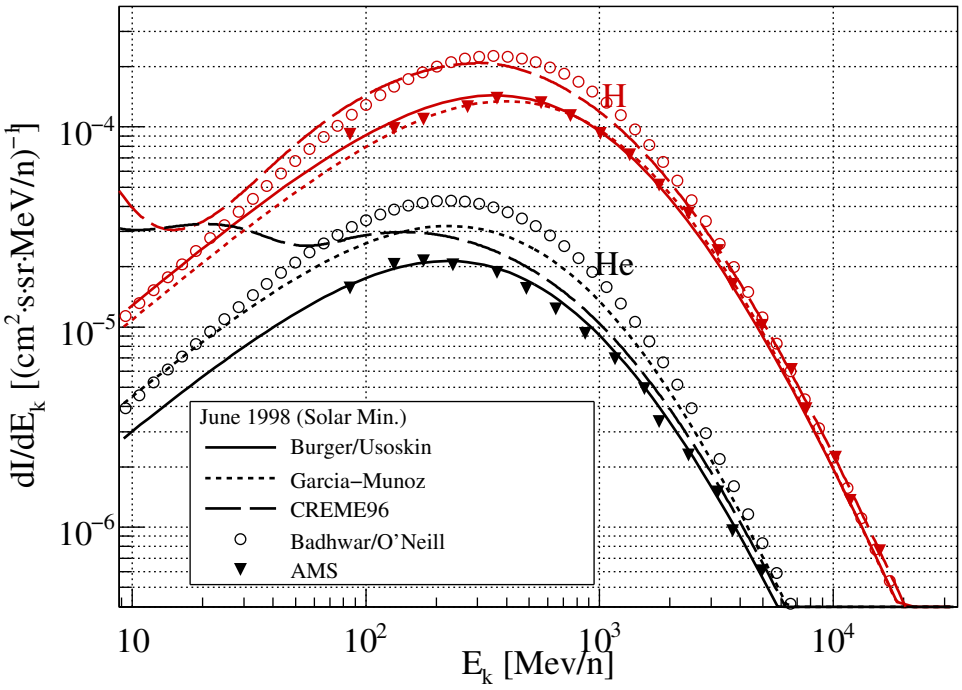


Figure 2.1: Near Earth differential intensities of primary H, He ions versus kinetic energy per nucleon from different models by Burger/Usoskin (*Burger et al.*, 2000; *Usoskin et al.*, 2005), Garcia-Munoz (*Garcia-Munoz et al.*, 1975), CREME96 (*Tylka et al.*, 1997), and Badhwar/O'Neill (*Badhwar and O'Neill*, 1996; *O'Neill*, 2006) for June 1998, i.e. solar minimum, compared to measurements from the AMS experiment (*Alcaraz et al.*, 2000b,a).

close to Earth are illustrated in addition to the experimental data in Fig. 2.1 and Fig. 2.2 A variety of models exists for the description of primary galactic cosmic rays in the interstellar space and the modulation of the particles on their way through the heliosphere (*Kota and Jokipii*, 1991; *Caballero-Lopez and Moraal*, 2004; *le Roux and Potgieter*, 1991). Among others *Garcia-Munoz et al.* (1975) (called Garcia-Munoz in the following) proposed a model for the local interstellar spectra (LIS) of galactic cosmic helium, hydrogen and carbon nuclei:

$$\begin{aligned} j_{\mathrm{LIS}}^{\text{Garcia-Munoz}}(E_k) &= A_i \cdot (E_k/\mathrm{MeV} + m)^{-\gamma_i}, \\ m &= B_i \cdot \exp\left(-C_i \cdot E_k\right), \end{aligned} \tag{2.2}$$

where $E_k$ is the kinetic energy per nucleon and $j$ is the differential particle intensity with respect to kinetic energy: $j \equiv dI/dE_k$. The parameters $A_i$, $B_i$, $C_i$ and $\gamma_i$ describing the spectra for the particular ion species $i$ are given in Table 2.1.
To derive the energy spectra of cosmic rays at Earth from Eq. 2.2, the modulation of primary particles in the heliosphere has to be taken into account. The transport equation for charged particles in the heliosphere was first described by *Parker* (1965) taking into account pitch angle scattering, diffusion, drift effects, convection in the solar wind and adiabatic energy gains and losses. *Caballero-Lopez and Moraal* (2004) showed that the force-filed model developed by *Gleeson and*

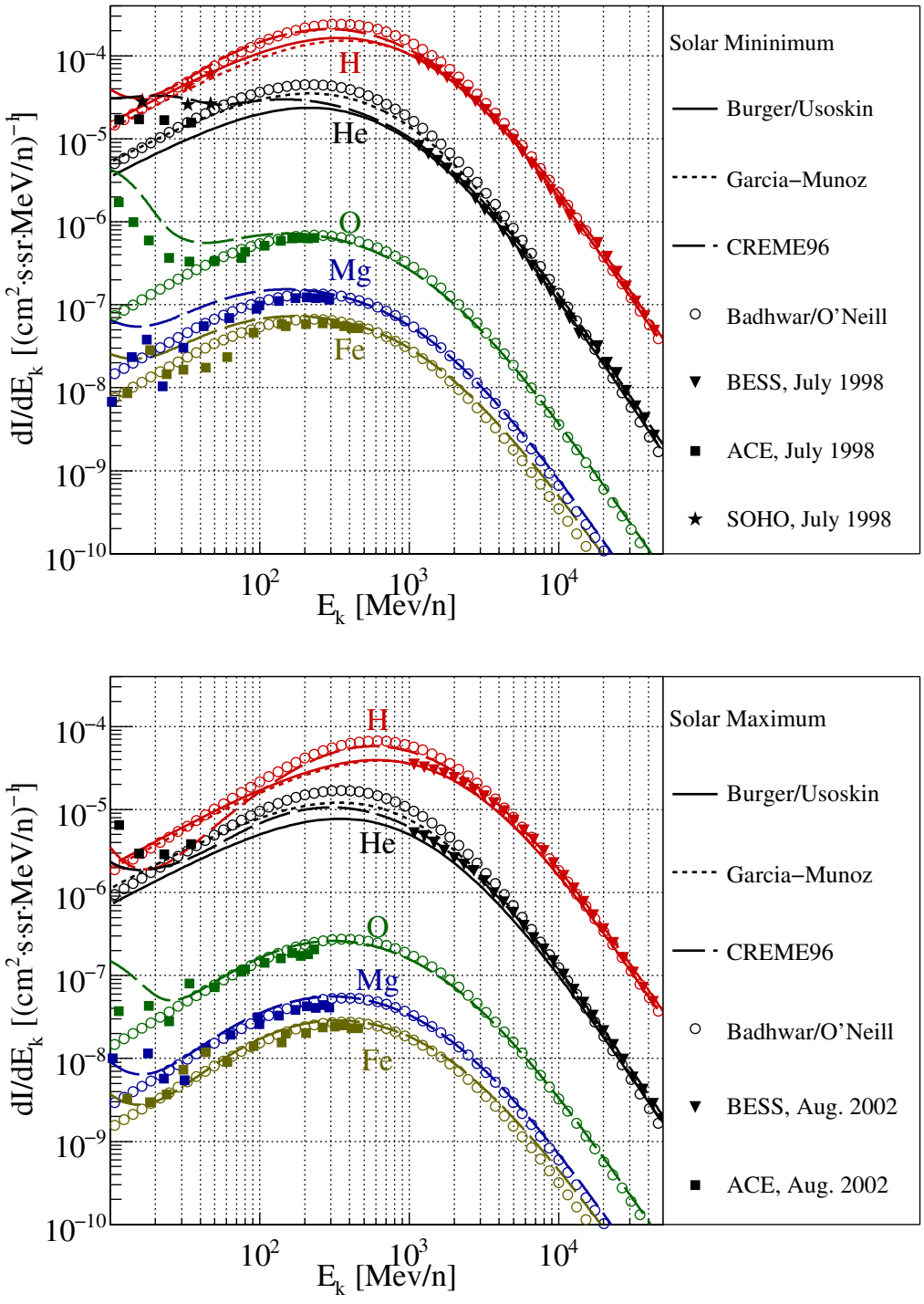


Figure 2.2: Near Earth differential intensities of primary H, He, O, Mg and Fe ions versus kinetic energy per nucleon from different models by Burger/Usoskin (*Burger et al.*, 2000; *Usoskin et al.*, 2005), Garcia-Munoz (*Garcia-Munoz et al.*, 1975), CREME96 (*Tylka et al.*, 1997), and Badhwar/O'Neill (*Badhwar and O'Neill*, 1996; *O'Neill*, 2006) for July 1998, i.e. solar minimum, (top panel) and August 2002, i.e. solar maximum, (bottom panel) compared to measurements from the BESS experiment (*Sanuki et al.*, 2000; *Haino et al.*, 2004), CRIS on-board ACE and EPHIN on-board SOHO.

Table 2.1: Parameters for Eq. 2.2 for the input spectra of hydrogen, helium and carbon nuclei from *Garcia-Munoz et al.* (1975).

| | $A$ $\left[\frac{1}{\mathrm{cm^2 \cdot s \cdot sr \cdot MeV/n}}\right]$ | $B$ | $C$ $[(\mathrm{MeV/n})^{-1}]$ | $\gamma$ |
|---|---|---|---|---|
| Hydrogen | $9.9 \cdot 10^4$ | 780 | $2.5 \cdot 10^{-4}$ | 2.65 |
| Helium | $1.8 \cdot 10^4$ | 660 | $1.4 \cdot 10^{-4}$ | 2.77 |
| Carbon | $1.8 \cdot 10^2$ | 620 | $5.2 \cdot 10^{-4}$ | 2.68 |

*Axford* (1968) satisfyingly describes the modulation of cosmic rays at a distance of one astronomical unit (AU) of the Sun, i.e. near Earth, and at particle energies above $\approx 100$ MeV. In the force-field model, the differential energy spectrum $j$ of galactic cosmic ray particles near Earth for a given LIS can be approximated by:

$$j^{1\mathrm{AU}}(E_k, \Phi) = j_{\mathrm{LIS}}(E_k + \Phi) \cdot \frac{E_k \cdot (E_k + 2 \cdot m_0 c^2)}{(E_k + \Phi) \cdot (E_k + \Phi + 2 \cdot m_0 c^2)}, \quad (2.3)$$

$$\Phi = |\frac{Ze}{A} \cdot \phi|. \quad (2.4)$$

$Z$ is the charge number, $A$ the mass number of the ion and $e$ is the elementary charge. $c$ is the speed of light and $m_0$ is the rest mass of the particle. Apart from the local interstellar spectrum the modulation parameter $\phi$ is the only free parameter in this model and characterizes the strength of the modulation. $\phi$ takes values between approximately 400 MV during solar minimum up to 1200 MV or more during solar maximum which reflects the fact that the strongest modulation occurs during solar maximum. The value of $\phi$ also depends on the model for the local interstellar spectrum and is not well-defined. Eq. 2.3 can be used to describe the modulation of arbitrary local interstellar spectra. The modulation in the heliosphere affects charged particles with magnetic rigidities below a few GV. The strength of the effect of a magnetic field on a charged particle decreases with the particle's rigidity $R$ which is defined as the ratio of the momentum and the charge $R = p/q$. With increasing rigidities the effect of the solar modulation decreases and the GCR spectra near Earth are identical to the interstellar spectra outside the solar system. The larger the charge over mass ration $Z/A$ of a particle is the larger is the corresponding modulation of its primary spectrum. Hydrogen has the largest possible charge over mass ration ($Z/A = 1$) and consequently experiences the strongest modulation in the heliosphere. The intensity of primary hydrogen (helium) nuclei derived from the presented models at around 1 GeV/nucleon is reduced by a factor of around 1/5 (1/3) during solar maximum ($\phi = 1200$ MV) with respect to solar minimum ($\phi = 400$ MV). At 10 GeV/nucleon the reduction is still in the order of 40% for hydrogen nuclei and 20% for helium nuclei. At 100 GeV/nucleon the differences between solar minimum and solar maximum account for several percent.

Another model for the LIS of galactic cosmic ray intensity was developed by *Burger et al.* (2000). *Usoskin et al.* (2005) provided the corresponding modulation parameter (the model using the LIS of *Burger et al.* (2000) and $\phi$ from

*Usoskin et al.* (2005) will be called Burger/Usoskin in the following). The differential particle intensity for hydrogen nuclei with respect to the kinetic energy in this model is given by:

$$\begin{aligned} j_{\mathrm{LIS}}^{\mathrm{Burger}}(E_k) &= \frac{1.9 \cdot 10^4 \cdot (p(E_k)/(\mathrm{GeV/c}))^{-2.78}}{1 + 0.4866 \cdot (p(E_k)/(\mathrm{GeV/c}))^{-2.51}}, \\ p(E_k) &= \sqrt{E_k \cdot (E_k + 2m_0)}, \end{aligned} \tag{2.5}$$

where $p$ is the momentum of the particle. *Usoskin et al.* (2005) used the force-field model (Eq. 2.3) to describe the particle energy spectra in the vicinity of the Earth and calculated the corresponding modulation parameter $\phi$ for the years from 1951 to 2004 based on Neutron Monitor count rates. Modulation parameters for later times are available at *http://cosmicrays.oulu.fi/phi/phi.html*. The LIS of helium nuclei is derived from Eq. 2.5 by using the helium to hydrogen ratio in particle numbers of 0.05, and the energy per nucleon spectrum for helium nuclei is obtained by multiplying Eq. 2.5 by this ratio. Concerning the solar modulation, *Usoskin et al.* (2005) also state that $\phi$ is not independent of the local interstellar spectrum. This effect has been recently studied for long term modulation by *Herbst et al.* (2009). The relation between the modulation parameters for the spectra described in Eq. 2.2 ($\phi_{GM}$) and Eq. 2.5 ($\phi_{BU}$) is given by *Usoskin et al.* (2005):

$$\phi_{GM} = 1.04\phi_{BU} - 76 \text{ MV} \tag{2.6}$$

For the calculations presented in the following chapters, the modulation potential was either taken from *Usoskin et al.* (2005) and if the model by Garcia-Munoz was used (Eq. 2.2) adapted with Eq. 2.6 or values provided by *Friedberg* (2007) and published online[3] were applied. Fig. 2.1 and Fig. 2.2 show very good agreement between the hydrogen measurements and the models by *Garcia-Munoz et al.* (1975) and *Burger et al.* (2000); *Usoskin et al.* (2005) for both solar minimum and solar maximum activity. Larger deviations between the experimental data and the model by *Garcia-Munoz et al.* (1975) occur in the helium data for solar minimum conditions where the model overestimates the measurements significantly.

*O'Neill* (2006) presented an updated version of the widely used Badhwar/O'Neill model (*Badhwar and O'Neill*, 1996) based on satellite measurements of the Advanced Composition Explorer (ACE) and Climax Neutron Monitor count rates. The LIS spectrum in this model is described by:

$$j_{\mathrm{LIS}}^{\mathrm{Badhwar/O'Neill}}(E_k) = \frac{j_{0,i}\beta^{\delta_i}}{(E_k + m_0)^{\gamma_i}}. \tag{2.7}$$

$\beta$ is the ratio of particle velocity to the speed of light. The free parameters $j_{0,i}$, $\delta_i$ and $\gamma_i$ describing the LIS were first obtained for oxygen by fitting data from IMP for hydrogen and helium and the CRIS/ACE detector for heavier elements. As the Badhwar/O'Neill model provides information about galactic cosmic ray

[3] http://www.faa.gov/education_research/research/med_humanfacs/aeromedical/radiobiology/heliocentric/

components from hydrogen up to elements as heavy as nickel it is very useful for applications in space where heavy ions play an important role. In the lower atmosphere, on the other hand, the most important contributions arise from hydrogen and helium nuclei. In comparison to the experimental data it becomes obvious that the model by *O'Neill* (2006) provides very accurate estimations for heavier ions in the energy range from a few tens up to several hundreds of MeV per nucleon. For hydrogen and helium, on the other hand, much higher particle intensities are predicted by the model than obtained by the measurements. Especially for the helium data deviations of more than a factor of two occur which makes the model less applicable for studies of the impact of galactic cosmic ray particles on the lower atmosphere.

The same features are observed for the model integrated in the "Cosmic Ray Effects on Micro-Electronics" (CREME96) tool[4] (*Tylka et al.*, 1997) which is illustrated in Fig. 2.1 and Fig. 2.2 as well. The CREME96 framework contains the galactic cosmic ray model developed by *Nymmik et al.* (1992). The modulation in this model is derived from the Wolf number (Sun spot number) which is related to solar activity taking into account that the actual modulation lags behind the solar activity for several months. This is due to the fact that the magnetic field responsible for the modulation is carried away from the Sun and to the outer heliosphere by the solar wind with a velocity of approximately $400$ km/s–$800$ km/s. It takes several month for the solar plasma to reach the outer boundary of the solar system causing a delay in the impact on the galactic cosmic rays which are affected on their way through the heliosphere. The rigidity spectra of the galactic particle in this model are given by:

$$j_{\mathrm{LIS}}^{Nymmik}(R,t) \quad = \quad \frac{D_i \beta^{\alpha_i}}{R^{\gamma^i}} \left( \frac{R}{R + R_0(t)} \right)^{\Delta_i(t)} . \tag{2.8}$$

$R = p/q$ is the particle's rigidity given by the momentum $p$ divided by the charge $q$. $D_i$, $\alpha_i$ and $\gamma_i$ are fixed parameters describing the spectrum for each individual GCR species $i$. The modulation of the spectrum is obtained by adapting the modulation parameter $R_0(t)$ and $\Delta_i(t)$ (for details see *Nymmik et al.* (1992)). For large rigidities $R$ the right part of Eq. 2.8 approaches one and the time dependent modulation vanishes. Consequently, in this region the rigidity spectrum is described by a power law in rigidity: $j \propto R^{-\gamma}$.

The values shown in Fig. 2.1 and Fig. 2.2 were obtained via the CREME96 web interface. The resulting ion spectra are very similar to those from *O'Neill* (2006) for energies above approximately 100 MeV. Below this energy the CREME96 model shows the characteristic increase in intensity at several tens of MeV for some ion species caused by anomalous cosmic rays (*Fichtner et al.*, 2000).

As for the model by *O'Neill* (2006) the CREME96 model shows a large overestimation compared to the AMS data in Fig. 2.1 but is consistent with the helium observations.

The comparison of the models presented above with the experimental data from the BESS and the AMS experiment as well as the satellite data was performed to find the most appropriate spectrum for the calculation of secondary particle

[4] https://creme96.nrl.navy.mil/

intensities and related quantities in the lower atmosphere. As already stated, the hydrogen and helium nuclei provide by far the largest contribution. The models by *Nymmik et al.* (1992) and *O'Neill* (2006) accurately describe the satellite data by ACE and SOHO for ions heavier than helium. Both models, however, overestimate the intensity of proton and alpha particles at energies above a few hundred MeV significantly and are therefore probably more applicable for the description of the radiation environment in space. Based on the good agreement between experimental data and the models by *Garcia-Munoz et al.* (1975) and *Burger et al.* (2000); *Usoskin et al.* (2005) it was decided to use these models (Eq. 2.2 and Eq. 2.5) in the subsequent chapters for the transport calculations in the magnetosphere and the atmosphere of the Earth and to derive the primary particle spectra on top of the atmosphere and the related secondary particle intensities produced by the interactions with the particles in the air.

## 2.2 Solar Energetic Particles

The second component playing an important role in the description of the radiation environment in near-Earth orbits and in the atmosphere is highly energetic particles produced at the surface or near the Sun. Charged particles are frequently accelerated to energies of several tens of MeV in so-called solar energetic particle (SEP) events. The majority of these events, however, is irrelevant in considerations concerning low-earth orbits or even processes in the lower atmosphere as only few events produce particles with energies affecting the radiation environment at near-Earth orbits and even less events contain particles that can penetrate deep into the atmosphere or even reach the ground. The consequences of the latter events are increases in particle fluences and radiation on ground and are accordingly called Ground Level Enhancements or Ground Level Events (GLEs). The first of such cosmic ray induced GLE was detected in the 1940s by *Lange and Forbush* (1942) and *Edward et al.* (1942) who recorded sharp enhancements in ionization rates due to cosmic ray particles followed with a delay of about one day by a longer lasting decrease in cosmic ray intensity, a so-called Forbush decrease, which coincided with the onset of a geomagnetic storm. *Forbush* (1946) suggested charged particles emitted by the Sun as the cause for the increases. The event reported by *Lange and Forbush* (1942) occurred on February 28th, 1942 and is the first Ground Level Enhancement in the chronological list containing 70 GLEs with the most recent event recorded on December 13th, 2006 by the time of the composition of this work. Ground Level Enhancements are usually recorded by the Neutron Monitor network (see Sec. 3.6), and information about the incoming particle spectra and direction can be derived by combining the responses of a number of stations.

The effects of these events on the radiation environment in the atmosphere and on ground are caused by secondary particles produced in interactions of primary solar particles with the atmosphere. Particles having an impact on the lower atmosphere and the ground are atomic nuclei accelerated near the Sun to relativistic energies and the dominant species is hydrogen nuclei, i.e. protons. Nevertheless, in some events neutrons are reported to be accelerated to high energies showing

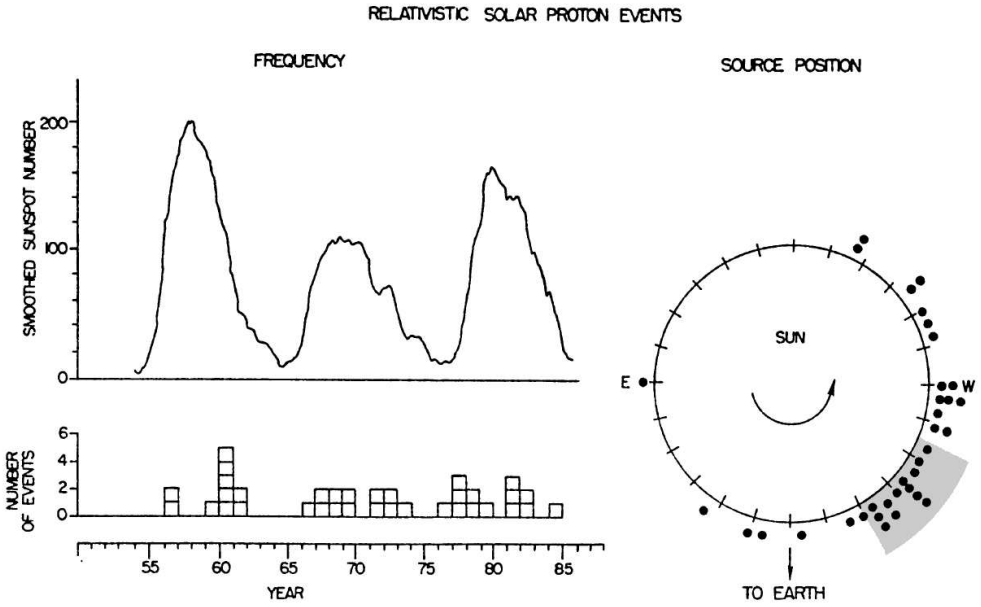


Figure 2.3: The mean Sun spot number (top panel on the left) compared to the number of Ground Level Enhancements per year (bottom panel on the left) during solar cycle 19, 20 and 21 and the solar longitude of the related X-ray flares (right panel) from *Shea and Smart* (1990). The shaded area on the right indicates the region magnetically best connected to Earth ($\approx 30°$W–$70°$W).

large but short-time effects on ground-based detectors preceding the solar proton event (*Shea et al.*, 1991; *Debrunner et al.*, 1997).

The threshold kinetic energy for a primary proton impinging on the top of the atmosphere to have an effect on the radiation environment at sea-level is approximately 500 MeV which corresponds to a magnetic rigidity of $R \approx 1$ GV. Solar protons at this energy and above are relativistic moving at velocities $v > 0.75 \cdot c$ ($c =$ speed of light) and reaching the Earth in about eleven minutes and less. Although solar energetic particle events are quite frequent, only the minority produces particles at these high energies. The average occurrence of such an event is about once a year with higher probabilities during solar maximum and less events during quiet solar conditions. *Shea and Smart* (1990) listed 218 discrete solar proton events during solar cycle 19, 20 and 21 from May 1954 to September 1986 with frequencies of up to 10-20 events per year near solar maximum. On the other hand, in the same 32 year time period, only 35 Ground Level Enhancements were recorded (No. 5–No. 39). The distribution over the three solar cycles was investigated by *Shea and Smart* (1990) and is shown in Figure 2.3 on the left where the accumulation around solar maximum activity is obvious.

The appearance of solar energetic particle events is related to a variety of phenomena occurring in advance, simultaneously or after the increase in highly energetic particle intensities. Most of the time GLE events are accompanied by X-ray flares on the surface of the Sun also emitting visible light in the wavelength of the H$\alpha$ line (656.3 nm) and being observable as bright eruptions. These flares usually occur several minutes prior to the detection of the energetic particles and

Table 2.2: Solar flare classification derived from the peak energy fluence rate of 1-8 Å X-ray measured by the Geostationary Operational Environmental Satellite (GOES).

| X-ray flare class | Peak Energy Fluence Rate $\Psi$ [W/m$^2$] |
|---|---|
| B | $\Psi < 10^{-6}$ |
| C | $10^{-6} \leqslant \Psi < 10^{-5}$ |
| M | $10^{-5} \leqslant \Psi < 10^{-4}$ |
| X | $\Psi > 10^{-4}$ |

are classified by their peak energy fluence rate $\Psi$ in X-rays with wavelengths of 1-8 Å measured by the Geostationary Operational Environmental Satellite[5] (GOES) as indicated in Table 2.2. Ground Level Enhancements are typically related to X-class flares which are additionally characterized by the absolute value of the peak energy fluence rate in the corresponding order of magnitude, e.g. a peak energy fluence rate of $1 \cdot 10^4$ W/m$^2$ corresponds to a X1-class flare, a peak energy fluence rate of $2 \cdot 10^4$ W/m$^2$ corresponds to a X2-class flare, etc. In addition to the emission of X-rays and visible light, the solar flare is usually accompanied by radio bursts.

Until recently it was believed that according to their duration most solar flares and related solar energetic particle events can be classified into two distinct classes, namely impulsive and gradual events. In the former energetic particles and increases in X-ray intensity are detected for several hours whereas the latter may last for several days. In addition to their temporal characteristics, the two classes show different elemental composition in the solar energetic particle populations, the ionization state of the accelerated ions, the type of radio bursts, the coincidence of a coronal mass ejection and the extent in longitude where energetic particles are observable (*Murdin*, 2001a). Nowadays, however, it is clear that most events exhibit features of both classes.

The positions of Ground Level Enhancement related X-ray flares during solar cycle 19, 20 and 21 were studied by *Shea and Smart* (1990) (right panel of Fig. 2.3). It is obvious that the vast majority of the X-ray flares connected to a GLE is located on the western hemisphere of the Sun. The reason for this behaviour is the magnetic connection between Sun and Earth. The field lines in the interplanetary magnetic field (IMF) exhibit a spiral structure, the so-called Parker spiral (*Parker*, 1958, 1963), and the field line connecting the Earth with the Sun has its foot-point at the western hemisphere of the Sun. The point directly connected to an observer by a magnetic field line is called the cob-point (connecting with the observer point). Charged particles accelerated in the SEP events propagate along the interplanetary magnetic field lines from Sun to Earth originating at the cob-point.

The arrival direction at Earth can be characterized by the angle $\phi$ between the magnetic field line at Earth and the radius vector connecting Earth and Sun. $\phi$ depends on the solar wind velocity $V_{SW}$ and the solar rotation with a period of approximately 26 days (angular rate $\Omega \approx 2\pi/(26d)$) at the solar equator and can

[5] http://www.oso.noaa.gov/goes/

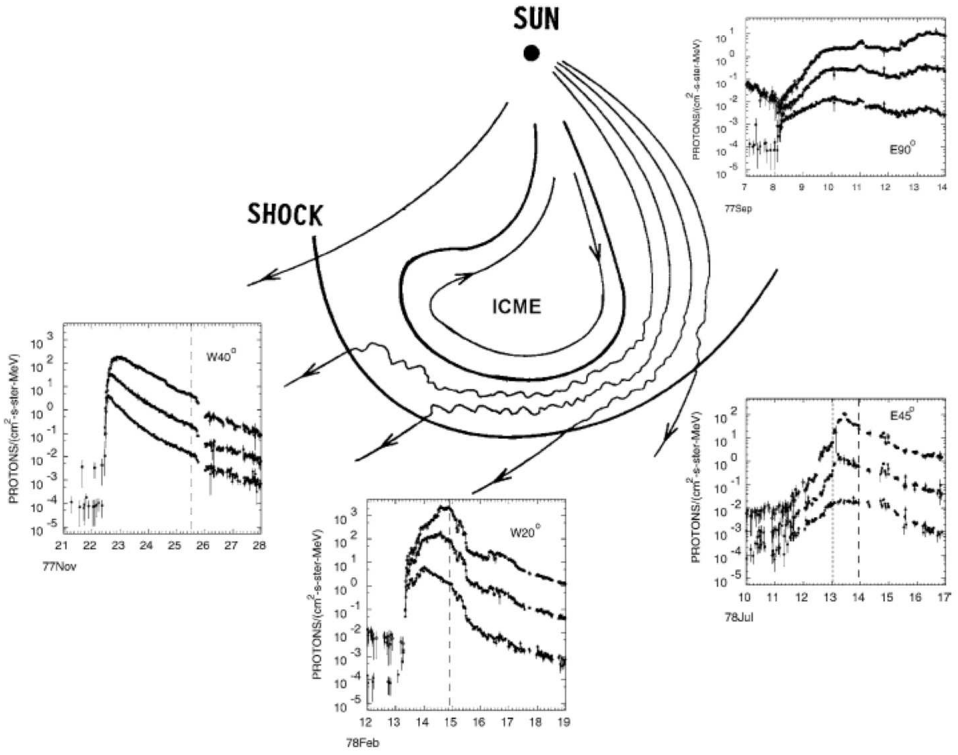


Figure 2.4: The interplanetary magnetic field lines and field lines forming around a coronal mass ejection driving an interplanetary shock (thick solid line). The small pictures show time profiles of solar energetic proton intensities for ∼5 MeV, ∼15 MeV and ∼30 MeV measured by IMP-8 in dependence on the location of the observer. The shock passage is indicated by the dashed lines in the small figures. From *Cane and Lario* (2006).

be approximated by:

$$\phi \quad = \quad tan^{-1}(r\Omega/V_{SW})) \tag{2.9}$$

where $r$ is the distance from the Sun. For typical solar wind velocities $V_{SW} = 400$ km/s–800 km/s and at a distance of one astronomical unit (1 AU $\approx 1.5 \cdot 10^8$ km), i.e. at Earth orbit, $\phi$ is approximately in the range from 45° to 30° and charged particles are expected to arrive at Earth east of the Sun-Earth line. The corresponding path length of the solar particles propagating along the Parker spiral from Sun to Earth is approximately 1.2 AU.

The wide distribution of the X-ray flare locations in Fig. 2.3 indicates that the source of relativistic particles is much wider than the comparatively narrow longitudinal extension the X-ray flares. Indeed, large solar energetic particle events are correlated with fast coronal mass ejections (CME) which are thought to accelerate the particles either from the ambient solar wind or from the solar corona in the shocks forming in front of the CME. The longitudinal extension of such an interplanetary CME (ICME) can reach up to 180° and is illustrated in Fig. 2.4 (*Cane and Lario*, 2006). It is obvious that the energetic particles can be observed from a wide range of longitudes and that the time profiles of proton intensities

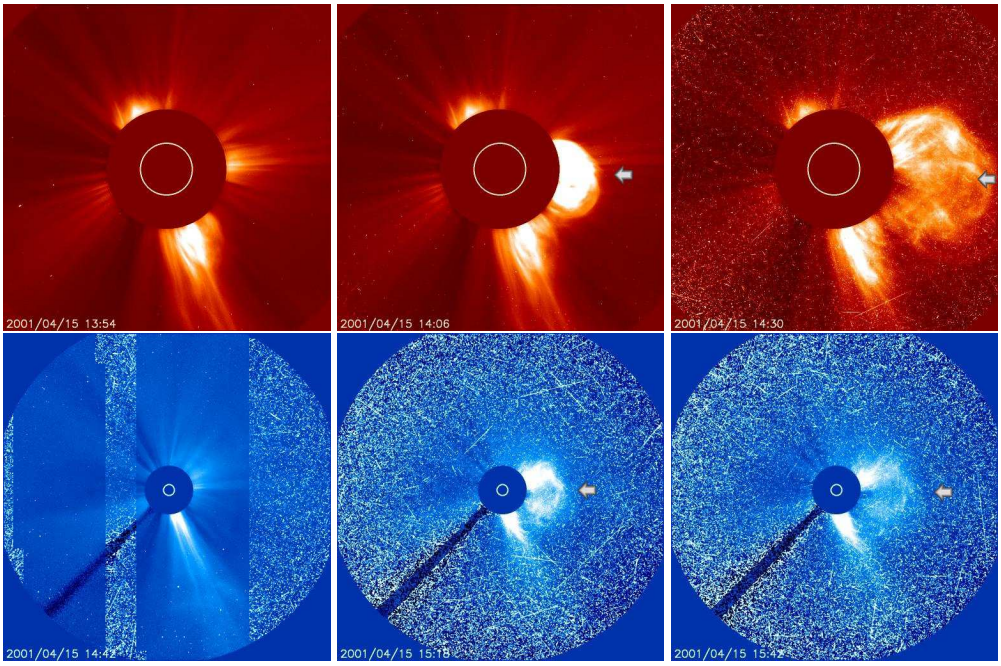


Figure 2.5: The evolving coronal mass ejection (indicated by the arrows) on April 15th, 2001 associated to Ground Level Event 60 observed with the LASCO C2 (top) and LASCO C3 (bottom) on-board SOHO (*Brueckner et al.*, 1995). The arriving solar energetic particles are visible as bright spots. From left to right and top to bottom the pictures were taken at 13:54 UTC, 14:06 UTC, 14:30 UTC, 14:42 UTC, 15:18 UTC, 15:42 UTC.

during different events are varying for different cob-points at the CME shock wave. For an observer magnetically connected to the very eastern part of the CME shock wave (very left picture in Fig. 2.4, W40°) the onset of the energetic protons is very sharp starting to decrease gradually shortly after the beginning of the event. The cob-point in this case is at the shock front only for a short time moving to the flank afterwards. At more western locations the cob-point is at the center of the shock front causing slower and long duration increases. Even though the observations in Fig. 2.4 are restricted to energies much lower than those relevant in the investigation of Ground Level Enhancements similar time profiles can be suspected for high energy particles in GLEs.

The advancing coronal mass ejection on April 15th, 2001 related to GLE 60 recorded by the Large Angle Spectroscopic Coronograph (LASCO) (*Brueckner et al.*, 1995) instrument on-board SOHO is shown in Fig. 2.5. The C2 and C3 coronographs have overlapping fields of view of 1.5–6 $R_\odot$ (C2) and 3.7–30 $R_\odot$ (C3). The figure shows the temporal evolution of the coronal mass ejection as observed by the C2 coronograph in the top row from 13:54 UTC to 14:30 UTC and afterwards by the C3 coronograph in the bottom row from 14:42 UTC to 15:42 UTC. In addition to the extending coronal mass ejection indicated by the arrow in the right part of the pictures the arriving solar energetic particles are clearly visible as bright spots in the detectors starting around 14:06 UTC.

Fig. 2.6 illustrates the typical chronology of X-ray and high energy particle measurements during Ground Level Enhancements for the example of GLE 60. The

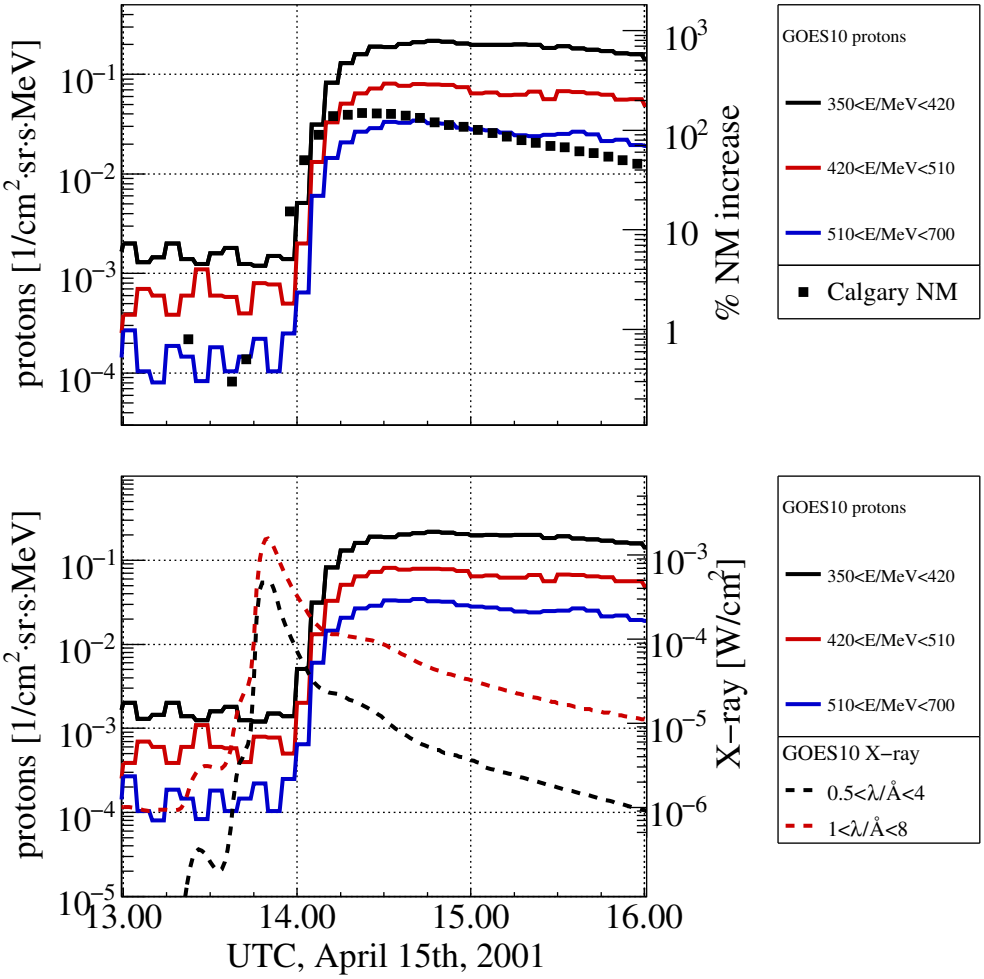


Figure 2.6: The onset of GLE 60 on April 15th, 2001 recorded by the Calgary Neutron Monitor (black squares) compared to the proton intensities measured by the HEPAD detector on-board GOES10 (top panel) and the increase in X-ray flux measured by GOES10 (dashed lines) prior to the arrival of the energetic protons at Earth (bottom panel).

increase in X-ray flux measured by GOES10 (in the lower panel) starts around 15 minutes prior to the arrival of energetic particles at Earth. In case of GLE 60 it was the Calgary Neutron Monitor (top panel) which showed the first response to solar energetic protons followed shortly afterwards by the High Energy Particle Detector (HEPAD) on-board GOES10. The X-rays originate directly from the emission of bremsstrahlung by highly energetic electrons in the plasma close to the solar flare site whereas the high energy protons are produced by shock acceleration in the shock driven by the fast coronal mass ejection following the X-class flare.

To estimate the impact of solar energetic particles on the lower atmosphere the composition, the energy spectrum and the angular distribution of particles arriving at Earth has to be known. The amount hydrogen nuclei in gradual solar

particle events exceeds the second most important component, helium nuclei, by a factor of 100 (*Murdin*, 2001a) and is therefore the dominant species.
Several approaches have been used to describe the energy spectrum of solar energetic particles. Energetic particles in gradual events are thought to be accelerated in shocks driven by fast coronal mass ejections (*Mikić and Lee*, 2006). *Ellison and Ramaty* (1985) developed a model for the description of shock accelerated particles deriving the differential intensity of the particles. The spectrum in this model is given by a power law in momentum $p$ with an exponential roll-over at higher energies $E$:

$$dI/dE \quad \propto \quad p^{-\gamma} \exp\left(-E/E_0\right), \tag{2.10}$$

where the parameter $E_0$ quantifies the energy where the exponential roll-over gains importance.
*Mewaldt* (2006) found that many solar energetic particle events could be fitted with the spectrum by *Ellison and Ramaty* (1985) up to energies of around 100 MeV/nucleon. For higher energies they suggested to use the double power law spectrum derived from *Band et al.* (1993):

$$dI/dE \quad \propto \quad \begin{cases} E^{\alpha} \exp\left(-E/E_0\right), & (\alpha-\beta)E_0 \geqslant E \\ E^{\beta} \exp\left(\beta-\alpha\right), & (\alpha-\beta)E_0 < E, \end{cases} \tag{2.11}$$

where $\alpha$ ($\beta$) describes the slope of the energy spectrum at lower (higher) energies. Other spectral forms that are frequently used are power laws in rigidity modified to account for the flatter spectrum at low rigidities (*Cramp et al.*, 1997b):

$$dI/dR \quad \propto \quad R^{-\gamma-\delta\gamma(R-1)} \tag{2.12}$$

or pure power laws in energy or rigidity:

$$dI/dR \quad \propto \quad E^{-\gamma} \tag{2.13}$$

$$dI/dR \quad \propto \quad R^{-\gamma}. \tag{2.14}$$

Values for the spectral index at energies above approximately 1 GeV are typically in the order of $\gamma \approx 3-5$ (*Duggal* (1979) and references therein). If anisotropy effects should be modeled it is necessary to account for the angular distribution of the primary particles. In the beginning of the majority of the solar energetic particle events the particle intensities show strong dependencies on the pitch angle between incoming direction and viewing direction. This anisotropy usually disappears after the first one or two hours. This is also one of the main differences in comparison to galactic cosmic ray particles which have an isotropic angular distribution and where anisotropy effects do not have to be taken into account.

### 2.2.1 Data on Solar Energetic Particle Events

The two main data sources on solar energetic particles that are available are satellite measurements and ground based Neutron Monitors (Sec. 2.7). Energetic particle detectors on-board satellites have the advantage of performing direct measurements of the galactic and solar particles. In contrast, Neutron Monitors are

sensitive only to secondary products from collisions of primary particles with target atoms in the air.
The Geostationary Operational Environmental Satellites (GOES) operated by the National Oceanic and Atmospheric Administration (NOAA) provides a variety of data of solar observation, for example measurements of X-rays, energetic electrons, protons and alpha particles. This data together with other spacecraft measurements, for example interplanetary magnetic field measurements, is available through the Space Physics Interactive Data Resource[6] (SPIDR, *Zhizhin et al.* (2008)). Other spacecraft providing data on solar energetic particles are the Solar and Heliospheric Observer (SOHO) and Advanced Composition Explorer (ACE). The major disadvantage of the currently available satellite-based data is the energy restriction of the measurements. For example, the uppermost differential energy channel for proton data on-board GOES covers the range $510\,\text{MeV} < E < 700\,\text{MeV}$. This is barely above the energy threshold for ground-based detection and only provides information at the lower end of the energy region of solar energetic particles affecting the lower atmosphere. Another disadvantage of the GOES data is the lack of directional information and consequently no information about the angular distribution and incoming direction of solar energetic particles can be derived.
Neutron Monitors at sea-level, on the other hand, are only sensitive to primary particles with comparatively high energies producing secondary particles detectable at sea-level. For example, only primary protons with kinetic energies above approximately 500 MeV affect the particle fluences on ground in such a way that the Neutron Monitor count rate is affected. The Neutron Monitor stations provide a single count rate, and accordingly, spectral information can not be derived from the measurements of a single detector. Only the combination of a number of stations can provide insights in the energy spectrum, the angular distribution and the incoming direction of the event. The analysis of the radiation environment at aviation altitudes in this work is restricted to solar energetic particle events producing Ground Level Enhancements and the Neutron Monitor network is used as the primary data source. Therefore, a detailed discussion of Neutron Monitor characteristics is given in Section 3.6. The Neutron Monitor data is published near real-time for many stations. The measurements of Neutron Monitor stations on Ground Level Enhancements in this work were obtained via the database run by IZMIRAN[7]. Additional information on Neutron Monitor stations and GLEs is provided by the Australian Antarctic Data Center[8] (AADC). Lists of useful links on cosmic ray data in general and to several Neutron Monitor stations are available for example through web-pages of Oulu and IZMIRAN Neutron Monitors[9,10] (see also App. A).

[6] http://spidr.ngdc.noaa.gov/spidr/index.jsp
[7] ftp://cr0.izmiran.rssi.ru/COSRAY!/
[8] http://data.aad.gov.au/aadc/gle/
[9] http://cr0.izmiran.rssi.ru/common/links.htm
[10] http://cosmicrays.oulu.fi/links.html

## 2.3 The Magnetosphere of the Earth

The region of the space around the Earth dominated by the influence of the magnetic field of the Earth is called the magnetosphere. Near Earth at distances of a few Earth radii the magnetic field is dominated by internal sources, and can be approximated by a dipole field. At larger distances, however, the field is strongly influenced by the solar wind causing large currents in different parts of the magnetosphere. For the outward flowing solar wind the magnetosphere forms an obstacle and the supersonic plasma is decelerated giving rise to the bow shock. In large parts the plasma contained in the magnetosphere can not mingle with the solar wind plasma. The boundary between the plasma of the solar wind and the plasma contained inside the magnetosphere is called magnetopause and is considered as the border of the magnetosphere (for details on the magnetosphere see e.g. (*Murdin*, 2001b)). The distance of the magnetopause along the Sun-Earth line is approximately ten Earth radii ($\approx 64000$ km). In the direction opposite to the incoming solar wind the magnetosphere extents to several hundreds of Earth radii.
Due to the deviation of charged particles by the Lorentz force the magnetosphere generates a shield around the Earth from high energy charged particles and is of great importance in the modeling of cosmic ray induced impacts in low Earth orbits or in the atmosphere (*Störmer*, 1930). In general, the dipole like magnetic field of the Earth provides the best protection at low geomagnetic latitudes due to the deviation of the charged particles by the magnetic field aligned parallel to the ground. In contrast, charged particles can propagate along the vertical field lines near the poles almost undisturbed. The significance of this behavior is studied in detail in Sec. 3.3.

## 2.4 The Atmosphere of the Earth

For the analysis of secondary particle fluences and derived magnitudes like radiological quantities, ionization rates or Neutron Monitor count rates it is necessary to calculate the transport of the primary particles through the atmosphere. The atmosphere of the Earth extends up to several thousand kilometers but more than 99.9% of the mass is contained in the region below 100 km above sea-level. The atmosphere contains mainly $N_2$ ($\approx 78\%$, in volume), $O_2$ ($\approx 21\%$), Ar ($\approx 0.9\%$), $CO_2$ ($\approx 0.03\%$) and other compounds like CO, $CH_4$, $N_2O$, etc. in minor fractions. The contribution of each constituent can change with altitude.
In this work, the atmosphere is considered up to altitudes of 200 km and the model of the atmosphere that is used is the implementation of the NRLMSISE-00 model[11] developed by *Picone et al.* (2002) and included in the PLANETOCOSMICS framework (see Sec. 3.2).
The most important parameter for the transport calculations apart from the elemental composition of the atmosphere is the amount of mass contained above a point of interest, i.e. the atmospheric depth $d$ = mass/area. The pressure $p$ at a given point in the atmosphere is given by the gravitational force $F$ per area $A$ of

[11] http://modelweb.gsfc.nasa.gov/atmos/nrlmsise00.html

the total mass content above the point which is related to the atmospheric depth. Therefore, the pressure and the atmospheric depth for a given gravitational acceleration $g$ are connected by:

$$p = \frac{F}{A} = \frac{m \cdot g}{A} = d \cdot g. \tag{2.15}$$

As the gravitational force varies slightly over the globe, the same pressure relates to different mass shielding at the equator and at the poles. This effect, however, is only in the order of tenths of percent and can be neglected in the context of this work as well as the altitude dependence of $g$. For the conversion from pressure to depth or vice versa a value of $g = 9.81$ m/s$^2$ will be used throughout this work. Atmospheric depth, density, pressure and temperature from the NRLMSISE00

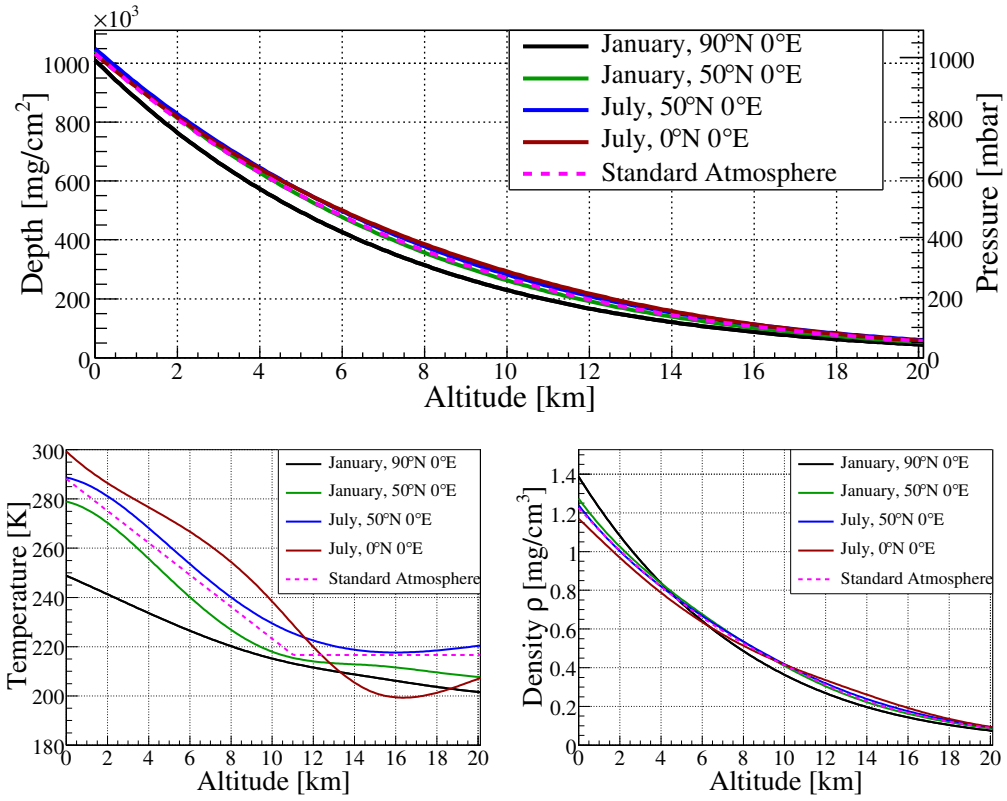


Figure 2.7: Seasonal and local variations in atmospheric depth (top), temperature (bottom left) and density (bottom right left) in the altitude range from sea-level to 20 km from the NRLMSISE-00 model (solid lines, (*Picone et al.*, 2002)) compared to the U.S. Standard Atmosphere Model 1976 (dashed line).

and the U.S. Standard Atmosphere 1976[12] are illustrated in Fig. 2.7. The NRLMSISE00 model provides estimates of these quantities with seasonal and latitudinal variation whereas the U.S. Standard Atmosphere models medium latitudes on the northern hemisphere. It is evident that significant differences exist in pressure, temperature and atmospheric depth at a given altitude for different

[12] http://www.pdas.com/atmos.htm

latitudes. Additionally, a strong seasonal variation is observed in the NRLMSISE00 model. This is especially pronounced for commercial aircraft altitudes from 9 km–13 km corresponding to atmospheric depth of around 350 g/cm$^2$ to 150 g/cm$^2$. As a consequence, the atmospheric depth will be used as the model parameter rather than the altitude. The impact on the primary particles arriving on top of the atmosphere and the related shielding provided by the mass above a certain altitude is given by the atmospheric depth. Results from different models of the atmosphere at a certain atmospheric depth are therefore comparable which is not necessarily true for results at a specific altitude which may correspond to different mass shielding. If results are related to a specific altitude in the following chapters the U.S. Standard Atmosphere was used for the conversion from depth to altitude, and the altitude for a real situation in the atmosphere may change significantly depending on the time of the year, location, etc.
In aviation the altitude of an airplane is expressed in flight levels (FL). One flight level corresponds to an altitude of 100 ft ($\approx 30.48$ m) in the U.S.Standard Atmosphere, and it is derived from the pressure measured at the airplane's altitude. Airplanes usually fly at constant pressures and the real altitude above sea-level may vary significantly for different atmospheric conditions.

## 2.5 Radiation

The most important definitions and properties of radiation and its interaction with matter are presented in this chapter. All radiation types that play an important role for the characterization of the radiation environment and dosimetry in space flight and aviation are described. This comprises charged particles together with neutrons and photons. Only a very short overview of most of the basic properties of the variation is given and more detailed descriptions may be found for example in *Krieger* (2002) and *Leo* (1994).

### 2.5.1 General Properties and Quantities

A variety of definitions of particle quantities exists in the literature. To avoid misunderstandings, the terms used in the following chapters are defined here following *ICRU* (1980):

$$F = \frac{dN}{dA} = \frac{\text{number of particles}}{\text{area}} = \text{fluence} \tag{2.16}$$

$$\frac{dF}{dt} = \frac{d^2N}{dAdt} = \frac{\text{number of particles}}{\text{area} \cdot \text{time}} = \text{fluence rate} \tag{2.17}$$

$$\Psi = \frac{d^2E}{dAdt} = \frac{\text{energy}}{\text{area} \cdot \text{time}} = \text{energy fluence rate} \tag{2.18}$$

$$I = \frac{d^2F}{dtd\Omega} = \frac{d^3N}{dAdtd\Omega} = \frac{\text{number of particles}}{\text{area} \cdot \text{time} \cdot \text{solid angle}} = \text{radiance or intensity} \tag{2.19}$$

To give a general description of energy or momentum spectra of a population of particles the differential intensity with respect to energy or momentum can be

used. It is defined as:

$$j_E \equiv dI/dE = \frac{d^4N}{dAdtd\Omega dE} = \frac{\text{number of particles}}{\text{area} \cdot \text{time} \cdot \text{solid angle} \cdot \text{energy}} \quad (2.20)$$
$$= \text{differential energy spectrum}$$
$$j_p \equiv dI/dp = \frac{d^4N}{dAdtd\Omega dp} = \frac{\text{number of particles}}{\text{area} \cdot \text{time} \cdot \text{solid angle} \cdot \text{momentum}} \quad (2.21)$$
$$= \text{differential momentum spectrum}$$

The particle fluence $F$ will be used frequently in the following and can be calculated for an energy interval $\Delta E$ and time interval $\Delta t$ from the differential intensity by integrating over time, energy and solid angle:

$$F = \int_{\Delta E} dE \int_{4\pi} d\Omega \int_{\Delta t} dt \; j_E(E, \Omega, t). \quad (2.22)$$

Accordingly, if the particle spectrum is isotropic and constant in time the fluence is given by:

$$F = 4\pi\Delta t \int_{\Delta E} dE \; j_E(E). \quad (2.23)$$

By traversing a certain volume of matter, the intensity of a given particle type is typically affected by the particles' interactions with the material contained in the volume. The probability for such an interaction with target material is quantified by the total cross section $\sigma$:

$$\sigma = \frac{\text{number of interactions}}{\text{number of particles/area}}. \quad (2.24)$$

The cross section depends on the projectile, its energy and the target material.
The total cross section as given in Eq. 2.24 is the sum of the partial cross sections describing the probability for the incidence of a variety of competing interactions. The mean free path $\lambda$ of a particle without interacting with the target material is related to $\sigma$ by

$$\lambda = \frac{1}{N\sigma}, \quad (2.25)$$

where $N$ is the number of scattering centers per volume in the target.
The energy lost by the projectile particle in the interactions with the target material may be transferred to secondary particles leaving the target volume or deposited in the volume. The effect on the target material induced by a certain type of radiation is related to this energy deposition. To quantify the energy deposition of a given type of radiation with energy $E$ it is useful to introduce the linear energy transfer $L_\Delta$ or $LET_\Delta$. It is defined as the energy $dE$ lost per pathlength $dl$ due to collisions with electrons in which the individual energy loss per collision is smaller than $\Delta$:

$$L_\Delta = \left(\frac{dE}{dl}\right)_\Delta \quad (2.26)$$

The unrestricted linear energy transfer $L_\infty$ is often denoted by $L$ or $LET$ omitting the subscript. The energy deposition per volume of a particle beam with fluence $F$ and linear energy transfer $L_\infty$ can be written as:

$$\epsilon_{Dep} = E_{Dep}/V \approx F \cdot L_\infty. \tag{2.27}$$

In this equation the energy transported by secondary particles leaving the volume is neglected.
In the case of heavy charged particles and for electrons and positrons at energies below the threshold where radiative energy loss is important ($E < 10$ MeV–$100$ MeV) the unrestricted linear energy transfer $L_\infty$ is identical to the total energy transfer.
For the description of the propagation of a charged particle in a magnetic field it is useful to introduce the magnetic rigidity $R$ of a particle:

$$R = \frac{p}{q}, \tag{2.28}$$

where $p$ is the momentum and $q$ the charge of the particle. The quantity is derived from expression for the gyro-radius $r$ of a charged particle in an uniform magnetic field $B$:

$$r = \frac{mv}{qB} = \frac{R}{B}, \tag{2.29}$$

and it is usually expressed using Planck units (speed of light $c = 1$) in Mega- or Giga-Volts (MV, GV). Particles with large rigidities are deviated less in a magnetic field. This fact plays an important role in the quantification of the impact of the magnetic field of the Earth on the primary galactic and solar particle intensities.
For relativistic particles with kinetic energy $E_k$, charge $q$ and rest mass $m_0$ the magnetic rigidity can be written as:

$$R = \frac{\sqrt{(E_k/c)^2 + 2E_k m_0}}{q}. \tag{2.30}$$

### 2.5.2 Interaction of Particles with Matter

#### Heavy Charged Particles

The category of heavy charged particles in this context contains all charged particles heavier than electrons and positrons. This comprises protons, muons, alpha particles and heavier nuclei among other particles. Of these, protons are especially important for the radiation environment in the lower atmosphere. Beside neutrons, protons contribute with the second largest fraction to the weighted radiation exposure at aircraft altitudes. Moreover, protons are by far the most abundant galactic cosmic ray and solar energetic particle species and accordingly are the major source for the particle cascades forming in the atmosphere.
The main energy loss process of heavy charged particles in matter is the inelastic scattering of atomic shell electrons either by ionizing the atom or lifting an

electron in an excited state. The energy loss in a single collision is very small compared to the energy of the projectile and as the number of collisions per path length is very high the process can be considered as continuous. The energy loss $dE$ per path length $dx$ of heavy charged particles is described by the Bethe-Bloch formula:

$$-dE/dx = 2\pi N_A r_e^2 m_e c^2 \rho \frac{Z}{A}\frac{z^2}{\beta^2}\left(\ln\left(\frac{2m_e\gamma^2 v^2 W_{max}}{I^2}\right) - 2\beta^2\right) \quad (2.31)$$

where $N_A$ is Avogadro's number, $r_e$ is the classical electron radius, $m_e$ the electron mass, $\rho$ the target density, $c$ the speed of light, $Z$ and $A$ are the atomic and mass number of the target material, $\beta = v/c$ is the ratio of the projectile's velocity $v$ and the speed of light, $z$ is the charge of the projectile in units of the elementary charge $e$, $\gamma = 1/\sqrt{1-\beta^2}$, $I$ is the mean excitation potential of the target, $W_{max}$ is the maximum energy transfer in a single collision, namely:

$$W_{\max} = \frac{2m_e c^2 \eta^2}{1 + 2s\sqrt{1+\eta^2} + s^2} \quad (2.32)$$

with $\eta = \beta\gamma$, $s = m_e/M$. $M$ is the mass of the projectile.
At energies in the GeV region and above Eq. 2.31 has to be modified by shell and density corrections (for details see (*Leo*, 1994)).
At non relativistic energies Eq. 2.31 is dominated by the term $1/\beta^2$. Accordingly, $dE/dx$ is increasing with decreasing velocity and energy. As a consequence, the energy deposition of heavy charged particles in matter increases along their path showing a characteristic maximum at the end, the so-called Bragg-peak.
A very important property of atomic nuclei which can be derived from the Bethe-Bloch formula is the scaling behaviour of the energy loss per nucleon. From Eq. 2.31 it can be followed that for a given material the energy loss is given by (see (*Leo*, 1994)):

$$-dE/dx = z^2 f(\frac{E_k}{M}), \quad (2.33)$$

where $z$ is the charge of the projectile, $E_k$ its kinetic energy, $M$ its mass and $f(E_k/M)$ is a function only depending on the energy to mass ratio of the projectile. For nuclei having energies per nucleon of $E_k/a$ it follows that the energy loss per nucleon is given by:

$$\frac{-dE/dx}{a} = \frac{z^2}{a} f(\frac{E_k}{am_0}), \quad (2.34)$$

where $a$ is the atomic number of the projectile and $m_0$ the nucleon mass. The rest masses of proton $m_0^{\mathrm{p}}$ and neutron $m_0^{\mathrm{n}}$ are assumed to be identical. The actual difference in the masses is less than 0.15%: $m_0^{\mathrm{p}} = 938.27203\,\mathrm{MeV/c^2}$, $m_0^{\mathrm{n}} = 939.56536\,\mathrm{MeV/c^2}$. This implies that for hydrogen and helium nuclei ($z^2/a = 1$) with the same energy per nucleon the energy loss per nucleon in a certain material is identical in the domain of the Bethe-Bloch equation. And, as a consequence, the range of these particles is similar while all heavier ions with

larger $z^2/a$ ratio have a much shorter range.
Several other processes contributing to the energy loss of heavy charged particles can usually be neglected: radiative energy loss through the emission of bremsstrahlung, elastic and inelastic collisions with atomic nuclei and the emission of Cherenkov radiation. The energy loss through multiple elastic scattering of charged particles of target nuclei is usually also negligible but has to be considered if the deflection of the particles is calculated.
High energy transfers in inelastic collisions with the atomic shell can result in the production of so-called $\delta$-electrons which have enough energy to propagate a certain path in the ambient matter. Therefore, the local energy deposition may be decreased by $\delta$-electron production. Apart from the creation of $\delta$-electrons, inelastic interactions of heavy charged particles can result in the production of secondary neutrons, protons or fragment nuclei either from the target or the incoming particle. A variety of mesons and baryons may also be produced in these collisions. Secondary muons being one of the most important components in the radiation environment in the atmosphere especially at low altitudes originate, for example, from the decay of pions produced in nuclear interactions. Additionally, after inelastic nuclear interactions the target nucleus may be left in an excited state and may deexcite by emitting so-called evaporation neutrons and protons or by $\alpha$ decay.

**Neutrons**

Secondary neutron radiation is the most important component concerning the weighted exposure in the radiation environment at aviation altitudes. The primary cosmic radiation does not contain a significant fraction of free neutrons but they can originate from the breakup of primary cosmic nuclei in inelastic collisions of the latter with atoms in the air. The energy range of neutrons in the atmosphere extends from cold and ultra-cold neutrons (milli- and micro-eV) over epithermic ($< 0.02$ eV) and thermic energies($\approx 0.2$ eV–$0.5$ eV) and fast neutrons ($> 0.5$ eV) up to relativistic and high-relativistic energies (MeV to GeV).
Neutrons are especially interesting in dosimetric considerations as they are uncharged and thus not directly ionizing particles but can transfer a large amount of energy to directly and densely ionizing particles in inelastic hadronic collisions. Therefore, neutrons can not be easily shielded but are still able to deposit a lot of energy inside the human body by creating charged secondary particles in nuclear interactions and thereby causing cellular damage.
The interactions of the uncharged neutrons with matter are mainly restricted to nuclear interactions via the strong force. Elastic scattering of neutrons of target nuclei is the dominant process for the energy loss of neutrons in the MeV energy region.
At thermal energies the most important process is neutron capture by a target nucleus. In the case of radiative neutron capture the final state of the reaction contains the target nucleus with mass number increased by one and a gamma particle. An important example for the interaction of neutrons in tissue is the radiative capture of thermal neutrons by a hydrogen nucleus releasing a gamma particle with energy $E = 2.225$ MeV originating from the binding energy of the

deuteron: p(n,$\gamma$)d. Other secondary products in the neutron capture processes can be charged particles such as p, d and $\alpha$ particles. These reactions can be used for the detection of neutrons by measuring the secondary charged particles, e.g. the detection of an $\alpha$ particle originating from a (n,$\alpha$) reaction in Neutron Monitor detector tubes (see Sec. 3.6). Additionally, the capture of neutrons may result in nuclear fission. The cross section for the neutron capture by a nucleus is approximately proportional to $1/v$, where $v$ is the neutron velocity and the process is therefore less important at higher energies.
One of the most important interactions of highly energetic neutrons ($E > 100\,\mathrm{MeV}$) with matter is the spallation of target nuclei. In this reaction, the target nucleus is broken up by the neutron resulting in the remnant nucleus and one or several lighter nuclei. Additionally, the remnant nucleus is often left in an excited state and can emit evaporation neutrons and protons in a second phase of the interaction. At very high neutron energies in the order of GeV this process may result in a hadronic cascade of secondary particles by repeated spallation reactions of primary neutrons and secondary products. This process is of great importance in the interaction of galactic cosmic ray particles with the atmosphere.

#### Electrons and Positrons

Electrons and positrons contribute with approximately 5% to the total radiation exposure in the lower atmosphere. In contrast to heavy charged particles for which the collisions with electrons are the main energy loss processes, electrons and positrons suffer energy loss both from collisions and from radiative emission of bremsstrahlung in Coulomb scattering of the electromagnetic field of the atomic nuclei. For heavy charged particles the second component can be neglected up to very high energies but for electrons and positrons, the radiative energy loss gains importance in the MeV energy region and is the dominant process above energies of 10 MeV to 100 MeV depending on the target material. The collision process can be described by modifying the Bethe-Bloch formula from Eq. 2.31 (for details see (*Leo*, 1994)). As in the case of heavy charged particles the energy loss through collisions with electrons is proportional to the ratio $Z/A$ of the target material and increases logarithmically with kinetic energy. The radiative energy loss on the other hand increases linearly with the energy which is the reason for the dominance of the radiation energy loss at higher energies.

#### Photons

At low energies in the order of $eV$ and below photons are non ionizing (low energy UV, visible light and longer wavelengths). At these energies the main interaction of photons with matter is coherent scattering of electrons in the atomic shell without energy loss .
At higher energies, where ionization of target atoms occurs, the main interactions of photons with matter are the photoelectric effect, Compton scattering and pair production.
The cross-section in the energy range up to several tens of keV is dominated by the photoelectric effect. In the photoelectric effect all energy minus the binding

energy is carried by the photo-electron after the interaction. The cross-section is proportional to the fourth to fifth power of the atomic number $Z$ and decreases with increasing photon energy. The highest absorption and the best shielding at these energies is therefore obtained by high Z material.
The Compton scattering process gains importance at higher photon energies and is the dominant process in the energy region of several MeV and for targets with low mass number. In the Compton process the photon scatters of an electron in the atomic shell transferring a certain amount of its energy to the electron which leaves the atomic shell.
The creation of an electron-positron pair in the pair production process has a lower energy threshold of $E = h\nu > 2 \cdot m_e \approx 1022$ MeV for the creation of the rest masses of the daughter particles. Above this threshold the cross section for pair production is increasing and pair production is the dominant process at higher energies (in the order of tens of MeV and above).
The absorption of photons in matter follows an exponential rule:

$$\Psi(x) \quad = \quad \Psi_0 \cdot e^{-\mu x}, \tag{2.35}$$

where $\Psi(x)$ is the energy fluence rate of the photon beam after a path length $x$ in the target, $\Psi_0$ the energy fluence rate before entering the target and $\mu$ is the absorption coefficient. In a material with molecular weight $A$ and density $\rho$ the absorption coefficient can be written as:

$$\mu \quad = \quad \sigma(N_A \rho / A), \tag{2.36}$$

where $N_A$ is Avogadro's number and $\sigma$ is the total cross-section.
The mean free path of photons in matter is much longer than that of charged particles at comparable energies making highly energetic photons much more penetrating than for example electrons, protons or heavy ions.

#### Hadronic and Electromagnetic Showers

Very high energy particles entering the atmosphere may produce a shower of secondary particles by repeated interaction with the atoms in the air and by subsequent interaction, decay or pair production of the produced secondary particles. Electrons, positrons and photons interact mainly with electrons in the atomic shell. These interactions can for example result in additional free electrons via Coulomb scattering or the photo effect or gamma rays may be produced via bremsstrahlungs processes. Photons may additionally decay via pair production in the Coulomb field of the nucleus adding an electron-positron pair to the cascade. Such showers mainly containing electrons and photons are called electromagnetic showers.
Primary or secondary hadrons, like protons, neutrons and atomic nuclei, may additionally produce free secondary nucleons and fragment nuclei adding to the particle cascade. Highly energetic primary particles can produce large air showers which may be detected by ground based arrays stretching over several square kilometers.

## 2.6 Dosimetry

On its way through a volume of matter radiation looses energy that is either transferred to secondary particles, e.g. electrons in ionization processes, or deposited locally in the volume. The ionization of atoms and the deposited energy may inflict damage in biological tissue such as DNA double strand breaks and resulting mutations, production of free radicals and correlated cell malfunctioning or cell death. The major tasks of the "**I**nternational **C**ommission on **R**adiological **P**rotection" (ICRP) are to quantify these effects, estimate the severeness of the damage caused by the radiation and recommending limits for the acceptable exposures.
The "**I**nternational **C**ommission on **R**adiation **U**nits and Measurements" (ICRU) was founded in 1925 to create a framework of units, a guideline of measurement techniques and procedures necessary to create and to follow the recommendations by the ICRP. Different quantities were introduced to facilitate a consistent formalism for radiation protection. The following explanations of the most important definitions in dosimetry are based on *ICRU* (1980) Report 33, *ICRP* (1990) Publication 60 and *ICRP* (2007) Publication 103.
The basic physical quantity in dosimetry is the absorbed dose $D$ which is the mean energy imparted $d\bar{\epsilon}$ in a volume containing the mass $dm$ by ionizing radiation in a given field:

$$D = \frac{d\bar{\epsilon}}{dm}. \tag{2.37}$$

The unit for the absorbed dose $D$ is Gray: $1$ Gy $= 1$ J/kg.
$D$ only depends on the deposited energy and is independent of the type of radiation, its energy and the linear energy transfer (LET). These attributes, however, play an important role for the effect on cells and have to be taken into account if the radiation's biological impact is to be estimated. Therefore, the ICRP introduced the equivalent dose $H_T$ which is the sum of absorbed doses $D_T$ in tissue or an organ $T$ caused by radiation type $R$ multiplied by the according radiation weighting factor $w_R$:

$$H_T = \sum_R w_R D_{T,R}. \tag{2.38}$$

The equivalent dose $H_T$ is measured in Sievert: $1$ Sv $= 1$ J/kg.
The different weighting factors reflect the relative biological effectiveness (RBE) of different radiation types by measuring the impact on biological tissue compared to low LET photons which have a radiation weighting factor $w_R = 1$ by definition. They estimate the effects of the given radiation type on the lifelong probability of developing lethal cancer. Two sets of radiation weighting factors recommended by the ICRP in 1990 and 2007 respectively are compared in Tab. 2.3. The results that are presented in this work are based on the older recommendations given in *ICRP* (1990). The reduction of the weighting factor of protons and the modification for neutrons would probably result in a decrease of the equivalent dose rates at aviation altitudes as the contributions of these particles are the most important.

Table 2.3: Radiation weighting factors according to *ICRP* (1990) and *ICRP* (2007).

| **Radiation type** | **Radiation weighting factor** $w_R$ | |
|---|---|---|
| | *ICRP* (1990) | *ICRP* (2007) |
| Photons | 1 | 1 |
| Electrons and muons | 1 | 1 |
| Protons and charged pions | 5 | 2 |
| Alpha particles, heavy ions | 20 | 20 |
| Neutrons (*ICRP*, 1990) | $w_R = \begin{cases} 5, & E_n < 1 \text{ keV} \\ 10, & 1 \text{ keV} \leqslant E_n \leqslant 100 \text{ keV} \\ 20, & 100 \text{ keV} < E_n \leqslant 2 \text{ MeV} \\ 10, & 2 \text{ MeV} < E_n < 20 \text{ MeV} \\ 5, & E_n > 20 \text{ MeV} \end{cases}$ | |
| Neutrons (*ICRP*, 2007) | $w_R = \begin{cases} 2.5 + 18.2e^{-(ln(E_n))^2/6}, & E_n < 1 \text{ MeV} \\ 5.0 + 17.0e^{-(ln(2E_n))^2/6}, & 1 \text{ MeV} \leqslant E_n \leqslant 50 \text{ MeV} \\ 2.5 + 3.25e^{-(ln(0.04E_n))^2/6}, & E_n > 50 \text{ MeV} \end{cases}$ | |

Another aspect that has to be taken into account for the definition of a whole body protection quantity in dosimetry is the sensitivity of different types of tissue or organs to the deposited equivalent dose $H_T$. For that reason the ICRP defined the tissue weighting factors $w_T$ ranging from 0.01 for skin and bone surface up to 0.20 for gonads (for details see *ICRP* (1990)). New weighting factors were introduced in 2008 in the new ICRP recommendations (*ICRP*, 2007). The most important change is that gonads have less weight now ($w_T = 0.08$). As in the case of radiation weighting factors values from *ICRP* (1990) for the weight of different types of tissue were used for the calculations in this work.
With the definition of the weighting factors the effective dose $E$ is given as the sum over all organ equivalent doses $H_T$ weighted by the $w_T$:

$$E = \sum_T w_T \cdot H_T = \sum_T w_T \cdot \sum_R w_R \cdot D_{T,R}. \tag{2.39}$$

The effective dose $E$ is also measured in Sievert (1 Sv = 1 J/kg).
It is not possible to directly measure the effective dose, and the dose equivalent $H$ (not to be mixed up with the equivalent dose $H_T$) is therefore used as operational quantity to estimate $E$. The dose equivalent $H$ is defined as the product of the absorbed dose $D$ with the quality factor $Q$. The latter is given as a function of the unrestricted linear energy transfer $L$ in water:

$$H = \int_0^\infty dL\, Q(L) \cdot \frac{dD(L)}{dL} \tag{2.40}$$

$$Q(L) = \begin{cases} 1, & L < 10 \text{ keV}/\mu\text{m} \\ 0.32L - 0.22, & 10 \text{ keV}/\mu\text{m} \leqslant L \leqslant 100 \text{ keV}/\mu\text{m} \\ 300/\sqrt{L}, & L > 100 \text{ keV}/\mu\text{m}. \end{cases} \tag{2.41}$$

The dose equivalent $H$ is measured in Sievert (Sv), just as the equivalent dose $H_T$ and the effective dose $E$.

The unrestricted linear energy transfer $L \equiv L_\infty = \left(\frac{dE}{dl}\right)_\infty$ is the energy lost by a charged particle $dE$ per path-length $dl$ due to collisions with electrons (see Eq. 2.26). The fact that the relative biological effectiveness of the traversing particle increases with increasing linear energy transfer below a certain threshold is expressed by Eq. 2.41. The decrease of the quality factor above $L = 100$ keV/$\mu$m is explained by the increasing probability of cell death and the related reduced probability for mutations in the DNA.
Two quantities derived from the dose equivalent are recommended by the ICRP: the individual dose equivalent $H_p(d)$ for personal dosimetry and the ambient dose equivalent $H^*(d)$ for area monitoring.
The ambient dose equivalent $H^*(d)$ is defined by *ICRU* (1985) as "[...] the dose equivalent that would be produced by the corresponding aligned and expanded field, in the ICRU sphere at a depth, d, on the radius opposing the direction of the aligned field". The ICRU sphere is defined to have a diameter of 30 cm and to be filled with tissue-equivalent composition of 76.2% oxygen, 11.1% carbon, 10.1% hydrogen and 2.6% nitrogen with a density of 1 g/cm$^3$. $H^*(d)$ is most commonly used for a depth $d = 10$ mm and accordingly $H^*(10)$ is the standard operational quantity for radiation protection in aviation.
The effective dose and the dose equivalent are used for the estimation of stochastic radiation effects in contrast to deterministic effects. The latter only occur above a certain threshold of a single short-time exposure and the severeness increases as the exposure increases. In *ICRP* (2007) several thresholds for deterministic effects are estimated for an 1 % occurrence, e. g. an absorbed dose $D \approx 0.1$ Gy in testes for temporal sterility, an absorbed dose $D \approx 0.5$ Gy in bone marrow for depression of blood-forming processes or an absorbed dose $D \approx 6$ Gy in the lung for developing pneumonia.
The risk for stochastic effects on the other hand is postulated to accumulate after a series of low exposures. This approach is based on the assumption that the probability for developing cancer or heritable diseases increases linear with dose and has no threshold at low exposures (linear no threshold theory, LNT). Even though no evidence exists neither for or against the LNT for low doses it is used in the ICRP recommendations for absorbed doses below 100 mGy. Following the LNT allows to sum up the effective doses and dose equivalents from a series of exposures to estimate a life-time probability for radiation induced stochastic effects.
The goal of this work is to numerically determine dose rates at aviation altitudes from the radiation environment induced by primary galactic and solar cosmic rays, and consequently the quantities presented above have to be calculated. For this purpose Monte-Carlo simulations (see Ch. 3 and Ch. 4) were used to determine secondary particle fluences at the point of interest, and from the secondary particle fluences the dosimetric quantities are derived. This can be done by using so-called fluence to dose conversion factors. For an incident fluence of a particle $p$ with kinetic energy $E_k$, *Ferrari et al.* (1996, 1997b,c,d, 1998)[13] used the Monte-Carlo code FLUKA (*Ferrari et al.*, 1992; *Ferrari et al.*, 2005; *Battistoni et al.*, 2007) to calculate the individual effective doses for different irradiation

[13] http://www.lnf.infn.it/lnfadmin/radiation/conversioncoefficient.htm

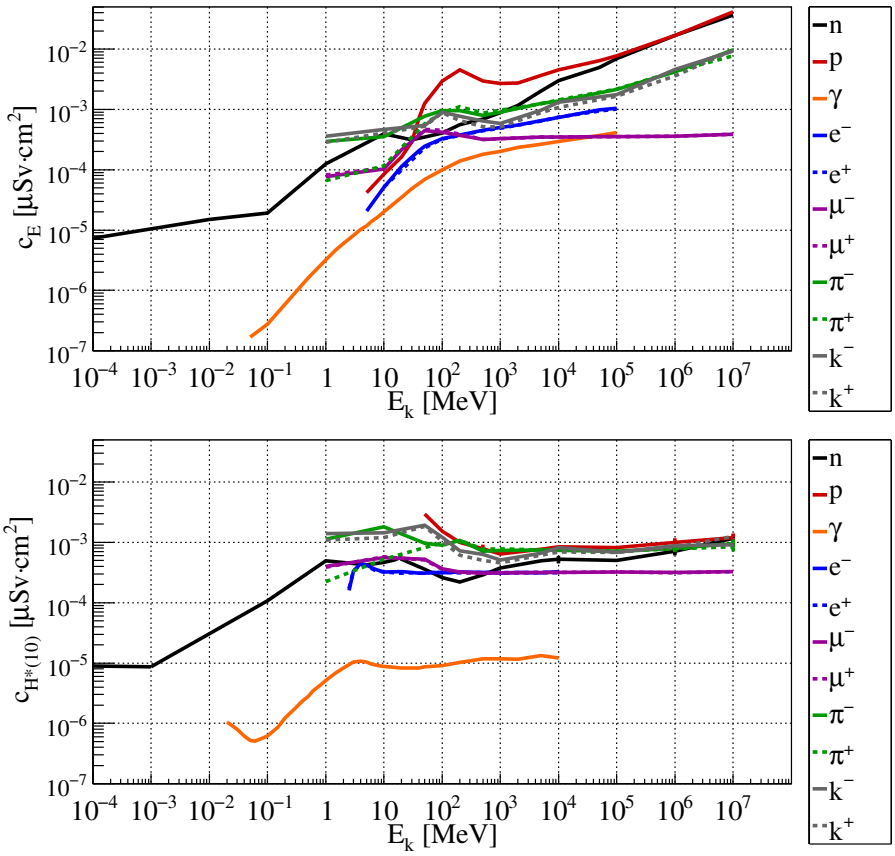


Figure 2.8: Fluence to dose conversion factors for effective dose $E$ in an isotropic radiation field (top) and ambient dose equivalent $H^*(10)$ (bottom) for all relevant particles from *Ferrari et al.* (1996, 1997a,b,c,d, 1998).

geometries and dose equivalents inside a human phantom model. The resulting fluence to dose conversion factors ($c_E$ for effective dose and $c_{H^*(10)}$ for the ambient dose equivalent) are illustrated in Fig. 2.8.
By using these conversion factors the effective dose $E_p$ for a continuous differential fluence of particle $p$ with respect to kinetic energy and the total effective dose $E$ from all contributing particles can be calculated by:

$$E_p = \int_{E_{k,min}}^{E_{k,max}} dE_k \; c_E^p(E_k) \cdot \frac{dF^p(E_k)}{dE_k}, \tag{2.42}$$

$$E = \sum_p E_p. \tag{2.43}$$

$E_p$ is the effective dose caused by particle type $p$ in the energy range from $E_{k,min}$ to $E_{k,max}$ and $c_E^p$ is the fluence to dose conversion factor for particle type $p$.
If the energy range from $E_{k,min}$ to $E_{k,max}$ is divided into energy intervals $\Delta E_{k,j} \equiv [E_{k,j}, E_{k,j+1}]$, the effective dose can be approximated from a discrete fluence distribution as the sum over all energy intervals $\Delta E_{k,j}$ of the particle's fluence in this interval times the conversion factor for this energy interval, given that the energy interval is small and both the conversion factor and the differential fluence

are approximately constant over the interval:

$$E = \sum_p \sum_j c_E^p(E_{k,j}) F^p(\Delta E_{k,j}). \tag{2.44}$$

The same formulas can be used for the ambient dose equivalent with the corresponding conversion factors:

$$H^*(10) = \sum_p \int_{E_{k,min}}^{E_{k,max}} dE_k \; c^p_{H^*(10)}(E_k) \cdot \frac{dF^p(E_k)}{dE_k}, \tag{2.45}$$

$$H^*(10) = \sum_p \sum_j c^p_{H^*(10)}(E_{k,j}) \cdot F^p(\Delta E_{k,j}). \tag{2.46}$$

## 2.7 The Neutron Monitor Network

The world-wide network of ground based Neutron Monitor stations is one of the most useful and most widely used tools to study Ground Level Enhancements and their impacts on the radiation exposure in aviation. Information about galactic or solar cosmic rays is obtained by measuring secondary particle intensities produced in interactions of the primary particles with the atmosphere. As the name implies the Neutron Monitor stations are especially sensitive to secondary neutrons. The variation of the Neutron Monitor count rate reveals information about the galactic and solar cosmic ray intensity as well as the structure of and changes in the heliosphere and the geomagnetic field of the Earth. The network contains a changing number of Neutron Monitors at various geomagnetic locations (see Fig. 2.9) and altitudes. By analyzing the count rates of Neutron Monitor stations at different positions it is possible to gain information about the energy and angular distribution and the temporal variation of primary cosmic ray particles outside the magnetosphere, on top of the atmosphere and the distribution of secondary particles caused by the interactions of primary particles with atoms in the air. A good model for each parameter influencing the Neutron Monitor's output, such as the geomagnetic field, the composition of the atmosphere and the transport of particles is needed to derive this information. Moreover, to obtain reliable results it is inevitable to analyze a multitude of stations. The information provided by one Neutron Monitor is a single count rate caused by all particles and energies that it is sensitive to. Therefore, no spectral or angular information can be derived from one Neutron Monitor station alone. On the other hand, it is possible to gain information about primary particle energies, anisotropies and incoming directions by making use of the altitude and latitude dependence of the count rate.

Mainly two different types of detectors are used at the Neutron Monitor stations, namely the IGY and the nowadays more common NM64 monitor, which were developed in the late 1950s and early 1960s respectively. The detectors were designed to study the nucleonic component of cosmic primary and secondary particles (*Hatton*, 1971). Therefore, environmental influences from the environment of the station had to be minimized by avoiding influences of thermal and subthermal neutrons on the detector's count rate. These very low energetic neutrons are highly dependent on deviations in atmospheric pressure and the conditions in the surrounding of the Neutron Monitor station.

Both types, IGY and NM64, use proportional counters in an array of detector tubes filled with boron trifluoride ($BF_3$) and surrounded by an inner moderator made of paraffin (IGY) or polyethylene (NM64). The inner moderator is additionally enclosed by a producer made of lead and the producer is again surrounded by the reflector made of paraffin in the case of IGY monitors or polyethylene in NM64 detectors. Low energy neutrons, charged particles and photons are absorbed, attenuated and reflected in the outer part of the detector, therefore called the reflector, reducing the sensitivity of the Neutron Monitor to thermic neutrons. Due to the much thinner reflector layer of the NM64 type monitor, the influence of lower energetic particles especially neutrons on this detector type is larger than in the case of the IGY design and consequently the

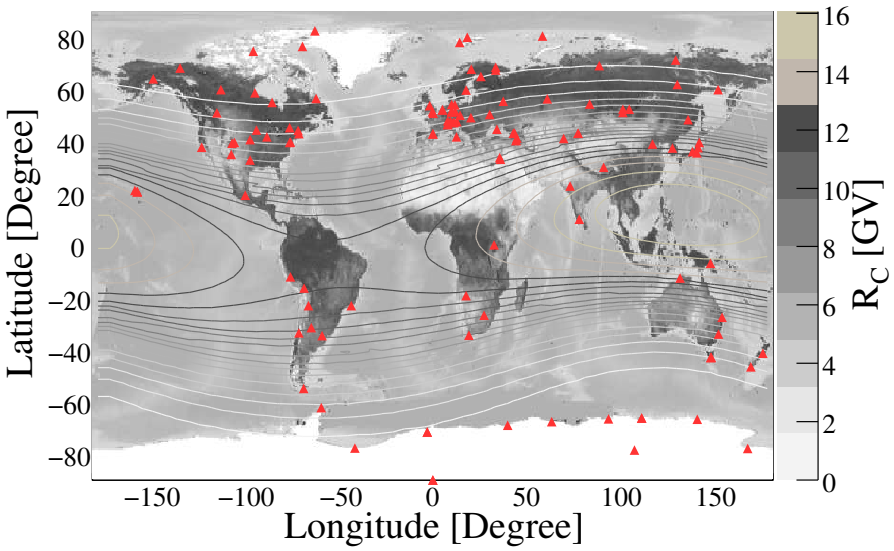


Figure 2.9: Positions of Neutron Monitor stations for which information is available together with lines of equal rigidity calculated for the year 2005 and with the IGRF eccentric dipole model. Many of the stations illustrated on the map provided data only for a very short time. The cut-off ranges from 0 GV at the geomagnetic poles up to 16 GV in south Asia.

detector exhibits an increased sensitivity to environmental conditions. Important factors influencing the count rate are for example the amount of water in the soil surrounding the detector station, snow- and rainfall or snow in the proximity.
For the detection of the neutrons in the proportional counter the neutron capture of a boron nucleus and the subsequent alpha decay to a lithium nucleus and an alpha particle is used (*Simpson*, 2000):

$$ {}^{10}_{5}\mathrm{B} + n \rightarrow {}^{11}_{5}\mathrm{B}^{*} \rightarrow {}^{7}_{3}\mathrm{Li} + {}^{4}_{2}\mathrm{He}^{++} \tag{2.47} $$

The reaction cross section is inversely proportional to the neutron velocity $1/v$ and thus decreasing with incident neutron energy ranging from approximately $6 \cdot 10^3$ b at $10^{-2}$ eV to $0.2$ b at 1 MeV (from JENDL-3.3, *Shibata et al.* (2002)). Sufficiently highly energetic neutrons can reach the moderator from outside the detector by penetrating the reflector and the producer or may originate from interactions of neutrons or other particles incident on the detector with nuclei in the material surrounding the tubes. The main source of these secondary neutrons is the producer due to the high neutron content in the lead nuclei.
By traversing the moderator, the neutrons are slowed down which leads to a higher reaction probability in the detector tube and consequently the count rate statistics of the detector is increased. *Clem and Dorman* (2000) have estimated the detector efficiencies for neutrons, protons, pions and muons incident on an NM64 detector (Fig. 2.10), i. e. the detector counts caused by a particle fluence of 1 $\mathrm{cm}^{-1}$ of the given species at a certain energy.
The main contribution to the total detector count rate is given by incident neutrons and protons. For a NM64 (IGY) detector *Hatton* (1971) estimated that

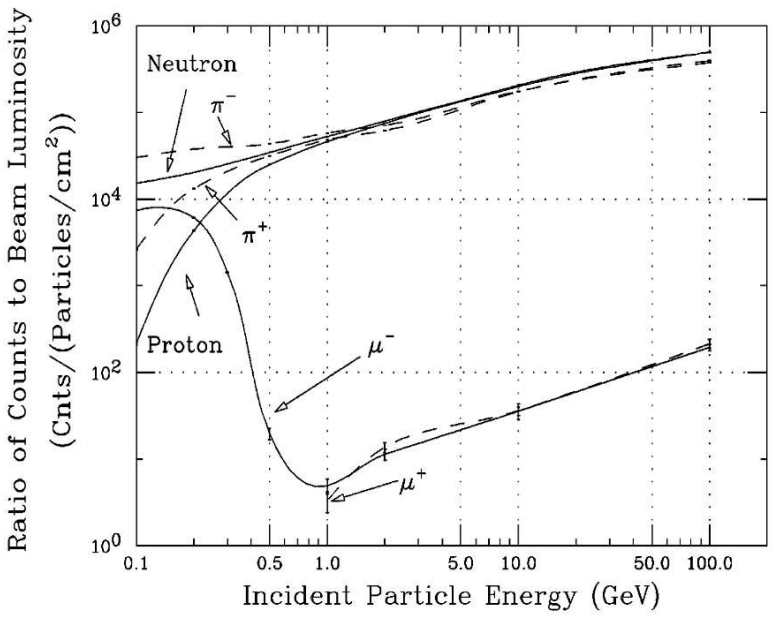


Figure 2.10: Detection efficiencies for a NM64 Neutron Monitor calculated by *Clem and Dorman* (2000).

85.2% (83.6%) of the Neutron Monitor counts are caused by neutrons and 7.2% (7.4%) by protons. The remaining fraction is given by pions and muons and the background rate which *Hatton* (1971) estimated to be in the order of 1%.
From Fig. 2.10 it is obvious that at high energies mainly secondary neutrons produced by nuclear interactions from protons and neutrons are responsible for the detector counts. The neutron and proton efficiencies are identical which would not be the case if electromagnetic interactions played a role. At energies below 1 GeV, on the other hand, the proton efficiency drops heavily due to the increasing stopping power caused by the electromagnetic interactions in the matter surrounding the detector tube. Detection efficiencies for the IGY type monitor were also estimated by *Clem and Dorman* (2000) and alternatively for both types by *Hatton* (1971). As the NM64 Neutron Monitor is the more common detector the analysis in this work is restricted to this type.
The Neutron Monitor's sensitivity to secondary neutrons produced by high energy particles entering the atmosphere makes it possible to indirectly study the variations in primary particles' intensities and the underlying phenomena. The largest periodic variation in the count rate is caused by modifications in the galactic cosmic ray intensities during the eleven year solar cycle. Other periodicities in the Neutron Monitor count rate reflect for example the 26 day rotation period of the Sun or daily variations caused by the asymmetry in the magnetosphere. The increase in secondary particle intensities during Ground Level Enhancements can lead to sharp increases of Neutron Monitor count rates up to several thousand percent above background. This is the basis of the analysis of solar energetic particle events presented in Chapter 4. A detailed study of the responses of Neutron Monitors to galactic cosmic rays and the variation of count rates with altitude, latitude and solar activity is presented in Section 3.6.

# Chapter 3

# Particle transport with PLANETOCOSMICS/GEANT4

The major part of this work is dedicated to the estimation of secondary particle fluences in the atmosphere caused by primary cosmic particles of galactic and solar origin and derived quantities as radiation dose and Neutron Monitor count rates. A variety of models exists for the description of galactic cosmic rays arriving at the earth's magnetosphere (Sec. 2.1). The output of these models is used as a starting point for the calculations performed in this and the following chapter. The primary particles entering the magnetosphere are subject to deviations and scattering in the magnetic field and after penetrating the atmosphere the particles interact with atoms in the air suffering energy-loss and producing secondary particles which again may collide with atmospheric particles forming a cascade of secondary particles. These secondary particles are the primary cause for the increased radiation levels at higher altitudes in the atmosphere.
The calculation of the primary particle spectra after traversing the magnetosphere and the propagation of particles in the atmosphere was calculated with the PLANETOCOSMICS tool-kit (*Desorgher*, 2006) providing a detailed description of the geometry of and different models for the atmosphere and the magnetosphere of the Earth. PLANETOCOSMICS is based on the GEANT4 Monte-Carlo package (*Agostinelli et al.*, 2003).
A short description of the Monte-Carlo method, the GEANT4 and PLANETOCOSMICS code is given in the following sections. Calculations of secondary particle fluences and derived dose rates from galactic cosmic rays are presented and compared to measurements in order to verify the results of the transport calculations.
Data of the Neutron Monitor network is used in Chapter 4 for the analysis of solar energetic particle events causing enhancements in the detector count rates. The increase in the secondary particle intensities have to be related to the measurements of the Neutron Monitor stations and it is therefore inevitable to study the sensitivity of the detectors to the energy of primary particles, the cut-off rigidity and the atmospheric depth. A detailed investigation of simulated Neutron Monitor count rates compared to measurements for galactic cosmic ray particles is presented in Section 3.6.

## 3.1 The Monte-Carlo Technique

Every measurable particle traversing a volume filled with matter may interact with the material in the volume in different ways. Depending on the kind of interaction it may be scattered, loose energy and produce secondary particles. Mainly two approaches exist to simulate these processes and the transport of particles through a defined geometry, namely deterministic transport calculations and the Monte-Carlo method. The GEANT4 software which is used in this work is based on the latter. The Monte-Carlo approach uses the fact that the interactions of particles with matter can be described by probability distributions which are sampled by drawing random numbers. In this way the type of interaction and the final state is determined, and the fact that the technique is based on drawing random numbers gives the Monte-Carlo method its name. The basic idea of simulating the particle interactions and transport by means of Monte-Carlo simulations is given below.
The starting point is a particle with a given momentum in a defined geometry. The probability of the particle to interact with the ambient matter is described by the total cross section $\sigma_T$ which is composed of all partial cross sections $\sigma_i$ quantifying the individual concurring interactions $i$ of the particle with the ambient matter:

$$\sigma_T = \sum_{i=1}^{n} \sigma_i, \tag{3.1}$$

where $n$ denotes the number of all possible interactions. As noted above, the mean free path of the particle to the next interaction point is given by $\lambda = 1/(N\sigma_T)$, where $N$ is the number of scattering centers per volume. The cumulative distribution function describing the number of free paths $n_\lambda$ of an individual particle before interacting is given by (*Nelson et al.*, 1985):

$$P(n_r < n_\lambda) \quad = \quad 1 - \exp\left(-n_\lambda\right). \tag{3.2}$$

$P(n_r < n_\lambda)$ is the probability that the length of the path of the particle before interacting is shorter than $n_\lambda$. The cumulative distribution function can be sampled by a random number generator producing a random number $\xi$ uniformly distributed between zero and unity, and the number of mean free paths is then given by:

$$n_\lambda \quad = \quad -\ln\left(1-\xi\right) \tag{3.3}$$

or equivalently

$$n_\lambda \quad = \quad -\ln\left(\xi\right). \tag{3.4}$$

By drawing a random number the path length to the next interaction point is determined, and once the interaction point is defined it has to be decided which of the concurring interactions $i$ occurred. The distribution function $F(i)$ describing the probability of an interaction $i$ to occur is given by

$$F(i) \quad = \quad \frac{\sum_{j=1}^{i} \sigma_j}{\sigma_T} \tag{3.5}$$

with the partial cross sections $\sigma_j$ and the total cross section $\sigma_T$. By drawing another random number $\zeta$ the type of interaction can be chosen by selecting the $i$ satisfying $F(i-1) < \zeta < F(i)$.
In the next step the final state of the interaction has to be determined. The state of the projectile, the target and possible secondary particles can be described by a set of $n$ parameters $x_k$ with $1 \leqslant k \leqslant n$, for example the momenta of the particles, the scattering angle, etc. The differential cross section for the process in the final state $\vec{x} = (x_1, ..., x_n)$ is $d^n\sigma_i(x_1, ..., x_n)/dx_1...dx_n$, and the cross section $\sigma_i$ for the interaction $i$ is given by the integral over all $x_k$:

$$\sigma_i = \int dx_1 ... \int dx_n \, \frac{d^n\sigma_i(x_1, ..., x_n)}{dx_1...dx_n}. \tag{3.6}$$

In general, the differential cross section $d^n\sigma_i(x_1, ..., x_n)/dx_1...dx_n$ for the interaction $i$ depends on the projectile, its energy and the target. One can define a normalized function

$$f(x_1, ..., x_n) = \frac{d^n\sigma_i(x_1, ..., x_n)/d^nx}{\sigma_i} \tag{3.7}$$

which can be sampled to determine the final state $\vec{x}$ of the reaction (see *Nelson et al.* (1985)). Once these parameters are given one can start from the beginning by determining the next interaction point as described above.
All secondary particles produced in such an interaction are then also treated as described above, and all particles are transported until they leave a defined geometry or the energy drops below a certain threshold usually defined by the user or the applicability of the physics models.
Apart from the simulation of the discrete interactions like scattering and decay of particles, continuous processes have to be taken into account. Moreover, the step size of the particles has to be limited to assure that the total cross section remains constant during one step. For a more detailed description of Monte-Carlo techniques see (*James*, 1980; *Sjöstrand et al.*, 2006; *Nelson et al.*, 1985).

## 3.2 PLANETOCOSMICS and GEANT4

The PLANETOCOSMICS[1] tool for the transport of particles through the magnetosphere and the atmosphere of the Earth was developed by L. Desorgher and is based on the GEANT4 Monte-Carlo package. It provides implementations of the geometry for the magnetosphere and the atmosphere of the Earth and other planets. Both for the atmosphere and the magnetosphere different models are available to choose from. The code was developed to calculate the propagation of charged particles in the magnetospheres of planets and the subsequent interactions of the primary particles with the atmosphere in order to derive the secondary particle production and energy deposition in the atmosphere. The software can either be run by using the incorporated galactic cosmic ray particle spectra by *Garcia-Munoz et al.* (1975) or by defining an arbitrary spectrum.

[1] http://cosray.unibe.ch/ laurent/planetocosmics/

Thereby it is possible to use different galactic cosmic ray models or spectra for solar energetic particles as primary sources.
For the geometry of the atmosphere one can choose from a spherical shell structure or a flat geometry arranged in layers of equal pressure, temperature and composition. For the calculations in this work the latter was chosen. The arising differences in path length for particles in non vertical incident directions for a flat geometry with respect to the spherical geometry is in the order 1% for a zenith angle of 40° and about 4% for a zenith angle of 70° . Therefore, a small error is introduced by using the approximation of a flat surface of the Earth. However, as primary particles arriving at larger zenith angles also have an increased path length with respect to vertically incident particles, the contribution of the former to the radiation in the lower atmosphere is minor. A particle arriving at 70°, for example, has a threefold longer path to reach a certain altitude. The influence of the chosen geometry on the secondary particle intensities was studied during this work, and it was found that the differences are negligible. In this analysis the atmosphere was considered up to an altitude of 200 km consisting of 86 layers, and the initial altitude of primary particles was set to 180 km above ground.
Additionally, PLANETOCOSMICS allows to define the composition and extent of the soil and its altitude above ground. The composition of the soil plays an important role for albedo particles produced by interactions in the soil or consisting of back scattered incoming particles. Here, the soil was chosen to consist of 10 m pure water (mass fractions: 11.2% hydrogen, 88.8% oxygen; density 1 g/cm$^2$) at sea-level altitudes. The particle transport below the soil, i.e. in this case 10 m below ground, is stopped and no further propagation and secondary particle production is considered.
To simulate the interactions of the primary particles with the atmosphere in PLANETOCOSMICS one can choose from a variety of models provided by the GEANT4 software describing the interactions of primary and secondary particles with the atmosphere. For most applications and especially for shielding and dosimetric calculations the GEANT4 collaboration suggests the use of either of the two model lists[2]: *QGSP_BIC_HP* or *QGSP_BERT_HP*. These include an implementation of the quark-gluon-string-precompound model (QGSP) for the inelastic interactions of protons, neutrons, pions and kaons with atomic nuclei at energies above 10 GeV. At lower energies the inelastic interactions are modeled either by the Binary Cascade (BIC) or Bertini (BERT) model of subsequent two particle interactions between the projectile and the nucleons contained in the target nucleus. The transport of neutrons below 20 MeV is treated by the neutron high precision (HP) model. Electromagnetic interactions are calculated with the Standard EM model provided by GEANT4. Details about these and other available model packages can be found in the GEANT4 "Physics reference manual"[3] and in the model catalog[4]. In the following sections the results of transport calculations using either the Bertini or the Binary Cascade model are presented and tested against experimental data to find the most appropriate model to calculate

[2] http://geant4.web.cern.ch/geant4/support/proc_mod_catalog/physics_lists/useCases.shtml
[3] http://geant4.web.cern.ch/geant4/support/userdocuments.shtml
[4] http://geant4.web.cern.ch/geant4/support/proc_mod_catalog/index.shtml

the transport of particles through the atmosphere.
A weakness of the GEANT4 Monte-Carlo package is the lack of a model describing the inelastic nucleus-nucleus interactions at energies above 10 GeV per nucleon. This means that for an alpha particle the energy is restricted to values smaller than 40 GeV. Although this is more than enough for most applications, for the calculation of galactic cosmic ray particles which have kinetic energies of hundreds of GeV and more it is not sufficient. Therefore, the implementation of an interface developed by *Koi et al.* (2003) for GEANT4 to the JQMD/JAM model (*Niita et al.*, 1995; *Nara et al.*, 1999) for the inelastic nucleus-nucleus interactions at very high energies is used to obtain the results presented in the following chapters. This model was implemented in the GEANT4/PLANETOCOSMICS framework. The influence of ions heavier than helium and the contribution of helium at energies $E > 10$ GeV/nucleon was investigated in the course of this work for atmospheric secondary particle fluences and for shielding calculations in open space (*Sihver et al.*, 2008).
In order to determine secondary particle intensities, several altitudes in the atmosphere were selected, and the corresponding quantities as particle fluence and energy deposition were calculated. To obtain the values of these quantities at intermediate altitudes the results for the next higher and lower altitude were interpolated. A list of the chosen altitudes can be found in App. B labeled by the command */PLANETOCOS/GEOMETRY/DetectorAtAltitude*.
The results presented in the following chapters have been obtained using PLANETOCOSMICS 2.0 in combination with GEANT-4.9.1 patch 02. An exemplary PLANETOCOSMICS macro file as it was used for the calculations of secondary particle intensities in this work is shown App. B. This specific macro file was used to calculate the transport of primary protons with kinetic energies from 100 MeV to 108 MeV through the atmosphere and the resulting secondary particle production at several altitudes using the Bertini model.

## 3.3 Transport in the Magnetosphere

The magnetosphere acts as a natural obstacle for charged particles from interplanetary space. Before the primary particles can enter the atmosphere they are subject to the deviations in the magnetic field in the vicinity of the Earth (Fig. 3.1), and as a consequence the intensity of charged particles on top of the atmosphere is reduced with respect to interplanetary space. To estimate this shielding effect of the magnetic field it is helpful to characterize particles by their magnetic rigidity $R$ rather than their energy as the impact of the Lorentz force on a charged particle is related to the former quantity. In the following the shielding effect of the magnetosphere on a charged particle will be expressed in relation to the particles rigidity.
The magnetosphere has a very complex structure and a variety of models exist for the description of its form, extent and field strength. The International Geomagnetic Reference Field[5] was released in the 10th generation (IGRF-10) in 2005 and models the magnetic field of the Earth from internal sources (*Maus*

[5] http://www.ngdc.noaa.gov/IAGA/vmod/igrf.html

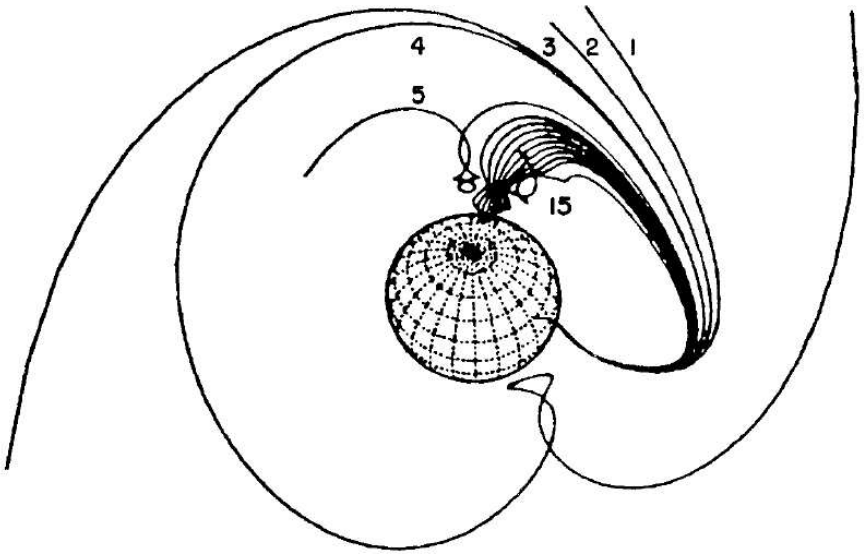


Figure 3.1: Particle trajectories for different rigidities and vertically incident particles on top of the atmosphere adapted from *Smart et al.* (2000). The largest rigidity labeled by 1 is showing the smallest deviation. Decreasing rigidities are marked by increasing numbers.

*et al.*, 2005) for the years 1900–2010. The magnetic field in this model is approximated by the negative gradient of the potential $V$ expressed in spherical harmonics:

$$V(r,\theta,\lambda,t) \;=\; R\sum_{n=1}^{n_{max}}\left(\frac{R}{r}\right)^{n+1}\sum_{m=0}^{n}[g_n^m(t)\cos(m\lambda)+h_n^m(t)\sin(m\lambda)]P_n^m(\theta),$$

where $P_n^m(\theta)$ are the semi-normalized associated Legendre functions of degree $n$ and order $m$, $(r,\theta,\lambda)$ are the geocentric coordinates of the point of interest at time $t$. $g_n^m$ and $h_n^m$ are the coefficients published by the International Association of Geomagnetism and Aeronomy (IAGA) every five years (for detail see (*Maus et al.*, 2005; *MacMillan and Maus*, 2005) and references therein).
Apart from the IGRF which describes the internal dipole like field of the Earth, various models exist to treat the influence of external sources on the magnetosphere (*Tsyganenko*, 1989, 1995, 2002). In this chapter the model described in *Tsyganenko* (1989) (TSY89) will be studied in addition to the IGRF model. The TSY89 aims to model the magnetosphere by incorporating a description of the tail current sheet on the night side of the Earth, the ring currents and the boundary of the magnetosphere. It provides a parametrization for modeling geomagnetic storms with seven states related to the $k_p$ index which is an indicator for the severeness of a geomagnetic storm. It has been shown that the shielding effect of the magnetic field of the Earth is reduced during geomagnetic storms, i.e. for large $k_p$ (*Leske et al.*, 2001; *Smart et al.*, 2006).
As noted above, charged particles are characterized by their magnetic rigidity $R$ to address the question about the influence of the magnetosphere. Particles with a given rigidity are subject to the same forces and propagate along the same path

in a magnetic field. To perform the calculations of the interaction of primary particles with the atmosphere for a certain location it is necessary to know the particle intensities on top of the atmosphere at that point after the propagation through the magnetosphere. In addition to the rigidity and the geographic position the incident direction of the primary particles on top of the atmosphere define their preceding path through the magnetosphere. Not all incoming directions are accessible for all magnetic rigidities, and to determine the allowed arriving directions for particles having a certain rigidity $R$ so-called backward calculations of inversely charged particles are performed for a range of outgoing directions starting at the point of interest on top of the atmosphere as illustrated in Fig. 3.1. If these mirror particles can leave the magnetosphere it can be concluded that the original particles have access to the location from outside the magnetosphere propagating along the same path in opposite direction.
For a specific geographic location and for particles with a fixed rigidity the influence of the Earth's magnetic field divides the space of all possible incoming directions into three domains, namely the forbidden cone, the penumbra and the allowed cone. As the name implies no particles can arrive from directions lying in the forbidden cone as these particles are either reflected by the magnetic field or captured in periodical orbits in the field. On the other hand, all particles arriving from directions lying in the main cone have access to the location of interest. The penumbra being located between these two regions contains directions that can be both forbidden and allowed for charged particles (for details about the terminology and the structure of the different regions see (*Cooke et al.*, 1991) and references therein).

### 3.3.1 The Cut-off Rigidity

A quite simple approach to estimate the influence of the geomagnetic field on the primary particle intensity on top of the atmosphere is the concept of the effective cut-off rigidity $R_C$. The cut-off rigidity is used as the lower threshold for particles accessing a certain point on top of the atmosphere, and it is assumed that particles with rigidities below the effective cut-off rigidity $R < R_C$ are deflected by the magnetic field of the Earth or trapped in periodic orbits without reaching the atmosphere. Particles above the threshold, on the other hand, can reach the point of interest, penetrate into the atmosphere and have to be taken into account for transport calculations and the estimation of secondary particle intensities in the atmosphere.
For a given arrival direction on top of the atmosphere and a specific location characterized for example by magnetic or geographic coordinates the possible rigidities can be grouped into three classes:

- $R \leqslant R_L$: At rigidities smaller than the lower cut-off rigidity $R_L$ **no** particles have access to the location.

- $R \geqslant R_U$: At rigidities above the upper cut-off rigidity $R_U$ **all** particles have access to the location.

- $R_L < R < R_U$: The so-called penumbra region for rigidities in the range between the lower and the upper cut-off rigidity. In this interval some rigidities allow access to the location whereas others do not.

The effective cut-off rigidity $R_C$ lying in the penumbra region between $R_L$ and $R_U$ is usually used for practical purposes. To determine these quantities for a specific location calculations are performed over a wide range of rigidities in small steps of $\Delta R$, and the access of a particle to the atmosphere is tested for each case. $R_L$ is approximated by the largest rigidity below the lowest value allowing access to the location of interest. Accordingly, the lowest value above the largest rigidity for that particles can not reach the atmosphere provides an estimation for $R_U$. The effective cut-off rigidity is approximated by

$$R_C \quad = \quad R_U - \sum_{R_L}^{R_U} \Delta R_i(allowed), \tag{3.8}$$

where the sum takes into account all values of $\Delta R_i(allowed)$ that provide access to the atmosphere. For simplicity the effective cut-off rigidity will be referred to as the cut-off rigidity in the following if not stated otherwise.
In a first approach the cut-off rigidity for vertically incident particles on top of the atmosphere is studied, and the relation of the vertical to non-vertical cut-off rigidities is investigated in the following section.
Therefore, the vertical cut-off rigidities were calculated for a grid of geograph-

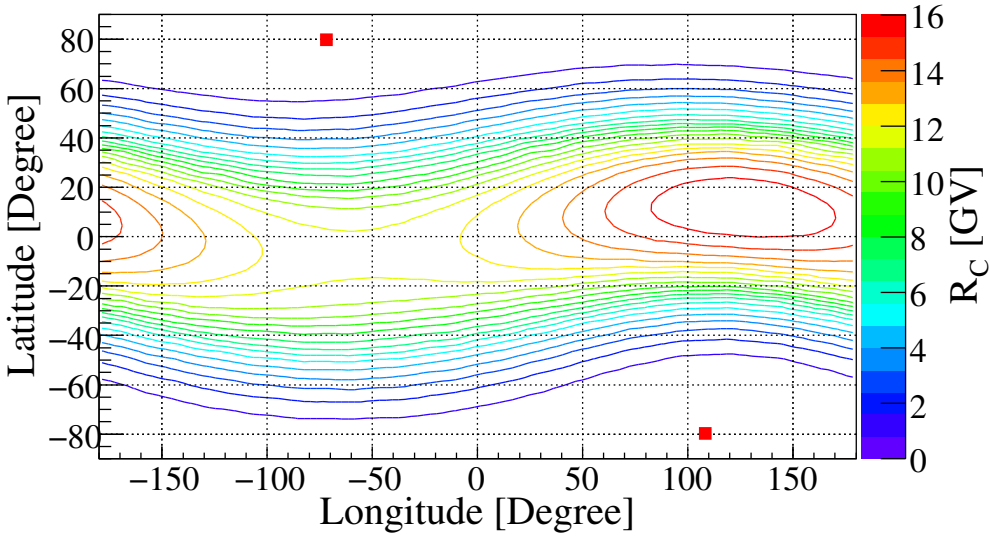


Figure 3.2: Vertical cut-off rigidities $R_C$ versus the geographic location for the year 2005 calculated with PLANETOCOSMICS using the IGRF-10 model. The red squares mark the position of the magnetic poles at that time.

ical coordinates over the whole globe using the IGRF-10 model to describe the magnetosphere. The results are illustrated in Fig. 3.2 and reveal the characteristic pattern with low cut-off rigidities ($R_C \approx 0$ GV) near the poles and the largest values at low latitudes ($R_C \approx 12$ GV–16 GV). The asymmetric distribution around the equator mirrors the tilt of the axis of the magnetic dipole field

of the Earth with respect to the axis of rotation. In the year 2005, for example, the magnetic pole on the northern hemisphere was located at (79.7°N, 71.8°W). The red squares in Fig. 3.2 indicate the position of the magnetic poles in 2005. The additional longitudinal asymmetry of the cut-off rigidities along the equator with maximum values in the south Asian region is a consequence of the shift of the dipole axis with respect to the center of the Earth.
The cut-off rigidities for a selection of Neutron Monitor stations around the world as calculated with different models and provided by the IZMIRAN data base are compared to each other in Fig. 3.3. The explanation of the abbreviations of the names, the geographic coordinates of the stations and additional information are summarized in App. A. Apart from the data provided by IZMIRAN for

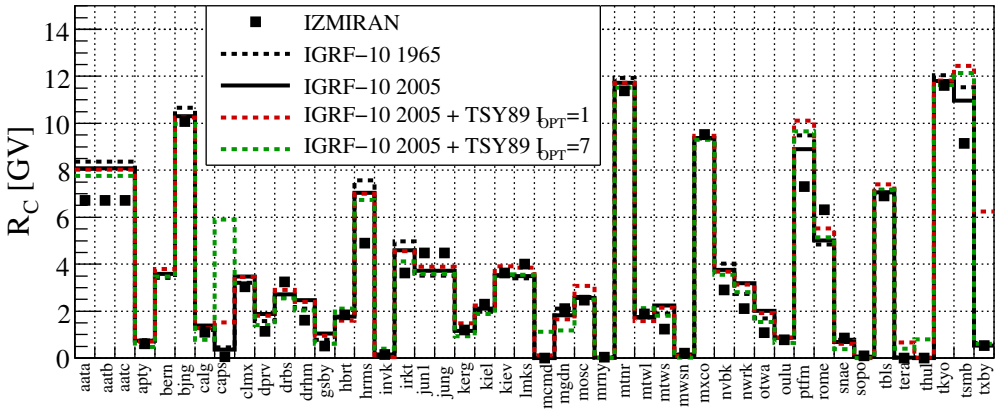


Figure 3.3: Vertical cut-off rigidities for Neutron Monitor stations calculated with PLANETOCOSMICS using the IGRF-10 model with and without the Tsyganenko-1989 model for the magnetosphere and as provided by IZMIRAN (for abbreviations and details about the Neutron Monitor stations see App. A).

the year 1965, the figure contains the results using the IGRF-10 model for the year 1965 and 2005 (labeled by IGRF-10) and a combination of IGRF-10 and TSY89 for the year 2005 (labeled TSY89) for minimal ($I_{OPT} = 1$ corresponding to $k_p = 0$) and maximal geomagnetic disturbance ($I_{OPT} = 7$ corresponding to $k_p > 6$) at the time 12:00 UTC. For most stations, the results from the different simulations are very similar, and in many cases they show good agreement with the data from IZMIRAN. The results for the year 2005 and 1965 differ by up to 10%. In some cases, however, unrealistic results are obtained from the simulations including the TSY89 model, e.g. Cape Schmidt (caps) and Tixie Bay (txby), where the calculated cut-off rigidities are much too high. A lot of effort was put into investigating these discrepancies without finding their origin. Neither changing the incoming angle of the particle nor increasing the accuracy of the simulation by choosing smaller steps in the integration of the particle's path had a significant influence on the observed effect which occurs at locations with local times of around 3 UTC–6 UTC, i.e. at the morning side of the Earth. It may be suspected that this effect is related to the modeling of the boundary between the solar wind upstream and downstream side of the magnetosphere. The possibility that this increase of the cut-off rigidity is a real effect can be rejected as no

related changes in Neutron Monitor count rates are observed. It was concluded that the TSY89 model at least as it is implemented in PLANETOCOSMICS has to be taken with care for the calculation of charged particle trajectories in the magnetosphere. The differences between the year 1965 and 2005 on the other hand are minor but temporal changes derived from the IGRF-10 model are considered in the following. For the rest of this work the analysis will be restricted to calculations performed with the IGRF-10 model alone.

### 3.3.2 Directional Cut-off Rigidities

Vertical cut-off rigidities for locations over the whole globe and for several Neutron Monitor stations in particular were presented in the previous section. Now, the question arises if the vertical cut-off is a good estimation for non-vertical cut-off rigidities for particles arriving from arbitrary directions at a specific location, for example at a Neutron Monitor station. To answer this question, calculations were performed to determine the cut-off rigidity for all arrival directions at several Neutron Monitor sites. For this purpose particles arriving from zenith angles $Z$ in the range $0° < Z < 90°$ in steps of 5° and azimuth angles $A$ in the range from $0° < A < 360°$ in steps of 15° were included in the simulation. The azimuth is given as the angle between the projection of the particle's incoming direction in the horizontal plane and the northward direction which means that an azimuth angle of 0° represents northward direction, 90° represents eastward direction, etc. The IGRF-10 model for the year 2005 was used to calculate the directional cut-off rigidities in dependence of the azimuth and zenith angle. The results for different stations are illustrated in Fig. 3.4 ordered by increasing vertical cut-off rigidities from left to right and from top to bottom. The McMurdo station with a vertical cut-off rigidity of $R_C \approx 0$ GV in the top left panel shows no variation related to the particle's incoming direction. At slightly higher vertical cut-offs in the order of 1 GV (Oulu and Kerguelen Neutron Monitors) an increase in the cut-off at very large zenith angles is observed. This phenomenon, however, is restricted to zenith angles larger than 80° and to a small range in the azimuth angle. The impact on the lower atmosphere of particles arriving from this solid angle range is negligible as they represent only a very small fraction of the number of particles arriving from all directions. Moreover, the large zenith angle implies an increased path length through the atmosphere, and the particles are subject to a significantly increased number of scattering and energy loss processes than vertically incident particles which additionally decreases their relevance at low altitudes. Even though the solid angle range with variations in the cut-off rigidity is increasing for the Kiel Neutron Monitor with a vertical cut-off $R_C \approx 2.0$ GV it is still restricted to zenith angles above 75° . Only at high and very high cut-off rigidities for the Alma-Ata ($R_C \approx 8.3$ GV) and the Tokyo ($R_C \approx 11.4$ GV) Neutron Monitor large deviations for significant solid angle ranges are observed. For particles arriving from eastward directions ($A \approx 90°$) a large increase in the cut-off rigidity is observed at larger zenith angles. For westward directions, on the other hand, the cut-off rigidity becomes smaller than the vertical cut-off. This is exactly what is expected for the trajectories in a dipole magnetic field where positively charged particles potentially arriving from east-

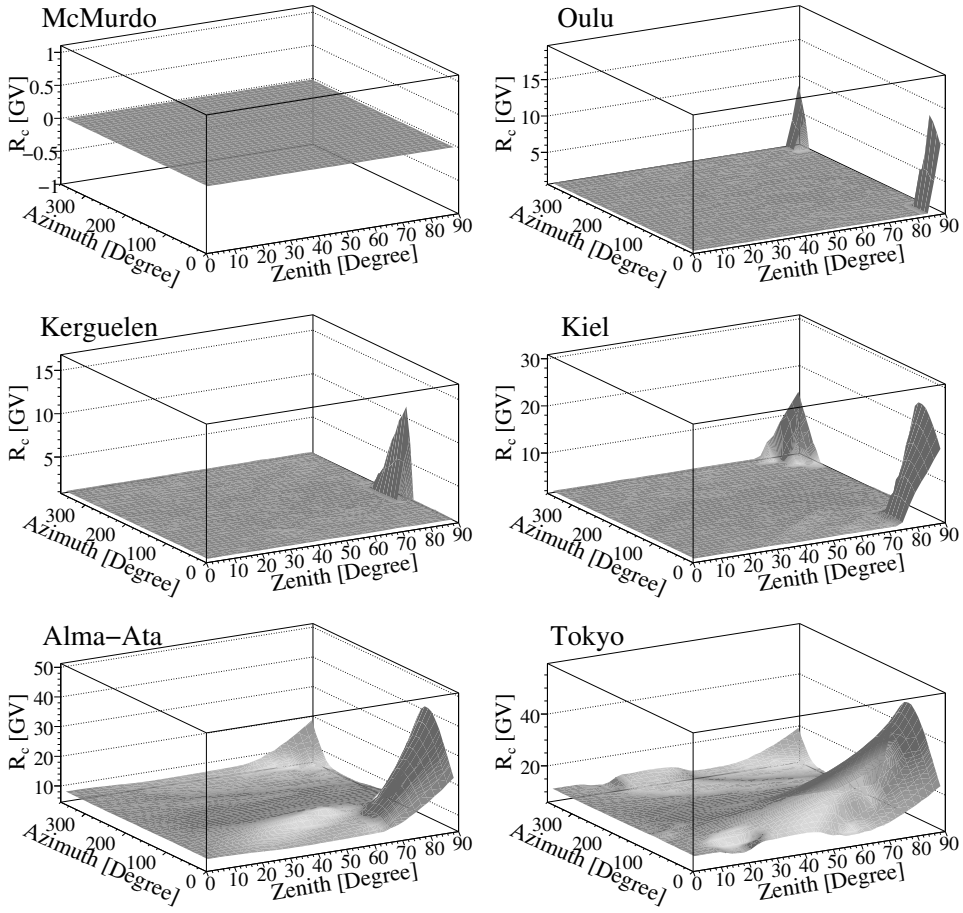


Figure 3.4: Cut-off rigidities $R_c$ versus azimuth and zenith angle of the incoming direction at different Neutron Monitor sites (details in App. A) in increasing order of the vertical cut-off rigidity from left to right and from top to bottom. For high latitude stations with low cut-off rigidities only small deviations from the vertical cut-off are observed.

ward directions are bound in periodic orbits (*Störmer*, 1930; *Alpher*, 1950; *Cooke et al.*, 1991) whereas particles from western directions have easier access to the inside of the magnetic field. The deviations in the cut-off rigidities are in the order of 25% for Alma-Ata and 50% for Tokyo at zenith angles around $30°$. At larger zenith angles the cut-off rigidity is rapidly increasing reaching values of several tens of GV for eastward azimuth angles.

For the calculations performed in the later chapters of this work the vertical cut-off rigidity will be used for all incoming directions. This approximation is very accurate at mid and high latitudes and less valid at very low latitudes. Nevertheless, as the impact of solar energetic particles at low latitudes is very small and most of the time negligible the use of the vertical cut-off rigidity does not affect the results from the analysis of the solar energetic particle events.

### 3.3.3 Asymptotic Viewing Directions

Due to the almost isotropic angular distribution of the galactic cosmic ray particles, the vertical cut-off rigidity is a good parameter to estimate the influence of the magnetosphere on the primary particle spectrum. In such a case, the original direction outside the magnetosphere of a primary particle arriving on top of the atmosphere is of no importance. It was shown above that the vertical cut-off rigidity in this case also provides a good approximation of the threshold for particles with non-vertical incident directions at the site of interest. In the case of an anisotropic spectrum as it is expected in the beginning of a solar energetic particle event, on the other hand, it is not only relevant if a particle with a certain rigidity has access to the atmosphere. In addition, it is of great importance to consider the incoming direction of the primary particle outside the magnetosphere as the intensity may depend on the pitch angle between the incoming direction of the event and the primary particle. To address this issue the asymptotic viewing direction or asymptotic arrival direction for a given location was introduced (see for example *Cooke et al.* (1991)) which is defined as the direction of a particle arriving at the location before entering the magnetosphere. Various trajectories of particles with different rigidities are illustrated in Fig. 3.1. Low numbers indicate large particle rigidities and vice versa. For infinitely extending magnetic fields with radially decreasing strength, e.g. the field of a dipole, the asymptotic direction is given as the direction the charged particle asymptotically approaches at very large distances. Apart from the structure of the magnetic field, the asymptotic direction depends, of course, on the final position of interest, e.g. a Neutron Monitor station, the incoming direction at the final location, and the rigidity of the particle. Accordingly, the asymptotic direction without a magnetic field or for particles with a very high rigidity which are not affected by the magnetic field is the same as the incoming direction at the location of interest. In the Earth's magnetosphere with its limited size, the asymptotic direction is usually illustrated as the direction of a particle with opposite charge calculated backwards starting at the point under investigation and a given direction at the exit point of the magnetosphere in geocentric coordinates.
Asymptotic viewing directions for the Oulu and South Pole Neutron Monitor stations are shown in Fig. 3.5 for several incident directions and a range of particle rigidities. The locations of the Neutron Monitor Stations are marked by the red filled squares. Each circle (square) illustrates the asymptotic viewing direction for the Oulu (South Pole) Neutron Monitor station for a particle with a given rigidity and direction at the Neutron Monitor's location. Particles arriving at a $10^\circ$ zenith angle and different azimuth angles are illustrated in the top panel for particle rigidities between 1 GV and 30 GV. As above, the azimuth angle is measured clockwise against northward direction, i.e. and azimuth of $0^\circ$ corresponds to northern direction, $90^\circ$ corresponds to eastern direction, etc. Each color corresponds to a certain incoming direction on top of the atmosphere. Starting from the largest rigidity (30 GV) for which the least deviation is observed the rigidity values decrease for each point by following a colored line in steps of 10 GV between 30 GV and 10 GV and steps of 1 GV for smaller rigidities. For a good illustration, in Fig. 3.5 only the results for the asymptotic viewing directions for

rigidities between 30 GV and 1 GV are shown. For the analysis of Ground Level Enhancements in Chapter 4, however, calculations were performed for rigidities from $R = 0.05$ GV to $R = 50$ GV to cover the relevant rigidity range ($R > 1$ GV for sea-level stations and $R > 0.5$ GV at very high altitudes of a few thousand meters).
The definition of the rigidity implies that higher rigidity corresponds to less de-

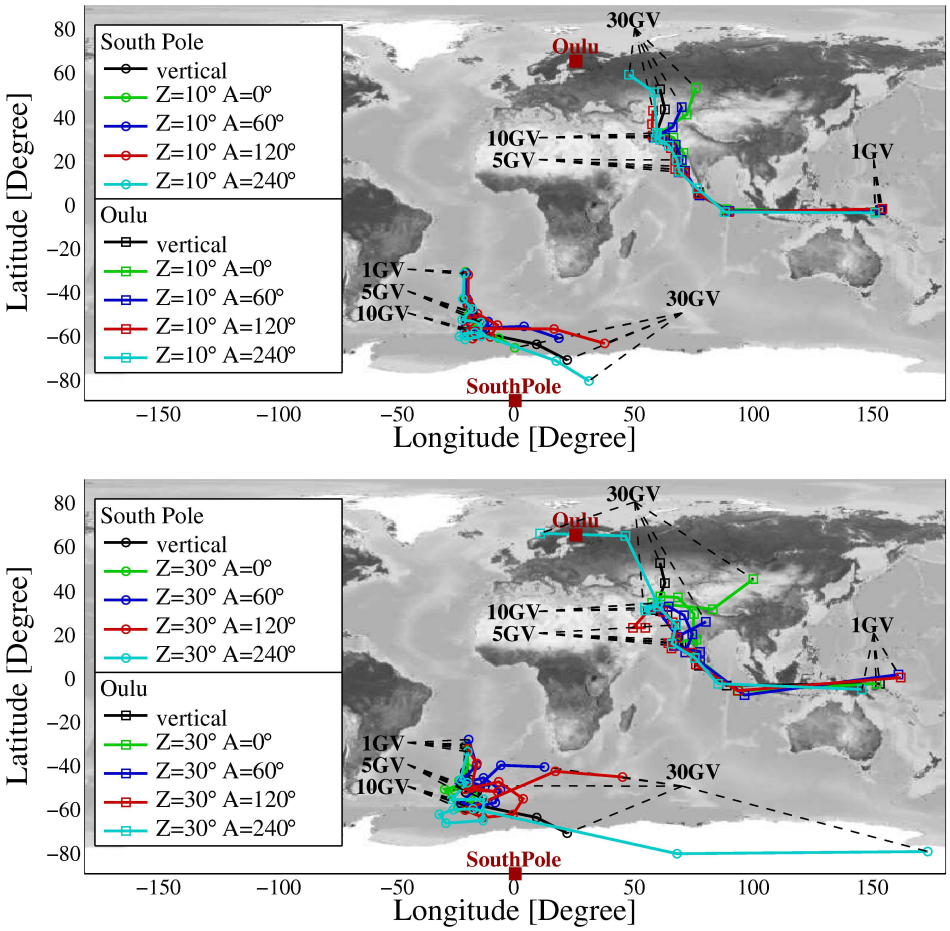


Figure 3.5: Vertical and non vertical asymptotic viewing directions for South Pole and Oulu Neutron Monitor stations of particles with rigidities 1 GV $< R <$ 30 GV. The filled squares mark the locations of the stations and the different colors indicate the zenith angle $Z$ and azimuth angle $A$ of the particle on top of the atmosphere. Zenith angles of 10° (30°) are compared to vertically incident particles in the top (bottom) panel.

viation in the magnetic field and lower rigidities correspond to larger deviations (see also Fig. 3.1). Particles with $R = 50$ GV and vertically incident on top of the atmosphere, for example, are only deviated by 20°–30° whereas particles at $R = 5$ GV change their direction by more than 40°–50°. It is therefore not surprising that particles with large rigidities arriving in different non-vertical directions on top of the atmosphere have different asymptotic arrival directions. Of course, these differences depend on the incoming directions and are bigger for

large differences in the incoming direction. Accordingly, the largest differences of asymptotic directions for a given rigidity in Fig. 3.5 occur for large rigidities (30 GV) and large differences in the incoming directions (zenith angle $30°$, different azimuth angles). At rigidities below $10$ GV, however, the differences in the asymptotic viewing directions for different incoming directions on top of the atmosphere decrease. Fig. 3.5 shows that the asymptotic directions at lower rigidities are very similar for all incoming directions. This is true even if the asymptotic incoming directions at very high rigidities might differ, for example $(Z = 30°, A = 60°)$ compared to $(Z = 30°, A = 240°)$. This effect is known as the focusing effect of the magnetic field (*Smart et al.*, 2000). Rigidities of particles in Ground Level Enhancements rarely exceed 10 GV and the asymptotic cone of acceptance which includes asymptotic directions for all initial directions can be approximated by the asymptotic direction of vertically incident particles (black lines in Fig. 3.5). This result will be used in the following chapter to determine the incident direction and the angular distribution of solar energetic particle during Ground Level Enhancements. The sensitivity of different Neutron Monitor stations to different arrival directions combined with the measured differences in the onset times and intensities of Ground Level Enhancements at the corresponding stations allow to derive information about the spatial structure of the event. For example, particles with a rigidity of around 5 GV arriving at the Oulu Neutron Monitor have an asymptotic arrival direction around (20°N, 70°E) while particles at a rigidity $R = 1$ GV arrive from (5°S, 150°E) (Fig. 3.5). As the asymptotic arrival directions of particles at high rigidities differ for different incoming directions the approximation using the vertical asymptotic direction is less valid if large rigidities are considered. This implies that for solar particle events containing particles with rigidities significantly larger than 10 GV the impact of the SEPs on the radiation environment in the atmosphere may not be accurately reproduced during anisotropic phases of the event if the vertical asymptotic direction alone is used.

## 3.4 Secondary Particles Induced by Galactic Cosmic Rays

The radiation exposure in the lower atmosphere caused by extraterrestrial radiation is due to secondary particles (*Reitz*, 1993), and for the estimation of the dose it is necessary to accurately simulate the composition and energy spectra of these secondary products of the interaction of primary radiation with the atmosphere. A lot of computational power is needed in order to perform the transport calculations of the very highly energetic primary galactic and solar nuclei with kinetic energies of tens and even hundreds of GeV through the atmosphere. As the primary particle spectrum varies with time and geomagnetic cut-off and shows large fluctuations in intensity and slope especially during solar energetic particle events, it is not reasonable to carry out calculations for all different premises. Instead, it is much more practical to calculate the transport for primary particles in certain energy intervals and to approximate the resulting secondary particle intensities by summing over all primary energy intervals multiplying by the corresponding primary particle intensity. In this way, results for arbitrary primary

particle spectra can be obtained without repeating the transport calculations.
Accordingly, secondary particle fluences in the kinetic energy interval $\Delta E_j \equiv [E_j, E_{j+1}]$ of particle type $i$ at an atmospheric depth $d$, $F^i_{\Delta\hat{E}_l}(\Delta E_j, d)$, induced by primary particles in the kinetic energy interval $\Delta\hat{E}_l \equiv [E_l, E_{l+1}]$ with a fluence of $\hat{F}(\Delta\hat{E}_l)$ were calculated for neutrons, protons, photons, electrons, positrons, muons, pions and kaons. For a sufficiently small primary energy interval $\Delta\hat{E}_l$ the primary particle fluence is assumed to be constant over the interval, and the secondary particle fluence per primary particle $f^p_{\hat{E}}$ with energy $\hat{E} \in \Delta\hat{E}$ is approximately given by:

$$f^i_{\hat{E}}(\Delta E_j, d) \approx \frac{F^i_{\Delta\hat{E}_l}(\Delta E_j, d)}{\hat{F}(\Delta\hat{E}_l)}. \tag{3.9}$$

For an arbitrary spectrum given by the $\hat{F}^p(\Delta\hat{E}_l)$ of a primary particle species $p$ the fluence $F^i$ of secondary particle type $i$ is given by

$$F^{p,i}(\Delta E_j, d) = \sum_l \hat{F}^p(\Delta\hat{E}_l) f^{p,i}_{\hat{E}_l}(\Delta E_j, d). \tag{3.10}$$

The sum is performed of all energy intervals between $\hat{E}^p_0$ and $\hat{E}^p_{\text{max}}$. The primary particle spectra at high energies are usually described by power laws with rapidly decreasing intensities. This decrease in the primary intensity allows to set an upper threshold $\hat{E}^p_{\text{max}}$ for the primary particle energies neglecting the influence of higher energetic particles. The lower threshold is given by the magnetic cut-off rigidity $R_C = p/q$ for a particle with momentum $p$ and charge $q$. For a relativistic particle with mass $m$ the threshold in kinetic energy is then given by:

$$E_0 = \sqrt{(R_C q)^2 c^2 + m^2 c^4} - mc^2, \tag{3.11}$$

where $c$ is the speed of light.
The total secondary particle fluences of particle $i$ is the sum over all relevant primary nuclei $p$ and can be calculated following:

$$\begin{aligned} F^i(\Delta E_j, d) &= \sum_p F^{p,i}(\Delta E_j, d) \\ &\approx \sum_p \sum_l \hat{F}^p(\Delta\hat{E}_l) f^{p,i}_{\hat{E}_l}(\Delta E_j, d). \end{aligned} \tag{3.12}$$

It is assumed that for small energy intervals the intensity of the primary particles is constant over one interval. Moreover, the analysis in this work is restricted to primary hydrogen and helium nuclei in the case of galactic cosmic rays and to hydrogen alone in the case of solar energetic particle events.
For solar quiet times the fluences $\hat{F}^p(\Delta\hat{E}_l)$ can be derived from the galactic cosmic ray particles' intensities $j(\hat{E})$ described by the models presented in Sec. 2.1 with the corresponding solar modulation:

$$\hat{F}^p(\Delta\hat{E}_l) = \int d\Omega \int dt \int_{\hat{E}_l}^{\hat{E}_{l+1}} d\hat{E}\; j^{\text{GCR}}(\hat{E}). \tag{3.13}$$

During solar energetic particle events, however, highly energetic particles accelerated during the events have to be taken into account and added to the GCR background:

$$\hat{F}^p(\Delta\hat{E}_l) \;=\; \int d\Omega \int dt \int_{\hat{E}_l}^{\hat{E}_{l+1}} d\hat{E}\; (j^{\mathrm{GCR}}(\hat{E}) + j^{\mathrm{SEP}}(\hat{E})). \qquad (3.14)$$

Results from modeling secondary particle fluences in the atmosphere for primary galactic cosmic ray particles are presented in the subsequent sections. The calculations were performed for different galactic cosmic ray models, and if not stated otherwise hydrogen nuclei were modeled in the energy range between 100 MeV and 2 TeV and helium nuclei in the energy range between 100 MeV and 1 TeV. The number of bins in the primary energy was 130 and 120 respectively with logarithmically increasing bin width. The results for the secondary particle fluences were calculated at different atmospheric depths between $1030$ g/cm$^2$ and $5 \cdot 10^{-4}$ g/cm$^2$ corresponding to altitudes between sea-level and 100 km above ground.

### 3.4.1 Secondary Protons

In this section results from the calculation of proton fluences induced by primary galactic cosmic ray are presented. Apart from secondary neutrons, protons contribute with the second largest fraction to radiation exposure at aircraft altitudes. Three mechanisms are involved in the production of atmospheric protons. First, if the energy is sufficient, primary protons being subject to a certain energy loss in traversing the upper part of the atmosphere contribute to the total proton fluence at a given altitude. The higher the altitude the less residual mass of air is contained above the location of interest and the relevance of this component increases due to the decreased energy loss and the decreased contribution of protons originating from scattering processes. Very highly energetic primary protons may even reach sea-level whereas protons with lower kinetic energies are stopped at much higher altitudes. For example, protons with a kinetic energy of 5 GeV have an approximate range of 2600 g/cm$^2$ in air. As consequence, they can easily reach sea-level corresponding to an atmospheric depth of around 1030 g/cm$^2$. Protons at 1 GeV, on the other hand, can only penetrate to an approximate depth of 370 g/cm$^2$ corresponding to an altitude of roughly 8 km above ground. The threshold energy for a primary proton to reach sea-level is approximately $2.75$ GeV which corresponds to a rigidity of $3.6$ GV. The second source adding to the proton component of the radiation environment in the atmosphere is the remnants of primary nuclei breaking up in collisions with particles in the air. The nucleons emerging from these collisions carry a large fraction of the kinetic energy of the parent nucleus and contribute with a significant part to the radiation environment. This is also a major source for secondary neutrons which will be studied in the next section. Finally, free secondary protons can be generated as fragments of target nuclei in inelastic collisions between primary or secondary particles with atomic nuclei in the air or evaporate from excited target nuclei.

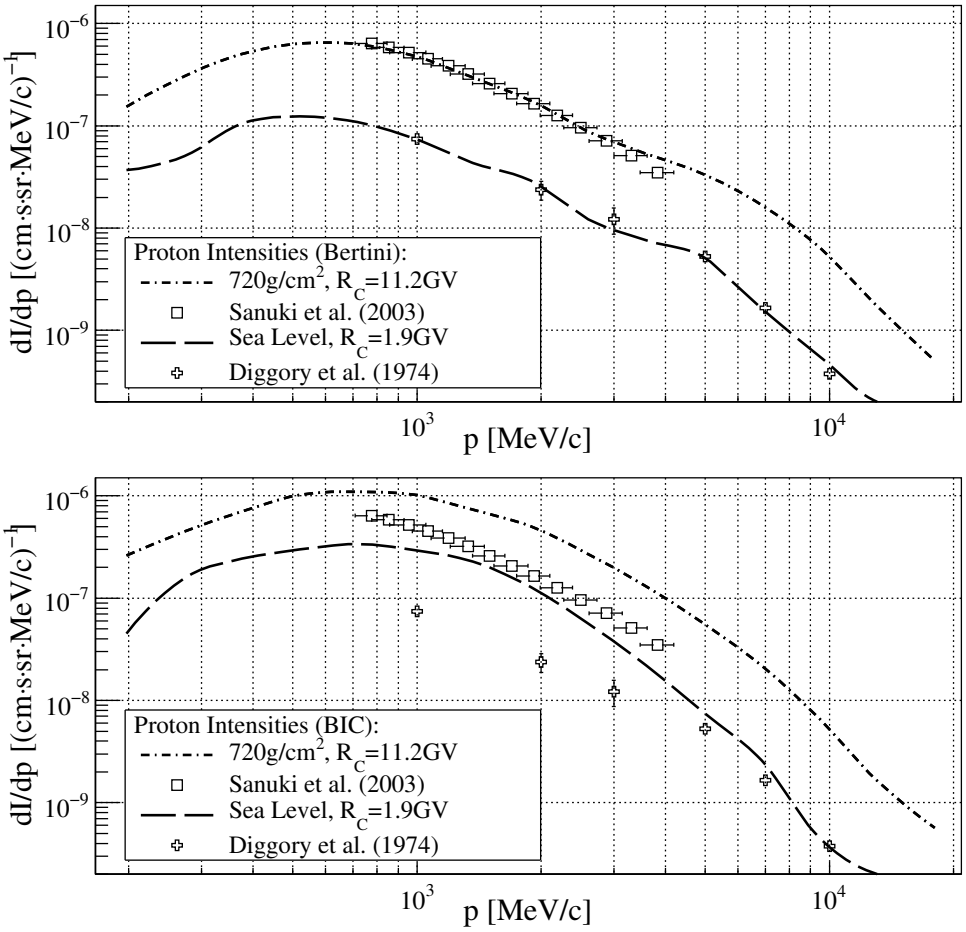


Figure 3.6: Secondary proton differential intensities at 720 g/cm$^2$ and at sea-level (cut-off rigidities $R = 11.2$ GV, $R = 1.9$ GV) calculated and compared to measurements by *Diggory et al.* (1974) and *Sanuki et al.* (2003). The top (bottom) panel shows the results using the Bertini (BIC) model. See text for details.

The decay of neutrons to protons, on the other hand, is no important source for secondary protons in the energy region under investigation. The mean lifetime of a neutron is $885.7 \pm 0.8$ s (*Amsler et al.*, 2008) and therefore neutrons produced in the atmosphere can easily reach the ground before decaying.

The differential momentum spectra of protons for two different locations and times reported by *Diggory et al.* (1974) and *Sanuki et al.* (2003) are presented in Figure 3.6 and compared to the results of the Monte-Carlo simulations of this work following Eq. 3.12. The results were obtained using the Bertini (top panel) and BIC (bottom panel) model for the inelastic nucleon-nucleus interactions below 10 GeV.

The measurements by *Sanuki et al.* (2003) were performed at Mt. Noriuka at an geomagnetic cut-off $R_c = 11.2$ GV and an altitude of 2770 m corresponding to an atmospheric depth of 742 g/cm$^2$. The heliospheric potential at the time of the experiment in September 1999 was $\phi = 685$ MV following *Usoskin et al.* (2005). The solar modulation parameters corresponded to a moderate solar activity at the

time of the measurements. *Diggory et al.* (1974) measured the differential momentum spectrum near sea-level (65 m) and geographic coordinates ($54.5°$N, $1.3°$W) in January–February 1971. For the calculation of the secondary proton spectra an atmospheric depth of 1020 g/cm$^2$ and $\phi = 634$ MV were used. The cut-off at the location of the experiment was calculated to be $R = 1.9$ GV and used in the simulation. The results for the secondary proton intensities were obtained for the primary GCR spectrum by Burger/Usoskin.

The differences of about one order of magnitude between the proton intensities for the two conditions in Fig. 3.6 are related to the different altitudes. The protons are attenuated traversing the additional mass of around 300 g/cm$^2$. The comparison between the experiments and the simulations reveals very good agreement if the Bertini model is used. In this case, the momentum spectra were well reproduced for both measurements with slightly higher results from the calculations at high momenta with respect to the results from *Sanuki et al.* (2003). The calculated proton intensities obtained with the BIC model, on the other hand, overestimate the experiment by a factor of 2 and more. A good agreement is only observed at large momenta ($p > 6$ GeV/c).

In addition to the differential momentum spectra for secondary protons in Figure 3.6, the intensity distribution over a wide range of atmospheric depths was determined by means of model calculations, and the results were compared to measurements from *Francke* (1999) obtained in August 1994 at a geomagnetic cut-off of $R_c \approx 500$ MV. The solar modulation at that time corresponded to $\phi \approx 515$ MV which is close to solar minimum activity. The results of the simulation were again obtained by using the two different models for inelastic hadronic interactions at medium energies, the Bertini in the top panel of Fig. 3.7 and the Binary Cascade (BIC) model in the bottom panel. Additionally, two different models for the primary hydrogen and helium spectra were taken into account using both the model by Garcia-Munoz (Eq. 2.2, solid lines) and by Burger (Eq. 2.5, dashed lines) for the local interstellar spectra. The differences arising from the utilization of the two input spectra are negligible and barely visible in Figure 3.7. It was shown in Sec. 2.1 that the primary galactic hydrogen spectra for the two models are very similar during solar minimum conditions but differ significantly for primary helium. By comparing the two models no significant differences in the secondary proton spectrum in the atmosphere are observed, and it can be concluded that the secondary proton fluence is dominated by the contribution of primary hydrogen. Obviously neither the fragmentation of the primary helium nuclei nor the break up protons from target nuclei hit by primary helium are of any importance. It is evident that the proton intensities at very low densities (very high altitudes) after no or every few interactions are identical to the primary hydrogen spectrum. At lower altitudes, on the other hand, contributions from other galactic nuclei may gain importance, but at least for helium this is obviously not the case.

Investigating the proton intensity versus atmospheric depth reveals steadily decreasing particle fluences. Only in the lowest momentum intervals a slight increase of proton intensity is observed leading to a maximum at a few tens of g/cm$^2$. This is in contrast to other secondary particles showing a pronounced

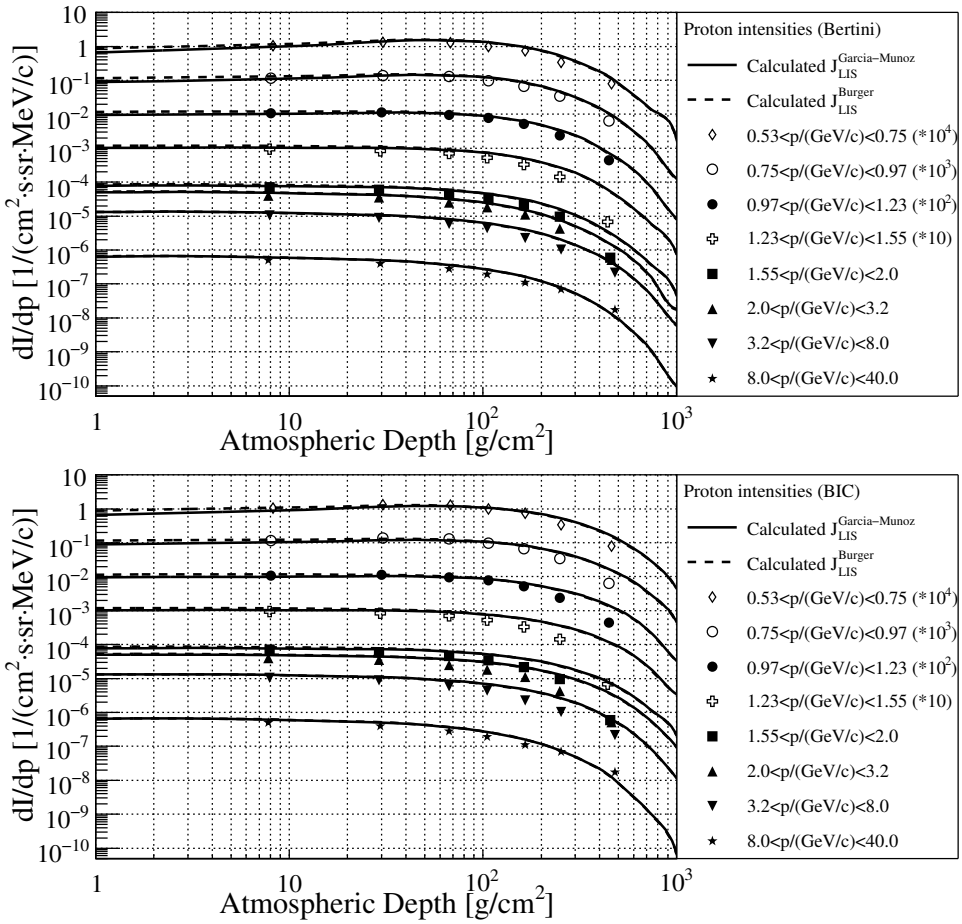


Figure 3.7: Calculated proton intensities versus the atmospheric depth close to solar minimum ( $\phi \approx 515$ MV) and for a cut-off rigidity $R = 0.5$ GV for different momentum regions (lines) and two different models for the local interstellar spectra (solid vs. dashed lines) compared to CAPRICE94 (*Francke*, 1999) measurements (symbols). The results for lower momenta are scaled by the factors indicated in parentheses for better distinction. The top panel shows results from using the Bertini model whereas for the results in the bottom panel the Binary Cascade (BIC) model was used.

intensity maximum at 20 km-30 km altitude. At higher proton momenta, the intensities are only slightly decreasing at depths below 100 g/cm$^2$ corresponding to altitudes above approximately 16 km. At lower altitudes the amount of protons is rapidly dropping and the intensity is significantly reduced in all momentum intervals under investigation. It will be shown later that as a consequence the importance of secondary protons for the radiation dose in the atmosphere is dropping from being the second most important component above 10 km to much lower contributions at sea-level.

The overall agreement between model calculations and experiment is good. Only for medium momenta of $1.23$ GeV/c $< p < 3.2$ GeV/c and large atmospheric depth (i.e. low altitudes) a strong overestimation of the measurements by the simulation is observed. This is true for both interaction models that were used. The overestimation of the Bertini model is stronger than for the Binary Cascade

model and extends to higher altitudes. This confirms the same trend found above, and the same is observed for other secondary particles as shown in the next sections.
The results of this chapter show that the transport and creation of secondary protons is satisfyingly modeled and reliable results can be obtained for both momentum (energy) spectra as well as for the integral proton fluences from very high altitudes down to approximately $200$ g/cm$^2$. The Bertini model produced results that are more consistent with the presented measurements. No significant difference was observed for the two different local interstellar spectra under consideration.

### 3.4.2 Secondary Neutrons

The next component of the variety of secondary particles produced in the atmosphere that will be studied is neutrons. In terms of dosimetry, neutrons are the most important component in the radiation environment in the lower atmosphere from aircraft altitudes down to sea-level. The galactic cosmic rays, however, do not comprise a significant amount of free neutrons. Instead, secondary neutrons emerge from collisions of primary nuclei with atmospheric molecules either as fragments of the projectile or remnants of target nuclei. The production of these neutrons is mainly in forward direction and fragments of the projectile carry a large fraction of the projectile's energy.
Another important source is evaporation neutrons from nuclei excited by scattering events with charged particles, neutrons or highly energetic photons. In contrast to the fragmentation process the evaporation neutrons have an isotropic distribution. The intensity of downward neutrons versus the atmospheric depth for different energy intervals for a solar modulation $\phi = 800$ MV is shown in Figure 3.8 (top: Bertini model, bottom: Binary cascade model) and a geomagnetic cut-off $R_c = 15$ GV. The results were obtained by restricting the zenith angles of neutrons to $Z < 10°$. A maximum in neutron intensity at low atmospheric depth is clearly visible for all energy intervals and it is also obvious that the altitude of the maximum depends on the neutron energy. The energy range 50 MeV$< E <$350 MeV has its maximum at the lowest altitudes of approximately 10 km–12 km ($\approx$200 g/cm$^2$–300g/cm$^2$).
Measurements performed by *Eyles et al.* (1972) for neutrons in the energy interval $50$ MeV $< E < 350$ MeV and represented by the green squares are superimposed to the results of the simulation. The data was recorded in the years from 1967–1970, and the modulation potential during those years was in the range from $600$ MV to $1000$ MV according to *Usoskin et al.* (2005). An average value of 800 MV for the calculations was chosen. The green lines correspond to the same energy interval as the experimental results and show good agreement with the measurements at depths below approximately 200 g/cm$^2$ (corresponding to $\approx$12 km). It is obvious from Fig. 3.8 that the Bertini model results in higher neutron intensities than the Binary Cascade model. The agreement of the calculations with the experimental data is much better for the former. This is in accordance with the observations in the former section where a better reproduction of measurements was obtained with the Bertini model as well.

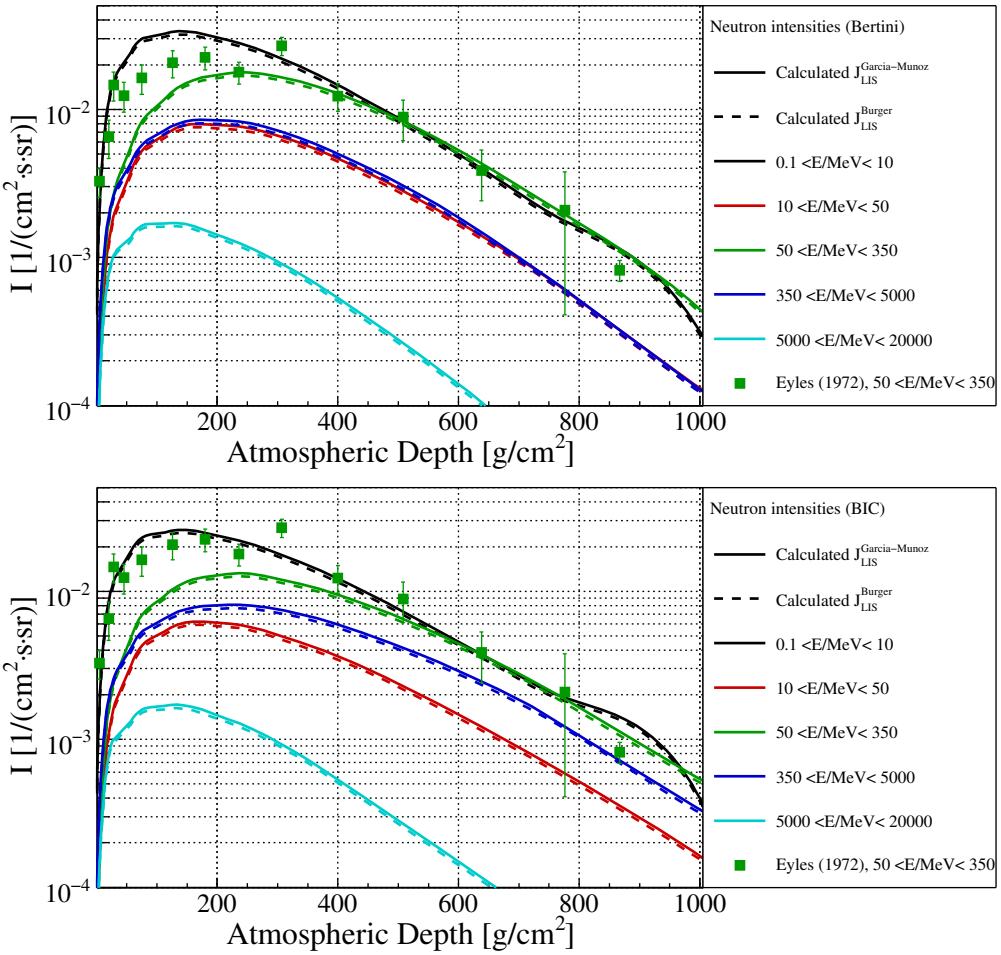


Figure 3.8: Neutron intensities versus atmospheric depth for different energy intervals and a vertical geomagnetic cut-off $R_c = 15$ GV calculated with the Bertini model in the top panel and the Binary Cascade model below. The numerical results were obtained with the models from Burger and Garcia-Munoz for the GCR intensities with a solar modulation $\phi = 800$ MV and are compared to measurements by *Eyles et al.* (1972) for the energies 50 MeV$< E <$350 MeV.

Some of the most famous neutron measurements in the lower atmosphere were performed by *Goldhagen et al.* (2004) who used a multi-sphere neutron spectrometer (Bonner spheres) to determine neutron energy spectra from 20 km altitude down to sea-level at various cut-off rigidities $0.7\,\text{GV} < R_C < 11.6\,\text{GV}$. The measurements were carried out during solar minimum conditions in June 1997 and the corresponding modulation parameter was $\phi = 404$ MV. The exact parameters for the various measurements published in *Goldhagen et al.* (2004) are plotted in Table 3.1.
The same parameters were adopted to calculate the neutron intensities. As before, the LIS models by *Burger et al.* (2000) and *Garcia-Munoz et al.* (1975) were used and the Bertini and Binary Cascade models were applied. The results of the calculations together with the experimental results from *Goldhagen et al.*

Table 3.1: Locations, cut-off rigidities and neutron effective dose rates for the different conditions as calculated and measured by *Goldhagen et al.* (2004).

| Lat. | Long. | Depth [g/cm$^2$] | Alt. [km] | $R_C$ [GV] |
|---|---|---|---|---|
| 19°N | 127°W | 53.5 | 20.3 | 11.6 |
| 54°N | 117°W | 56 | 20.0 | 0.8 |
| 56°N | 121°W | 101 | 16.2 | 0.7 |
| 38°N | 122°W | 201 | 11.9 | 4.3 |
| 37°N | 76°W | 1030 | 0 | 2.7 |

(2004) and calculations from the PARMA model by *Sato et al.* (2008) are shown in Figure 3.9 and Figure 3.10. The results of PARMA where obtained with the EXPACS[6] implementation of the model. Some of the results in this section were also published in *Matthiä et al.* (2008).
The figures show the omnidirectional neutron intensities

$$\frac{dI^{4\pi}}{dE_k} = \int_{4\pi} d\Omega \, \frac{dI}{dE_k} \tag{3.15}$$

multiplied by the kinetic energy $E_k$ of the neutrons for a more readable illustration.
The general shape of the spectrum exhibits only minor changes for different altitudes and geomagnetic cut-offs and possesses a two peak structure with maxima at around 1 MeV and 100 MeV. At the highest point $d = 53.5$ g/cm$^2$ a small peak is observable at energies of several GeV up to more than 10 GeV. This peak corresponds to fragments from the primary alpha particles and knock-on neutrons originating in the target fragmentation in nucleon-nucleus or nucleus-nucleus collisions. The cut-off rigidity of 11.6 GV corresponds to an energy per nucleon of around 5 GeV for alpha particles and this is exactly the energy where the maximum in the small peak is observed. For lower cut-off rigidities this fragment peak is hidden by neutrons produced in the fragmentation of lower rigidity helium nuclei.
The comparison of the measurements with the model calculations using the Binary Cascade model (Fig. 3.10) reveal very good agreement for all altitudes but sea-level. At large altitudes and high cut-offs the simulations predict smaller values for the neutron fluences as measured. For the Bertini model in Fig. 3.9 it is quite the opposite and excellent agreement is accomplished for ground-level over the whole energy range for very cold up to high relativistic neutrons. At higher altitudes, on the other hand, the experimental data is overestimated by the calculations at energies below a few hundred MeV. This effect is especially strong for the low cut-off rigidity measurements where the calculated fluences exceed the experiment by several tens of percent at energies of 1 MeV and below. This may be an indicator for an overestimation of the primary galactic cosmic ray particle flux at energies below several GeV. This part of the primary spectrum is irrelevant both for large cut-off rigidities and for very low altitudes where the major contribution to the secondary neutron fluence is caused by higher energetic primary particles. In contrast to the energies of secondary neutrons extending to

[6] http://phits.jaea.go.jp/expacs/index.html

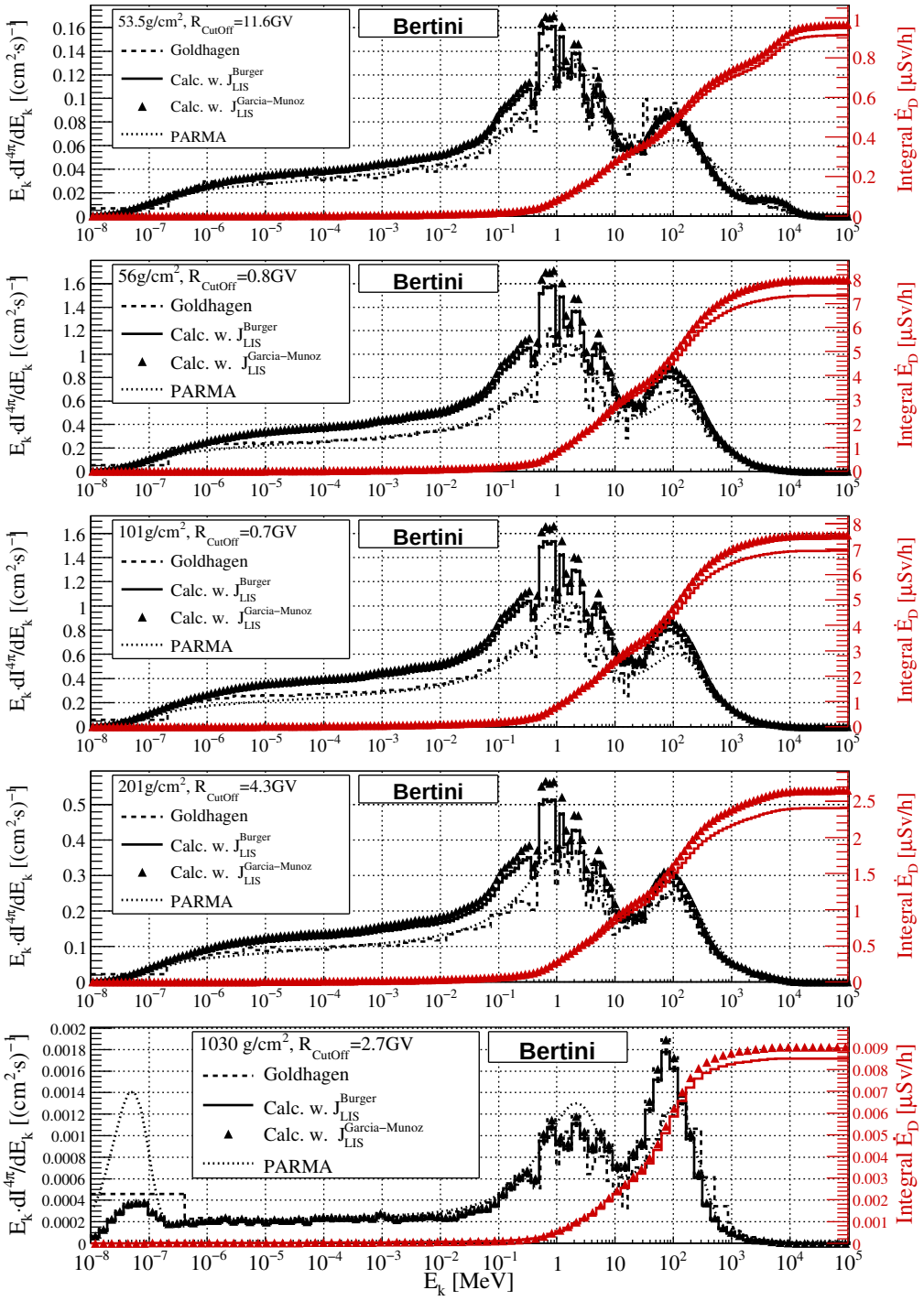


Figure 3.9: Omnidirectional secondary neutron differential intensities at different atmospheric depths and magnetic cut-offs calculated with two different models for primary galactic hydrogen and helium spectra compared to measurements by *Goldhagen et al.* (2004) and the PARMA model (*Sato et al.*, 2008). Also shown is the resulting integral neutron effective dose rate $\dot{E}_D$. The calculations were performed using the Bertini model.

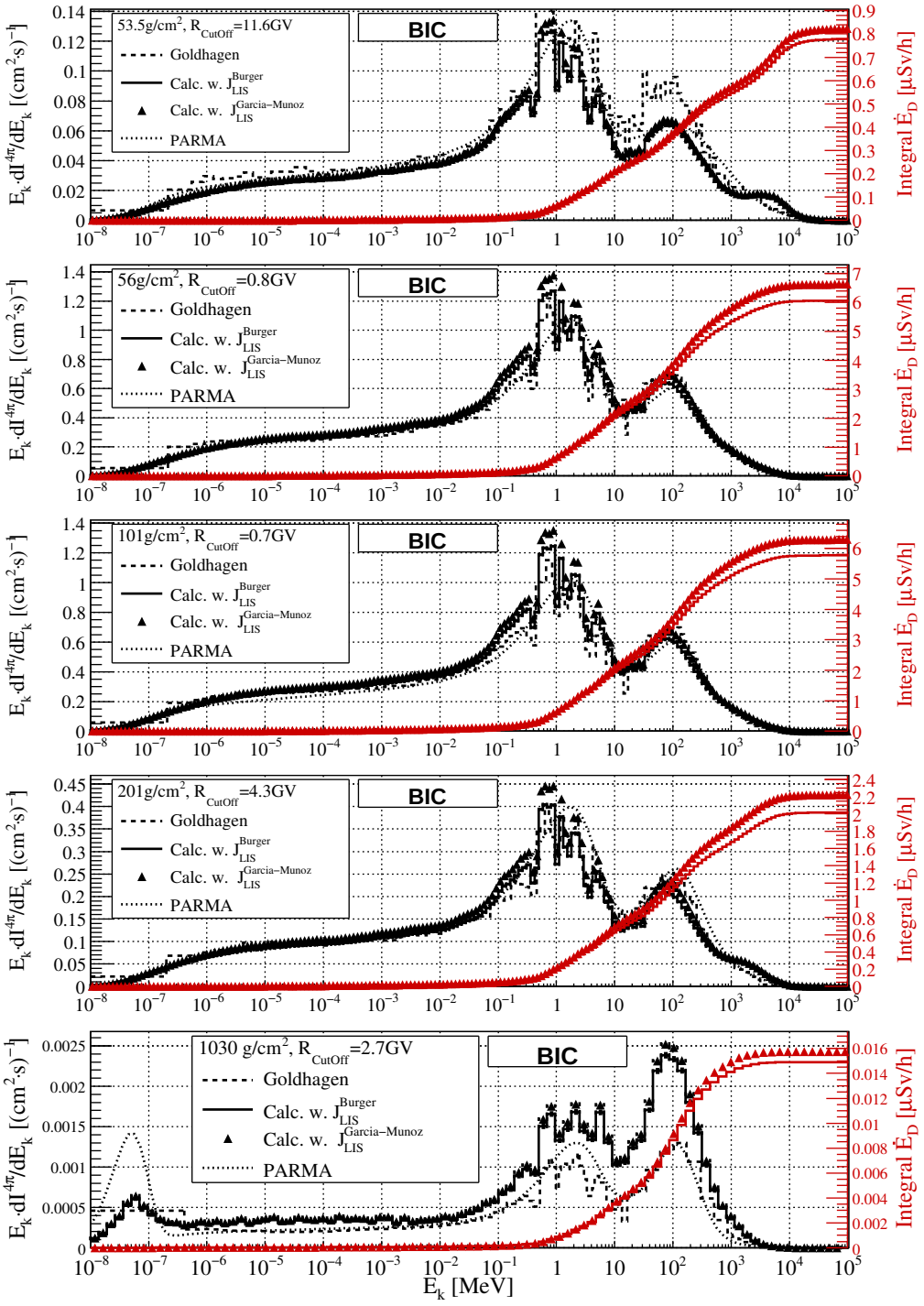


Figure 3.10: Omnidirectional secondary neutron differential intensities at different atmospheric depths and magnetic cut-offs calculated with two different models for primary galactic hydrogen and helium spectra compared to measurements by *Goldhagen et al.* (2004) and the PARMA model (*Sato et al.*, 2008). Also shown is the resulting integral neutron effective dose rate $\dot{E}_D$. The calculations were performed using the Binary Cascade model (BIC).

Table 3.2: Neutron effective dose rates as calculated (see also *Matthiä et al.* (2008)) and as measured by *Goldhagen et al.* (2004). Fluence to dose conversion was performed as described in Section 2.6.

| Alt. [km] | $R_C$ [GV] | Neutron Effective Dose Rate [$\mu$Sv/h] | | | | |
|---|---|---|---|---|---|---|
| | | **This work using** | | | | Goldhagen |
| | | Bertini | | Binary Cascade | | |
| | | $j_{\mathrm{LIS}}^{\mathrm{Burger}}$ | $j_{\mathrm{LIS}}^{\mathrm{Garcia\text{-}Munoz}}$ | $j_{\mathrm{LIS}}^{\mathrm{Burger}}$ | $j_{\mathrm{LIS}}^{\mathrm{Garcia\text{-}Munoz}}$ | |
| 20.3 | 11.6 | 0.91 | 0.97 | 0.78 | 0.82 | 0.88 |
| 20.0 | 0.8 | 7.3 | 8.0 | 6.1 | 6.3 | 5.8 |
| 16.2 | 0.7 | 6.9 | 7.5 | 5.8 | 6.3 | 5.5 |
| 11.9 | 4.3 | 2.4 | 2.7 | 2.0 | 2.2 | 2.05 |
| 0 | 2.7 | 0.0090 | 0.0085 | 0.015 | 0.016 | 0.0090 |

very low energies the secondary protons studied in the previous chapter were restricted to energies above several hundreds of MeV. It could be suspected that this energy region is dominated by highly energetic primary particles as well and is therefore insensitive to a possible overestimation of the primary galactic cosmic ray flux of the applied models. For the PARMA model *Sato et al.* (2008) used a modified version of the galactic cosmic ray model developed by *Nymmik et al.* (1992), and obtained good agreement with the experiments.
In addition to the neutron intensities, the effective dose rate induced by neutrons for the different setups was calculated. In Fig. 3.9 and Fig. 3.10 the integral neutron effective dose rate is shown:

$$\text{Integral dose rate} \quad = \quad \int_0^{E_k} dE_k' \, \frac{d\dot{E}_D(E_k')}{dE_k'} \tag{3.16}$$

where $\dot{E}_D$ is the effective dose rate and $E_k$ is the kinetic energy of the neutrons. It turns out that only neutrons with kinetic energies between approximately 1 MeV and 10 GeV are relevant for the calculation of the effective dose rate. The values of the total neutron effective dose rate obtained from the Monte-Carlo simulations using the different interaction and primary GCR models are summarized and compared to the results from *Goldhagen et al.* (2004) in Tab. 3.2. The agreement between the results of the Monte-Carlo simulations performed in this work and the experimental data is reasonable for the Bertini model using the Burger/Usoskin galactic cosmic ray parametrization. For the large cut-off values at 20 km and for sea-level this combination results in the best agreement whereas at intermediate altitudes the Binary Cascade model offers better compatibility with the measurements.
It must be stated here, that the experimental determination of neutron spectra is difficult and that the authors of (*Goldhagen et al.*, 2004) do not provide uncertainties on their measurements. Therefore, it is difficult to choose the most appropriate combination of galactic cosmic ray and interaction models studied in this chapter from the comparison to the neutron data measurements. Moreover, the results from the comparison to (*Goldhagen et al.*, 2004) contradict the analysis of the measurements by *Eyles et al.* (1972) were a strong underestimation of the data by the Monte-Carlo simulation results was observed. Here, we

observe a very good agreement at high cut-off rigidities. The effective dose rate may also be reduced by taking into account the additional shielding provided by the structure of the aircraft. *Battistoni et al.* (2005) estimated that the effective dose during solar minimum and at low cut-off rigidities in an Airbus A-340 is reduced by up to 14% compared to a position sourrounded by air.

### 3.4.3 Secondary Muons

The most important component of secondary particles at sea-level is muons. The fluences of $\mu^+$ and $\mu^-$ contribute with more than fifty percent to the total effective dose at sea-level. At aircraft altitudes, on the other hand, the fraction of the dose caused by secondary muons is only in the order of several percent depending on the magnetic cut-off rigidity. Secondary muons originate from the charged decay of pions produced in nucleon-nucleus or nucleus-nucleus collisions of primary or secondary particles with target nuclei in the atmosphere. $\pi^+$ and $\pi^-$ mesons decay with a branching fraction of almost 100% to muons and muon neutrinos with a mean life-time $\tau \approx 2.6 \cdot 10^{-8}$ s (*Amsler et al.*, 2008): $\pi^{+,-} \rightarrow \mu^{+,-} + \nu_{\mu,\bar{\mu}}$. As the production of muons from the decay of pions is governed by inelastic nuclear interactions of primary particles with target particles the reproduction of secondary muon intensities is a good test for the physical models describing these processes. $\mu^+$ and $\mu^-$ intensities for a wide range in atmospheric depth and for different momentum intervals are illustrated in Fig. 3.11 for solar maximum conditions. The neutron intensity builds up with increasing atmospheric depth reaching a maximum at 200 g/cm$^2$ to 300 g/cm$^2$ (approximately 12 km to 9 km) and decreasing at lower altitudes. The additionally shown experimental results from *Bellotti et al.* (1999) were obtained on September 23, 1991 during solar maximum ($\phi = 1191$ MV following *Usoskin et al.* (2005)) for a cut-off rigidity $R_C = 4.3$ GV. The calculations were performed with the same parameters, and the vertical intensity was estimated by using particles with a maximum zenith angle below $cos(Z) < 0.99$ corresponding to approximately $8°$. The angular distribution of secondary muons is known to be proportional to $cos^2(Z)$ (Amsler-etal-2008), and therefore, the arising uncertainty is smaller than 2%. At low altitudes of several hundreds of g/cm$^2$ a good agreement for all combinations of models (Bertini and Binary Cascade; Garcia-Munoz, Burger) was observed at low and intermediate momentum intervals. At the highest momentum interval the experimental data is slightly underestimated by the simulation. At lower depths (higher altitudes) the underestimation of the experimental data by the simulation is more systematic for almost all momentum regions. This effect is especially pronounced for the results calculated with the Binary Cascade model in the lower panel of Fig. 3.11. Still, the disagreement is mainly in the order of 10% or below which is very acceptable for the estimation of doses.
As in the previous sections in addition to the atmospheric depth profiles of the particle intensities differential spectra for certain conditions are presented (Fig. 3.12). The CAPRICE94 experiment at an altitude of 360 m (1000 g/cm$^2$) and the CAPRICE97 experiment at an altitude of 1270 m (900 g/cm$^2$) (*Kremer et al.*, 1999) performed in July 1994 and April/May 1997 during solar minimum conditions were chosen as reference measurements. Again, the corresponding

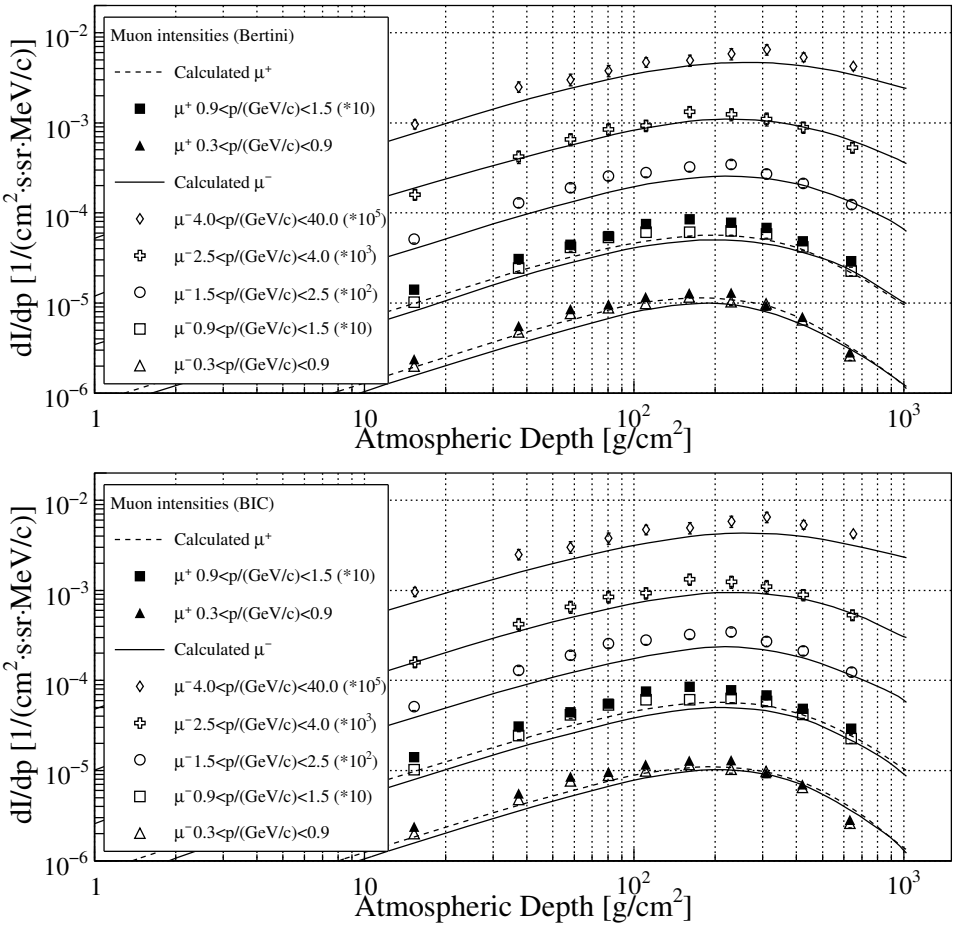


Figure 3.11: The dependency on the atmospheric depth of secondary muon intensities for different momentum intervals calculated for primary GCR H and He nuclei (solid (dashed) line for $\mu^-(\mu^+)$) and compared to measurements from *Bellotti et al.* (1999). The cut-off rigidity is $R_C = 4.3$ GV and the solar modulation at the time of the experiment was $\phi = 1191$ MV according to *Usoskin et al.* (2005). The results for lower momenta are scaled by the factors indicated in parentheses for better distinction. The top panel shows results using the Bertini model whereas in the bottom panel the Binary Cascade (BIC) model is used.

modulation parameter was taken from *Usoskin et al.* (2005) and adapted to the model by Garcia-Munoz by using Eq. 2.6. In comparison to the experiment the presented particle spectra for CAPRICE-1994 reveal the same characteristics that can be observed for the depth profile in Fig. 3.11. The usage of the Bertini model leads to good agreement for the lower momentum intervals and an underestimation at very high momenta for $\mu^-$ and slight underestimation of the $\mu^+$ intensity at momenta below 1 GeV/c. The Binary Cascade model, on the other hand, shows good agreement for the lower momentum intervals and an underestimation at very high momenta for both $\mu^-$ and $\mu^+$.

The application of the two models for the GCR spectra does not lead to differences in the secondary muon intensity at momenta below several GeV/c. At

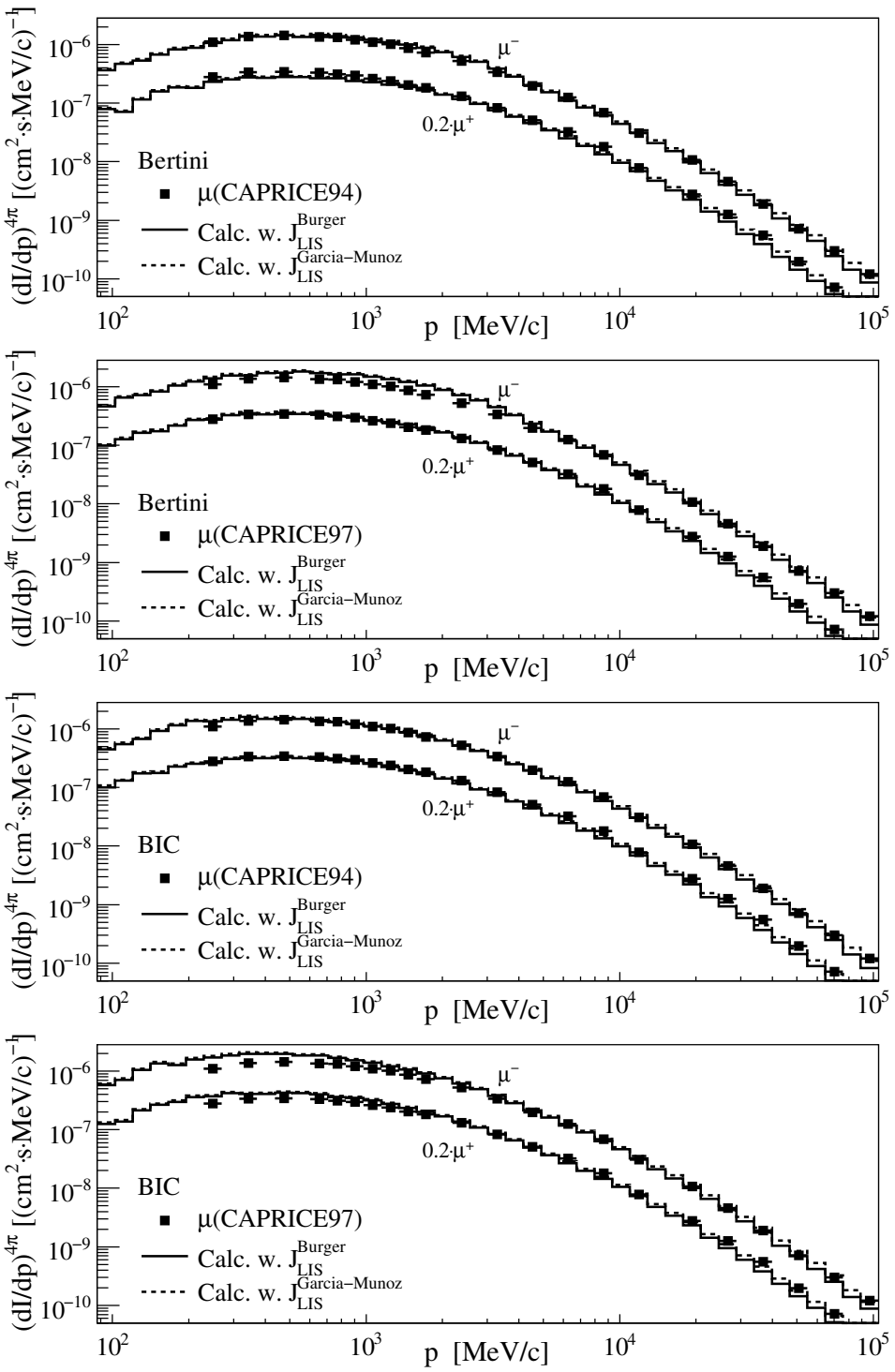


Figure 3.12: Calculated vertical differential secondary $\mu^-$ and $\mu^+$ intensities with respect to momentum compared to measurements by *Kremer et al.* (1999) from the CAPRICE94 (altitude 360 m; $R_c = 0.5$ GV; solar modulation potential of $\phi = 485$ MV for the GCR model by Garcia-Munoz and $\phi = 540$ MV for Burger) and CAPRICE97 (altitude 1270 m; $R_c = 4.2$ GV; $\phi = 350$ MV for Garcia-Munoz and $\phi = 480$ MV for Burger) experiments. The results for $\mu^+$ were scaled by a factor of 0.2 for distinction. The upper two panels show the results obtained with the Bertini model, and the lower two panels contain the data from the Binary Cascade model.

higher momenta, on the other hand, the results obtained with the Garcia-Munoz model yield a better compatibility with the data of both experiments. This may be an indication for a better description of the primary galactic cosmic ray spectra by Garcia-Munoz at very high energies.
It should be noted here that the determination of the secondary muon intensities to such high momenta as presented here (100 GeV/c) makes it necessary to include primary particles up to very high energies. During the simulation of the particle transport it was noticed that primary particles with energies of at least 1 TeV and more have to be calculated to get reliable results. This behaviour, however, is restricted to relatively high muon momenta of several tens of GeV/c where the particle intensity is several orders of magnitude smaller than at around 1 GeV. Therefore, particles with such large energies are irrelevant in dosimetric questions.

## 3.5 Dose Rates in Aviation from Secondary Particles Induced by Galactic Cosmic Rays

In the previous section the secondary particle intensities of protons, muons and neutrons were presented for different solar conditions and for various positions in the atmosphere. The next step in the direction of determining the doses during Ground Level Enhancements is to derive the radiation exposure from a given set of secondary particle intensities. In this section, the analysis is restricted to doses induced by galactic cosmic ray particles, and the results for solar energetic particle events will be presented in the next chapter. To investigate the reliability of the results from the calculation of the dose a comparison with measurements performed by *Meier et al.* (2009) and *Hubiak* (2008) is presented. Additionally, results from several widely used tools for the determination of radiation doses are compared to values obtained in this work.
The results in the previous section led to the decision that the modeling of secondary particle fluences from galactic cosmic ray particles can be satisfyingly achieved using the GCR model by *Burger et al.* (2000) with modulation parameters provided by *Usoskin et al.* (2005) in combination with the Bertini interaction model. Nevertheless, it is possible that the good results from the previous section might be even improved by using different models included in GEANT4 and applying other models for the spectra of the galactic nuclei. Due to the computational cost of calculations needed to study additional models it was not possible to include these models in the analysis presented in this work.
In this section the conversion of the secondary particle fluence to dose for several scenarios is performed and the results are compared to measurements performed on-board aircraft and to existing models providing estimations of doses at aircraft altitudes. The quantities required for the description of the radiation environment were introduced in Sec. 2.6. The most important and most often used quantities in this context are the effective dose $E$ and the ambient dose equivalent $H^*(10)$. These quantities are derived from secondary particle fluences following the procedure described in Sec. 2.6 using Eq. 2.42 and Eq. 2.45. The results presented in this chapter are obtained with calculations taking into account primary hydrogen (protons) and helium (alpha particles) nuclei with kinetic energies from 100 MeV to 2 TeV.
The dose rate in the atmosphere caused by galactic cosmic rays is related to basically three quantities describing the conditions during the exposure, namely the shielding provided by the atmosphere corresponding to the atmospheric depth or altitude of the exposure, the geomagnetic shielding represented by the cut-off rigidity and the solar modulation. From the previous section it is evident that the atmospheric depth plays a major role. It was shown that the intensity of neutrons and muons is maximal at depths of a few hundred grams per square centimeter. Additionally, the proton intensities in the momentum intervals under investigation stayed almost constant to a depth of around 100 g/cm$^2$, and at lower altitudes the intensity drops significantly. Therefore, it is no surprise that the radiation exposure is increasing with the altitude as it is evident from the altitude profile of the effective dose rate $\dot{E}$ and the contribution of individual secondary

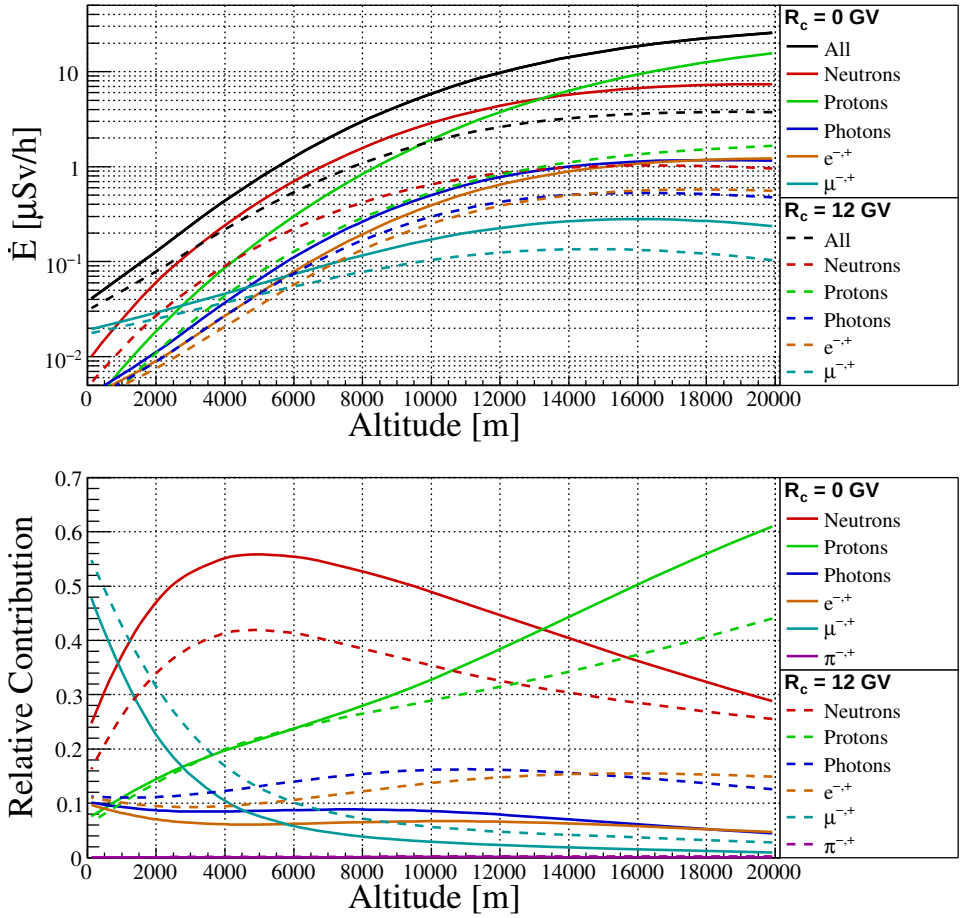


Figure 3.13: Calculated effective dose rates $\dot{E}$ during solar minimum ($\phi = 400$ MV) in the top panel for all relevant particles and the relative contribution to the total effective dose rate by the individual particles in the lower panel. Results are shown for very high latitudes ($R_C = 0$ GV, solid lines) and near the equator ($R_C = 12$ GV, dashed lines). Numerical values can be found in Tab. D.1.

particle species illustrated in Fig. 3.13. The total effective dose rate in the lower atmosphere and the contribution of individual particles versus the altitude above sea-level is indicated by the black and colored lines respectively in the top panel of the figure. The solid lines show the effective dose rates near the geomagnetic pole whereas the dashed lines represent the exposure rates at low latitudes near the equator ($R_C \approx 12$ GV). The latter cut-off rigidity corresponds to the value on the Greenwich meridian. At 100°E to 150°E, however, the shielding by the magnetic field is much larger and the cut-off reaches values up to 16 GV (see Fig. 3.2). The results were obtained for a range of atmospheric depths which were converted to altitudes using the US Standard Atmosphere 1976 model. It has to be stated that the doses at a given altitude may differ significantly for conditions deviating from the Standard Atmosphere. It was shown in Section 2.4 that the atmospheric depth at a given altitude may show seasonal variations of several tens of g/cm$^2$.

The increase of the dose rate with altitude is clearly visible and extends over several orders of magnitude from several tens of nSv/h at sea-level up to more than 20 $\mu$Sv/h at 20 km and $R_C = 0$ GV. The effective dose rate at positions corresponding to large cut-off rigidities ($R = 12$ GV), on the other hand, does not exceed 4 $\mu$Sv/h which clearly illustrates the importance of the geomagnetic shielding. Considered particles for the calculation of the dose were protons, neutrons, photons, $\mu^{-,+}$, $e^{-,+}$ and $\pi^{-,+}$. The contributions from particles and antiparticles for electrons, muons and pions are summed up in the representation in Fig 3.13.

At larger altitudes the restriction to primary hydrogen and helium nuclei and consequently the disregard of secondary particles produced by heavier nuclei becomes more relevant, and the presented results probably underestimate the total effective dose rate induced by all primary galactic cosmic ray nuclei. Moreover, nuclei may not only produce secondary particles adding to the dose rate but they may also contribute directly to the radiation exposure. Due to the short range in matter this contribution is safely negligible at lower altitudes but gains importance at low atmospheric depth. The EXPACS tool considers all galactic nuclei up to nickel and additionally includes the direct contribution of helium nuclei. According to EXPACS, the fraction of the effective dose during solar minimum and at low geomagnetic cut-offs due to helium nuclei is about one percent at 300 g/cm$^2$ ($\approx 9$ km) and increases to 16% at 55 g/cm$^2$ ($\approx 20$ km).

The contributions of the secondary particles are illustrated in the bottom panel of Fig. 3.13. At higher altitudes and at low cut-off rigidities the effective dose rate is dominated by the contribution of protons (60%) due to their large abundance in the primary galactic cosmic rays and neutrons (30%) from projectile and target fragmentation. Photons and electrons contribute in equal parts with around 5%. It is noteworthy that this fraction is much higher for large cut-off rigidities which may be explained by the increased radiation energy loss of the higher energetic protons and the fact that more energy is transferred to secondary electrons than deposited locally. Large fractions of energy can be transferred from the projectile to so-called delta electrons in head-on collisions increasing the relative contribution of electrons to the total dose (*Meier et al.*, 1998).

At lower altitudes the contribution of protons steadily decreases and secondary neutrons gain importance reaching a maximum at around 4000 m. At commercial aircraft cruising altitudes ($\approx$ 9 km–12 km) the total radiation exposure is mainly divided into contributions from neutrons ($\approx 30\%$–$50\%$), protons ($\approx 30\%$–$40\%$), $e^{-,+}$ ($\approx 10\%$–$15\%$), photons ($\approx 10\%$-$15\%$) and muons ($\approx 5\%$) depending on the altitude and the cut-off rigidity. The contribution of secondary muons is steadily increasing with decreasing altitudes, and at sea-level secondary muons dominate the radiation field.

In order to verify the computed dose rates induced by galactic cosmic ray particles and to test the accuracy of the restriction to primary hydrogen and helium nuclei the results from the Monte-Carlo simulation are compared to measurements performed by *Meier et al.* (2009) and *Hubiak* (2008) on-board aircraft on polar and equatorial routes (Fig. 3.14). The experimental data was taken with a tissue equivalent proportional counter (TEPC) which measures the ambient dose

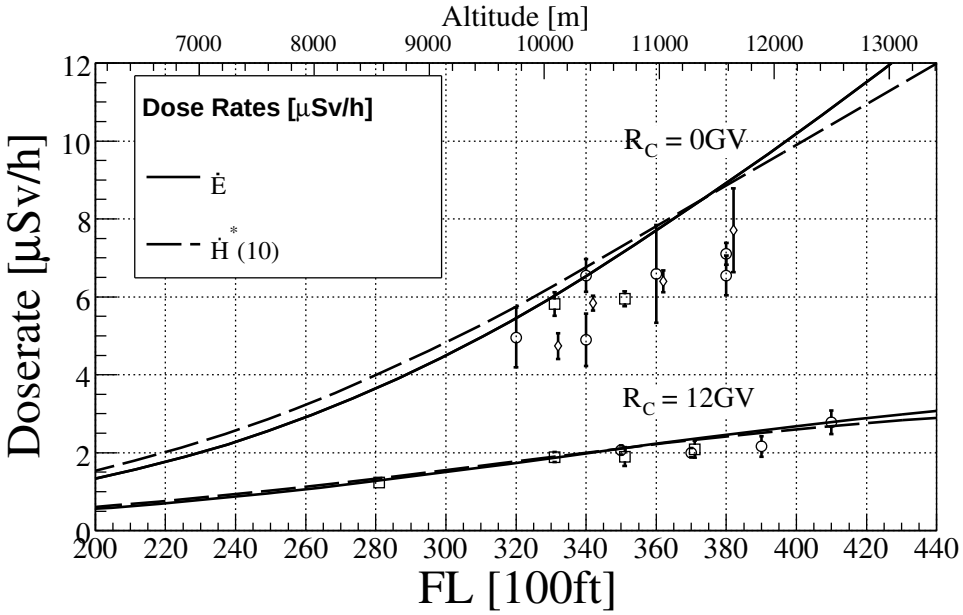


Figure 3.14: Calculated effective dose rates $\dot{E}$ (solid line) and ambient dose rates $\dot{H}^*(10)$ (dashed line) at commercial aviation altitudes during solar minimum and two different cut-off rigidities compared to measurements on different flights (symbols) performed by *Meier et al.* (2009) and *Hubiak* (2008).

equivalent $H^*(10)$. Measurements taken at geomagnetic latitudes larger than $60°$N were used to obtain the data for low cut-off rigidities in Fig. 3.14. Allowing for such a large latitude range is justified by the fact that for a given atmospheric shielding only particles above a certain threshold energy have an impact on the radiation field at the corresponding altitude. If the cut-off rigidity falls below this threshold the radiation field remains unchanged. Therefore, at latitudes above the corresponding value the dose rate is constant as a consequence of this atmospheric cut-off. For the atmospheric shielding corresponding to aircraft altitudes on the northern hemisphere this value is approximately $60°$N.
For large cut-off rigidities the experimental data is restricted to measurements performed at geomagnetic latitudes between $15°$N and $15°$S, and it was recorded on several flights from Germany to Africa. The cut-off rigidities at the positions along these routes in the equatorial region are $R_C \approx 12$ GV (see 3.2). The data on these flights was taken at typical aircraft altitudes corresponding to flight levels (FL) between 320 and 400. The results for the ambient dose equivalent obtained from the model calculations for polar ($R_C = 0$ GV) and equatorial ($R_C = 12$ GV) positions exhibit excellent agreement with the experimental data over the investigated altitudes and for large geomagnetic al cut-offs. At very low cut-off rigidities in the polar region the experimental data is slightly overestimated by the calculations. Fig. 3.14 additionally shows that $H^*(10)$ is a good estimation for the effective dose $E$ especially at large geomagnetic shielding. At low cut-off rigidities, on the other hand, the ambient dose is a conservative estimate for the effective dose only below approximately 11 km. This is related

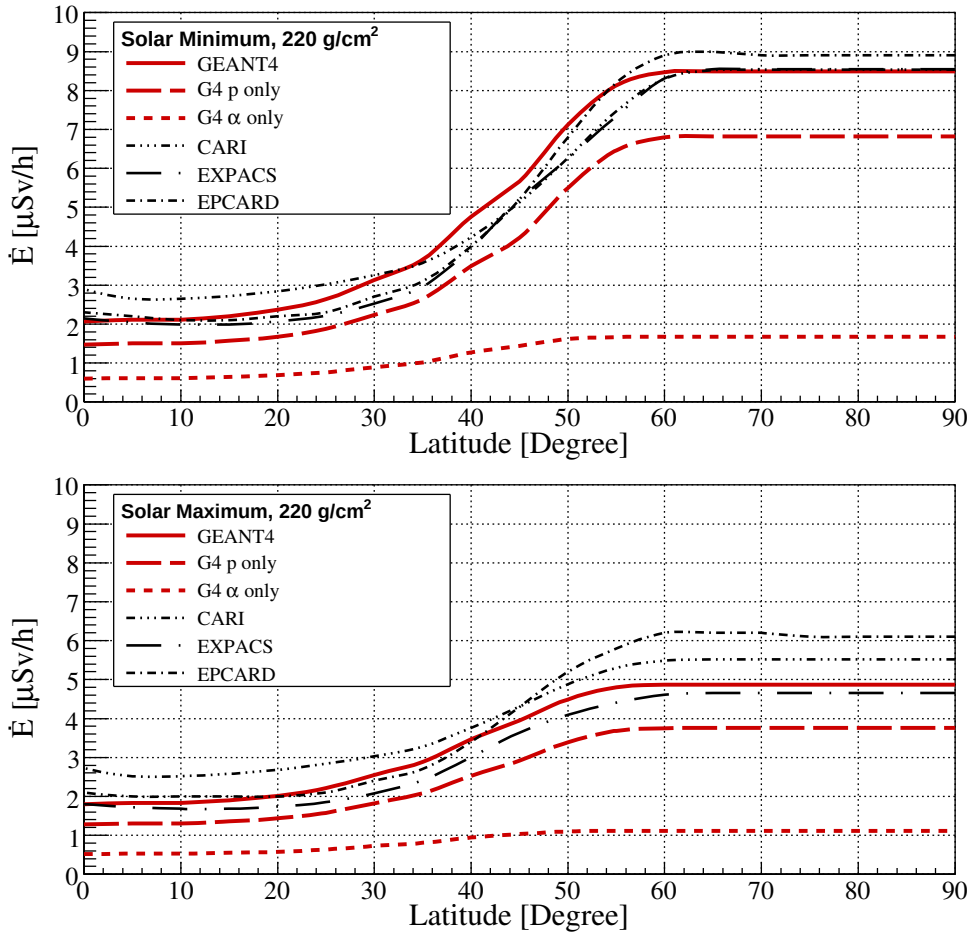


Figure 3.15: A comparison of the results from this work (marked as GEANT4) and from different tools for the calculation of effective dose rates at 220 g/cm$^2$ (corresponding to $\approx$ 11 km altitude) over a wide range of northern latitudes along the Greenwich meridian. Solar maximum (minimum) conditions are shown in the top (bottom) panel and the dashed lines indicate the dose induced by primary protons and alpha particles respectively.

to the fact that the neutron effective dose rate is overestimated by the neutron ambient dose equivalent by a factor $\approx 1.3$ (compare Tab. D.1 and Tab. D.2). In the case of protons, on the other hand, the effective dose rate is about twice as high as the ambient dose equivalent. With decreasing altitude the proton component becomes weaker and the neutron induced exposure increases leading to an overestimation of $E$ by $H^*(10)$.

The agreement between the experimental data for large cut-off rigidities and the simulation is excellent. A possible explanation for the overestimation of the measurements by the calculations at low geomagnetic shielding is the neglected shielding of the aircraft structures. As noted above, *Battistoni et al.* (2005) estimated that taking into account the shielding provided by the aircraft would result in a reduction of up to 14% of the effective dose rate.

The effect of the geomagnetic shielding is also evident in Fig. 3.15 where effec-

tive dose rates calculated in this work (marked as GEANT4 and red lines) are compared to other models developed for the estimation of radiation exposure at aircraft altitudes (EXPACS[7], CARI[8] and EPCARD[9]) over geomagnetic latitudes from $0°$N to $90°$N along the Greenwich meridian and for an atmospheric depth of 220 g/cm$^2$. For the US Standard Atmosphere this corresponds to an altitude of 11.3 km and this value was used to obtain the results from the EPCARD web interface which does not allow for using the atmospheric depth. The radiation exposure during solar minimum ($\phi = 400$ MV) is shown in the top panel and the effective dose rate for maximal solar activity ($\phi = 1200$ MV) is illustrated below. The suppression of low energetic primary galactic cosmic particles during solar maximum is expressed by the significantly decreased dose rate at large latitudes ($\approx 8.5$ $\mu$Sv/h during solar minimum versus $\approx 5$ $\mu$Sv/h during solar maximum). In the equatorial region, on the other hand, the solar cycle has no effect on the radiation exposure as the modulation by the interplanetary magnetic field leading to this effect is only relevant at energies that do not contribute to the dose rate at large geomagnetic cut-offs.
The comparison between the different models yields differences of up to 20%–30%. Large differences occur especially at very low latitudes comparing CARI with the other models and for EPCARD at very large geomagnetic cut-offs. The agreement of the results obtained in this work with the EXPACS model is in the order of 5%–10% and less.
In addition to the total effective dose, the contributions from primary proton and alpha particles are indicated by the dashed red lines. Around 20% of the total dose during both solar minimum and solar maximum at low cut-off rigidities is caused by primary alpha particles. For high geomagnetic shielding close to the equator the fraction rises to around 30% due to the larger rigidity of alpha particles compared to protons with the same energy per nucleon.

## 3.6 Modeling Neutron Monitor Count Rates

The modeling of Neutron Monitor count rates is used for the determination of the primary solar proton spectrum and for the validation of the transport calculations of the galactic cosmic particles through the atmosphere. The increase of the count rates during Ground Level Enhancements provides information on the primary particle intensities of the solar particles. Unfortunately, the Neutron Monitor count rates and consequently the numerical modeling is strongly dependent on a variety of parameters which are not always very accurately known. The dependency on the solar cycle, the geomagnetic cut-off and the atmospheric depth is studied in this section.
As mentioned in Section 2.7, the Neutron Monitor detectors are mainly sensitive to secondary neutrons and protons and to a minor degree to muons and pions. Fig. 2.10 shows the detector efficiencies for a standard 6-NM64 Neutron Monitor derived by *Clem and Dorman* (2000). The 6-NM64 is a detector of NM64

[7] http://phits.jaea.go.jp/expacs/
[8] http://www.faa.gov/data_research/research/med_humanfacs/aeromedical/radiobiology/cari6/
[9] http://www.helmholtz-muenchen.de/epcard-portal/

type comprising 6 detector tubes. All results in this section are obtained for the NM64 detector type, and for Neutron Monitor stations using detectors with a deviating number of tubes a linear dependence of the count rate on the number of detector tubes is assumed. It is unclear how good this assumption is but due to the lack of Neutron Monitor detection efficiencies for NM64 with larger or smaller number of detector tubes the efficiencies for 6-NM64 will be used for all stations with a corresponding scaling factor.
For the calculation of the detector count rate at an atmospheric depth $d$ the secondary particle fluences $F^i(\Delta E_j, d)$ of particle type $i$ in a kinetic energy interval $\Delta E_j \equiv [E_j, E_{j+1}]$ are used. The secondary particle fluence can be calculated from galactic cosmic ray and solar energetic particles during Ground Level Enhancements as described in Section 3.4:

$$F^i(\Delta E_j, d) = \sum_{\mathrm{p}} \sum_l \hat{F}^p(\Delta \hat{E}_l) f^{p,i}_{\hat{E}_l}(\Delta E_j, d), \tag{3.17}$$

where $p$ denotes the primary particle type with fluence $\hat{F}^p(\Delta \hat{E}_l)$ in the energy interval $\Delta \hat{E}_l \equiv [\hat{E}_l, \hat{E}_{l+1}]$.
Together with the detection efficiencies $r^i(E_j)$ by *Clem and Dorman* (2000) which give the number of counts per fluence of particles vertically incident on the detector the count rate $C$ at depth $d$ in a time interval $\Delta t$ is given by:

$$C(d) \approx \frac{1}{\Delta t} \sum_i \sum_j r^i(E_j) F^i(\Delta E_j, d) \tag{3.18}$$

$$\approx \frac{1}{\Delta t} \sum_i \sum_j r^i(E_j) \sum_{\mathrm{p}} \sum_l \hat{F}^p(\Delta \hat{E}_l) f^{p,i}_{\hat{E}_l}(\Delta E_j, d) \tag{3.19}$$

$$\approx \frac{1}{\Delta t} \sum_{\mathrm{p}} \sum_l \hat{F}^p(\Delta \hat{E}_l) \sum_i \sum_j r^i(E_j) f^{p,i}_{\hat{E}_l}(\Delta E_j, d) \tag{3.20}$$

$$\approx \frac{1}{\Delta t} \sum_{\mathrm{p}} \sum_l \hat{F}^p(\Delta \hat{E}_l) Y^p(\hat{E}_l, d). \tag{3.21}$$

The Neutron Monitor yield function for primary particles $p$

$$Y^p(\hat{E}, d) = \sum_i \sum_j r^p(E_j) f^{p,i}_{\hat{E}}(\Delta E_j, d) \tag{3.22}$$

is introduced to simplify the calculations of Neutron Monitor count rates for an arbitrary primary particle spectrum. Considering a solar energetic particle event, for example, the primary particle fluence can be written as the sum of galactic cosmic rays and solar energetic particles: $\hat{F}^p(\Delta \hat{E}) = \hat{F}^p_{\mathrm{GCR}}(\Delta \hat{E}) + \hat{F}^p_{\mathrm{SEP}}(\Delta \hat{E})$. The yield functions $Y(\hat{E}, d)$ are defined as the Neutron Monitor counts caused by an isotropic irradiation of primary particles on top of the atmosphere with a fluence of one particle per square-centimeter.
Once the Neutron Monitor yield functions are calculated the count rate can be determined by simply multiplying the corresponding value with the primary particle fluence and the time interval for which the fluence was calculated. Each

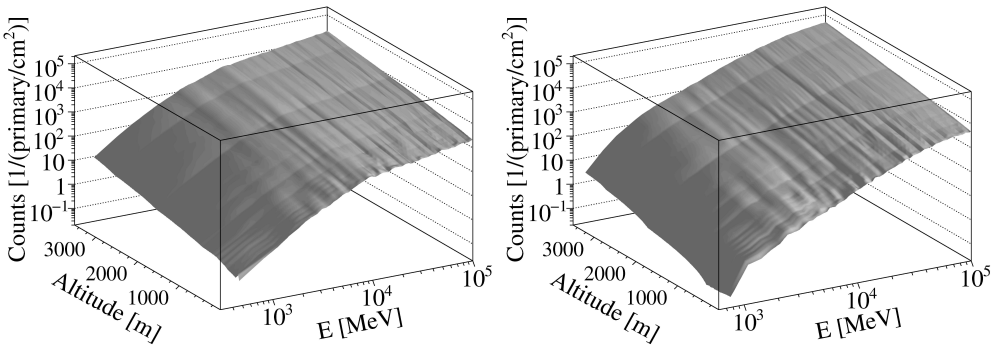


Figure 3.16: Neutron Monitor yield functions: Counts of a standard 6-NM64 detector at a given atmospheric depth for an isotropic fluence of one primary particle with kinetic energy $E$ per square centimeter for protons (left) and alpha particles (right) calculated with detector efficiencies by *Clem and Dorman* (2000).

primary particle species has its own yield function, and $Y(\hat{E}, d)$ varies with the primary's kinetic energy $\hat{E}$ and the atmospheric depth or altitude of the detector's location. For the results derived in this section it is assumed that the total detector count rate can be approximated as generated by secondary particles from hydrogen and helium nuclei only, and the influence of heavier ions is neglected.
The Neutron Monitor yield functions for primary hydrogen and helium nuclei calculated for the standard 6-NM64 detector are shown in Figure 3.16 for a wide range of primary energies and altitudes using the US Standard Atmosphere for the conversion from atmospheric depth to altitude. Naturally, the yield function increases with increasing particle energy and altitude. The slope of the function steepens at energies below a several GeV and primary particles below a certain threshold do not have an effect on the Neutron Monitor stations' count rates. At sea-level, for instance, this atmospheric cut-off energy for hydrogen (helium) is $E_{k,C} \approx 300$ MeV–500 MeV ($E_{k,C} \approx 800$ MeV–1000 MeV) corresponding to a rigidity of $R \approx 800$ MV–1000 MV ($R \approx 1300$ MV–1500 MV). Nevertheless, it will be shown later that the Neutron Monitor count rate for sea-level stations is not significantly influenced by galactic cosmic ray nuclei with rigidities below 2 GV. This is due to decreasing yield function in the lower rigidity range combined with the relatively flat spectrum of the primary galactic cosmic ray intensities in this range. The primary galactic cosmic ray ion spectra have their maximum around 1 GV/nucleon, and the intensity close this value is only moderately changing. Therefore, the decreasing yield functions dominate the response of the Neutron Monitor count rates to particles at this rigidity. At higher rigidities, however, the larger yield functions compensate for the effect of steeply decreasing primary particle intensity, and primary particles up to several tens of GV influence the measurements of Neutron Monitors as illustrated in the top panel of Fig. 3.17. In this figure the response of Neutron Monitors located at different geomagnetic cut-offs during solar minimum ($\phi = 400$ MV) and solar maximum ($\phi = 1200$ MV) was calculated by the technique described above. On the left scale the values normalized to a cut-off $R_C = 0$ GV during solar mini-

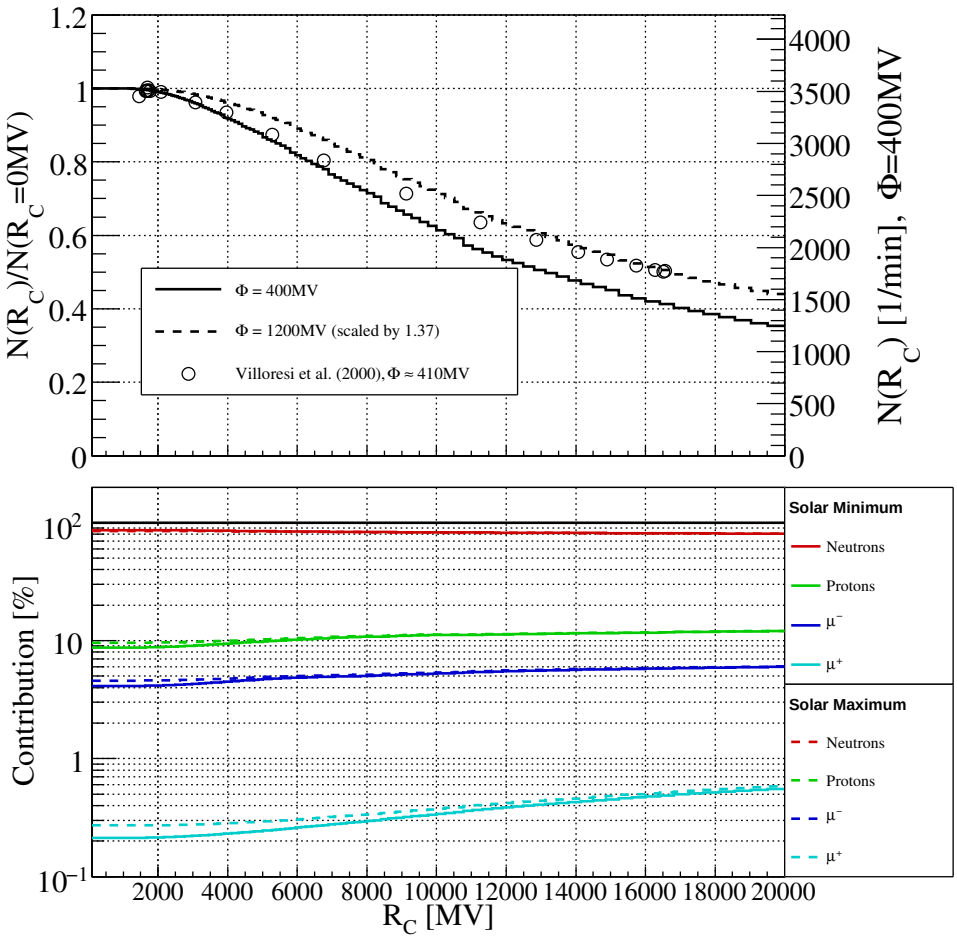


Figure 3.17: Latitude dependency of 6-NM64 Neutron Monitor count rates at sea-level (1025 g/cm$^2$) in the top panel calculated for solar minimum ($\phi = 400$ MV, solid line) and solar maximum ($\phi = 1200$ MV, dashed line) compared to measurements from *Villoresi et al.* (2000) performed during solar minimum. Relative count rates with respect to $R_C = 0$ GV during solar minimum are illustrated on the left scale and absolute values on the right scale. In the bottom panel the contributions of the individual secondary particles incident on the Neutron Monitor detector are shown.

mum can be read whereas the right scale shows the absolute numbers. Absolute values of Neutron Monitor count rates for a sea-level station at a cut-off rigidity $R_C < 2$ GV are in the order of 3500 counts per minute and drop to around 40% of that value ($\approx$ 1400 counts/min) at a cut-off rigidity $R_C \approx 16$ GV. The count rate during solar maximum for low cut-off rigidities is smaller by a factor 1/1.37 (values in the figure have been scaled by this factor to simplify the comparison to solar minimum conditions). As the solar modulation is most effective for low rigidity particles the differences in the count-rate are reduced at higher cut-offs and the decrease in count-rates is weaker. At $R_C = 20$ GV the values are almost identical.

By comparing these results to the measurements of Neutron Monitor stations it becomes obvious that the count rates depend on additional factors. Unfortu-

nately, very few Neutron Monitor stations use 6-NM64 detectors whereas the majority operates detectors with larger or smaller tube numbers which complicates a comparison. The LARC Neutron Monitor station on King George island in the Antarctica ($62°20'$S, $58°96'$W) is the only 6-NM64 station near sea-level. The station's count rates are normalized to a pressure of 1013 mbar corresponding to an atmospheric depth $d \approx 1033$ g/cm$^2$ for an Earth's gravitation $g = 9.81$ m/s$^2$ and the cut-off rigidity is $R_C = 3$ GV. For the comparison between solar minimum and solar maximum we will relate to data from January 1997 and March 1991 respectively as these dates correspond to solar modulation of $\phi = 417$ MV and $\phi = 1261$ MV respectively following (*Usoskin et al.*, 2005). During these solar minimum and solar maximum periods the LARC station recorded count rates of 4660 counts/min and 3770 counts/min respectively. These numbers are about 35% (solar minimum) to 50% (solar maximum) larger than the numerically predicted count rates in this work (3393 counts/min during solar minimum and 2540 counts/min during solar maximum). A possible explanation of this effect is the influence of the surrounding of the Neutron Monitor stations. The simulations were performed for soil consisting of pure water. For real Neutron Monitor stations, however, the ground contains a variety of materials. Due to the large amount of hydrogen, i.e. nuclei only consisting of a single proton, in water very little secondary neutrons are produced in this material. The amount of albedo neutrons is significantly higher for other materials which may significantly increase the count rate of a neutron detector located on and surrounded by such materials compared to the calculations. The fraction of the count rate of a Neutron Monitor caused by neutrons incident on the detector is around 90% (Fig. 3.17, bottom panel) compared to only about 10% from protons and 4%-5% of $\mu^-$. Although the contribution of protons and muons increases slightly at higher cut-offs, the neutron component remains the most important. Another explanation for the underestimation of the Neutron Monitor counts by the calculations may be inaccurate transport calculations through the atmosphere or that the primary particle spectrum does not describe the galactic cosmic ray spectra very well. Neglecting the contribution of primary ions heavier than helium may be another aspect.

Other Neutron Monitor stations being located near sea-level and at low cut-off rigidities show even larger count rates. The Oulu station at $R_C = 0.8$ GV for example recorded numbers of 6500 counts/min ($\approx 9/6 \cdot 4330$ counts/min) in January 1997 operating 9 detector tubes in a 9-NM64 type. Even larger numbers are measured by the McMurdo Neutron Monitor (18-NM64) with a count rate of around 16580 counts/min ($\approx 18/6 \cdot 5530$ counts/min). Obviously, Neutron Monitor stations with larger numbers of detector tubes have higher count rates per tube. As no detector efficiencies are available for these detectors the results for the solar energetic particle events in the following chapter are derived by normalizing the count rate to the number of tubes. A more detailed analysis may reveal a better method to compare Neutron Monitor detectors with different numbers of detector tubes but could not be performed within this work.

Measurements over a wide range of latitudes performed by *Villoresi et al.* (2000) during solar minimum activity are shown in addition to the results from this

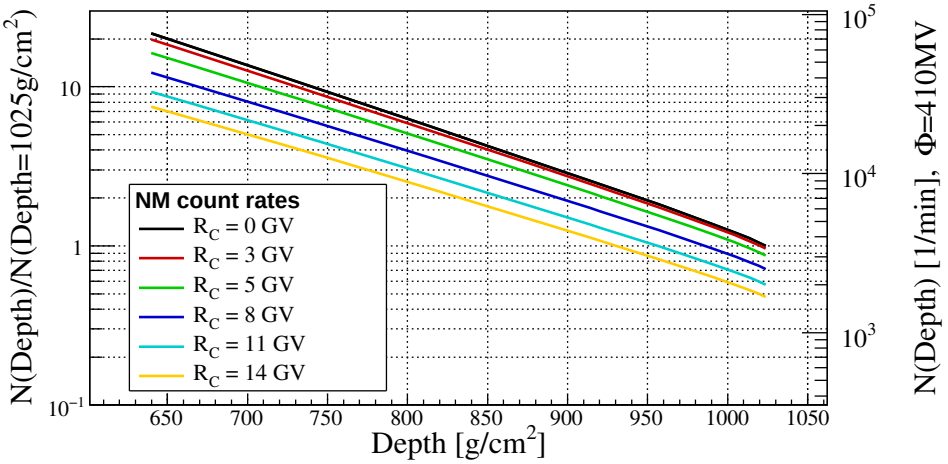


Figure 3.18: Variation of Neutron Monitor count rate with atmospheric depth during solar minimum ($\phi = 400$ MV) for various cut-off rigidities $R_C$ normalized to the absolute count rate at 1025 g/cm$^2$ and $R_C = 0$ GV.

work in Fig. 3.17. The absolute count rates of the ship-bound 3-NM64 detector used in the experiment at low cut-off rigidities are 9182.1 counts/(5·minutes) ($\approx 1/2 \cdot 3673$ counts/min) which is only 8% larger than the numbers obtained in this work. This decreased count rate compared to on-shore Neutron Monitors (see above) may be either an effect of the detector type (3-NM64) or due to the large fraction of water below the ship-bound detector. On the other hand, compared to the calculations assuming a soil of pure water the large amount of iron and other heavy elements in the materials of the ship may have an effect on the count rate. *Clem and Dorman* (2000) derived a similar number on a latitude scan with a 3-NM64 detector on-board a ship in 1994–1995 ($\approx 11 \cdot 10^4$ counts/hour $\approx 1/2 \cdot 3700$ counts/minute). The count rates for the 3-NM64 detector on the latitude survey drop to around 50% at cut-off rigidities $R_C = 16$ GV compared to high latitude and low cut-off measurements. In the calculations on the other hand the decrease of the count rates with increasing magnetic shielding is steeper and the numbers go down to a little more than 40%. The reason for these discrepancies is unknown but may be related to the different detector types or again the surrounding of the detector. It is also possible that the contribution of the primary galactic cosmic ray ions plays a role. The rigidity of a particle at a given energy per nucleon is proportional to the ratio $A/Z$ where $A$ is the mass number and $Z$ the atomic number of the element. This means that hydrogen nuclei ($A/Z$=1) are the ions having the smallest rigidity and including heavier ions may result in an increased ratio of count rates at high cut-offs compared to low cut-offs. However, most Neutron Monitor stations are located at cut-off rigidities below $R_C = 6$ GV where the deviations are in the range of a few percent and the calculations provide satisfying accuracy.

Another very important factor influencing the Neutron Monitor count rates is the mass of air above the station providing the shielding from the galactic or solar particles. The mass or atmospheric depth $d$ above the detector is related to the pressure $p$ at the station and the dependency of the count rate on the pressure

or atmospheric depth is usually described by (e.g. (*Hatton*, 1971; *Moraal et al.*, 1989)):

$$N(p) = N_0 e^{-\alpha_p p} \tag{3.23}$$
$$N(d) = N_0 e^{-\alpha_d d}. \tag{3.24}$$

The attenuation coefficients $\alpha_p$ and $\alpha_d$ determine the steepness of the increase of the Neutron Monitor count rates with decreasing pressure or atmospheric depth, and the pressure related attenuation coefficient is in the order of $\alpha_p = 0.7 - 1.0$ %/mmHg (*Raubenheimer and Stoker*, 1974). The exponential behavior is confirmed by the results from this work presented in Fig. 3.18 where the Neutron Monitor count rates for six different cut-off rigidities versus the atmospheric depth are illustrated. As the computation of the secondary particle fluences is very time consuming the transport calculations were performed only once for a ground at sea-level. That means that the influence of the ground is diminishing with increasing altitude and the count rates represent values for a detector surrounded entirely by air. By fitting the data presented in this figure with Eq. 3.23 the attenuation coefficient $\alpha_d$ was derived for the various cut-off rigidities (Tab. 3.3). The variation of the attenuation coefficient with atmospheric depth was hereby neglected. It is obvious that the decrease at very low altitudes ($d > 950$ g/cm$^2$) becomes significantly steeper. In contrast, (*Raubenheimer and Stoker*, 1974) observed the contrary effect with decreasing attenuation coefficients at pressures above $600$ mm/Hg. The calculations in this work have been performed with the soil at sea-level for all altitudes. Therefore, the moderating effect of the water becomes important only at very low altitudes. (*Raubenheimer and Stoker*, 1974) measuring above solid ground observe a positive effect of the soil on the Neutron Monitor count rate.
The last aspect of Neutron Monitors that will be studied in this section is the

Table 3.3: Attenuation coefficients $\alpha_d$ during solar minimum.

| $R_C$ [GV] | $\alpha_d$ [%/(g/cm$^2$)] |
|---|---|
| 0 | $(7.77 \pm 0.05) \cdot 10^{-1}$ |
| 3 | $(7.66 \pm 0.04) \cdot 10^{-1}$ |
| 5 | $(7.38 \pm 0.04) \cdot 10^{-1}$ |
| 8 | $(7.13 \pm 0.07) \cdot 10^{-1}$ |
| 11 | $(7.01 \pm 0.06) \cdot 10^{-1}$ |
| 14 | $(6.91 \pm 0.07) \cdot 10^{-1}$ |

dependence of the count rate on the solar cycle. As shown in the previous section, the dose rate depends significantly on the solar activity. It comes as no surprise that the same is true for the measurements of the Neutron Monitor stations. In Fig. 3.19 the variation of average monthly count rates of two Neutron Monitor stations over the last decades is compared to the variation of the solar activity expressed by the Sun spot number and the related modulation parameter $\phi$ from (*Usoskin et al.*, 2005). In the top panel, the modulation parameter between 1965 and 2005 is compared to the Sun spot number. The correlation between the two magnitudes is obvious. The time lag between the solar activ-

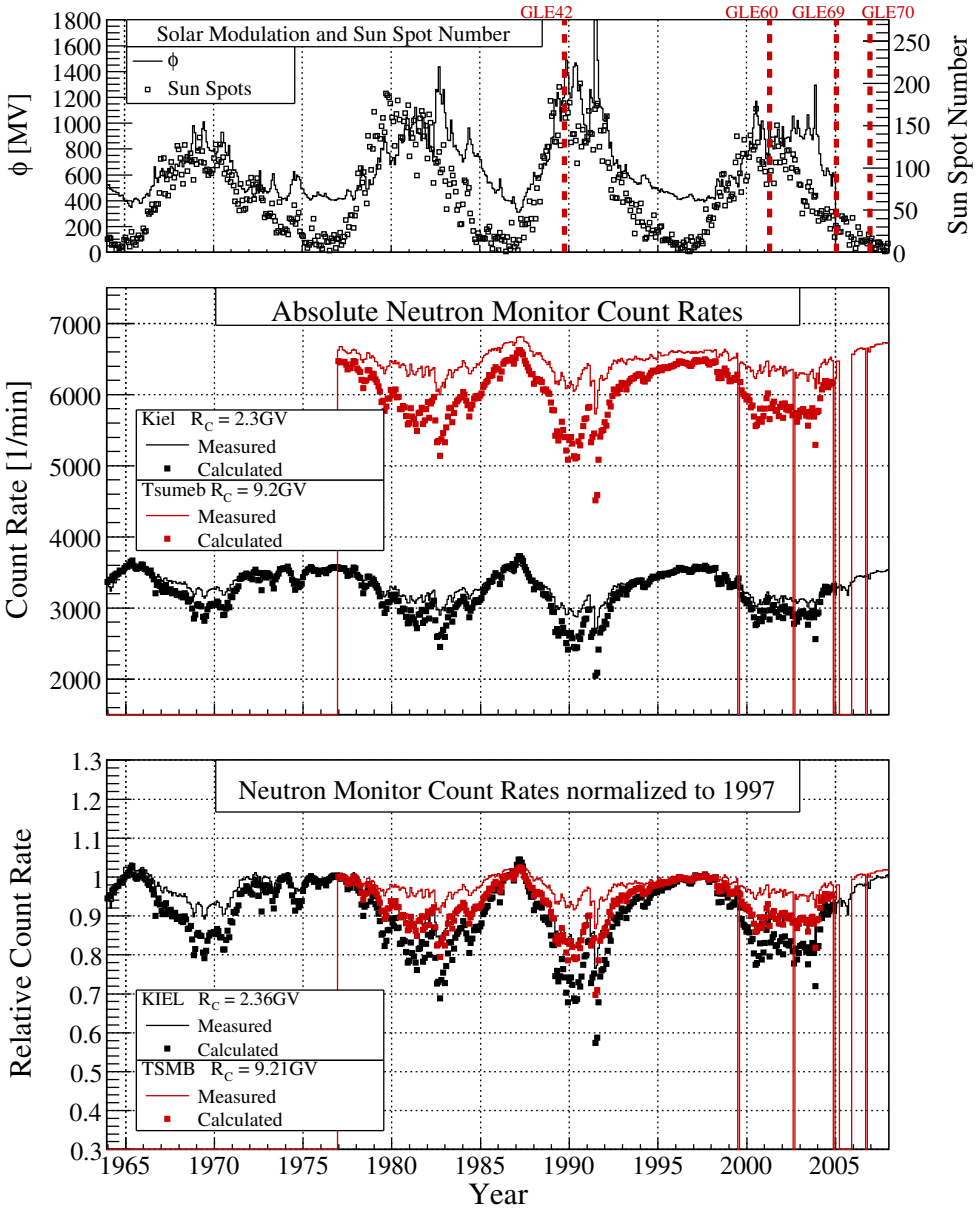


Figure 3.19: Solar activity expressed by the Sun spot number and the related solar modulation parameter $\phi$ by *Usoskin et al.* (2005) in the top panel, and the variation of the absolute and relative Neutron Monitor count rates of Kiel ($R_C$ = 2.3 GV, altitude 54 m) and Tsumeb ($R_C$ = 9.2 GV, altitude 1240 m) station over various solar cycles below. The relative count rate was normalized to the average count rate in 1997. The measured count rates in the second panel were scaled by a factor of $1/3$ to account for the differences between the 18-NM64 detector used at these stations and the 6-NM64 response functions used for the calculation. The anti-correlation of the count rate to solar activity is clearly visible.

ity and the modulation of the galactic cosmic ray intensity noted in Sec. 2.1 is especially pronounced during the solar minimum periods in the early 1980s and 2000s where it is in the order for several months. The Sun spot numbers reached

peak values of around 200 during the solar maxima around 1980 and 1990. The modulation parameter $\phi$ from *Usoskin et al.* (2005) ranges from around 400 MV during solar minimum up to 800 MV–1200 MV and even larger values during very active periods. The dates of the Ground Level Enhancements analyzed in the following chapter are also indicated in the top panel. Two of these events, namely GLE 42 and GLE 60, occurred during solar maximum activity, one in the declining phase of the solar cycle at medium activity (GLE 69) and the most recent took place during solar minimum activity (GLE 70).

The second panel illustrates the absolute count rates of the Tsumeb ($R_C \approx 9.2$ GV, altitude 1241 m, $d \approx 900$ g/cm$^2$) and Kiel ($R_C \approx 2.3$ GV, altitude 55 m, $d \approx 1000$ g/cm$^2$) stations. The measurements provided by the Neutron Monitors are indicated by the solid lines and compared to the results from the calculations performed in this work (solid squares). The Neutron Monitor count rate was not calculated during periods where the modulation parameter was not available, i.e. after 2004, or if other data such as the nominal pressure was not given in the data files of the Neutron Monitor. To account for the fact that the Neutron Monitor count rates were simulated using a response function for 6-NM64 detectors the measured count rate was scaled according to the number of detector tubes. Both Tsumeb and Kiel stations use an 18-NM64 detector and, accordingly, were scaled by a factor of 1/3. In the following, all Neutron Monitor data is presented normalized to a 6-NM64 detector. The Tsumeb and Kiel count rates are pressure corrected values with a reference pressures of 880 mbar and 1006.7 mbar respectively. The atmospheric depth $d$ for the simulation of the Neutron Monitor count rates was derived from the pressure $p$ following Eq. 2.15: $d = p/(9.81 \text{ m/s}^2)$. The bottom panel of Fig. 3.19 shows the count rates normalized to the average count rate in 1997.

The expected anti-correlation of the Neutron Monitor count rate with the solar activity is clearly visible, the smallest count rates occurring around solar maximum ($\phi > 800$ MV) and maximum count rates during solar minimum ($\phi \approx 400$ MV). The decrease of the Neutron Monitor count rates during solar maximum is in the order of 20%–30% for Kiel, i.e. at low magnetic shielding, and around 5%–10% for Tsumeb. The lower modulation at the Tsumeb station is related to its large magnetic cut-off. Due to this large cut-off the low energetic particles which experience the largest modulation during solar maximum do not contribute to the total count rate, and as a consequence the change of the count rate over the solar cycle is smaller. It is also obvious that the elevated location of the Tsumeb station causes a much higher detector count rate compared to the Kiel station which is located near sea-level. In fact, this effect is much stronger than the expected decrease in the count rate due to the large cut-off rigidity.

The agreement between simulation and measurement for the Kiel station during the solar minimum periods is excellent since only differences in the order of less than 2% are observed. Slightly larger differences occur between the simulation results for the Tsumeb station and the measured count rates ($\approx 3\%$). During solar maximum, on the other hand, the measured Neutron Monitor count rates are underestimated by the calculation by 10% to 15% (Kiel) and around 20% (Tsumeb). Several facts might explain this behaviour. In general, differences

between the simulated and the calculated count rates may occur due to environmental parameters of the Neutron Monitor. In the simulation, the soil contained pure water and was placed at sea-level. This means that higher altitude stations are simulated as surrounded by air. The count rates of real Neutron Monitors, on the other hand, may be influenced by different compositions of the soil, constructions close to the detector station or the geometry of the building containing the detector. Taking into account a solid ground for the simulation of the Tsumeb stations, for example, may result in higher count rates caused by neutrons produced in the ground. A detailed study of this phenomenon, however, could not be performed within this work. Nevertheless, it would be helpful to investigate the exact influence of the soil on the Neutron Monitor count rate, especially as the count rates of some Neutron Monitor stations at similar geomagnetic shielding and altitude measure very different count rates. At sea-level and low geomagnetic shielding, for example, Barentsburg, Yakutsk and Tixie Bay (all 18-NM64) have count rates very similar to the Kiel station and the simulated values. Other stations at similar conditions, on the other hand, like Oulu or Apatity (9-NM64) record about 25% larger values if normalized to the number of detector tubes. At large cut-offs and high altitudes these discrepancies between different stations are observed as well. While the measurements by the Tsumeb (18-NM64) and Mexico station (6-NM64) agree quiet well with the prediction of the simulation, Alma-Ata B (18-NM64) and other stations record significantly different values (see also App. C). To clarify the origin of these significant differences it would be necessary to study differences in the response function of the different detector types and the influence of the surrounding of the detector station. Unfortunately, only response functions for the 6-NM64 detector type are available.
In addition to the environment of the Neutron Monitor, the disregard of heavier GCR nuclei may cause an underestimation of the count rates especially during solar maximum and at high cut-off rigidities. As noted in Sec.2.1 the reduction of the intensity during solar maximum is maximal for primary hydrogen. Additionally, at identical energies per nucleon hydrogen has the lowest rigidity of all GCR nuclei. Accordingly, the decrease in primary intensity for helium and heavier nuclei is smaller than for hydrogen both at large cut-off rigidities and during strong solar modulation compared to low magnetic shielding and solar minimum conditions. As the best agreement is observed for low geomagnetic shielding during solar minimum and the worst at large cut-offs and during solar maximum this effect may well contribute to the differences between simulation and experiment.
Another aspect that has to be noted is the model of the primary particle spectrum and the modulation parameter $\phi$. The modulation parameter is derived from simulated Neutron Monitor count rates and is therefore dependent on transport calculations of the galactic cosmic rays through the atmosphere. Consequently, different transport calculations may result in different modulation parameters.
Most probably, the observed differences are a consequence of a combination of the factors described above. For the analysis of the solar energetic particle events in the following, however, only the relative count rate increase is of importance. It will be assumed that the scaling factor between the simulated and measured

count rates stays constant during the solar energetic particle event. The comparison of measured relative increases with the results from the simulation can then be used to analyze the solar energetic particle event.

# Chapter 4

# Modeling Solar Energetic Particle Events

The impact of solar energetic particle events producing high relativistic particles reaches deep in the atmosphere and may even be measured by ground-based detectors. With the ability to calculate the transport of particles through the Earth's magnetosphere and the atmosphere it is possible to derive information about the event by analyzing Neutron Monitor count rates during the ongoing event. Due to the Neutron Monitors' different locations and the corresponding sensitivity to different incoming directions, the angular distribution and the energy spectrum of the primary particles, the Neutron Monitors can be used as a tool for the characterization of the solar energetic particle event. The complexity of the problem makes it necessary to include as many stations as possible for a detailed analysis of an event. Moreover, from the high temporal variability of the incoming particles arises the necessity for a stepwise investigation for short time intervals during the whole duration of the event. The exact procedure fulfilling these requirements is explained in the following, and results for different Ground Level Events are shown.

## 4.1 Analyzing Ground Level Events by using relative Neutron Monitor increases

As described in Section 3.6, the Neutron Monitors are mainly sensitive to secondary neutrons and protons and to a minor degree to other secondaries produced in interactions of cosmic nuclei with atoms in the atmosphere. An increase in fluence of these particles at the Neutron Monitor site during solar energetic particle events triggers a rise in detector count rates (see Fig. 2.6). This increase is related to highly energetic solar particles arriving at Earth. In contrast to the mainly isotropic galactic cosmic ray spectrum the intensities of the solar particles usually show a strong angular dependence. It was demonstrated in Sec. 3.3 how the asymptotic viewing directions of a Neutron Monitor station can be determined and that the vertical asymptotic viewing direction can be used as an approximation for the incoming direction which a Neutron Monitor station is sensitive to. As the Neutron Monitor's response to such an event is related to its asymptotic

viewing directions the sharpness and the extent of the increase will vary from station to station, especially in the very beginning of the event when the intensity of the primary particles shows a strong angular dependence. As a consequence, the change in the detector count rate of a given station is not only affected by the geomagnetic cut-off rigidity and the altitude as in the case of the galactic cosmic ray background but also by the asymptotic viewing directions and the angular distribution of the solar particles. For a precise description of the event it is therefore inevitable to take this dependency into account by calculating the viewing directions for a wide range of rigidities of all stations under investigation and by modeling the angular distribution of the event.

To characterize the temporal and spatial evolution of the solar energetic particle event, it is necessary to model the incoming primary particle spectrum. In this work it is assumed that the changes registered by the Neutron Monitors are exclusively caused by solar hydrogen nuclei which is by far the most abundant ion species produced in solar energetic particle events (*Reames*, 1998; *Mason et al.*, 1984).

The goal is to derive information about the primary proton energy or rigidity spectrum, the angular distribution and the incoming direction during the whole event. With this information it is possible to calculate the secondary particle intensities and the corresponding radiation doses at an arbitrary point in the atmosphere. The difficulty of the procedure consists in the extraction of the free parameters from the single count rate that is recorded by a Neutron Monitor. As noted above, by using many different stations and by making use of the different sensitivities to changes in the primary particle spectrum due to different geomagnetic cut-offs, locations and altitudes the characteristics of the event can be derived. The dependencies of the Neutron Monitor count rates on these magnitudes were described in detail in Section 2.7 and Section 3.6.

The comparison of different Neutron Monitors for the analysis of solar particle events was first used by (*Shea and Smart*, 1982), and the technique was adopted and developed by various authors since, e.g. (*Cramp et al.*, 1997a; *Vashenyuk et al.*, 2007). The initial step is to choose a function to describe the primary proton spectrum in kinetic energy $E$ or rigidity $R$ and the pitch angle distribution. Simple functions that are commonly used for the description of the differential intensity spectrum are power laws in kinetic energy $E$ or rigidity $R$:

$$\frac{dI}{dE}(E) = \left(\frac{dI}{dE}\right)_0 \cdot E^{-\gamma}, \tag{4.1}$$

$$\frac{dI}{dR}(R) = \left(\frac{dI}{dR}\right)_0 \cdot R^{-\gamma}. \tag{4.2}$$

A steepening effect in the energy distribution of the primary particles may be taken into account by an exponential modulation (*Cramp et al.*, 1997a). Such an effect may occur due to the energy and velocity dispersion in the solar particles and the corresponding differences in the arrival time at Earth.

Typically, the primary particle spectrum is not isotropically distributed over all incoming directions. Therefore, the influence of the viewing directions on the particle intensity has to be taken into account. The angular distribution of the

primary solar energetic particle intensities is usually expressed as a function of the pitch angle $\alpha$ between the incoming direction of the event and the direction of the particles. The angular distribution is usually assumed to be rotationally symmetrical around an axis of symmetry which is used to characterize the incoming direction of the event and which is expressed in latitude $\phi_S$ and longitude $\lambda_S$. The intensity is assumed to be maximal in the incoming direction decreasing at larger pitch angles. For a specific location $L$ on top of the atmosphere the pitch angle for particles of a certain rigidity $R$ is given by the angle between the asymptotic arrival direction and the axis of symmetry of the solar particles: $\alpha_L(R,t) = \alpha_L(R,t,\phi_S(t),\lambda_S(t))$. If the angular distribution is given by $f(\alpha,t)$ the primary particle differential intensity $j_L$ at the location $L$ can be written as:

$$j_L(R,t) = \frac{dI}{dR}(R,t) \cdot f(\alpha_L(R,t),t) \tag{4.3}$$

$$j_L(E,t) = \frac{dI}{dE}(E,t) \cdot f(\alpha_L(R(E),t),t). \tag{4.4}$$

The differential intensity can be given either as a function of kinetic energy $E$ or rigidity $R$.
The formalism for the calculation of the secondary particle fluences, the doses and the Neutron Monitors presented in Sec. 2.6 and Sec. 3.4 was based on the differential intensity spectrum with respect to energy. These quantities can be derived from a primary particle spectrum described by a differential intensity with respect to rigidity by converting the latter to a differential intensity with respect to energy:

$$\frac{dI}{dE}(E,t) = \frac{dI}{dR}(R(E),t) \cdot \frac{dR}{dE}(E). \tag{4.5}$$

With

$$R = \frac{1}{q}\sqrt{E^2/c^2 + 2Em} \tag{4.6}$$

this becomes

$$\frac{dI}{dE}(E,t) = \frac{E/c^2 + m}{q\sqrt{E^2/c^2 + 2Em}} \cdot \frac{dI}{dR}(R(E),t), \tag{4.7}$$

where $c$ is the speed of light, $q$ the particle's charge and $m$ its rest mass. The differential intensity $j_L(E,t)$ can then be used to calculate the secondary particle fluences, radiation exposure and Neutron Monitor count rates for the location $L$ as explained in the previous chapters.
A simple assumption for the angular distribution $f$ in the primary spectrum is a linear dependence on the pitch angle $\alpha$ allowing only positive values:

$$f(\alpha,t) = \begin{cases} (1 - b(t) \cdot \alpha) & \text{if } b(t) \cdot \alpha < 1, \\ 0 & \text{otherwise.} \end{cases} \tag{4.8}$$

$b(t)$ is the time dependent measure for the anisotropy of the event, and large values of $b(t)$ indicate that high particle intensities are restricted to small pitch

angles.
*Smart et al.* (1971) used a Gaussian distribution in $\alpha$ with width $\sigma(t)$ for the description of the pitch angle distribution:

$$f(\alpha, t) \quad = \quad e^{-\alpha^2/2\sigma(t)^2}. \tag{4.9}$$

Other authors described the pitch angle distribution by an exponential function (*Cramp et al.*, 1997a; *Humble et al.*, 1991):

$$f(\alpha, t) \quad = \quad \exp\left(\frac{-0.5 \cdot (\alpha - \sin(\alpha)\cos(\alpha))}{A - 0.5(A-B)(1-\cos(1-\cos(\alpha)))}\right). \tag{4.10}$$

The disadvantage of the latter function is the fact that it has two free parameters $A$ and $B$ instead of one as the linear angular distribution and the Gaussian distribution. All of the presented distributions were used in this work to model the pitch angle distribution. It was found, however, that the linear description provides a good description in most cases and shows the most robust convergence behaviour in the minimization procedure described in the following.
To derive the characteristics of a solar energetic particle event it is necessary to determine the free parameters from the energy or rigidity and angular distribution. For example, if the power law in rigidity (Eq. 4.2) is chosen together with a linear angular distribution (Eq. 4.8), five parameters have to be adapted, namely $(dI/dR)_0$, $\gamma$, $b$ and $(\phi_S, \lambda_S)$. The set of free parameters that is to be derived will be named $\vec{x}$ in the following.
Once a specific function to describe the primary spectrum together with a set of parameters $\vec{x}$ is chosen, the secondary particle intensities for a given location can be calculated as follows. As a first step it is necessary to calculate the asymptotic viewing directions for this location. The asymptotic directions at a specific point obviously depend on the magnetic field and the particle's rigidity $R$. Additionally, the viewing directions of a Neutron Monitor depend on the zenith and azimuth angle of the incoming particle on top of the atmosphere after traversing the magnetosphere. The differences between non-vertical and vertical asymptotic directions were shown in Figure 3.5. The deviation of non-vertically from vertically incident protons is neglected in this part of the work and the vertical asymptotic directions are used as an approximation for all incoming directions.
The pitch angle $\alpha(R)$ for a given rigidity $R$ is calculated as the angle between the vertical asymptotic viewing direction for this rigidity and the incoming direction $(\phi_S, \lambda_S)$. In this way, the individual primary proton spectrum $j_i$ can be obtained point wise for each Neutron Monitor station $i$ from the pitch angle and energy distribution (Eq. 4.3). The expected increased count rate $C_i^{Tot}$ can be modeled by adding the contribution of solar energetic proton fluence to the galactic cosmic ray background from Equation 3.21:

$$\begin{aligned} C_i^{Tot} \quad &= \quad C_i^{\text{GCR}} + C_i^{\text{SEP}} \\ &\approx \quad \frac{1}{\Delta t}\left(\sum_p \sum_l \hat{F}^{\text{GCR},p}(\Delta\hat{E}_l) Y_i^p(\hat{E}_l) + \sum_p \sum_l \hat{F}^{\text{SEP},p}(\Delta\hat{E}_l) Y_i^p(\hat{E}_l)\right), \end{aligned} \tag{4.11}$$

where $p$ denotes the different primary nuclei and the $Y_i^p$ are the corresponding Neutron Monitor yield functions for station $i$. The sum over $l$ contains all

primary energy intervals $\Delta\hat{E}_l$. In the following analysis of solar energetic particle events, the considerations are restricted to primary hydrogen and helium nuclei for the galactic cosmic ray particles and hydrogen only for solar energetic particles. The local interstellar spectra by *Burger et al.* (2000) with the corresponding modulation from *Usoskin et al.* (2005) were used to describe the GCRs for the analysis of Ground Level Events. The impact of heavier nuclei of much smaller abundance on the lower atmosphere is neglected. In solar energetic particle events, the contribution of helium is usually less than 1%.
From Eq. 4.11 the simulated relative count rate increase for an individual station for a set of parameters $\vec{x}$ can be derived:

$$c_i(\vec{x}) = \frac{C_i^{Tot}(\vec{x}) - C_i^{\mathrm{GCR}}}{C_i^{\mathrm{GCR}}}. \tag{4.12}$$

The goal is to find the set of parameters $\vec{x}$ for which the resulting count rate increases $c_i(\vec{x})$ deliver the best fit to the actual measurements from the Neutron Monitor stations. The sum of squares $s(\vec{x})$ of the differences between simulated and measured count rate increases delivers a measure for the quality of the modeled primary proton spectrum:

$$s(\vec{x}) = \sum_i \Delta c_i(\vec{x})^2 \tag{4.13}$$

$$= \sum_i (c_i^{modeled}(\vec{x}) - c_i^{measured})^2. \tag{4.14}$$

The sum includes all Neutron Monitor stations under consideration. By minimizing $s(\vec{x})$ it is possible to derive a parameter set $\vec{x}$ to fit the measured Neutron Monitor count rates and by that fitting the primary proton spectrum. It is essential to use as many stations as possible to get a reliable result for the primary spectrum. Results from this minimization procedure are presented in the following sections where data from around 30 different stations was analyzed to model the primary particle spectra for several Ground Level Enhancements and the related Neutron Monitor count rate increases and radiation exposures. The minimization procedure was performed with the MINUIT (*James and Roos*, 1975; *James*, 2000) package implemented in the ROOT analysis software[1].
All Neutron Monitor data used for the analysis of the Ground Level Events presented in the following sections was obtained from the IZMIRAN cosmic ray data base[2], and the analysis is based on five minute averages of the Neutron Monitor count rates provided by IZMIRAN. In case that only one minute averages were available a five minute average of the one minute data was used.

## 4.2 Ground Level Enhancement 70

The most recent Ground Level Enhancement took place on December 13th, 2006 and will be discussed as a first example where the minimization procedure introduced above provides very good results. Some of the results presented in this

[1] http://root.cern.ch/drupal/
[2] *ftp://cr0.izmiran.rssi.ru/COSRAY!/*

section were also published in *Matthiä et al.* (2009a).
The first indication for a large solar energetic particle event on December 13th, 2006 was an optical and X-ray solar flare located at (5° S, 23° W) on the Sun. The beginning of a visible H$\alpha$ 4B class flare was observed at 2:20 UTC (*Bieber et al.*, 2008). It was followed by the X3.4 X-ray flare registered by the GOES-10 and GOES-11 spacecraft starting at 2:22 UTC and reaching its maximum around 2:39 UTC (indicated by the red line in Fig. 4.1). The related coronal mass ejection was seen by LASCO on-board SOHO at 2:25 UTC with an estimated speed of around 1770 km/s (*Abbasi et al.*, 2008). High relativistic electrons ($2.7\,\mathrm{MeV} < E < 10\,\mathrm{MeV}$) with velocities of more than $0.98c$ were observed by EPHIN on-board SOHO simultaneously with the maximum of the X-ray flare (Fig. 4.1 top panel). Protons in the energy range $25\,\mathrm{MeV} < E < 53\,\mathrm{MeV}$ corresponding to velocities of $0.22c < v < 0.32c$ were registered by EPHIN with a delay of around 15–30 minutes. About 20–25 minutes after the onset of the X-ray flare an increase of highly energetic particles in the integral proton channel ($E > 700$ MeV, $v \geqslant 0.8c$) of the HEPAD instruments on-board GOES-10 and GOES-11 was measured (2:50 UTC). At the same time the increase of several Neutron Monitor stations' count rates indicated the beginning of a Ground Level Enhancement.
Together with other stations located at eastern geographic longitudes the Oulu station was one of the first Neutron Monitors to record significant count rate increases in the five minute interval from 2:50 UTC to 2:55 UTC. Oulu was also the station showing the largest increase in five minute average count rates reaching 92% between 3:05 UTC and 3:10 UTC, marking the climax of the event. Other stations with comparable low cut-off rigidities but located at western longitudes both on the southern and the northern hemisphere (e.g. McMurdo, Inuvik) recorded much slower increases delayed by 20 minutes and more with respect to the Oulu station. This behaviour indicated a strong anisotropy in the beginning of the event and incoming directions of solar particles affecting mainly Neutron Monitors located at eastern longitudes. The increases of five selected stations are illustrated in the top panel of Figure 4.2 where count rate measurements by the stations are indicated by solid lines. The total strength of the Ground Level Enhancements on December 13th, 2006 was medium to weak in comparison to other GLEs when relative increases of several hundreds or event thousands of percent were recorded (GLE 69 or GLE 42, see below). In contrast, the increase of five minute average count rates of the Neutron Monitor stations was several tens of percent and not more than 100% during GLE 70.
To understand the clearly visible early increase of the Oulu, Kerguelen and Kiel stations and their relatively strong response, the asymptotic viewing directions of these monitors have to be analyzed. The asymptotic viewing directions were calculated using the IGRF model for the magnetosphere for all Neutron Monitors considered in this analysis for particles with rigidities $50\,\mathrm{MV} < R < 50\,\mathrm{GV}$ for vertically incident directions at the Neutron Monitor site. The results for the most relevant rigidity range in ground level enhancements for the Neutron Monitors Oulu, Thule, Kiel, Kerguelen, Terre Adelie, Inuvik, Pewanuk, Calgary, South Pole and McMurdo are illustrated in Fig. 4.3. Although, the asymptotic direc-

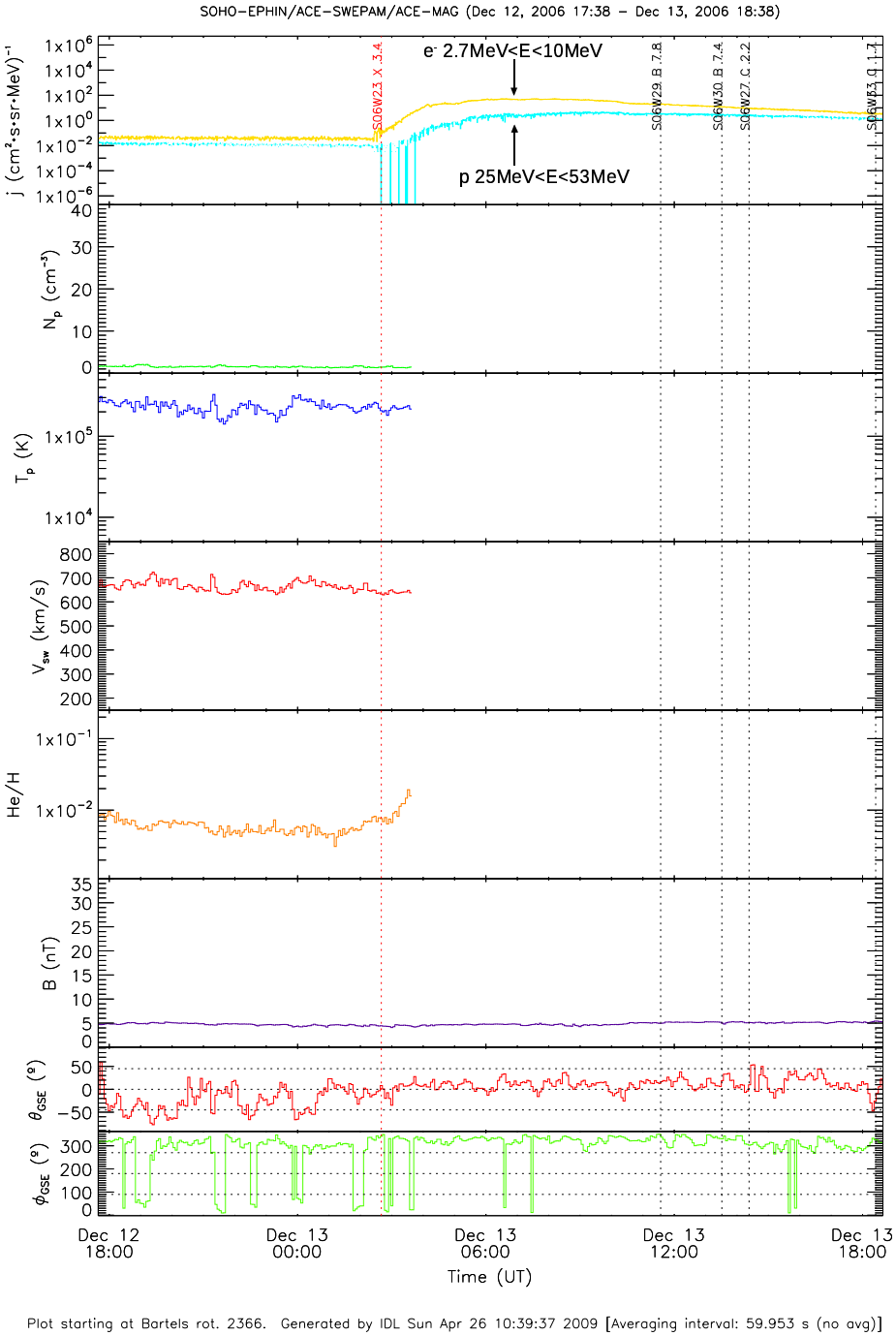


Figure 4.1: The figure shows from top to bottom five minute averages of 2.7 MeV to 10 MeV electrons and 25 MeV to 53 MeV protons ($j$), solar wind density ($N_p$), solar wind temperature ($T_p$), solar wind speed ($V_{SW}$), helium to hydrogen ratio (He/H), magnetic field strength ($B$), azimuth and longitude ($\theta_{\mathrm{GSE}}$, $\phi_{\mathrm{GSE}}$) of the IMF on December 12th and 13th, 2006 . Plasma and magnetic field data is from the SWEPAM and MAG instrument aboard ACE and the energetic particle data is from EPHIN aboard SOHO. Horizontal dotted lines indicate solar X-ray flares. Several detectors did not provide data after the arrival of the energetic protons.

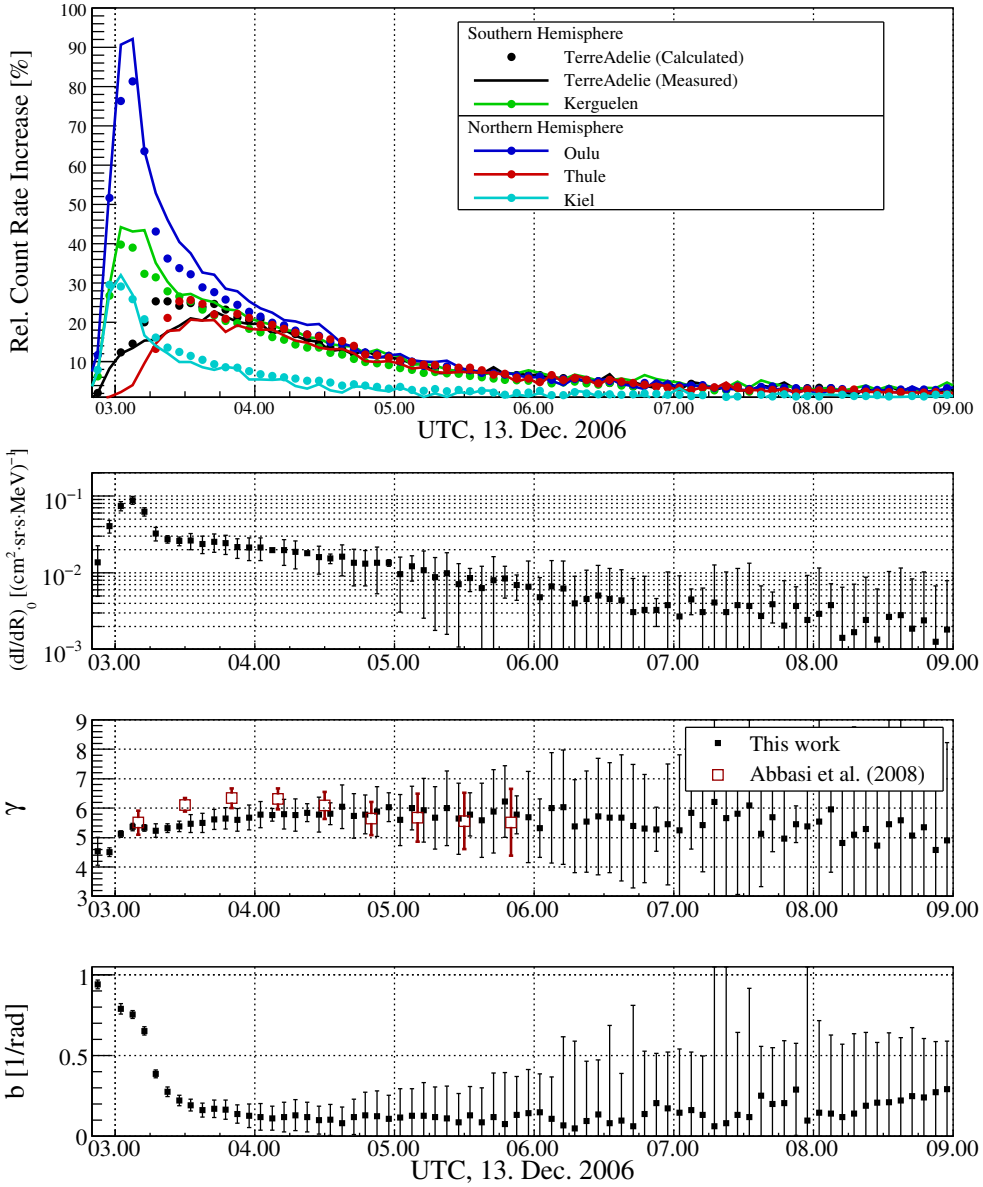


Figure 4.2: Relative Neutron Monitor count rate increases during GLE 70 for selected stations in the top panel. Solid lines show the measured values and the circles illustrate the results from the fit of the primary proton spectrum by a power law in rigidity and a linear angular distribution. The corresponding parameters are shown below, from top to bottom: the absolute intensity $(dI/dR)_0$, the spectral index $\gamma$ and the anisotropy parameter $b$ (see text for details). Results for the spectral index from *Abbasi et al.* (2008) are also shown.

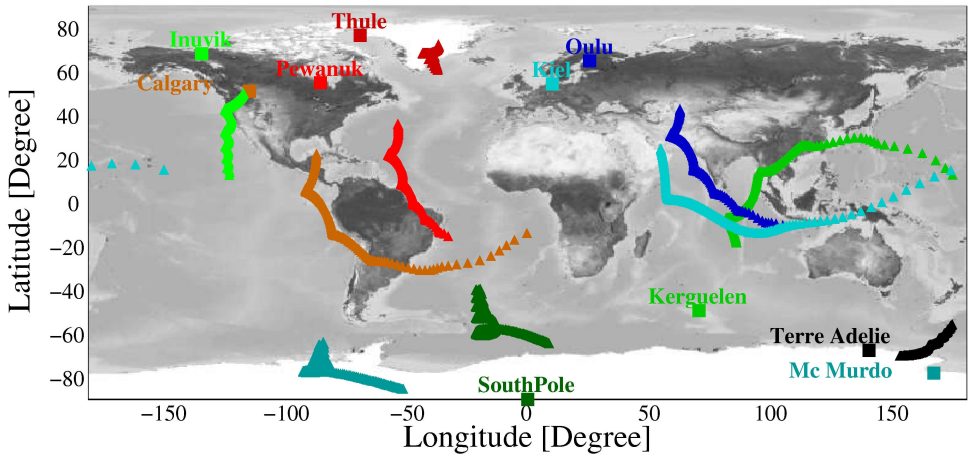


Figure 4.3: Vertical asymptotic viewing directions of selected Neutron Monitors during GLE 70 on December 13th, 2006 for particles with rigidities $1.5\,\mathrm{GV} < R < 20\,\mathrm{GV}$. The squares mark the location of the Neutron Monitor stations.

tions were calculated exactly for the time of all Ground Level Enhancements to obtain the results for each individual event discussed in the following the results presented in Fig. 4.3 can be used to understand the responses of the Neutron Monitors qualitatively for all events. As no disturbance in the Earth's magnetic field was taken into account, the change in cut-off rigidities and asymptotic directions between GLE 70 and other events is minor. Fig. 4.3 will therefore be used in the following as a reference picture to clarify the spatial characteristics of the events.

By looking at the asymptotic viewing directions of the selected Neutron Monitors it is clear that solar energetic particles during the GLE 70 must have been initially arriving at low latitudes and longitudes between $50°$E and $100°$E. The asymptotic viewing directions of the Oulu, Kiel and Kerguelen stations, which showed the early increase, indicate that these monitors are most sensitive to particles arriving from these directions. After a few minutes, the angular distribution of the event broadened causing the rise in the Terre Adelie station's count rates and some minutes later in Thule. The Ground Level Enhancement lasted several hours but the Neutron Monitor count rate increases were down to 10% or less at 5:00 UTC and thereafter. Compared to other large Ground Level Enhancements, for example GLE 42 and GLE 69, it was a rather short event.

To study the fraction of helium nuclei, i.e. alpha particles, during the event relative to solar protons the a6 and p6 channels of GOES-11 were compared to each other. These channels correspond to the differential particle intensities with similar energies per nucleon (300 MeV–500 MeV alpha particles (a6) and 80 MeV–165 MeV protons (p6)) which have identical $Z^2/A$ ratios and therefore similar ranges in the atmosphere (see Sec. 2.5.2). Prior to the event the ratio of helium to hydrogen nuclei in this energy per nucleon region measured by GOES-11 is very unstable showing values from 0.1 up to 1 with a majority of the measurements in the order of 0.1 to 0.4. The fraction of GCR alpha particles to protons in this en-

ergy range is approximately 20% (*Alcaraz et al.*, 2000b,a). With the onset of the Ground Level Enhancement at 2:50 UTC the fraction of primary alpha particles drops to values of 3%–4% during the first 15 minutes and below 1% during the following hours. Based on this observation it will be assumed in the following that the effects on the lower atmosphere and the Neutron Monitor count rates is only related to primary solar protons.
The modeling of the Ground Level Event 70 was performed using the minimization procedure described above with 28 different Neutron Monitor stations: Alma-Ata B, Apatity, Athens, Baksan, Barentsburg, CapeSchmidt, FortSmith, Herrmanus, Inuvik, Irkutsk, Kerguelen, Kiel, Kingston, Larc, Lomnicky, Magdan, Mawson, McMurdo, Moscow, Nain, Novosibirsk, Oulu, Sanae, TerreAdelie, Thule, TixieBay, Tsumeb and Yakutsk. Several shapes were used to fit the primary solar energetic particle spectrum and to minimize the differences between the resulting calculated count rate increases and the data from the Neutron Monitor stations. As five minute average data was used and the event was modeled over several hours it was not practicable to adapt the free parameters by hand for every time interval in order to find converging solutions. Therefore, it was necessary to find a description for the primary spectrum being very robust in the fitting procedure, i.e. converging to meaningful results without too much human intervention. As noted above, it was assumed that the effects on the ground based Neutron Monitors during the event were exclusively caused by primary protons, and the best results were found using a power law in rigidity (Eq. 4.2) for the differential intensity spectrum of primary solar protons together with a linear angular dependence (Eq. 4.8):

$$\frac{dI}{dR}(R,\alpha,t) = \begin{cases} \left[\left(\frac{dI}{dR}\right)_0(t)\cdot(R/\mathrm{GV})^{-\gamma(t)}\right] & \\ \cdot(1-b(t)\cdot\alpha) & \text{if } b(t)\cdot\alpha < 1\,. \\ 0 & \text{otherwise.} \end{cases} \quad (4.15)$$

The advantage of this description for the primary particle spectrum is the low number of free parameters. The angular distribution only contains the single parameter $b$ in contrast to other more complex distributions (e.g. the exponential form presented in Eq. 4.10). Additionally, the convergence behaviour of the Gaussian angular distribution turned out to be very unstable and, accordingly, the Gaussian function was not usable for the description of the angular distribution of the solar protons during GLE 70.
The results for the free parameters in the energy distribution $\left(\frac{dI}{dR}\right)_0(t)$ and $\gamma(t)$ together with the steepness of the angular distribution expressed by $b(t)$ are shown in the lower three panels of Figure 4.2. Additionally, the geographic latitude and longitude of the related incoming direction of the solar energetic particles are compared to the interplanetary magnetic field measured by ACE in Figure 4.4. The event was modeled in five minute interval steps for nine hours starting with the interval from 2:40 UTC–2:45 UTC. Only the results for the time before 9:00 UTC are shown as the relative count rate increases of all Neutron Monitor stations used in this analysis are less than 4% afterwards which led to very large uncertainties in the results.
The evolution of the SEP event on December 13th, 2006 can be analyzed by

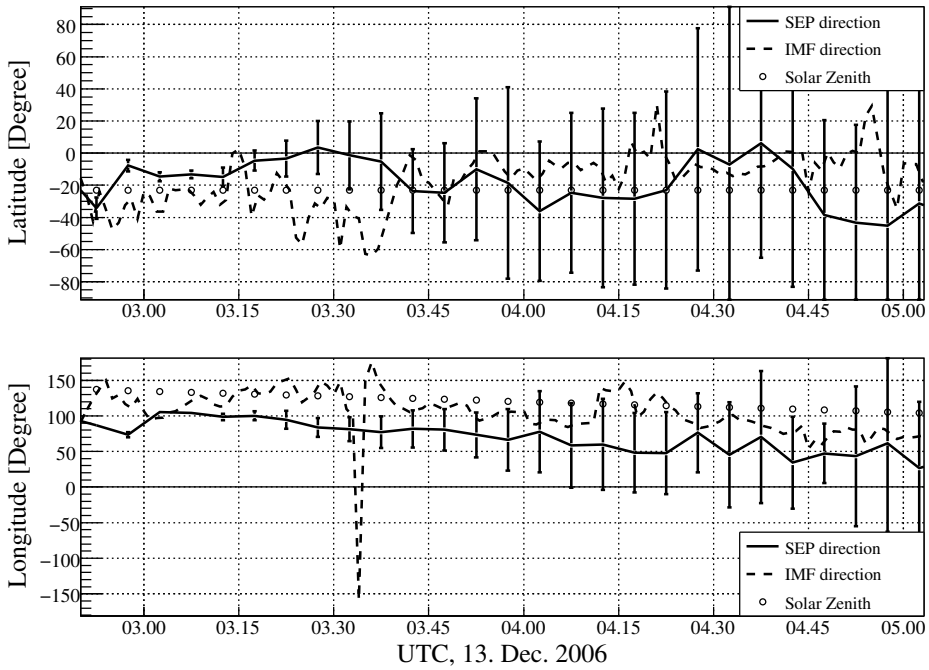


Figure 4.4: The temporal development of the incoming direction of Ground Level Event 70 compared to the interplanetary magnetic field (IMF) measured by ACE and the solar zenith direction in geographic coordinates.

looking at the lower panels in Figure 4.2 where the free parameters derived in this work are illustrated. The parameter $(dI/dE)_0$ gives the differential primary particle intensity at a rigidity $R = 1$ GV ($E \approx 500$ MeV) and is a measure for the total particle intensity. During the first 20 minutes of the event a very steep increase in $(dI/dE)_0$ is observed with a rise of one order of magnitude (second panel in Fig. 4.2) reaching its maximum at the time from 3:05 UTC–3:10 UTC. Afterwards the intensity gradually decreases over the next hours. It is evident that the statistical uncertainties originating from the minimization procedure become very large after around 5:00 UTC. This is due to the fact that the low Neutron Monitor count rate increases ($< 10\%$) at that time do not allow for a more accurate determination of the primary particle spectrum.
The spectral index $\gamma$ is shown in the third panel of Fig. 4.2 and reveals a very hard spectrum in the beginning of the event with relatively small values of $\gamma = 4.5$ from 2:50 UTC to 3:00 UTC and a softening spectrum afterwards reaching values of $\gamma \approx 6$ at around 4:00 UTC. This behaviour is typical for solar energetic particle spectra near Earth. An effect of the softening of the primary proton spectrum after 3:00 UTC is the reduction or complete disappearance of count rate increases of lower latitude stations with higher cut-off rigidities. The Kiel station for example shows an increase of around 30% at 3:00 UTC which had faded away to a few percent after 5:00 UTC. In addition to the values for the spectral index during GLE 70 obtained in this work, results from *Abbasi et al.* (2008) derived from measurements of the IceTop air shower array located at the

South Pole are illustrated in Fig. 4.2. The agreement between the two sets of spectral indices is good and the general trend of the softening spectrum in the beginning of the event was also observed by *Abbasi et al.* (2008). Again, the analysis exhibits significantly increasing uncertainties after 5:00 UTC.
The strong anisotropy in the angular distribution of the primary proton spectrum in the beginning of the event was already briefly discussed above. It corresponds to the large values of $b > 0.5$ during the first thirty minutes of the event reflecting the locally restricted effects of the solar energetic particles. At later times the event becomes less and less anisotropic and after around 5:00 UTC the anisotropy parameter $b$ is compatible with zero indicating an isotropic angular distribution.
The incoming direction of the solar protons estimated quantitatively above can be confirmed by the numerically determined direction of the incoming particles in Figure 4.4. Indeed, the incident direction in the beginning of the event was at eastern latitudes between $50°$E and $100°$E. Together with the high anisotropy this fact explains the late onset of Neutron Monitors mainly sensitive to other directions, e.g. Terre Adelie and Thule. The broadening of the angular distribution at later times causes the increase of the latter stations. In addition to the incoming direction of the solar particles determined in this work, the interplanetary magnetic field (IMF) measured by the ACE spacecraft is shown in Figure 4.4 by the dashed line. The ACE IMF data is originally provided in geocentric solar ecliptic (GSE) coordinates and was transformed to geographic coordinates (GEO) following *Hapgood* (1992, 1997) in order to compare it to the results of this work. Additionally, the times of the measurements were shifted by 35 minutes to account for the time difference between the ACE measurement performed at a distance of around $1.5 \cdot 10^6$ km of the Earth and the arrival of the solar wind at Earth flowing at a speed of approximately $700$ km/s and carrying the magnetic field. The same procedure was performed for the ACE IMF data in the following sections for the different Ground Level Enhancements. The comparison yields a strong correlation between the solar particles' incoming direction and the IMF which indicates that the charged particles accelerated at the Sun traveled to Earth along the IMF quasi scattering free in the beginning of the event. After 5:00 UTC this correlation disappears when the angular distribution becomes less anisotropic and solar energetic particles arrive at Earth from all directions. Both the IMF and the SEP's longitude before 5:00 UTC are orientated west of the sub-solar point's longitude which is expected from *Parker* (1958). The sub-solar point marks the coordinates on the Earth where the Sun stays in zenith, i.e. directly overhead. For a solar wind speed of around 500 km/s to 700 km/s as it was observed during the days prior to the event (see fourth panel Fig. 4.1) Eq. 2.9 predicts an IMF incoming longitude of around 30° to 40° west of the direct Sun-Earth line which is confirmed in Fig. 4.4. The solar energetic particles are mainly incident on southern mid-latitudes fluctuating around $23°$S which was the solar zenith latitude at that time which implies that the solar particles mainly propagated in the ecliptic plane.
The resulting primary proton spectrum are explicitly shown for several times during the event in Figure 4.5 for a pitch angle $\alpha = 0$, i.e. along the axis of

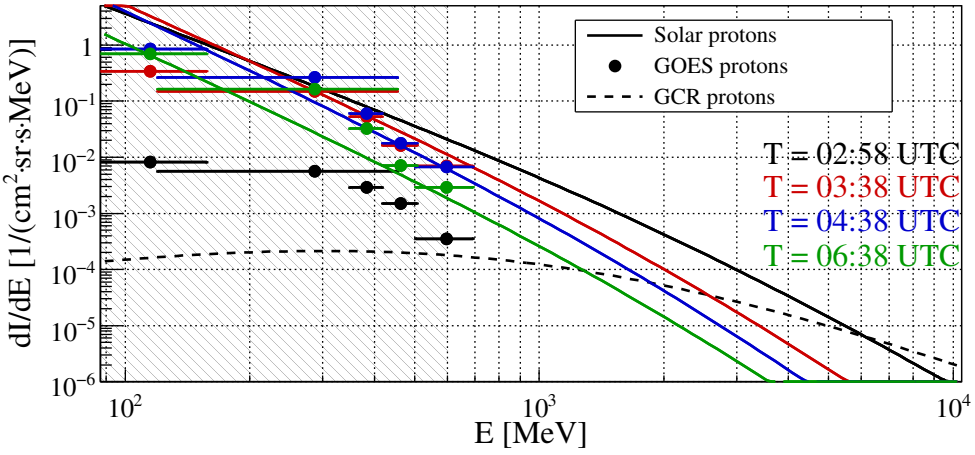


Figure 4.5: Differential intensity of primary solar energetic protons at different times during GLE 70 (solid lines) compared to the galactic cosmic ray protons (dashed line) and the measurements of GOES-11.

symmetry and showing the maximum of the intensity. The differential particle intensity with respect to kinetic energy is shown in comparison to measurements of GOES-11 and the galactic cosmic ray proton spectrum during that time (solar modulation $\phi = 440$ MV). As noted above, the shielding of the atmosphere corresponds to a cut-off energy of around 300 MeV–500 MeV for primary protons, and particles below this threshold have no significant impact on the radiation environment at sea-level. Consequently, the spectral information that can be obtained by the analysis of sea-level Neutron Monitors is restricted to values above $\approx$ 500 MeV. The majority of the Neutron Monitor stations used in this work is at or near sea-level and the information about particles below the atmospheric cut-off is therefore limited. Accordingly, the hatched area marks the extrapolation of the primary spectra in the energy range that is not accessible by sea-level Neutron Monitor stations. Very good agreement between the GOES data and the extrapolated spectra is observed at the times after 3:00 UTC. The differences at earlier times are caused by the high anisotropy of the event combined with the fact that the GOES detector does not measure in the direction of the highest particle intensity. Therefore, the particle intensity measured by GOES corresponds to a pitch angle $\alpha > 0$ which results in lower intensity values. At later times when the event was basically isotropic the differences caused by the GOES viewing directions are minor. The softening of the primary spectrum at later times during the event is also obvious. It is evident that the primary proton spectrum was very hard during the initial phase of the event (2:58 UTC, $\gamma \approx 4.5$) when the solar energetic proton intensities exceeded the galactic cosmic ray contribution up to energies of 5 GeV to 6 GeV.

### 4.2.1 Effective doses during GLE 70

To evaluate the evolution of GLE 70 under the aspect of dosimetry in aviation, the effective dose rate for different assumed flight routes and locations in the at-

mosphere was calculated. For a given position and time the parameters presented above were used to determine the primary particle spectrum on top of the atmosphere at the point of interest by calculating the asymptotic viewing directions at this point, the resulting pitch angles and the corresponding proton intensities. From the corresponding primary particle spectrum the secondary particle fluences at arbitrary altitudes and the related effective dose rates were calculated.
The effective dose rate $\dot{E}$ at an atmospheric depth of $200$ g/cm$^2$ corresponding to an altitude of approximately 12 km was calculated for the whole latitude range from $90°$S to $90°$N along a longitude of $25°$E and during the time period from 2:45 UTC until 11:00 UTC in five minute averages. In the beginning of the event, during the time of high anisotropy, the dose rates at other longitudes may vary considerably from the values along this longitude. As noted above, in contrast to the effective dose rate caused by isotropic GCR the exposure during anisotropic events depends on the asymptotic viewing direction at each point. Therefore, during anisotropic phases with very steep angular distributions the exposure at higher cut-off rigidities may be larger than at low cut-off rigidities if the location's viewing directions are closer to the event's incoming direction. As the largest increases in the beginning of GLE 70 were observed at the Oulu station the same longitude was chosen for the calculation of the effective doses to get an estimate for the upper limit of the exposure rate.
The asymptotic viewing directions were calculated for each latitude and longitude, and the corresponding primary proton spectrum for each position and point in time was determined from the parameters displayed in Figure 4.2 and added to the galactic cosmic ray proton spectrum. The resulting effective dose rates at 200 g/cm$^2$ ($\approx$ 12 km altitude) from GCR (protons and alpha particles) and SEP (protons) during the event are illustrated in Figure 4.6 in the top panel. The picture below shows the relative increase of effective dose rates during the Ground Level Event compared to the galactic cosmic ray background. The onset of the Ground Level Enhancement at around 2:50 UTC–3:00 UTC coincided with a sharp increase in the effective dose rate at high latitudes which rose from around 10 $\mu$Sv/h prior to the event to $40$ $\mu$Sv/h to $45$ $\mu$Sv/h at very northern latitudes. This corresponded to a relative increase of about a factor 4.0–4.5 above the GCR background. The peak value was reached in the time interval from 3:05 UTC–3:10 UTC and coincided with the maximum count rate increase measured by the Oulu Neutron Monitor. At the same time, the effective dose rates at southern latitudes reached peak values of around 35 $\mu$Sv/h corresponding to an increase of about a factor 3.5 above background. Between 5:00 UTC and 6:00 UTC the dose rates at high latitudes were still increased by a factor of 2 to 1.5. After 7:00 UTC the effects of GLE 70 on the radiation exposure had dropped to an increase of less than 20%. At lower latitudes between $50°$N and $40°$S the increase of the effective dose rate was below 10% during the first hour of the event and less than 5% afterwards.
For the estimation of the total exposure in aviation during this event two flight profiles were chosen as representatives for north Atlantic and polar flights, namely one from Frankfurt to Los Angeles (FRA–LAX) and from New York to Beijing (JFK–PEK). In addition, the total effective dose for a constant stay at the North

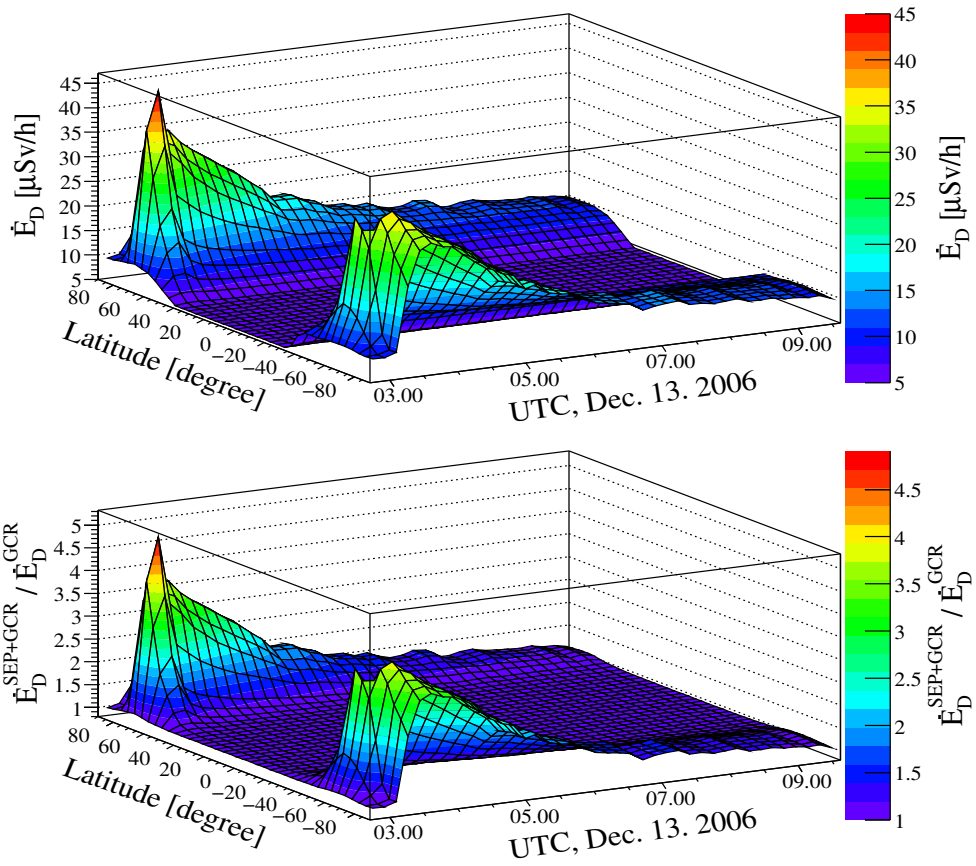


Figure 4.6: The variation of the effective dose rate at an atmospheric depth of 200 g/cm$^2$ corresponding to an altitude of about 12 km during the main phase of GLE 70 on December 13th 2006 at a longitude of 25°E in dependence on the geographic latitude in the top panel and the relative increase of the dose rate above GCR background below.

and South Pole was calculated. In the worst case the aircraft are already flying at northern latitudes corresponding to low cut-off rigidities and high exposure during the onset of the event, when the dose rate is maximal. Therefore, the flights were chosen to start around 90 minutes before the onset of the event at 1:30 UTC. Two altitudes corresponding to the approximate limits of commercial cruising altitudes were calculated, and the flight routes were set to constant atmospheric depths of either 200 g/cm$^2$ corresponding to about 12 km altitude or to 300 g/cm$^2$ corresponding to about 9 km altitude. For simplicity the route was calculated on the great circle between departure and destination point. The velocity of the aircraft was set to 900 km/h, and the coordinates were calculated every 15 min. For each set of times and coordinates the effective dose rate was determined. The exposure on the route between every two points was calculated by interpolating the effective dose rates at the individual points and by summing over all 15 minute time steps.
The expected dose rates during the selected flights are illustrated in the top panel of Figure 4.7 and for the North and South Pole below. Dose rates induced by GCRs are indicated by the squares and the sum of GCRs and solar energetic

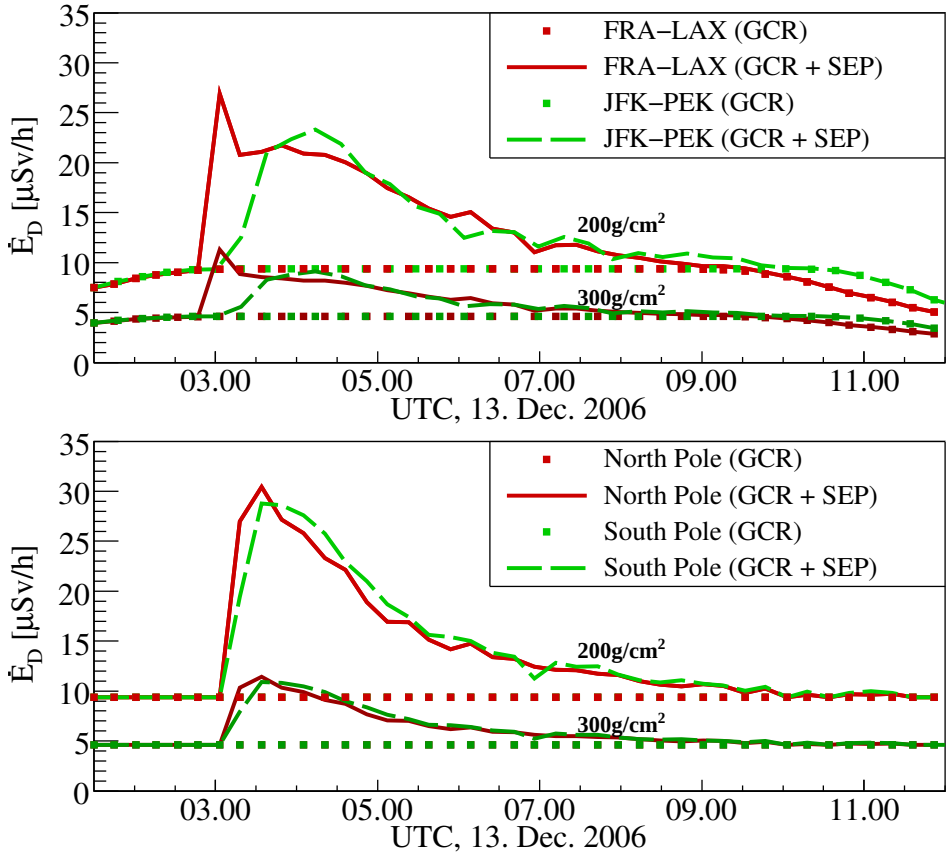


Figure 4.7: The effective dose rates for exemplary flights during GLE 70 from GCR background and solar energetic protons (SEP). In the top panel, the route from Frankfurt to Los Angeles (FRA–LAX) was chosen as an example for a north Atlantic flight and New York to Beijing (JFK–PEK) as a polar flight. The flights were set to start at 1:30 UTC, cruising at fixed atmospheric depths of 200 g/cm$^2$ and 300 g/cm$^2$ corresponding to approximately 12 km and 9 km. The lower panel shows the dose rate at the North and South Pole at these altitudes.

particles is depicted by the dashed and solid lines for the flights JFK–PEK and FRA–LAX respectively. The two different flight altitudes are indicated by the lighter and darker colors and the larger values (lighter color) correspond to the lower atmospheric depth of 200 g/cm$^2$ or approximately 12 km altitude. The very sharp onset of the flight from FRA–LAX reaching an effective dose rate of around 27 $\mu$Sv/h is related to the relatively eastern location of the aircraft at the beginning of the event. At its location it was sensitive to incoming directions close to the maximum intensity of the solar particles. On the route from New York to Beijing, on the other hand, the onset is slightly delayed due to the western location of the aircraft where the solar particles could not be seen during the anisotropic phase of the event. The maximum effective dose rate on the polar flight at 200 g/cm$^2$ ($\dot{E}_D = 23.3\,\mu$Sv/h) is reached after a relatively slow increase at around 4:15 UTC and corresponded to a factor 2.5 above the GCR background. In addition to the effect of the anisotropy combined with the location of the aircraft, the slow and late maximum is also caused by the continuing

decrease of the cut-off rigidity during the northward flight. The maximum dose rate at the North Pole, on the other hand is reached earlier at around 3:30 UTC with a peak value of 30.5 $\mu$Sv/h. For the flight from Frankfurt to Los Angeles the effective dose rate reaches a maximum of $\dot{E}_D = 26.9$ $\mu$Sv/h. The values of the total effective doses and dose rates calculated for the selected flights and North and South Pole are summarized in Tab 4.1 and Tab 4.2. The average effective dose rates were calculated by dividing the total effective dose on a flight by the duration of the flight. The values are to be understood as estimates for similar flights, and the exact effective doses and dose rates always depend on the exact flight route, the altitude and the departure time. For North and South Pole the average was taken over 10.5 h starting at 1:30 UTC. The same time span with an adapted departure time will be used to calculate the total exposures and event averaged dose rates at the North and South Pole for the events analyzed in the following. The relative increase above the GCR background at an atmospheric depth of 200 g/cm$^2$ (12 km) amounts to around 30% on the polar flight and 40% for the north Atlantic flight and the polar locations. By decreasing the flight altitude from 12 km to 9 km the increase caused by solar energetic particle during GLE 70 is reduced from 30%–40% to 20%–30%.
The contribution of the individual particles to the total dose was also calculated, and the fraction of the total effective dose caused by secondary neutrons increases due to the solar energetic particles from around 50% to 60% whereas the relative contribution of all other particles decreases. The enhanced fraction of neutron induced effective dose is related to the shape of the primary proton spectrum described by a power law. The large amount of relatively low energetic protons at a few hundreds of MeV produces a large number of neutrons contributing to the effective dose at aircraft altitudes. The primary protons themselves, on the other hand, do not have enough energy to reach the lower atmosphere and do not contribute directly to the radiation exposure. In the galactic cosmic ray spectra this part of the spectrum is suppressed due to the solar modulation.

Table 4.1: Effective doses $E_D$ for different flight routes and locations at different atmospheric depths $d$ during GLE 70 from solar energetic particles (SEP) compared to the galactic cosmic ray (GCR) background.

| Route/Loc. | $d$ [g/cm$^2$] | | $E_D^{\text{GCR}}$ [$\mu$Sv] | $E_D^{\text{GCR+SEP}}$ [$\mu$Sv] | $E_D^{\text{GCR+SEP}}/E_D^{\text{GCR}}$ |
|---|---|---|---|---|---|
| **North Pole** | **200** | **Total** | **92** | **1.3e+02** | **1.4** |
| | | neutron | 43 (47%) | 75 (58%) | 1.7 |
| | | photon | 7.7 (8.3%) | 8.7 (6.7%) | 1.1 |
| | | proton | 33 (36%) | 38 (29%) | 1.1 |
| | | $e^{+,-}$ | 6.3 (6.8%) | 6.5 (5%) | 2.5 |
| | | $\mu^{+,-}$ | 2.1 (2.3%) | 2.1 (1.6%) | 2.2 |
| **North Pole** | **300** | **Total** | **47** | **60** | **1.3** |
| | | neutron | 24 (51%) | 36 (59%) | 1.5 |
| | | photon | 4.2 (8.9%) | 4.5 (7.5%) | 1.1 |
| | | proton | 14 (30%) | 15 (25%) | 1.1 |
| | | $e^{+,-}$ | 3.1 (6.7%) | 3.2 (5.3%) | 2.5 |
| | | $\mu^{+,-}$ | 1.5 (3.1%) | 1.5 (2.5%) | 2.1 |
| **South Pole** | **200** | **Total** | **92** | **1.3e+02** | **1.4** |
| | | neutron | 43 (47%) | 76 (58%) | 1.8 |
| | | photon | 7.7 (8.3%) | 8.8 (6.7%) | 1.1 |
| | | proton | 33 (36%) | 38 (29%) | 1.1 |
| | | $e^{+,-}$ | 6.3 (6.8%) | 6.5 (4.9%) | 2.5 |
| | | $\mu^{+,-}$ | 2.1 (2.3%) | 2.1 (1.6%) | 2.2 |
| **South Pole** | **300** | **Total** | **81** | **95** | **1.2** |
| | | neutron | 42 (51%) | 54 (57%) | 1.3 |
| | | photon | 7.2 (8.9%) | 7.6 (7.9%) | 1 |
| | | proton | 25 (30%) | 26 (27%) | 1 |
| | | $e^{+,-}$ | 5.4 (6.7%) | 5.5 (5.8%) | 2.4 |
| | | $\mu^{+,-}$ | 2.6 (3.1%) | 2.6 (2.7%) | 2.1 |
| **FRA-LAX** | **200** | **Total** | **87** | **1.2e+02** | **1.4** |
| | | neutron | 40 (46%) | 63 (53%) | 1.6 |
| | | photon | 7.5 (8.6%) | 8.5 (7.2%) | 1.1 |
| | | proton | 32 (36%) | 39 (32%) | 1.2 |
| | | $e^{+,-}$ | 6.2 (7.1%) | 6.5 (5.5%) | 2.5 |
| | | $\mu^{+,-}$ | 2.1 (2.4%) | 2.1 (1.8%) | 2.2 |
| **FRA-LAX** | **300** | **Total** | **45** | **57** | **1.3** |
| | | neutron | 23 (50%) | 32 (57%) | 1.4 |
| | | photon | 4.1 (9.1%) | 4.4 (7.8%) | 1.1 |
| | | proton | 14 (30%) | 15 (27%) | 1.1 |
| | | $e^{+,-}$ | 3.1 (6.9%) | 3.2 (5.7%) | 2.5 |
| | | $\mu^{+,-}$ | 1.5 (3.3%) | 1.5 (2.6%) | 2.1 |
| **JKF-PEK** | **200** | **Total** | **98** | **1.3e+02** | **1.3** |
| | | neutron | 45 (45%) | 68 (54%) | 1.5 |
| | | photon | 8.6 (8.8%) | 9.4 (7.4%) | 1.1 |
| | | proton | 35 (36%) | 39 (31%) | 1.1 |
| | | $e^{+,-}$ | 7.1 (7.2%) | 7.3 (5.8%) | 2.4 |
| | | $\mu^{+,-}$ | 2.4 (2.4%) | 2.4 (1.9%) | 2.1 |
| **JFK-PEK** | **300** | **Total** | **51** | **61** | **1.2** |
| | | neutron | 25 (50%) | 34 (56%) | 1.3 |
| | | photon | 4.7 (9.3%) | 5 (8.2%) | 1.1 |
| | | proton | 15 (30%) | 16 (27%) | 1.1 |
| | | $e^{+,-}$ | 3.6 (7.1%) | 3.6 (6%) | 2.4 |
| | | $\mu^{+,-}$ | 1.7 (3.3%) | 1.7 (2.8%) | 2.1 |

Table 4.2: Average effective dose rates $\dot{E}_D$ for different flight routes and locations at different atmospheric depths $d$ during GLE 70 from solar energetic particles (SEP) compared to the galactic cosmic ray (GCR) background.

| Route/Loc. | $d$ [g/cm$^2$] | | $\dot{E}_D^{\text{GCR}}$ [$\mu$Sv/h] | $\dot{E}_D^{\text{GCR+SEP}}$ [$\mu$Sv/h] | $\dot{E}_D^{\text{GCR+SEP}}/\dot{E}_D^{\text{GCR}}$ |
|---|---|---|---|---|---|
| **North Pole** | **200** | **Total** | **8.9** | **13** | **1.4** |
| | | neutron | 4.2 (47%) | 7.2 (58%) | 1.7 |
| | | photon | 0.74 (8.3%) | 0.84 (6.7%) | 1.1 |
| | | proton | 3.2 (36%) | 3.6 (29%) | 1.1 |
| | | $e^{+,-}$ | 0.6 (6.8%) | 0.62 (5%) | 2.5 |
| | | $\mu^{+,-}$ | 0.2 (2.3%) | 0.2 (1.6%) | 2.2 |
| **North Pole** | **300** | **Total** | **4.5** | **5.8** | **1.3** |
| | | neutron | 2.3 (51%) | 3.4 (59%) | 1.5 |
| | | photon | 0.4 (8.9%) | 0.43 (7.5%) | 1.1 |
| | | proton | 1.4 (30%) | 1.5 (25%) | 1.1 |
| | | $e^{+,-}$ | 0.3 (6.7%) | 0.31 (5.3%) | 2.5 |
| | | $\mu^{+,-}$ | 0.14 (3.1%) | 0.14 (2.5%) | 2.1 |
| **South Pole** | **200** | **Total** | **8.9** | **13** | **1.4** |
| | | neutron | 4.2 (47%) | 7.3 (58%) | 1.8 |
| | | photon | 0.74 (8.3%) | 0.84 (6.7%) | 1.1 |
| | | proton | 3.2 (36%) | 3.7 (29%) | 1.1 |
| | | $e^{+,-}$ | 0.6 (6.8%) | 0.62 (4.9%) | 2.5 |
| | | $\mu^{+,-}$ | 0.2 (2.3%) | 0.2 (1.6%) | 2.2 |
| **South Pole** | **300** | **Total** | **4.5** | **5.3** | **1.2** |
| | | neutron | 2.3 (51%) | 3 (57%) | 1.3 |
| | | photon | 0.4 (8.9%) | 0.42 (7.9%) | 1 |
| | | proton | 1.4 (30%) | 1.4 (27%) | 1 |
| | | $e^{+,-}$ | 0.3 (6.7%) | 0.31 (5.8%) | 2.4 |
| | | $\mu^{+,-}$ | 0.14 (3.1%) | 0.14 (2.7%) | 2.1 |
| **FRA-LAX** | **200** | **Total** | **8.4** | **11** | **1.4** |
| | | neutron | 3.8 (46%) | 6.1 (53%) | 1.6 |
| | | photon | 0.72 (8.6%) | 0.82 (7.2%) | 1.1 |
| | | proton | 3.1 (36%) | 3.7 (32%) | 1.2 |
| | | $e^{+,-}$ | 0.6 (7.1%) | 0.62 (5.5%) | 2.5 |
| | | $\mu^{+,-}$ | 0.2 (2.4%) | 0.2 (1.8%) | 2.2 |
| **FRA-LAX** | **300** | **Total** | **4.3** | **5.5** | **1.3** |
| | | neutron | 2.2 (50%) | 3.1 (57%) | 1.4 |
| | | photon | 0.39 (9.1%) | 0.43 (7.8%) | 1.1 |
| | | proton | 1.3 (30%) | 1.5 (27%) | 1.1 |
| | | $e^{+,-}$ | 0.3 (6.9%) | 0.31 (5.7%) | 2.5 |
| | | $\mu^{+,-}$ | 0.14 (3.3%) | 0.14 (2.6%) | 2.1 |
| **JKF-PEK** | **200** | **Total** | **8** | **10** | **1.3** |
| | | neutron | 3.7 (45%) | 5.6 (54%) | 1.5 |
| | | photon | 0.7 (8.8%) | 0.77 (7.4%) | 1.1 |
| | | proton | 2.9 (36%) | 3.2 (31%) | 1.1 |
| | | $e^{+,-}$ | 0.58 (7.2%) | 0.6 (5.8%) | 2.4 |
| | | $\mu^{+,-}$ | 0.2 (2.4%) | 0.2 (1.9%) | 2.1 |
| **JFK-PEK** | **300** | **Total** | **4.1** | **5** | **1.2** |
| | | neutron | 2.1 (50%) | 2.8 (56%) | 1.3 |
| | | photon | 0.38 (9.3%) | 0.41 (8.2%) | 1.1 |
| | | proton | 1.3 (30%) | 1.3 (27%) | 1.1 |
| | | $e^{+,-}$ | 0.29 (7.1%) | 0.3 (6%) | 2.4 |
| | | $\mu^{+,-}$ | 0.14 (3.3%) | 0.14 (2.8%) | 2.1 |

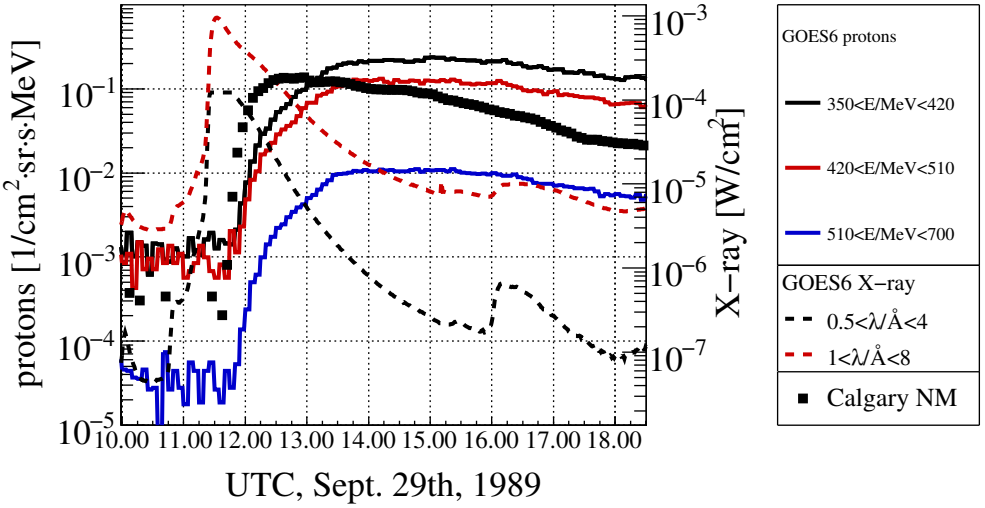


Figure 4.8: The first hours of GLE 42 on Sept. 29th, 1989 recorded by the Calgary Neutron Monitor (black squares), the preceding increase in X-ray flux measured by GOES-6 (dashed lines) and the proton intensities measured by the HEPAD detector on-board GOES-6 (solid lines). Neutron Monitor count rates are given in arbitrary units.

## 4.3 Ground Level Enhancement 42

The Ground Level Enhancement 42 was first observed by the North American Neutron Monitor stations Calgary and Inuvik and the Thule Neutron Monitor located in Greenland during the five minute time interval from 11:45 UTC to 11:50 UTC on September 29th, 1989. In the following hours, count rate increases were recorded by Neutron Monitors all around the world up to very high cut-off rigidities. Even the Tokyo station at a cut-off rigidity of around 11.5 GV recorded a peak increase of almost 30% showing the presence of very highly energetic solar particles. Based on hourly underground muon telescope data, *Swinson and Shea* (1990) estimated an exceptionally large upper threshold rigidity of the solar energetic particles of approximately 25 GV. The onset of the Ground Level Enhancement was preceded by a solar X9-class X-ray flare located on the western limb of the Sun (90°W, 26°S). The increase in the 1–8 Å X-ray flux started before 11 UTC (Fig. 4.8) showing a relatively slow rise and reaching its maximum at 11:32 UTC (GOES-6). The lack of a visible H$\alpha$ flare related to the event indicated a flare location behind the western limb of the Sun. *Swinson and Shea* (1990) identified the NOAA active region 5698 located at 105°W solar longitude at the time of the onset of the Ground Level Enhancement as the origin of the flare. According to *Cliver et al.* (1993) the solar flare was accompanied by a coronal mass ejection with a supposed longitudinal extent of around 70°. Therefore, a shock driven by this CME would expand to solar longitudes magnetically directly connected to Earth, and the origin of solar energetic particles accelerated at this shock and reaching Earth would be located at the eastern flank of the shock. It was noted above (Fig. 2.4) that particles accelerated at the flank of a shock show a rather slow and long lasting increase. This is in

good agreement with the observation of the Calgary Neutron Monitor and the proton intensities recorded by GOES-6 (Fig. 4.8). The maximum in the Neutron Monitor count rate during GLE 42 was not reached until one hour after the solar X-ray flare maximum and stayed rather constant during the following hours. It took even longer until the maximum in the proton intensities measured by GOES was reached (≈13:30 UTC–14:00 UTC). Some Neutron Monitors revealed an uncommon behaviour in their count rate profile (top panel Fig. 4.9). Various stations, for example McMurdo, showed a multiple peak structure in the count rate profile while Inuvik registered a strong increase (11:15 UTC–12:15 UTC) followed by a period of around one hour of constant count rates and a subsequent second increase (13:20 UTC). The South Pole Neutron Monitor registered additional increases at around 15:20 UTC and 18:05 UTC. These successive rises in the Neutron Monitor count rates were not related to solar X-ray flares (Fig. 4.8), and it is unlikely that additional events on the Sun occurred. Possible explanations for this behaviour are changes in the Earth's magnetic field, the interplanetary field or the structure of the CME driven shock.

To model the event the same technique as above was used, and the Neutron Monitor five minute average count rates of the following stations were analyzed: Alma-Ata B, Apatity, Calgary, Cape Schmidt, Deep River, Durham, GooseBay, Herrmanus, Hobart, Inuvik, Kerguelen, Kiel, Lomnicky Stit, Magdan, Mawson, McMurdo, Mexico, Mirny, Moscow, Novosibirsk, Oulu, South Pole, Terre Adelie, Thule, Tixie Bay and Tsumeb. Several functions were used to fit the primary proton spectrum but none could accurately reproduce the Neutron Monitor count rates in the beginning of the event. The power law in rigidity combined with a linear angular dependence (Eq. 4.15) showed good convergence behaviour and acceptable results at later times during the event. The complex structure of the count rate profiles of the Neutron Monitors before around 16:00 UTC, on the other hand, could not be modeled by such a simple description (top panel Fig. 4.9). While some measurements are reproduced quite accurately, the differences in the modeled and experimental count rates for other stations amount to 30%–50%. The derived free parameters of the primary spectra during the event are shown in the lower panels in Fig. 4.9. Based on the comparison of the simulated and the measured count rates, the parameters are supposed to bear an uncertainty of around 30%–50% as well. In the beginning of the event during the first hour of the event the primary spectrum is exceptionally hard $\gamma \approx 3.3$–$3.5$. During the following hours it gradually softens reaching values of $\gamma \approx 5$ at 16:00 UTC–18:00 UTC and $\gamma \approx 5.5$ afterwards. By comparing two Neutron Monitor stations with different response functions *Bieber and Evenson* (1991) estimated a spectral index $\gamma = 3.01$ in the beginning of the event and $\gamma = 4.57$ at later times, although, later is not defined more precisely by the authors. Their value of $\gamma = 4.57$ agrees to the results of this work at around 14:00 UTC–15:00 UTC.

The incoming direction of the solar energetic particles derived from the linear angular dependence and the response of the Neutron Monitors is illustrated in Fig. 4.10 and compared to the measurements of the interplanetary magnetic field by the IMP8 spacecraft. The IMP8 data provided in geocentric solar magne-

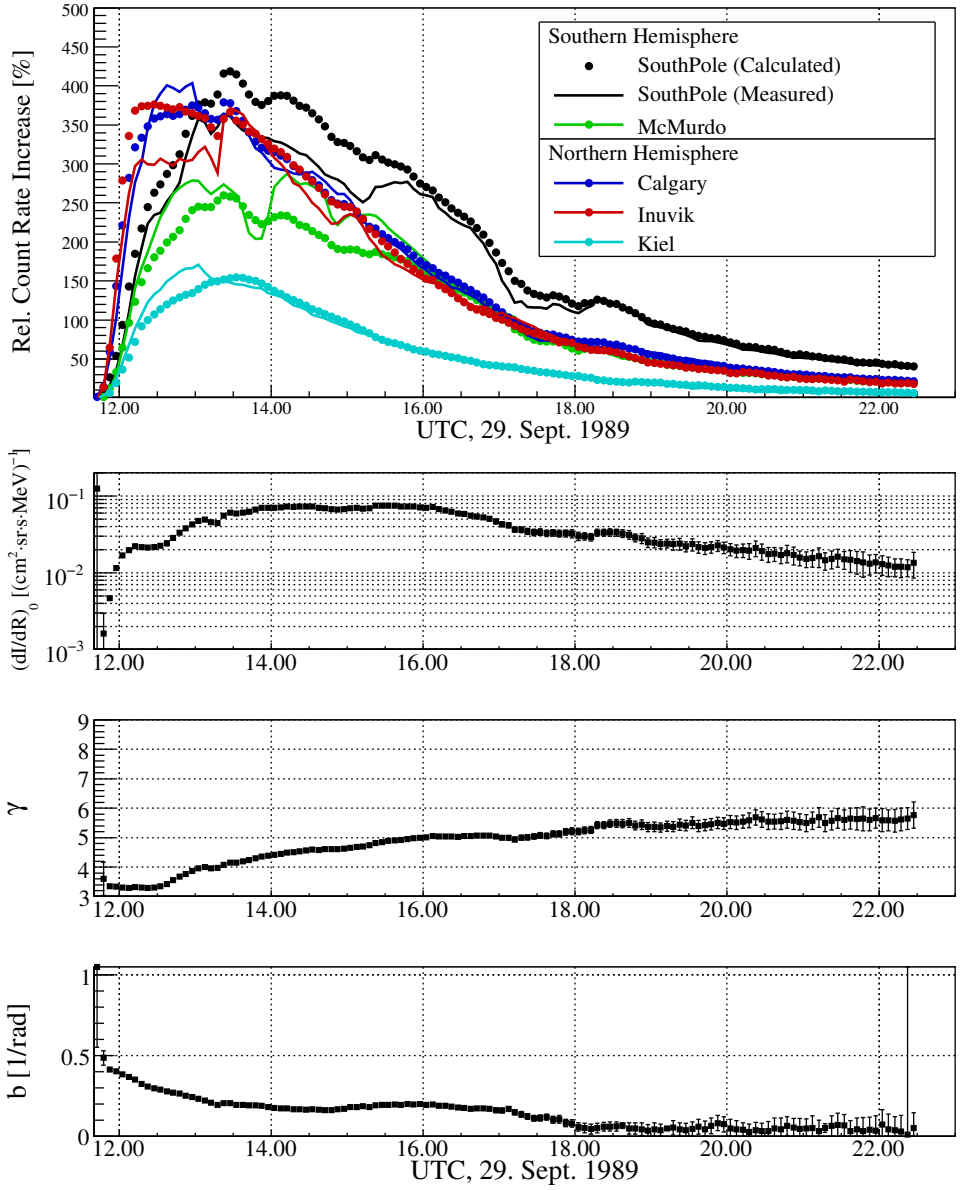


Figure 4.9: Relative Neutron Monitor count rate increases during GLE 42 for selected stations in the top panel. Solid lines show the measured values and the circles illustrate the results from the fit of the primary proton spectrum by a power law in rigidity and a linear angular distribution. The corresponding parameters are shown below, from top to bottom: the absolute intensity $(dI/dR)_0$, the spectral index $\gamma$ and the anisotropy parameter $b$ (see text for details).

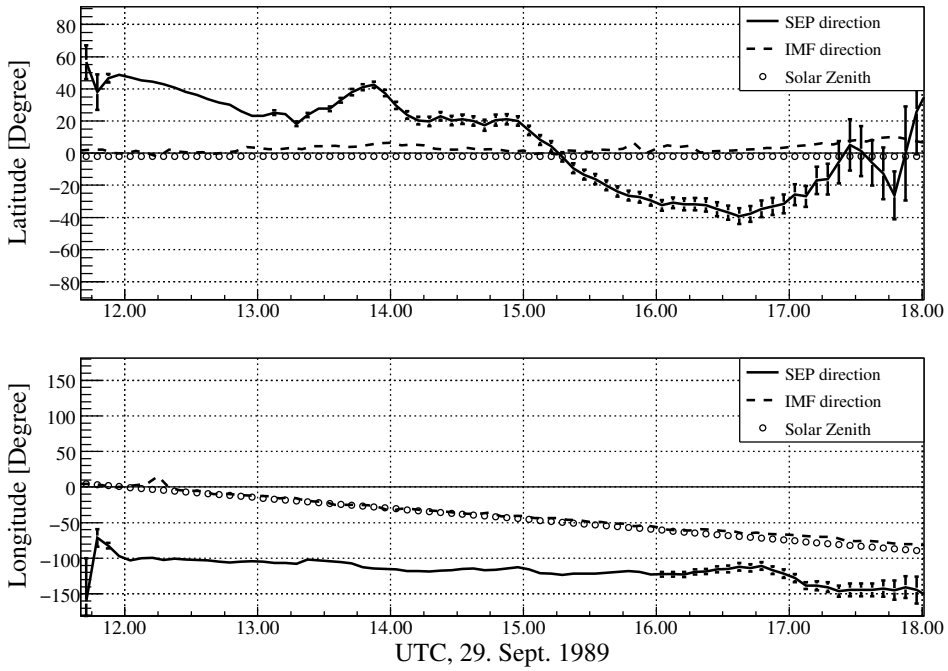


Figure 4.10: The temporal development of the incoming direction of Ground Level Event 42 compared to the interplanetary magnetic field (IMF) measured by IMP8 and the solar zenith direction in geographic coordinates.

tospheric (GSM) coordinates is converted to geographic coordinates following *Hapgood* (1992, 1997). The agreement between the SEP incoming directions and the IMF is rather poor. The incoming latitudes of the solar energetic particles during GLE 42 were determined to be on the northern hemisphere in the beginning of the event moving to southern latitudes between 15.00 UTC and 15.30 UTC. This extreme shift in the latitude of the solar energetic particles' incoming direction was also reported by *Lovell et al.* (1998) who associated it to a change in the IMF. No such behaviour, however, is observed in the IMP8 measurements. The shift of the incoming direction to southern latitudes is the cause for the increasing count rates at southern hemisphere stations (South Pole, McMurdo, see top panel in Fig. 4.9). *Lovell et al.* (1998) also reported a bi-directional flow of energetic particles around 13:25 UTC which coincides with the second increase recorded by the Inuvik and other Neutron Monitor stations. Obviously, the angular distribution during the first hours of the event was too complex to be approached by a linear or Gaussian function or the exponential form given in Eq. 4.10. Fitting the primary spectrum with these functions yielded very similar results for the absolute intensity, the spectral index and the incoming direction of the solar protons but failed to give a better description of the complex count rate profiles in the beginning of the event.

The comparison of the primary proton spectra with the measurements of GOES-6 (Fig. 4.11) shows very good agreement for the intermediate energy channels at a few hundred MeV at all times but in the very beginning of the event at

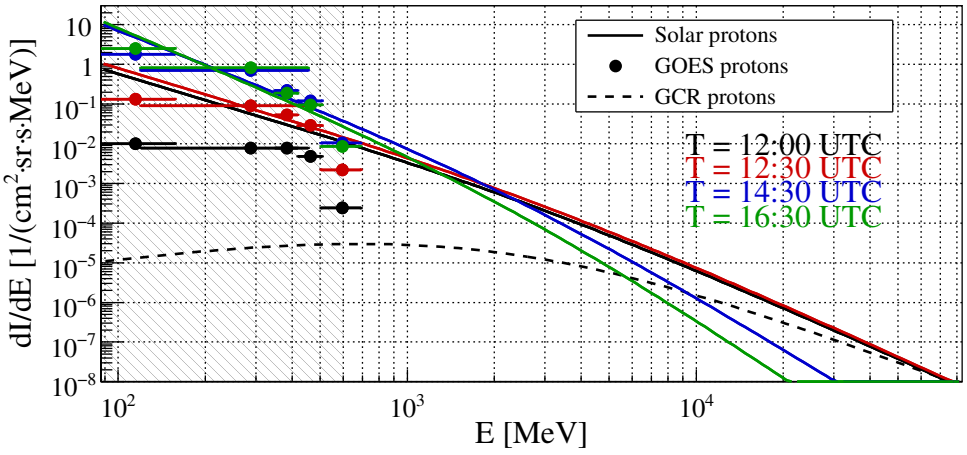


Figure 4.11: Differential intensity of primary solar energetic protons at different times during GLE 42 (solid lines) compared to the galactic cosmic ray protons (dashed line) and the measurements of GOES-6.

12:00 UTC. Again, the reason for the disagreement is the anisotropy and the related strong decrease in proton intensity at larger pitch angles. The GOES detectors are not necessarily measuring in the direction of the largest intensity and an underestimation of the maximum intensity by the GOES data is expected during anisotropic periods.
It is also obvious that very highly energetic particles were present for a relatively long time during GLE 42. At 12:30 UTC the solar proton intensities exceeded the GCR background at energies up to several tens of GeV. Even more than 2.5 h after the beginning of the event at around 14:30 significant proton intensities occurred up to 10 GeV and more. It was shown in Sec. 3.3 that the asymptotic arrival directions of non vertically incident particles at rigidities above 10 GV are not very accurately described by the vertical asymptotic directions. The reproduction of the Neutron Monitor count rate increases presented above and the derived parameters describing the primary protons spectrum, however, are based on the asymptotic arrival directions of vertically incident particles. As a consequence, the simulation can not reproduce the Neutron Monitor count rates during anisotropic phases of Ground Level Enhancement if very highly energetic particles are present. Taking into account the asymptotic directions of non vertical particles is a possible solution to this problem. For the majority of the Ground Level Enhancements, however, the rigidities of the solar particles is restricted to values where the technique presented here is sufficient.

### 4.3.1 Effective doses during GLE 42

Neutron Monitors in North America and Greenland recorded the earliest and largest increase in the count rate during GLE 42. With an increase of more than 300% during the early phase of the event the Thule, Goose Bay and Inuvik monitors showed the largest response of all sea-level stations. It can be assumed that the most significant increase in the effective dose occurred close the location

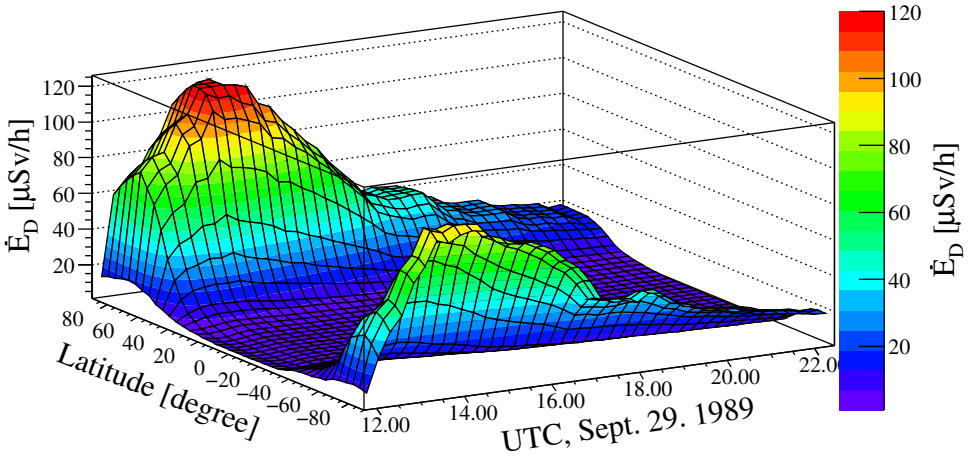


Figure 4.12: The variation of the effective dose rate at an atmospheric depth of 200 g/cm$^2$ corresponding to an altitude of about 12 km during the main phase of GLE 42 on September 29th 1989 in dependence on the geographic latitude for a longitude of 100°W.

of those stations. To quantify the radiation exposure, the effective dose rates were calculated over all latitudes for a longitude of 100°W (Fig. 4.12). Peak values of 130 $\mu$Sv/h in the effective dose rates at 70°N and up to 100 $\mu$Sv/h at southern latitudes were reached at around 14.00 UTC. This corresponded to increases of factors of around 24 and 18 compared to the effective dose induced by GCR of around 5.5 $\mu$Sv/h.

Additionally, the total effective dose and dose rate during GLE 42 were estimated for the same two flights as for GLE 70 in the previous chapter: from Frankfurt to Los Angeles (FRA–LAX) and from New York to Beijing (JFK–PEK). Moreover, the radiation exposure at North and South Pole was calculated. The development of the effective dose rates is illustrated in Fig. 4.13. An effect of the onset of the event is first seen at the North Pole at 11:30 UTC followed by the north Atlantic and polar flight at around 11:45 UTC. The increase, however, is much stronger on the route from New York to Beijing. This fact is related to the western location of the aircraft in the beginning where it was sensitive to incoming directions corresponding to high primary proton intensities. The peak values in the effective dose rates are reached at around 14:00 UTC to 14:30 UTC with around 80 $\mu$Sv/h (FRA–LAX, South Pole) up to approximately 120 $\mu$Sv/h (JFK–PEK).

The total effective doses and the average dose rates on the flights and at the North and South Pole are summarized in Tab. 4.1 and Tab. 4.2. At 200 g/cm$^2$ the estimated total effective doses were increased above the galactic cosmic ray background by factors of 5.6 (FRA–LAX) up to 8.1 (North Pole) corresponding to a total exposure of 300 $\mu$Sv and 450 $\mu$Sv respectively. 65% to 75% of this dose is caused by secondary neutrons which reflects the increase of the fraction of the effective neutron dose.

The effects of the Ground Level Enhancement 42 on the radiation environment in the lower atmosphere were quite large. It is very likely that the impact would have been even higher if the event had occurred some days earlier at a location on the Sun magnetically better connected to Earth. Still, GLE 42 was one of

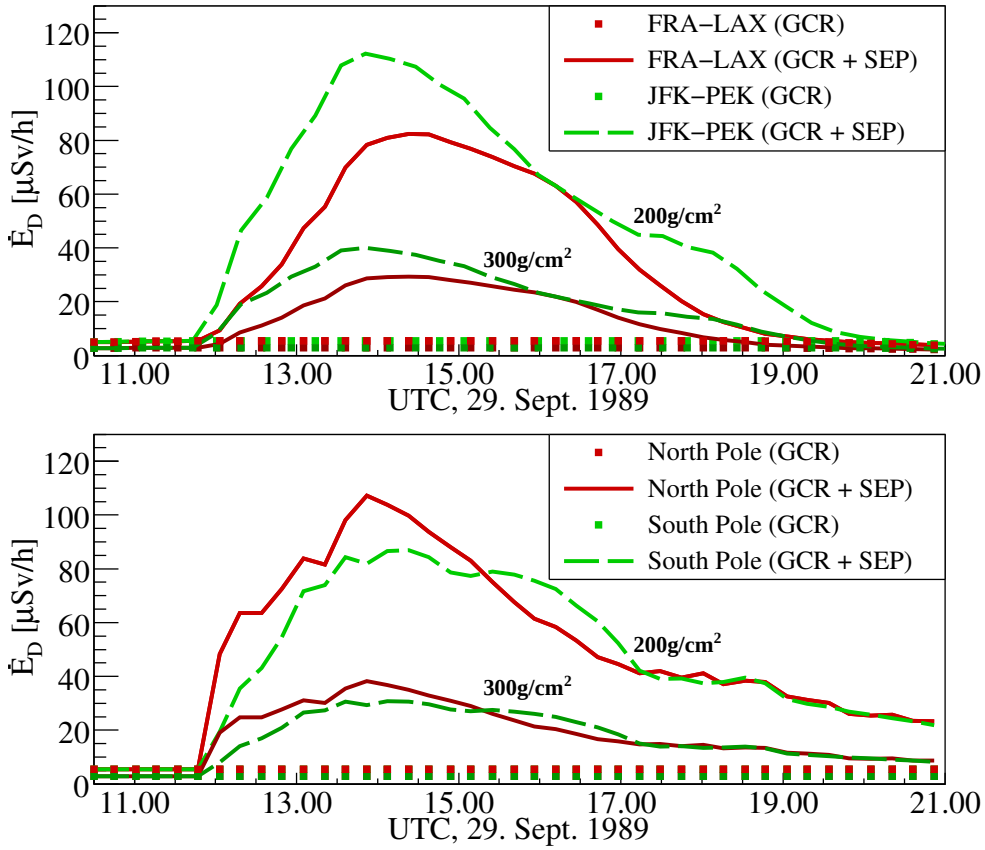


Figure 4.13: The dose rates for exemplary flights during GLE 42 from GCR background and solar energetic protons (SEP). In the top panel, the route from Frankfurt to Los Angeles (FRA–LAX) was chosen as an example for a north Atlantic flight and New York to Beijing (JFK–PEK) as a polar flight. The flights were set to start at 10:30 UTC, cruising at fixed atmospheric depths of 200 g/cm$^2$ and 300 g/cm$^2$ corresponding to approximately 12 km and 9 km. The lower panel shows the dose rate at the North and South Pole at the same altitudes.

the largest Ground Level Enhancements ever recorded. A more detailed study of the count rate profiles in the beginning of the event could help to improve the understanding of the acceleration mechanisms and trajectories of solar energetic particles. This, however, is beyond the scope of the present work.

## 4.4 Ground Level Enhancement 60

The 60th Ground Level Event in the records occurred in the afternoon of April 15th, 2001 following a X14 flare on the western limb of the Sun (S 20, W 85). The subsequent coronal mass ejection recorded by LASCO was already shown in Figure 2.5. The maximum X-ray flux of $1.45 \cdot 10^{-3}$ W/m$^2$ ($1.58 \cdot 10^{-3}$ W/m$^2$) measured by GOES-8 (GOES-10) was reached at 13:50 UTC. The first solar energetic particles detected by GOES-8 and GOES-10 arrived at 14:00 UTC, and this time also marks the beginning of the first 5 minute interval showing significant count rate increases at several stations (top panel in Figure 4.14). Slight increases of a few percent were registered during the previous five minute interval (13:55 UTC–14:00 UTC) by some Neutron Monitors revealing a time delay of the solar energetic particles of 5–10 minutes with respect to the peak in solar X-ray flux. The ground based neutron monitor detector array GRAND measured an increase in secondary muons in the time from 14:00 UTC to 14:35 UTC (*Poirier and D'Andrea*, 2002).

The largest Neutron Monitor count rate increase in the earliest time interval from 13:55 UTC to 14:00 UTC was recorded by the Calgary station with 15.3%. Other northern hemisphere stations measured increases of up to 10% (Thule, Nain, Fort Smith) while southern hemisphere stations only showed minor responses to the solar energetic particles: McMurdo (3.8%) and South Pole (2.8%). Some northern stations, like Oulu for example, were not affected at all by the Ground Level Enhancement at that time. By comparing these observations with the asymptotic viewing directions shown in Figure 4.3 it can be derived that the event's incoming direction in the initial phase was at low northern geographic latitudes and western longitudes to which the Calgary station and Neutron Monitors close by are sensitive. Oulu, on the other hand, has more western asymptotic viewing directions which were not affected during the very anisotropic initial phase of the event.

In the following 30 to 45 minutes, the Neutron Monitor count rate increases rose to peak values of more than 100%. Due to its elevation and the related increased sensitivity to lower energetic primary particles, the South Pole Neutron Monitor registered the largest increase (225% during 14:30 UTC–14:35 UTC). At sea-level, however, the Ground Level Enhancement had a slightly larger impact on northern hemisphere stations (Nain 118%, 14:30 UTC–14:35 UTC; Pewanuk 113% 14:10 UTC–14:15 UTC) compared to the southern hemisphere (McMurdo 102%, 14:30 UTC–14:35 UTC). Comparing these observations to the asymptotic viewing directions of the stations shows that the incoming direction at later times is expected to be at low southern latitudes and western longitudes. The Athens Neutron Monitor at a geomagnetic cut-off of $R_C \approx 8$ GV did not register any significant increase during the whole event while the Alma-Ata station at a slightly lower magnetic shielding ($R_C \approx 6.6$ GV) measured an increase of a few percent until around 15:00 UTC. This corresponds to an upper threshold in the kinetic energy of the primary protons of around 6 GeV to 7 GeV.

For the analysis of the event with the minimization technique described above the following 27 Neutron Monitor stations were used: Alma-Ata B, Apatity, Athens, Calgary, CapeSchmidt, FortSmith, Herrmanus, Irkutsk, Jungfrau2, Ker-

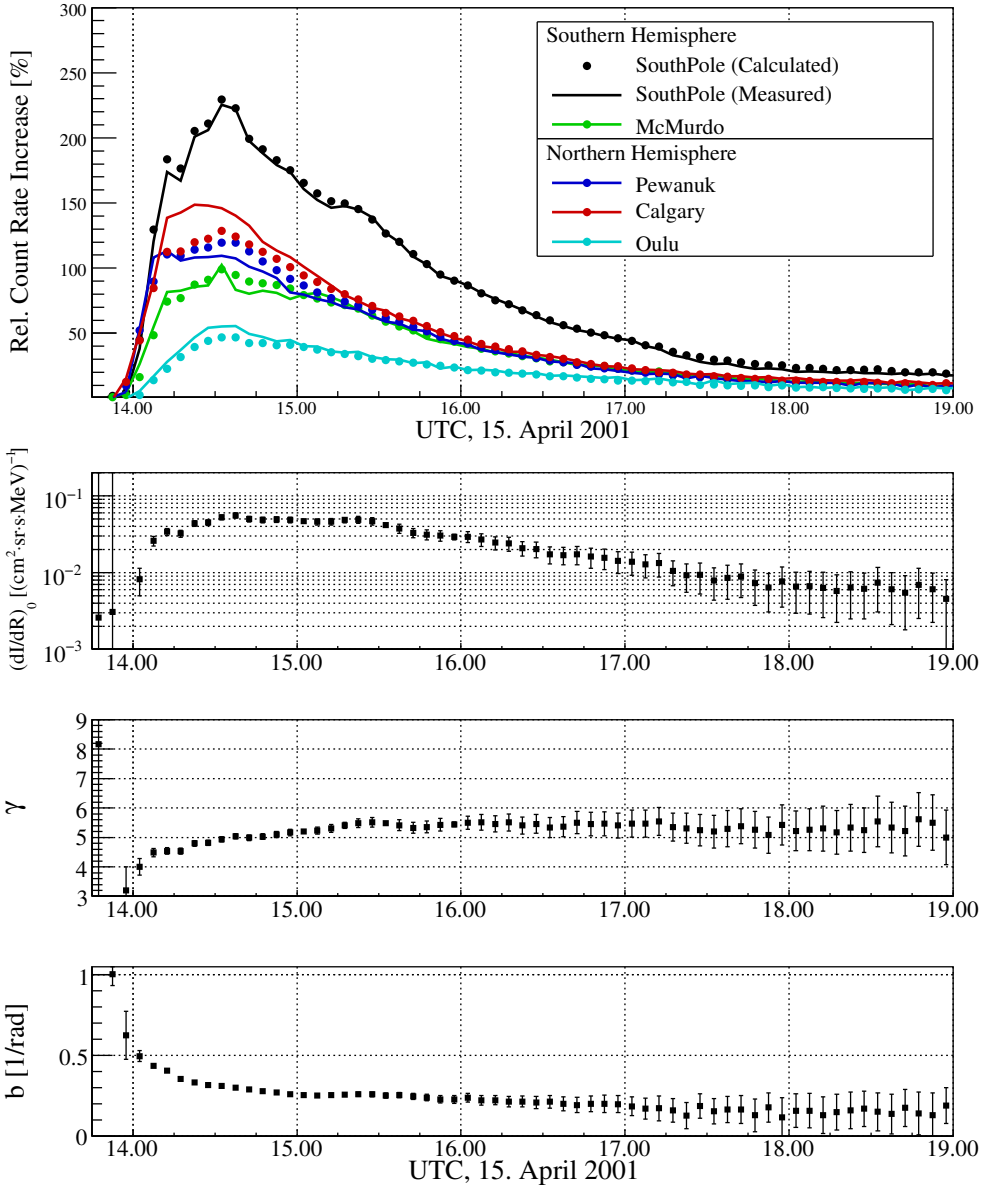


Figure 4.14: Relative Neutron Monitor count rate increases during GLE 60 for selected stations in the top panel. Solid lines show the measured values and the circles illustrate the results from the fit of the primary proton spectrum by a power law in rigidity and a linear angular distribution. The corresponding parameters are shown below, from top to bottom: the absolute intensity $(dI/dR)_0$, the spectral index $\gamma$ and the anisotropy parameter $b$ (see text for details).

guelen, Kiel, Lomnicky, McMurdo, Magdan, Moscow, Nain, Norilsk, Novosibirsk, Newark, Oulu, Pewanuk, Rome, SouthPole, TerreAdelie, Thule, TixieBay and Yakutsk. The results of the minimization procedure using a power law in rigidity and a linear angular distribution (Eq. 4.15) are illustrated in Figure 4.14. The top panel shows the comparison of the simulated count rate increases with the measured values for five selected stations. The agreement between the sim-

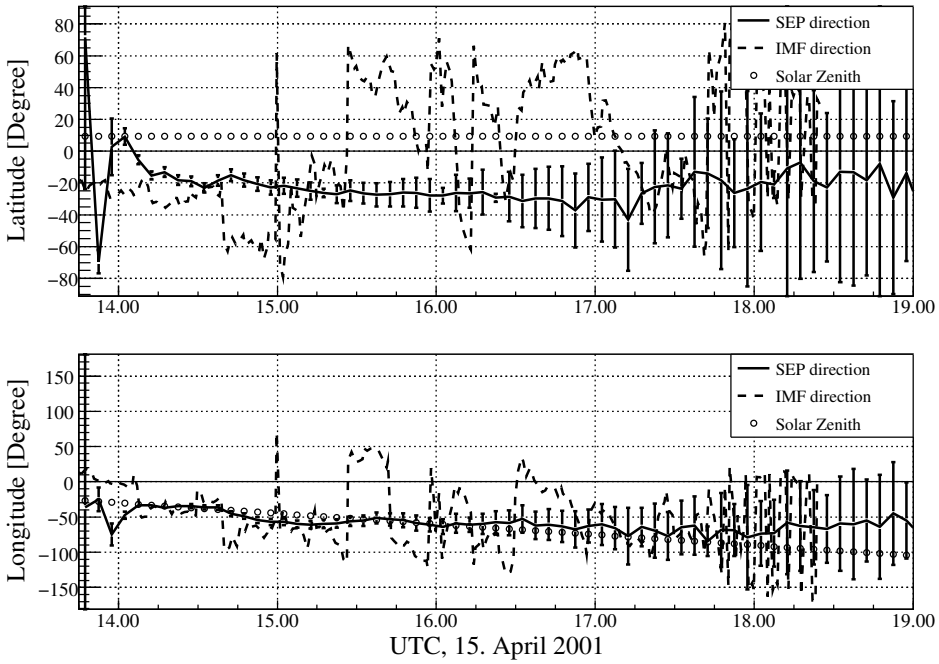


Figure 4.15: The temporal development of the incoming direction of GLE 60 compared to the interplanetary magnetic field measured by ACE and the solar zenith direction in geographic latitude (top) and longitude (bottom).

ulation and the measurements is very good, and only the results for the Calgary station before 14:45 UTC exhibit a disagreement in the order of 20% percent. Below the panel containing the Neutron Monitor count rate increases the evolving parameters for the description of the primary proton spectrum are shown. The onset of the Ground Level Event was in the time interval from 13:55 UTC–14:00 UTC. During this period the primary particles had a very hard spectrum with $\gamma \approx 3$. Subsequently, the spectrum softens gradually to $5 < \gamma < 5.5$ after 15.00 UTC. The softening of the primary proton spectrum is accompanied by a flattening in the angular distribution. As for the events discussed above, the slope of the angular distribution in the beginning of the event reveals a strong dependence of the primary particle intensity on the pitch angle. At later times, however, the dependence on the pitch angle weakens but the spectrum remains anisotropic.

Fig. 4.15 illustrates the results for the incoming direction of the solar energetic particles in comparison to the interplanetary magnetic field measured by ACE and the latitude and longitude of the sub-solar point (solar zenith) in geographic coordinates. The ACE data was shifted by 40 minutes due to the delayed arrival of the solar wind at Earth in comparison to the time of the measurements. The solar wind speed of approximately $600$ km/s at the time of GLE 60 was lower compared to GLE 70 and GLE 69 and yielded longer propagation times of the solar wind from ACE to Earth. The ACE spacecraft recorded a rapidly changing IMF as it is typical during the solar maximum conditions prevailing at the time of the event. The incoming direction of the solar energetic particles, however,

does not reveal the same behaviour. In the beginning of the event the incoming direction is located at low northern latitudes and low eastern longitudes and coincides with the location of the sub-solar point. This implies that the energetic particles at that time traveled scattering free through the interplanetary medium along the direct Sun-Earth line. At later times the incoming direction of the solar particles moves to southern latitudes but stays close to the longitude of the sub-solar point. The particles obviously traveled outside the ecliptic plane reaching the Earth from southern directions.
As for the previously analyzed solar energetic particle events, the fitted pri-

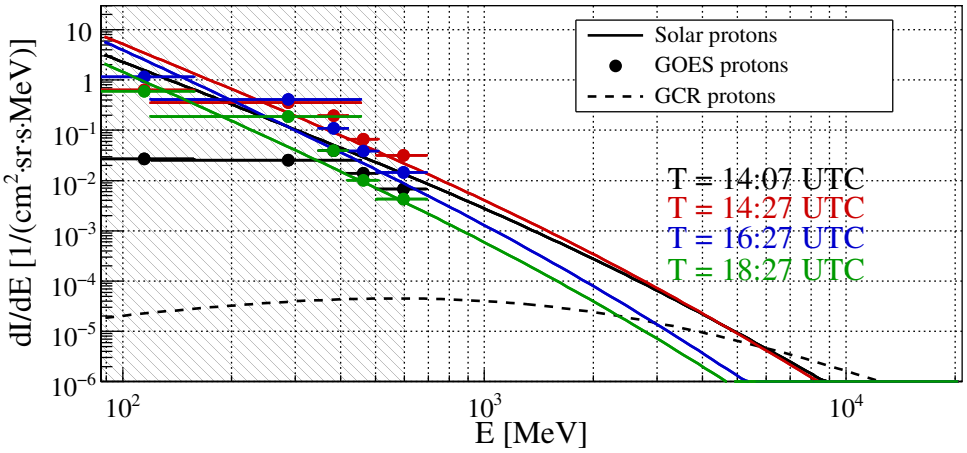


Figure 4.16: Differential intensity of primary solar energetic protons at different times during GLE 60 (solid lines) compared to the galactic cosmic ray protons (dashed line) and the measurements of GOES-8.

mary proton spectra show good agreement with the measurements by GOES (Fig. 4.16). Only in the beginning of the event, the extrapolation of the primary proton spectrum derived from the Neutron Monitor count rates overestimates the GOES data. Again, the softening of the primary spectra is obvious. The solar energetic proton intensities at 14:07 UTC and 14:27 UTC exceed the GCR intensities at energies up to 5 GeV–6 GeV. At later times, on the other hand, the solar protons only dominate at energies below 2 GeV–3 GeV. The time of the largest count rate increases was around 14:30 UTC. The primary proton spectrum at that time was slightly softer than in the beginning of the event but the particle intensities were much larger.

### 4.4.1 Effective doses during GLE 60

The largest increases apart from the South Pole station were seen by Calgary (114.1°W), Nain (61.7°W) and Pewanuk (85°W). A longitude of 80°W was therefore chosen to estimate the upper threshold for the effective dose rates at all latitudes. The results for the effective dose rate at 200 g/cm$^2$ (12 km altitude) along this longitude during GLE 60 are illustrated in Fig. 4.17. The effective dose rates at northern latitudes reached peak values of up to 57 $\mu$Sv/h between 14:30 UTC and 14:35 UTC corresponding to an increase of more than a factor of

nine compared to the GCR background. At the same time at southern latitudes the effective dose rate rose up to 72 $\mu$Sv/h which is almost twelve times as much as the dose induced by GCR.
The results for the calculation of the effective dose rates on the model flights

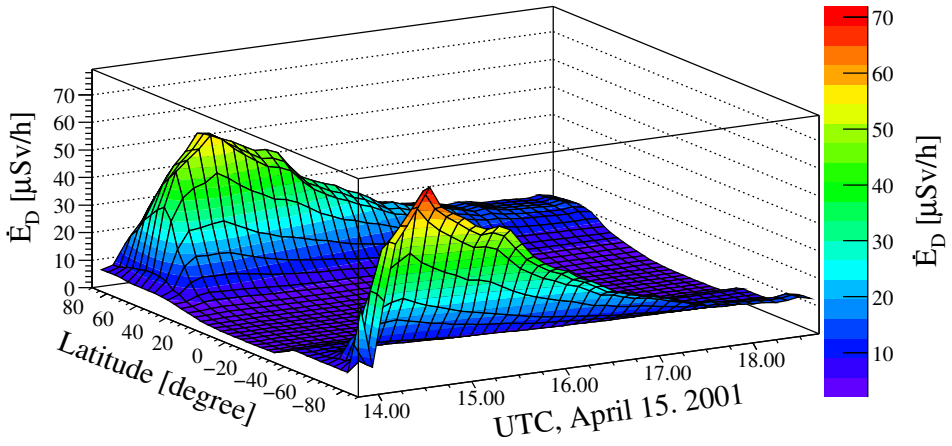


Figure 4.17: The variation of the effective dose rate at an atmospheric depth of 200 g/cm$^2$ corresponding to an altitude of about 12 km during the main phase of GLE 60 on April 15th, 2001 in dependence on the geographic latitude for a longitude of 80°W.

during GLE 60 are shown in Fig. 4.18. Peak values of more than 50 $\mu$Sv/h (25 $\mu$Sv/h) at the larger altitude of 12 km corresponding to 200 g/cm$^2$ are reached on the polar (north Atlantic) flight. The largest effective dose rate occurred at the South Pole with more than 70 $\mu$Sv/h at 200 g/cm$^2$. On the northern hemisphere, the largest effective dose rates were not reached at the lowest cut-off but at more southern locations which is a consequence of the southern incoming direction in combination with the anisotropy of the event. More southern locations are more sensitive to incoming directions at small pitch angles and the related larger proton intensities.
The total effective doses (Tab. D.5) on the flights from Frankfurt to Los Angeles and from New York to Beijing for a departure time of 12.30 UTC and a flight altitude of 12 km (200 g/cm$^2$) were 110 $\mu$Sv and 150 $\mu$Sv respectively. At 9 km (300 g/cm$^2$) the radiation exposure is significantly lower (52 $\mu$Sv and 68 $\mu$Sv). The event averaged effective dose rates for these flights and at the North and South Pole reach from 11 $\mu$Sv/h to 17 $\mu$Sv/h at 200 g/cm$^2$ and 5 $\mu$Sv/h to 7 $\mu$Sv/h at 300 g/cm$^2$ (Tab. D.6). The values for the total effective doses and the averaged effective dose rates correspond to increases of factors from 1.6 to 2.8 above the galactic cosmic ray background. All together, the GLE 60 was a rather weak event. The total effective dose at the South Pole may be regarded as a worst case estimation. The exposure during a 12 h stay at 12 km altitude at the South Pole were 170 $\mu$Sv which is less than three times the effective dose caused by GCR alone on a north Atlantic or polar flight.

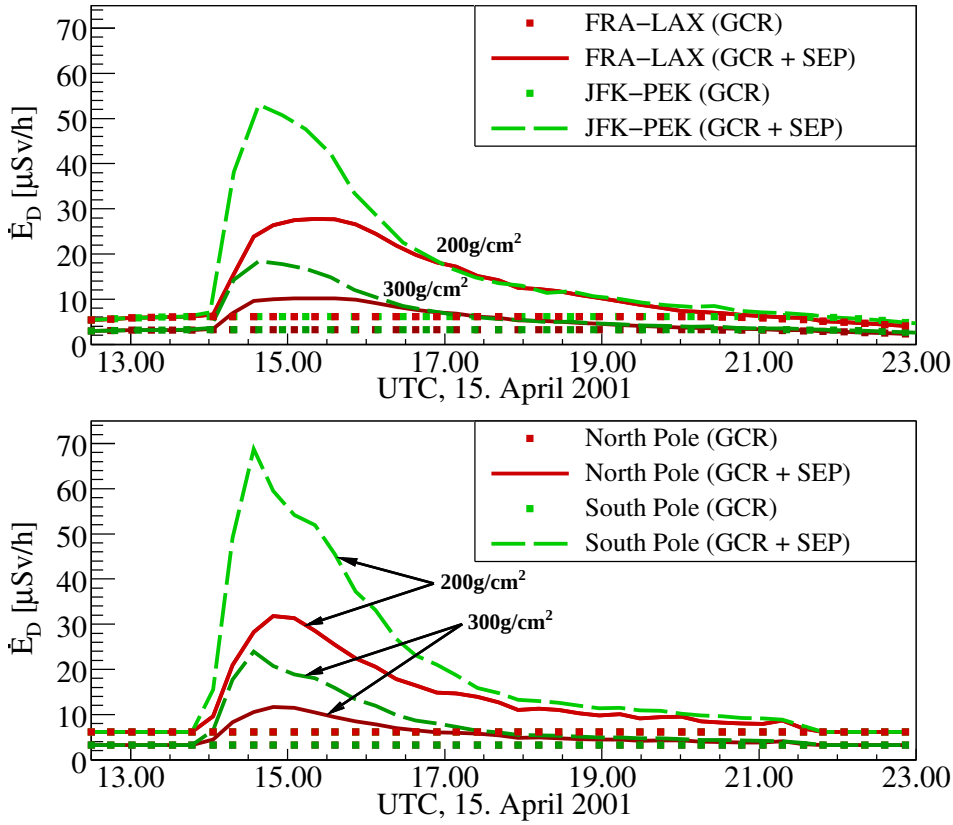


Figure 4.18: The dose rates for exemplary flights during GLE 60 from GCR background and solar energetic protons (SEP). In the top panel, the route from Frankfurt to Los Angeles (FRA–LAX) was chosen as an example for a north Atlantic flight and New York to Beijing (JFK–PEK) as a polar flight. The flights were set to start at 12:30 UTC, cruising at fixed atmospheric depths of 200 g/cm$^2$ and 300 g/cm$^2$ corresponding to approximately 12 km and 9 km. The lower panel shows the dose rate at the North and South Pole at the same altitudes.

## 4.5 Ground Level Enhancement 69

On January 20th, 2005 shortly before 7:00 UTC Neutron Monitors in the Antarctic (McMurdo, South Pole or Terre Adelie) recorded increases up to a few thousand percent marking the onset of the extraordinary Ground Level Enhancement 69. On one hand the event caused these extremely large count rate increases at southern latitude stations; on the northern hemisphere, on the other hand, the responses of Neutron Monitors were smaller by an order of magnitude revealing an anisotropy with a very strong angular dependence. Additionally, the extreme count rate increases at southern latitudes lasted only for a relatively short time. 30–40 minutes after the onset of the event the count rate increases of sea-level stations in the Antarctic had dropped to around 100%. During GLE 42 much larger increases were recorded for several hours. These facts show that the largest impacts of the event were restricted both in duration and geographic position. Some of the results of the analysis of the Ground Level Enhancement

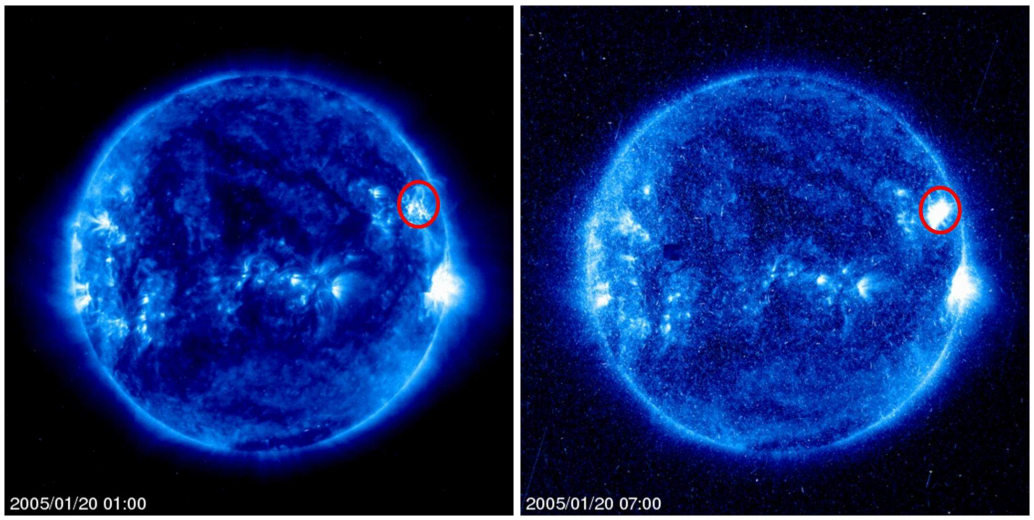


Figure 4.19: EIT images of the Sun at 17.1 nm. While the left image was taken several hours before the event on January 20th, at 1:00 UTC the right one shows the eruption in the NW-quadrant at 7:00 UTC.

69 presented in the following were published in *Matthiä et al.* (2009b).
GLE 69 was caused by a GOES class X 7.1, optical class 2B flare from the active region 10720 at N12 W58 on the visible solar disc. Figure 4.19 was taken with the Extreme Ultraviolet Imaging Telescope EIT (*Delaboudinière et al.*, 1995) on the Solar and Heliospheric Observatory (SOHO) spacecraft and shows one image before (1:00 UTC) and shortly after (7:00 UTC) the flare onset.
The flare occurred in the northwest quadrant of the Sun as indicated by the circle. The onset in $H_\alpha$ was given as 06:41 UTC on 20 January, 2005 (Solar Geophysical Data, US Dept. of Commerce, Boulder, CO). The Reuven Ramaty High Energy Solar Spectroscopic Imager (RHESSI), observed the flare in the energy range from 3 keV (soft X-rays) up to 20 MeV (gamma rays). In soft X-rays the flare started gradually, a hard X-ray burst started at 06:38 UTC and reached its maximum intensity at about 06:46 UTC. The onset of the event in X-rays at MeV energies followed the soft X-rays at 06:44 UTC also reaching its peak intensity around 06:46 UTC (*Simnett*, 2006). In addition, *Grechnev et al.* (2008) investigated the $\gamma$-ray flux from the CORONAS-F/SONG instrument to above 60 MeV including radiation from the $\pi^0$-decay, which started at 6:46 UTC. *Simnett* (2006) also used EIT difference images in order to determine the speed of the disappearing loop of $58 \pm 6$ km/s in the plane of the sky. At 6:48 UTC loops erupted together with a somewhat more extensive coronal mass ejection (CME). The latter reached a sky-plane speed of 2000–2500 km/s (*Grechnev et al.*, 2008).
Figure 4.20 displays from top to bottom five minute averages of 2.7 to 10 MeV electron, 8 to 25 MeV proton intensities from the Electron Proton Helium Instrument (EPHIN) (*Müller-Mellin et al.*, 1995), solar wind density, solar wind temperature, solar wind speed, helium to hydrogen ratio from the Solar Wind Electron, Proton, and Alpha Monitor (SWEPAM) (*McComas et al.*, 1998), magnetic field strength, azimuth and longitude from the Magnetic Field Experiment

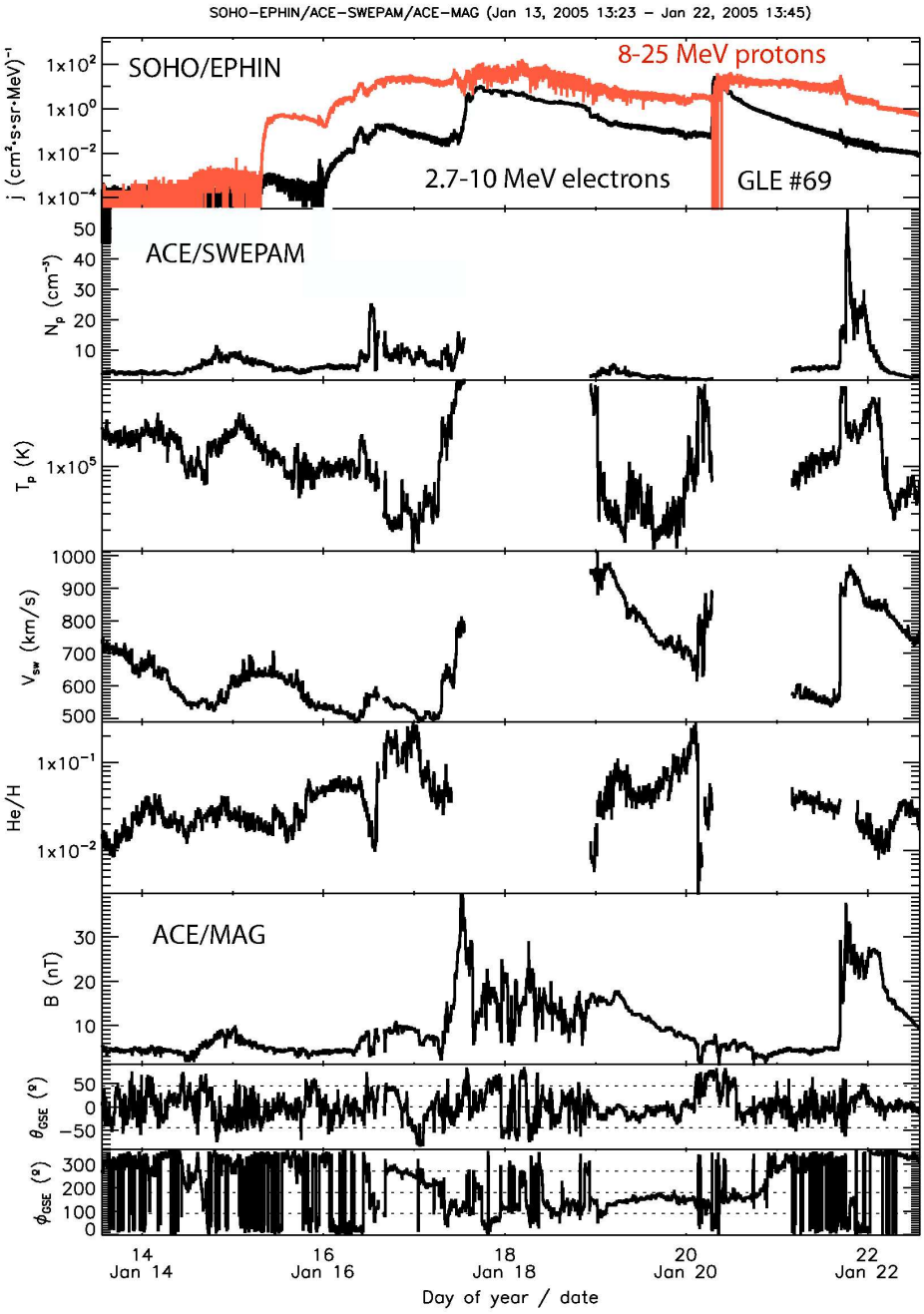


Figure 4.20: The figure shows from top to bottom five minute averages of 2.7 to 10 MeV electrons and 8 to 25 MeV protons ($j$), solar wind density ($N_p$), solar wind temperature ($T_p$), solar wind speed ($V_{SW}$), helium to hydrogen ratio (He/H), magnetic field strength ($B$), azimuth and longitude ($\theta_{\rm GSE}$, $\phi_{\rm GSE}$) from January 13 to January 23 . While the plasma and magnetic field data are from the SWEPAM and MAG instrument aboard ACE the energetic particle data are from EPHIN aboard SOHO.

(MAG) (*Smith et al.*, 1998) during the period from January 13 to January 23.

The active region 10720 caused three solar X-ray flares and high speed CMEs prior to the January 20 Ground Level Event: The January 15 at 22:48 UTC, January 17 at 09:43 UTC, and January 19 at 8:32 UTC were X2.6, X3.8, and X1.3 flares with CME speeds of 2860 km/s, 2550 km/s, and 2020 km/s respectively. The strong activity is also reflected in the solar wind plasma and magnetic field data as shown in Figure 4.20. The Ground Level Event occurred during a period of enhanced particle intensities as indicated by the 2.7 to 10 MeV electron and the 8 to 25 MeV proton flux in the upper panel of the figure. The electron and proton intensities before the onset of the GLE were three and four orders of magnitude above the quiet time fluxes. The intensity at Neutron Monitor energies was slightly reduced prior to the event due to three large Forbush Decreases (*Simnett*, 2006).

The high energy proton and alpha channels of GOES-11 were studied to estimate the contribution of nuclei with $Z > 1$ to the highly energetic primary particle spectrum and to confirm the assumption that a restriction to primary protons is valid. The p6 and a6 channel representing similar energy per nucleon intervals were compared (p6: $80$ MeV–$165$ MeV for protons and a6: $300$ MeV–$500$ MeV for alpha particles). It was found that the fraction of alpha particles is less than one percent of the proton intensities during the whole event. Heavier ions are even less significant due to their shorter ranges and even smaller intensities. It was therefore assumed that the effects on the ground and in the lower atmosphere observed in the solar energetic particle event are solely caused by primary protons.

The earliest increase in Neutron Monitor count rates of a few percent was measured in the 5-minute interval from 6:45 UTC to 6:50 UTC with the South Pole station showing the largest increase of 13%. This slight rise was followed by huge count rate increases in a number of southern latitude stations up to 3353% (South Pole) (6:45 UTC–6:50 UTC). Neutron Monitor stations on the northern hemisphere, however, had not yet responded to the GLE at that time. The count rate maximum at northern latitude stations was recorded 10–30 minutes later (Oulu: 7:00–7:05 UTC; Inuvik: 7:05–7:10 UTC; Thule: 7:30–7:35 UTC). After a rapid decrease of the extreme count rates in the beginning of the event low count rate increases lasted more than a day, and after 24 h the count rates of the South Pole station were still increased by almost 10%.

The minimization was performed using the power law in rigidity and the linear angular distribution for five minute intervals for a 12 h period starting at 6:45 UTC on January, 20. 2005. The results for the count rate increase of five selected stations are shown in the top panel of Fig. 4.21. The measurements are reproduced accurately by the calculated count rates for both northern and southern hemisphere. The late increase of the northern stations, especially the Thule station, is very well fitted by the model, showing that the anisotropy of the event is accurately described. The Thule Neutron Monitor has the most northern asymptotic viewing directions of the selected stations (Fig. 4.3) and the late increase is no surprise taking into account that in the beginning the incoming direction of the event was located on the southern hemisphere.

The result of the minimization process for the parameters describing the primary

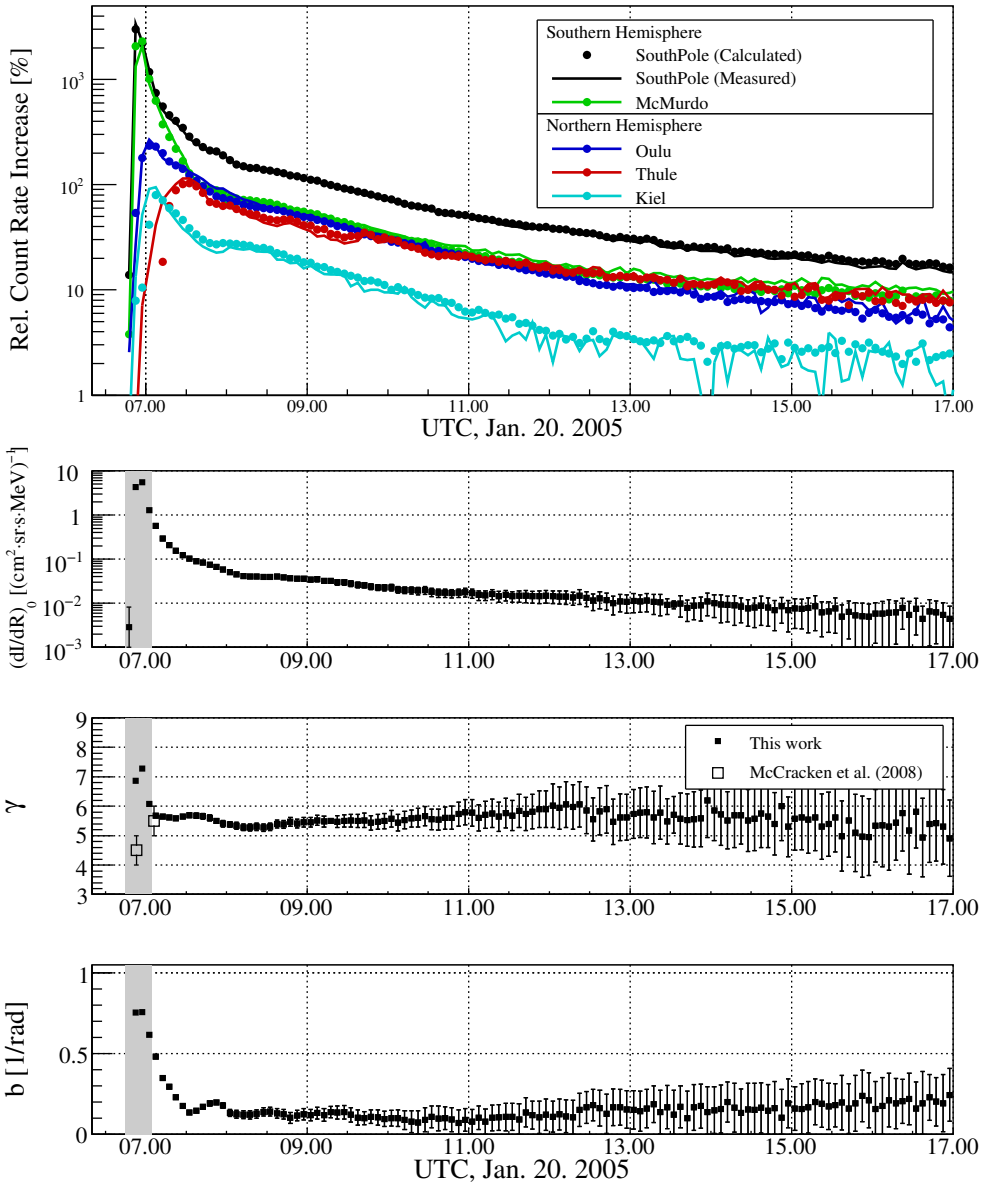


Figure 4.21: Relative Neutron Monitor count rate increases during GLE 69 for selected stations in the top panel. Solid lines show the measured values and the circles illustrate the results from the fit of the primary proton spectrum by a power law in rigidity and a linear angular distribution. The corresponding parameters are shown below, from top to bottom: the absolute intensity $(dI/dR)_0$, the spectral index $\gamma$ and the anisotropy parameter $b$ (see text for details).

particle spectrum is shown in the lower three panels of Fig. 4.21. After a period of fast variation of the primary spectrum during the first hour of the event, only minor changes in the parameters are observed. The spectral index during the first five minute interval, i.e. from 6:45 UTC to 6:50 UTC, is $\gamma \approx 6$. During these five minutes, only the South Pole monitor registered a slight count rate increase due to its southern and elevated location at an altitude of 2820 m. Due to the fact that the result for this interval is based only on the increase of one station it is not very reliable. However, during the next ten minutes a strong increase in a number of Neutron Monitors and in total proton fluence is observed, and the spectrum is much softer ($\gamma \approx 7$–$7.5$). This is in good agreement with the results of other authors analyzing the same event (e.g. *Bütikofer et al.* (2008), *Bombardieri et al.* (2008) and *Plainaki et al.* (2007)). In the following hour the spectrum hardened again, and the spectral index reached a value of $\gamma = 5.5$. While *Plainaki et al.* (2007) and *Bütikofer et al.* (2008) determined the spectral index to be larger, $\gamma \approx 7$, *Bieber et al.* (2005) found a similar spectral index of $\gamma \approx 5$. Basically no changes in the slope of the primary proton spectrum are observed after 8:00 UTC.

In the beginning of the event before 7.05 UTC a very large spectral index ($\gamma > 7$) was obtained in this work and is supported by other publications using a similar technique (*Bütikofer et al.*, 2008; *Bombardieri et al.*, 2008; *Plainaki et al.*, 2007). In contrast, authors comparing the response of two neutron monitors with different sensitivities presented values of $\gamma < 6$ (*Bieber et al.*, 2005; *McCracken et al.*, 2008). The discrepancies occur during the time of very strong anisotropy and mirror the limited accuracy in the description of the angular distribution of the energetic particles. Additionally, the minimization of the differences in measured and calculated count rate increases is governed by Neutron Monitors showing very large responses. These stations are located at low geomagnetic cut-offs and are more sensitive to lower energetic primary particles. This may lead to an overestimation of the lower part of the energy spectrum and to large spectral parameters. The affected time period is indicated by the hatched area in the lower panels of Fig. 4.21. In addition, the spectral indices reported by *McCracken et al.* (2008) are indicated. Even though the primary spectrum may not very accurately describe the primary particle spectrum outside the magnetosphere during that time, the good reproduction of the Neutron Monitor count rates show that the secondary particle fluences and the derived dose rates in the lower atmosphere are reliable.

The changes in the parameters of the primary proton energy spectrum during the event are shown explicitly for four times in Fig. 4.22. As discussed above, the slope of the spectrum is almost constant at times after 7:27 UTC while a strong decrease in total intensity is observed. The atmospheric cut-off energy of primary protons restricts the range that is accessible by analyzing sea-level Neutron Monitor stations to values above 300–500 MeV. In addition to the directly accessible energy range, the extrapolation to lower energies is shown in Figure 4.22 in the hatched area. The results from the extrapolation of the energy spectrum agree very well with the measurements of GOES for all times but the beginning of the event (6:57 UTC). The disagreement in the very beginning can

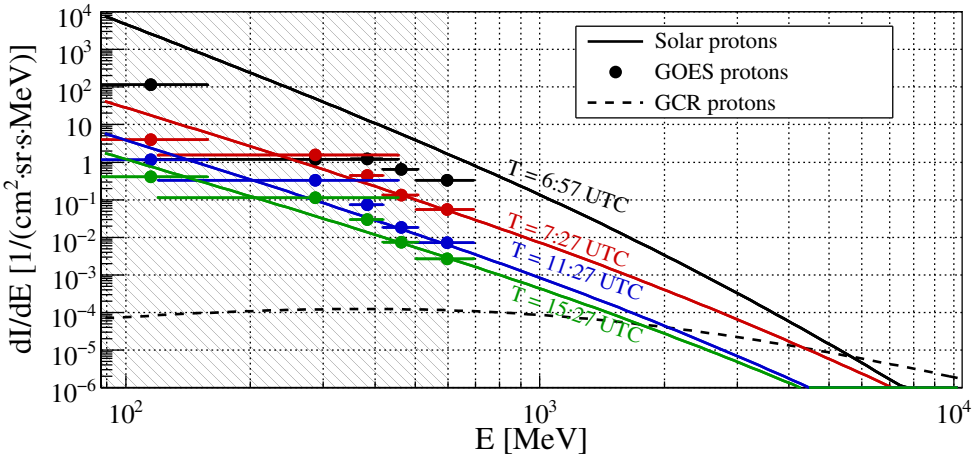


Figure 4.22: Differential intensity of primary solar energetic protons at different times during GLE 69 (solid lines) compared to the galactic cosmic ray protons (dashed line) and the measurements of GOES-11. The lowest point of the GOES data ($E = 80$ MeV–165 MeV) for T=6:57 UTC was multiplied by 100 to discriminate it from the point at 11:27 UTC.

be explained by two facts. First, it is obvious that the very highly energetic particles in the beginning of the event traveled to Earth much faster than particles with lower energies which had not arrived yet. As our analysis is based on particles above approximately 500 MeV it is clear that an overestimation at lower energies occurs. The second and more important point is that the GOES viewing direction does not coincide with the axis of symmetry of the primary spectrum for which the energy distribution is shown in Fig. 4.22. The intensity in direction of the particle detector on-board GOES may therefore be much lower. At later times the anisotropy is much weaker and the detector's viewing directions have no influence on the measurement anymore. Nevertheless, the agreement with the GOES data at later times is an indicator for the quality of the derived spectra. Considering the very beginning of the event it seems that the pure power law spectrum does not fit the real spectrum over the whole energy range from 100 MeV to tens of GeV. A possible solution could be to use a modified power law for which *Bombardieri et al.* (2008) found a flatter distribution for lower energies during the first 10 minutes of the event. The anisotropy expressed by the parameter $b$ (lowest panel in Fig. 4.21) decreased from around 0.8 to 0.2 during the first hour of the event indicating long mean free paths in interplanetary space (*Bieber et al.*, 2002). Afterwards, it remains constant and even twelve hours after the beginning of the event a certain level of anisotropy was observed.
From the anisotropy and the response of Neutron Monitor stations with different viewing directions it is possible to determine the incident direction of the primary protons. For the chosen angular distribution (linear in the pitch angle) it is assumed that the proton fluence is maximal in this direction and symmetric in the pitch angle. The incident longitude and latitude for the solar energetic particles is shown in Fig. 4.23 from 6:00 UTC to 17:00 UTC together with the interplanetary

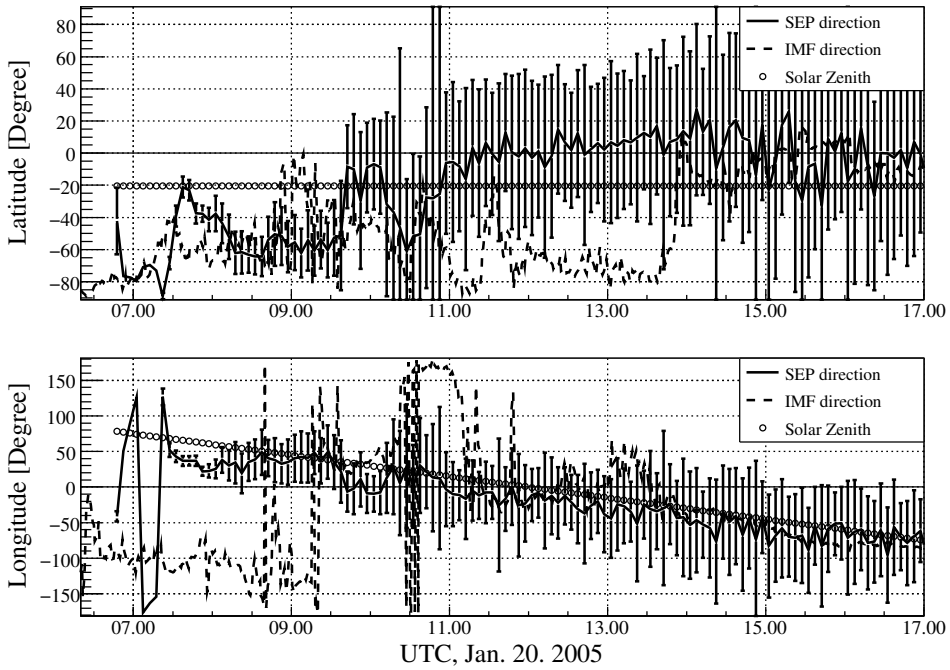


Figure 4.23: The temporal development of the incoming direction of Ground Level Event 69 compared to the interplanetary magnetic field measured by ACE and the solar zenith direction in geographic latitude (top) and longitude (bottom).

magnetic field (IMF) measured by the ACE spacecraft and the direct Sun-Earth line in geographic coordinates. As for GLE 70 the ACE data was shifted by 35 minutes to correct for the delayed arrival of the solar wind at Earth. Aside from the time period between 12:00 UTC and 13:30 UTC the upper panel of Fig. 4.23 indicates that the latitudes of the IMF and the incoming direction of the solar particles coincide. In the beginning, the event hits the Earth at southern latitudes but shifts to lower latitudes during the following hours. In the second half of the analyzed time period, the event's incoming direction equals the Sun-Earth line both for longitude and latitude.

The IMF longitude is expected to be around $20°$–$30°$ west of the Sun-Earth line (*Parker*, 1958) for solar wind speeds of 700 km/s to 1000 km/s measured by ACE in the days prior to the event (see Fig. 4.20). This behavior is only observed for the time after 17:00 UTC. The IMF's longitude changes very rapidly before that time expressing the highly variable magnetic conditions during that period. The SEP incoming longitude on the other hand follows the straight Sun-Earth line. The fact that after around 11:30 UTC both longitude and latitude of the SEP incident direction coincide with the Sun-Earth line indicates the complexity of the energetic particle propagation in interplanetary space to Earth. The information about the anisotropy of the event and the interplanetary magnetic field during the event can probably be improved by using a more precise model of the geomagnetic field and its modifications during the ongoing event and by using Neutron Monitor asymptotic directions that depend on the primary particles incoming di-

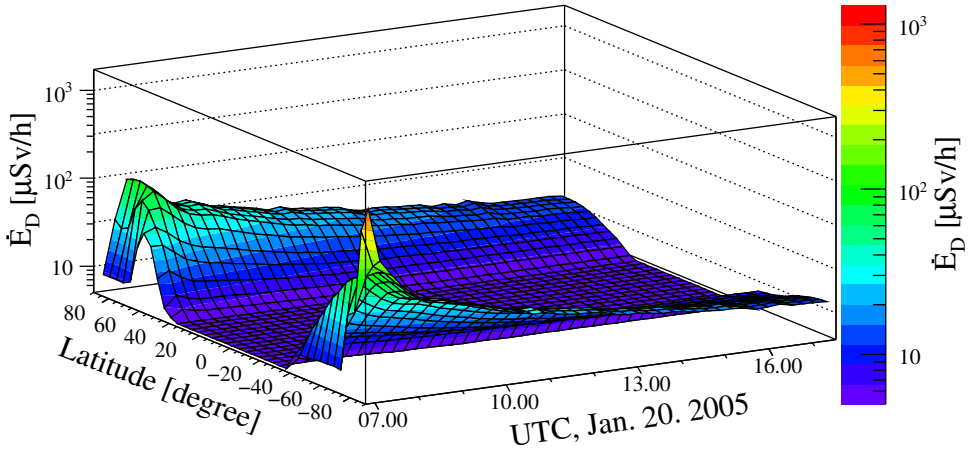


Figure 4.24: The variation of the effective dose rate at an atmospheric depth of 200 g/cm$^2$ corresponding to an altitude of about 11 km during the main phase of GLE 69 on January 20th, 2005 in dependence on the geographic latitude along the Greenwich meridian.

rection. This investigation was restricted to asymptotic directions of vertically incident protons as an approximation.

### 4.5.1 Effective doses during GLE 69

The time profile of the effective dose rate along the Greenwich meridian illustrated in Fig. 4.24 shows the impact of the anisotropic angular distribution of the solar particles on the radiation exposure at 200 g/cm$^2$ (12 km) for latitudes from 90°N to 90°S. Close to the South Pole the effective dose rate reaches values of up to 1.2 mSv/h (6:55 UTC–7:00 UTC) corresponding to an immensely strong increase of an factor of almost 150 above the galactic cosmic background. On the northern hemisphere, on the other hand, the maximum in the effective dose rate with a value of 100 $\mu$Sv/h is reached around 30 minutes later between 7:25 UTC and 7:35 UTC during the less anisotropic phase of the event. Around 8:00 UTC the dose rate had dropped to 52 $\mu$Sv/h and 65 $\mu$Sv/h at very high northern and southern latitudes. The large discrepancies between northern and southern locations and the rapidly decreasing effective dose rate after the maximum show that the exposures on flights during this event were strongly dependent on the route and the time of flight.
In Fig. 4.25 the dose rates on the polar and north Atlantic flights (top panel) are illustrated together with the values at the North and South Pole (bottom panel). While the effective dose rates at the chosen flight profiles (departure time 6:00 UTC) reached peak values of 33 $\mu$Sv/h to 40 $\mu$Sv/h at the higher flight altitude of 12 km (200 g/cm$^2$), much larger values in the order of 1 mS/h were expected for a position close to the South Pole. The steep primary energy spectrum of the solar particles around 7:00 UTC caused a rapid decrease in the effective dose rate with decreasing altitudes. At the lower altitude of 9 km (300 g/cm$^2$) at the South Pole the dose rate had dropped to roughly 25% (250 $\mu$Sv/h) compared to 12 km altitude.

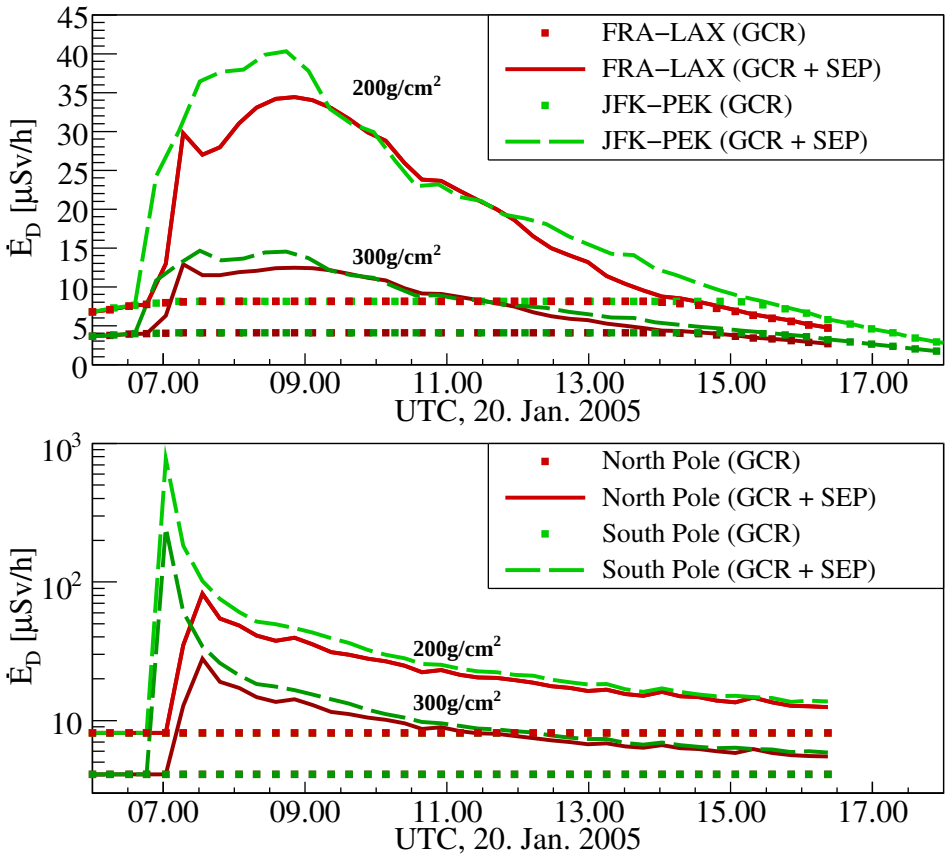


Figure 4.25: The dose rates for exemplary flights during GLE 69 from GCR background and solar energetic protons (SEP). In the top panel, the route from Frankfurt to Los Angeles (FRA–LAX) was chosen as an example for a north Atlantic flight and New York to Beijing (JFK–PEK) as a polar flight. The flights were set to start at 6:00 UTC, cruising at fixed atmospheric depths of 200 g/cm$^2$ and 300 g/cm$^2$ corresponding to approximately 12 km and 9 km. The lower panel shows the dose rate at the North and South Pole at the same altitudes.

The total effective dose at 200 g/cm$^2$ (12 km) on the calculated flight routes was 170 $\mu$Sv and 200 $\mu$Sv for FRA–LAX and JFK–PEK respectively (Tab. D.7). At the lower altitude (300 g/cm$^2$, 9 km) the exposure was reduced to approximately 40% of these values (FRA–LAX: 73 $\mu$Sv and JFK–PEK: 86 $\mu$Sv). Significant differences occurred between the flights on the northern hemisphere and the values at the South Pole where the total effective doses for the time between 6.00 UTC and 16.30 UTC were 450 $\mu$Sv (200 g/cm$^2$) and 170 $\mu$Sv (300 g/cm$^2$). Detailed numbers of the total doses and event averaged dose rates can be found in Tab. D.7 and Tab. D.8. *Copeland et al.* (2008) estimated the effective dose for a 10 h high latitude flight at 40 kft ($\approx$12km) to be 390 $\mu$Sv.
GLE 69 was an extraordinarily strong event which exhibited a strong angular dependence. While the effective dose rates on the northern hemisphere were comparable to the large GLE 42, the values on the southern hemisphere exceeded GLE 42 by an order of magnitude. Due to the temporal limitation of the extreme values in the effective dose rates, however, the total effective dose rates were

comparable to GLE 42.

# Chapter 5

# Summary

Measurements of particle spectra in the atmosphere are rare and spatially and temporally restricted and consequently do not allow a comprehensive characterization of the radiation environment in the atmosphere. This is particularly valid during solar energetic particle events. Computer based calculations provide an alternative for the estimation of the influence of galactic cosmic rays and solar energetic particles on the atmosphere. The complexity of the Sun-Earth system, however, complicates this challenge.

**The model**

This work presents a detailed study of the radiation environment in the lower atmosphere caused by extraterrestrial radiation both during times of dominating galactic cosmic ray influence and during Ground Level Enhancements. The procedure of determining the radiation exposure in the atmosphere contains several steps:

- The determination of the relevant primary particle compositions, energy spectra and angular distributions near Earth outside the magnetosphere.
- The influence of the Earth's magnetosphere on the primary particle spectra on top of the atmosphere, i. e. calculating the transport of charged particles through the magnetosphere.
- The transport of the primary particles through the Earth's atmosphere and secondary particle production.
- The conversion of the particle fluences at a given point and time to the relevant dosimetric quantities: effective dose and ambient dose equivalent.

While the determination of the primary particle spectra for galactic cosmic rays in this work is based on existing models describing the particle intensities at Earth and their periodic modulation during the solar cycle, the analysis of Ground Level Enhancements is more complex and treated in more detail. It is based on count rate increases of ground based Neutron Monitors which additionally makes it necessary to

- calculate the Neutron Monitor count rates induced by galactic cosmic rays and the expected increases during a Ground Level Enhancement.

This problem is closely linked to the first three points mentioned above: the determination of the primary particle spectra, the propagation of the particles in the magnetosphere and the transport through the atmosphere. As a consequence, the result of each of these sub tasks depends on the outcome of all others and erroneous assumptions or results would propagate to the consequent results. Therefore, a considerable part of this work is dedicated to the verification of each of the individual sub tasks. The verification during solar energetic particle events is difficult as measurements of secondary particle fluences and dose rates during Ground Level Enhancements are very scarce, and the available satellite data on primary particle spectra is limited in energy and does not provide directional information in the relevant energy range. Therefore, secondary particle spectra from galactic cosmic rays were calculated and compared to existing measurements to test the accuracy of the simulated propagation through the magnetosphere and the interactions within the atmosphere.
The directional sensitivity of Neutron Monitor stations to solar energetic particles based on the asymptotic viewing directions of the detectors play a crucial role in the analysis of Ground Level Enhancements. During the anisotropic phase of an event the asymptotic viewing directions strongly affect the response of a Neutron Monitor. In addition to the angular distribution and incoming direction, the energy spectrum of the particles defines the impact of the event on the atmosphere.
The model presented in this work allows to fit the energy spectrum, the angular distribution and the incoming directions of the solar particles based on the count rate increases of a number of Neutron Monitor stations. The results are obtained by applying a minimization technique and it is possible to describe the event with an unprecedented high temporal resolution of five minute averages during the whole event. With a sufficiently large data base of Neutron Monitor data with higher temporal resolution this can easily be improved. Based on the description of the primary particle spectra it is possible to estimate the secondary particle fluences induced by the Ground Level Enhancement and the related dosimetric quantities. The model permits to calculate the radiation exposure on individual flight routes and to estimate the effects of the anisotropy of the event.

#### Verification of the model

The calculation of secondary particle fluences and radiation exposures induced by galactic cosmic rays are used in the present work for the verification of the transport calculations and the determination of the radiation exposure by comparing the results to experimental measurements and existing model calculations. From the comparison to experimental data adequate models for the description of the galactic cosmic ray spectra and their modulation are chosen and the influence of the Earth's magnetosphere on charged particles is described by a single parameter, namely the effective cut-off rigidity $R_C$. The general agreement with the data provided by the Neutron Monitor network is good, although differences

in the order of 30% are observed between the effective cut-off rigidities of some Neutron Monitor stations determined in this work and the values provided by the Neutron Monitor network. Using the effective cut-off rigidities implies a restriction to cut-offs calculated for vertically incident particles and neglecting non-vertical cut-offs. It was shown, however, that the differences arising between vertical and non-vertical particles are small for high and medium latitude stations.
After the effect of the magnetosphere was investigated, the secondary particle intensities caused by galactic cosmic rays and the related effective dose rates were calculated for a variety of locations. Very good agreement was observed for the majority of the reproduced experiments. Secondary muon and proton intensities were well reproduced both in shape and magnitude. The results for secondary neutrons also showed good agreement to measurements in large parts.
The total effective dose and ambient dose equivalent rates were derived from the secondary particle fluences in the atmosphere and the contributions of individual secondary particles to the radiation exposure were calculated. The results show good agreement to experiments and model calculations performed by other authors.
In order to draw conclusions from the responses of Neutron Monitor stations about the primary particle spectra during Ground Level Enhancements it is necessary to investigate and understand the response of the Neutron Monitor detectors to energetic particles entering the atmosphere. The simulation of Neutron Monitor count rates at different geomagnetic and atmospheric shieldings induced by galactic cosmic rays and the changes related to the varying solar modulation was used to study the capability to reproduce the response of Neutron Monitor stations to variations in the primary energy spectrum. For the first time the accurate reproduction of absolute Neutron Monitor count rates of different stations over several decades is presented in this work.
The reproduction of secondary particle fluences as well as the radiation exposures and the Neutron Monitor count rates and the good agreement with the experimental results prove that the transport calculations provide an adequate estimate of these quantities and are suited for the analysis of Ground Level Enhancements.

**Ground Level Enhancements**

Based on the model developed in this work, the rigidity and energy spectra, the angular distributions and the incoming directions of the solar energetic particles during four different Ground Level Enhancements were determined and the related increases in the effective dose rates were estimated. During all of the four analyzed events, the angular distribution was found to be anisotropic in the beginning of the event, especially during the first thirty minutes the primary particle intensity significantly depended on the particles' arriving directions. It was possible to estimate the incoming direction of the solar particles during the anisotropic phases of the events, and for the majority of the analyzed time periods the estimated incoming directions of the solar particles coincided with the nominal interplanetary magnetic field and with the measurements of the inter-

planetary magnetic field by ACE. In the analyzed events, the primary particles typically exhibited a relatively hard spectrum in the beginning containing a large fraction of high energy particles, and a softening of the spectrum was observed in the course of the event. Typical values of the spectral index for a power law in rigidity during the analyzed events were in the range of three to six. The extrapolation of the estimated primary energy spectra to lower energies agreed well with the measurements by the GOES satellites during less anisotropic phases of the events.
Based on the fact that the incoming direction and the angular distribution of the solar particles could be estimated it was found that the radiation exposure in the atmosphere during anisotropic phases strongly depends on the geographic location of interest and the corresponding viewing directions. Event averaged effective dose rates on the northern and southern hemisphere during the large GLE 69, for example, differed by more than a factor of two. The analysis of the Ground Level Enhancements in this work contained two of the largest events in the last decades, and it was found that the effective dose on north Atlantic and polar flights was increased by up to several hundred percent.

**Outlook**

This work presents a model capable of reproducing Neutron Monitor count rates during quiet solar times and during Ground Level Enhancements and for estimating the effects on the radiation environment in the lower atmosphere related to Ground Level Enhancements. For extreme conditions, however, like the strong anisotropy in combination with very high energetic particles which was observed in the beginning of GLE 42 the results may be improved by considering additional effects. The exact influence of the non-vertical cut-off rigidities on secondary particle intensities, dose rates and Neutron Monitor count rates, for example, is worth additional investigation but would significantly increase the computational complexity and could not be approached within this work. Considering non-vertical asymptotic directions may also have a significant influence on the reproduction of the Neutron Monitor count rates. It was shown, however, that this affects only particles with rigidities of several tens of GeV and can be neglected in the majority of the events.
The utilization of spacecraft data may give valuable contributions to the analysis of solar energetic particle events in the future providing information about energy spectra for specified viewing directions and directional information.
The results of the presented work show that it is possible to estimate the characteristics of the primary particle spectra during Ground Level Enhancements from the data of the Neutron Monitor network and to determine the related effective dose and ambient dose equivalent rates at aviation altitudes. The Neutron Monitors provide valuable information about energy ranges which are not directly accessible through current space craft data. Based on the results of this work, it will be possible to develop a short time alert system in the future to warn against increased radiation exposure during Ground Level Events. By increasing the accuracy of the transport calculations through the magnetosphere and by

taking into account the disturbances of the geomagnetic field the capability of the model to gain information about the propagation and the properties of solar energetic particles in the interplanetary space may be improved and may permit further insight into the processes in the heliosphere and their interplay with the Earth's magnetosphere.

# Acknowledgments/Danksagungen

Als erstes möchte ich Herrn Dr. Günther Reitz danken, dass er mir die Möglichkeit gab diese Dissertation zu verfassen und für sein stetes Vertrauen in meine Arbeit. Zu ebenso großem Dank bin ich Herrn Prof. Dr. Bernd Heber verpflichtet für die Betreuung der Arbeit und für die viele Unterstützung die ich während des Anfertigens meiner Dissertation durch ihn erfuhr. Herrn Dr. Matthias Meier möchte ich besonders danken für seine stetige und unerlässliche Unterstützung in allen Bereichen meiner Arbeit und dafür, dass ich mich stets auf ihn verlassen konnte. Bei Herrn Dr. Thomas Berger möchte ich mich für die vielen konstruktiven Gespräche und Anregungen bedanken. Der kompletten Abteilung Strahlenbiologie danke ich für eine tolle Gemeinschaft, besonders erwähnt sei hier Frau Britta Rowehl und ihre unermüdliche Hilfe bei allen administrativen Dingen.

Special thanks go to Prof. Lembit Sihver for his constant support and his understanding. I would like to thank all members of the Nuclear Engineering department at Chalmers University of Technology, especially Chiara La Tessa, Davide Mancusi and Katarina Gustafsson for their friendliness, support and friendship during my stays in Göteborg.

I would like to thank all researches and scientists for providing the data and support which was essential for the composition of this work, especially Dr. Laurent Desorgher for his help and for providing the PLANETOCOSMICS software.

Meiner Familie möchte ich für ihr Interesse an meiner Arbeit und ihre Unterstützung danken. Besonderen Dank spreche ich am Ende dem wichtigsten Menschen in meinem Leben, Catharina Carstens, für ihre große Geduld und ihr Verständnis aus und dafür, dass ich alle Momente mit ihr teilen darf.
Tina, Deine wundervolle Persönlichkeit erfüllt mein Leben mit Glück.

# List of Figures

# List of Tables

# Bibliography


Abbasi, R., et al. (2008), Solar energetic particle spectrum on 2006 december 13 determined by icetop, *Astrophysical Journal*, *689*, L65–L68, doi: 10.1086/595679.

Agostinelli, S., et al. (2003), Geant4-a simulation toolkit, *Nuclear Instruments and Methods in Physics Research A*, *506*, 250–303.

Alcaraz, J., et al. (2000a), Helium in near Earth orbit, *Physics Letters B*, *494*, 193–202.

Alcaraz, J., et al. (2000b), Protons in near earth orbit, *Physics Letters B*, *472*, 215–226.

Alpher, R. A. (1950), Theoretical geomagnetic effects in cosmic radiation, *Journal of Geophysical Research*, *55*, 437, doi:10.1029/JZ055i004p00437.

Amsler, C., et al. (2008), Review of Particle Physics, *Physics Letters B*, *667*, 1–5, doi:10.1016/j.physletb.2008.07.018.

Badhwar, G. D., and P. M. O'Neill (1996), Galactic cosmic radiation model and its applications, *Advances in Space Research*, *17*, 7–17, doi:10.1016/0273-1177(95)00507-B.

Band, D., et al. (1993), BATSE observations of gamma-ray burst spectra. I - Spectral diversity, *Astrophysical Journal*, *413*, 281–292, doi:10.1086/172995.

Battistoni, G., A. Ferrari, M. Pelliccioni, and R. Villari (2005), Evaluation of the doses to aircrew members taking into consideration the aircraft structures, *Advances in Space Research*, *36*, 1645–1652, doi:10.1016/j.asr.2005.04.037.

Battistoni, G., F. Cerutti, A. Fassò, A. Ferrari, S. Muraro, J. Ranft, S. Roesler, and P. R. Sala (2007), The FLUKA code: description and benchmarking, in *Hadronic Shower Simulition Workshop*, *American Institute of Physics Conference Series*, vol. 896, edited by M. Albrow and R. Raja, pp. 31–49, doi: 10.1063/1.2720455.

Beach, A. S., et al. (2001), Measurement of the cosmic-ray antiproton-to-proton abundance ratio between 4 and 50 gev, *Phys. Rev. Lett.*, *87*(27), 271,101, doi: 10.1103/PhysRevLett.87.271101.

Bellotti, R., et al. (1999), Balloon measurements of cosmic ray muon spectra in the atmosphere along with those of primary protons and helium nuclei over midlatitude, *Physical Review D*, *60*(5), 052,002.

Bieber, J. W., and P. Evenson (1991), Determination of energy spectra for the large solar particle events of 1989, in *International Cosmic Ray Conference*, *International Cosmic Ray Conference*, vol. 3, p. 129.

Bieber, J. W., J. Clem, P. Evenson, R. Pyle, M. Duldig, J. Humble, D. Ruffolo, M. Rujiwarodom, and A. Saiz (2005), Largest GLE in half a century: Neutron Monitor observations of the January 20, 2005 event, in *International Cosmic Ray Conference*, *International Cosmic Ray Conference*, vol. 1, p. 237.

Bieber, J. W., J. Clem, P. Evenson, and et al. (2008), A maverick GLE: The relativistic solar particle event of December 13, 2006, in *International Cosmic Ray Conference*, *International Cosmic Ray Conference*, vol. 1, pp. 229–232.

Bieber, J. W., et al. (2002), Energetic particle observations during the 2000 July 14 solar event, *Astrophysical Journal*, *567*, 622–634, doi:10.1086/338246.

Bombardieri, D. J., M. L. Duldig, J. E. Humble, and K. J. Michael (2008), An improved model for relativistic solar proton acceleration applied to the 2005 January 20 and earlier events, *Astrophysical Journal*, *682*, 1315–1327, doi: 10.1086/589494.

Brueckner, G. E., et al. (1995), The Large Angle Spectroscopic Coronagraph (LASCO), *Solar Physics*, *162*, 357–402, doi:10.1007/BF00733434.

Burger, R. A., M. S. Potgieter, and B. Heber (2000), Rigidity dependence of cosmic ray proton latitudinal gradients measured by the Ulysses spacecraft: Implications for the diffusion tensor, *J. Geophys. Res.*, *105*(A12), 27,447–27,455.

Bütikofer, R., E. Flückiger, L. Desorgher, and M. Moser (2008), The extreme solar cosmic ray particle event on 20 January 2005 and its influence on the radiation dose rate at aircraft altitude, *Science of The Total Environment*, *391*(2-3), 177 – 183.

Caballero-Lopez, R. A., and H. Moraal (2004), Limitations of the force field equation to describe cosmic ray modulation, *Journal of Geophysical Research (Space Physics)*, *109*, 1101, doi:10.1029/2003JA010098.

Cane, H. V., and D. Lario (2006), An introduction to CMEs and energetic particles, *Space Science Reviews*, *123*, 45–56, doi:10.1007/s11214-006-9011-3.

Clem, J. M., and L. I. Dorman (2000), Neutron Monitor Response Functions, *Space Science Reviews*, *93*, 335–359, doi:10.1023/A:1026508915269.

Cliver, E. W., S. W. Kahler, and et al. (1993), On the origin of gamma-ray emission from the behind-the-limb flare on 29 September 1989, in *International Cosmic Ray Conference*, *International Cosmic Ray Conference*, vol. 3, p. 91.

Cooke, D. J., J. E. Humble, M. A. Shea, D. F. Smart, and N. Lund (1991), On cosmic-ray cut-off terminology, *Nuovo Cimento C Geophysics Space Physics C*, *14*, 213–234.

Copeland, K., H. H. Sauer, F. E. Duke, and W. Friedberg (2008), Cosmic radiation exposure of aircraft occupants on simulated high-latitude flights during solar proton events from 1 January 1986 through 1 January 2008, *Advances in Space Research*, *42*, 1008–1029, doi:10.1016/j.asr.2008.03.001.

Cramp, J. L., M. L. Duldig, E. O. Flückiger, J. E. Humble, M. A. Shea, and D. F. Smart (1997a), The October 22, 1989, solar cosmic ray enhancement: An analysis of the anisotropy and spectral characteristics, *Journal of Geophysical Research*, *102*, 24,237–24,248, doi:10.1029/97JA01947.

Cramp, J. L., M. L. Duldig, and J. E. Humble (1997b), The effect of a distorted interplanetary magnetic field configuration on the December 7-8, 1982, ground level enhancement, *Journal of Geophysical Research*, *102*, 4919–4926, doi: 10.1029/96JA03698.

Cucinotta, A. F., H. Wu, M. R. Shavers, and K. George (2003), Radiation dosimetry and biophysical models of space radiation effects, *Graviational and Space Biology*, *16*(2), 11–18.

Debrunner, H., et al. (1997), Energetic neutrons, protons, and gamma rays during the 1990 May 24 solar cosmic-ray event, *Astrophysical Journal*, *479*, 997, doi: 10.1086/303895.

Delaboudinière, J.-P., et al. (1995), EIT: Extreme-Ultraviolet Imaging Telescope for the SOHO mission, *Solar Physics*, *162*, 291–312, doi: 10.1007/BF00733432.

Desorgher, L. (2006), The planetocosmics code, *Tech. rep.*, http://cosray.unibe.ch/∼laurent/planetocosmics.

Diggory, I. S., J. R. Hook, I. A. Jenkins, and K. E. Turver (1974), The momentum spectra of nuclear active particles in the cosmic radiation at sea level. I. Experimental data , *Journal of Physics A Mathematical General*, *7*, 741–764.

Duggal, S. P. (1979), Relativistic solar cosmic rays, *Reviews of Geophysics and Space Physics*, *17*, 1021–1058.

DuVernois, M. A., et al. (2001), Cosmic-ray electrons and positrons from 1 to 100 gev: Measurements with heat and their interpretation, *The Astrophysical Journal*, *559*(1), 296–303.

Edward, B., S. J. Berry, and V. F. Hess (1942), Study of cosmic rays between New York and Chile, *Journal of Geophysical Research*, *47*, 251–256, doi: 10.1029/TE047i003p00251.

Ellison, D. C., and R. Ramaty (1985), Shock acceleration of electrons and ions in solar flares, *Astrophysical Journal*, *298*, 400–408, doi:10.1086/163623.

Eyles, C. J., A. D. Linney, and G. K. Rochester (1972), A measurement of the atmospheric neutron flux in the energy range 50< $E$ <350 MeV, *Planet. Space Sci.*, *20*, 1915, doi:10.1016/0032-0633(72)90124-9.

Ferrari, A., P. R. Sala, R. Guaraldi, and F. Padoani (1992), An improved multiple scattering model for charged particle transport, *Nuclear Instruments and Methods in Physics Research B*, *71*, 412–426, doi:10.1016/0168-583X(92)95359-Y.

Ferrari, A., M. Pelliccioni, and M. Pillon (1996), Fluence to Effective Dose and Effective Dose Equivalent Conversion Coefficients for Photons from 50 keV to 10 GeV, *Radiation Protection Dosimetry*, *67*(4), 245–251.

Ferrari, A., M. Pelliccioni, and M. Pillon (1997a), Fluence to effective dose and effective dose equivalent conversion coefficients for electrons from 5 MeV to 10 GeV, *Radiation Protection Dosimetry*, *69*(2), 97–104.

Ferrari, A., M. Pelliccioni, and M. Pillon (1997b), Fluence to Effective Dose Conversion Coefficients for Protons from 5 MeV to 10 TeV, *Radiation Protection Dosimetry*, *71*(2), 85–91.

Ferrari, A., M. Pelliccioni, and M. Pillon (1997c), Fluence to Effective Dose Conversion Coefficients for Neutrons up to 10 TeV, *Radiation Protection Dosimetry*, *71*(3), 165–173.

Ferrari, A., M. Pelliccioni, and M. Pillon (1997d), Fluence-to-Effective Dose Conversion Coefficients for Muons, *Radiation Protection Dosimetry*, *74*(4), 227–233.

Ferrari, A., M. Pelliccioni, and M. Pillon (1998), Fluence to Effective Dose Conversion Coefficients for Negatively and Positively Charged Pions, *Radiation Protection Dosimetry*, *80*(4), 361–370.

Ferrari, A., P. R. Sala, A. Fasso, and J. Ranft (2005), *FLUKA: A multi-particle transport code (program version 2005)*, CERN, Geneva.

Fichtner, H., A. Czechowski, H. J. Fahr, and G. Lay (2000), Energetic particles beyond the heliospheric shock: Anomalous Cosmic Rays (ACRs), Pick-up Ions (PUIs) and the Associated Energetic Neutral Atoms (ENAs), in *AIP Conf. Proc. 528: Acceleration and Transport of Energetic Particles Observed in the Heliosphere*, p. 345.

Forbush, S. E. (1946), Three unusual cosmic-ray increases possibly due to charged particles from the sun, *Physical Review*, *70*, 771–772, doi: 10.1103/PhysRev.70.771.

Francke, T. (1999), A new measurement of the atmospheric proton and muon fluxes, in *International Cosmic Ray Conference*, *International Cosmic Ray Conference*, vol. 2, p. 80.

Friedberg, W. (2007), private communication.

Garcia-Munoz, M., G. M. Mason, and J. A. Simpson (1975), The anomalous He-4 component in the cosmic-ray spectrum at below approximately 50 MeV per nucleon during 1972-1974, *Astrophysical Journal*, *202*, 265–275.

Gleeson, L. J., and W. I. Axford (1968), Solar modulation of galactic cosmic rays, *Astrophysical Journal*, *154*, 1011.

Goldhagen, P., J. M. Clem, and J. W. Wilson (2004), The energy spectrum of cosmic ray-induced neutrons measured on an airplane over a wide range of altitude and latitude, *Rad. Prot. Dosim.*, *110*, 387–392.

Grechnev, V. V., et al. (2008), An extreme solar event of 20 January 2005: Properties of the flare and the origin of energetic particles, *Solar Physics*, *252*, 149–177, doi:10.1007/s11207-008-9245-1.

Haino, S., et al. (2004), Measurements of primary and atmospheric cosmic-ray spectra with the BESS-TeV spectrometer, *Physics Letters B*, *594*, 35–46, doi: 10.1016/j.physletb.2004.05.019.

Hapgood, M. A. (1992), Space physics coordinate transformations - A user guide, *Planet. Space Sci.*, *40*, 711–717, doi:10.1016/0032-0633(92)90012-D.

Hapgood, M. A. (1997), Space Physics coordinate transformations: a user guide, *Planet. Space Sci.*, *45*, 1047.

Hatton, C. J. (1971), The Neutron Monitor, in *Progress in elementary particle and cosmic ray physics, Vol. X*, edited by J. G. Wilson and S. A. Wouthuysen, North-Holland Publishing Co., Amsterdam.

Herbst, K., A. Kopp, B. Heber, D. Matthiä, H. Fichtner, and K. Scherer (2009), On the interpretation of the solar modulation parameter, *submitted to Journal of Geophysical Research (Space Physics)*.

Hubiak, M. (2008), Experimentelle Bestimmung von Dosisraten auf Reiseflughöhen im solaren Minimum, Ph.D. thesis, Fachhochschule Münster - University of Applied Sciences.

Humble, J. E., M. L. Duldig, D. F. Smart, and M. A. Shea (1991), Detection of 0.5-15 GeV solar protons on 29 September 1989 at Australian stations, *Geophysical Research Letters*, *18*, 737–740, doi:10.1029/91GL00017.

ICRP (1990), *1990 Recommendations of the International Commision on Radiological Protection*, *Annals of the ICRP*, vol. 60, Pergamon Press.

ICRP (2007), *The 2007 Recommendations of the International Commision on Radiological Protection*, *Annals of the ICRP*, vol. 103, Elsevier.

ICRU (1980), Radiation quantities and units, *ICRU Report 33*, International Commision on Radiation and Measurements.

ICRU (1985), Determination of dose equivalents resulting from external radiation sources, *ICRU Report 39*, International Commision on Radiation and Measurements.

James, F. (1980), Monte Carlo theory and practice, *Reports on Progress in Physics*, *43*(9), 1145–1189.

James, F. (2000), Minuit - function minimization and error analysis - reference manual, http://wwwasdoc.web.cern.ch/wwwasdoc/minuit/minmain.html.

James, F., and M. Roos (1975), MINUIT: a system for function minimization and analysis of the parameter errors and corrections., *Comput. Phys. Commun.*, *10*(CERN-DD-75-20), 343–367.

Koi, T., M. Asai, D. H. Wright, K. Niita, Y. Nara, K. Amako, and T. Sasaki (2003), Interfacing the JQMD and JAM nuclear reaction codes to Geant4, *SLAC-PUB 9978*, SLAC.

Kota, J., and J. R. Jokipii (1991), The role of corotating interaction regions in cosmic-ray modulation, *Geophysical Research Letters*, *18*, 1797–1800, doi: 10.1029/91GL02307.

Kremer, J., et al. (1999), Measurements of ground-level muons at two geomagnetic locations, *Physical Review Letters*, *83*, 4241–4244.

Krieger, H. (2002), *Strahlenphysik, Dosimetrie und Strahlenschutz, Band 1, Grundlagen*, Teubner, ISBN 3-519-43052-5.

Lange, I., and S. E. Forbush (1942), Further note on the effect on cosmic-ray intensity of the magnetic storm of March 1, 1942, *Journal of Geophysical Research*, *47*, 331–334, doi:10.1029/TE047i004p00331.

le Roux, J. A., and M. S. Potgieter (1991), The simulation of Forbush decreases with time-dependent cosmic-ray modulation models of varying complexity, *Astronomy & Astrophysics*, *243*, 531–545.

Leo, W. (1994), *Techniques for Nuclear and Particle Physics Experiments*, Springer, ISBN 3-540-57280-5.

Leske, R. A., R. A. Mewaldt, E. C. Stone, and T. T. von Rosenvinge (2001), Observations of geomagnetic cutoff variations during solar energetic particle events and implications for the radiation environment at the Space Station, *Journal of Geophysical Research*, *106*, 30,011–30,022, doi: 10.1029/2000JA000212.

Lovell, J. L., M. L. Duldig, and J. E. Humble (1998), An extended analysis of the September 1989 cosmic ray ground level enhancement, *Journal of Geophysical Research*, *103*, 23,733–23,742, doi:10.1029/98JA02100.

MacMillan, S., and S. Maus (2005), International Geomagnetic Reference Field - the tenth generation, *Earth, Planets, and Space*, *57*, 1135–1140.

Mason, G. M., G. Gloeckler, and D. Hovestadt (1984), Temporal variations of nucleonic abundances in solar flare energetic particle events. II - Evidence for large-scale shock acceleration, *Astrophysical Journal*, *280*, 902–916, doi: 10.1086/162066.

Matthiä, D., L. Sihver, and M. Meier (2008), Monte-Carlo calculations of particle fluences and neutron effective dose rates in the atmosphere, *Radiation Protection Dosimetry*, *131*(2), 222–228, doi:10.1093/rpd/ncn130.

Matthiä, D., B. Heber, G. Reitz, M. Meier, L. Sihver, and T. Berger (2009a), The ground level event 70 on December 13th, 2006 and related effective doses at aviation altitudes, *submitted to Radiation Protection Dosimetry*.

Matthiä, D., B. Heber, G. Reitz, M. Meier, L. Sihver, T. Berger, and K. Herbst (2009b), Temporal and spatial evolution of the solar energetic particle event on January 20th, 2005 and resulting radiation doses in aviation, *Journal of Geophysical Research*, doi:10.1029/2009JA014125, in press.

Maus, S., et al. (2005), The 10th-Generation International Geomagnetic Reference Field, *Geophysical Journal International*, *161*, 561–565, doi: 10.1111/j.1365-246X.2005.02641.x.

McComas, D. J., S. J. Bame, P. Barker, W. C. Feldman, J. L. Phillips, P. Riley, and J. W. Griffee (1998), Solar Wind Electron Proton Alpha Monitor (SWEPAM) for the Advanced Composition Explorer, *Space Science Reviews*, *86*, 563–612, doi:10.1023/A:1005040232597.

McCracken, K. G., H. Moraal, and P. H. Stoker (2008), Investigation of the multiple-component structure of the 20 January 2005 cosmic ray ground level enhancement, *Journal of Geophysical Research (Space Physics)*, *113*(A12), 12,101, doi:10.1029/2007JA012829.

Meier, M. M., J. U. Schott, K. Strauch, and K. O. Groeneveld (1998), Detection of $\delta$-electron events in charge coupled devices: a fingerprint of single swift heavy ions, *Nuclear Instruments and Methods in Physics Research B*, *146*, 601–606.

Meier, M. M., M. Hubiak, D. Matthiä, M. Wirtz, and G. Reitz (2009), Dosimetry at aviation altitudes (2006-2008), *submitted to Radiation Protection Dosimetry*.

Mewaldt, R. A. (2006), Solar energetic particle composition, energy spectra, and space weather, *Space Science Reviews*, *124*, 303–316, doi:10.1007/s11214-006-9091-0.

Mikić, Z., and M. A. Lee (2006), An introduction to theory and models of CMEs, shocks, and solar energetic particles, *Space Science Reviews*, *123*, 57–80, doi: 10.1007/s11214-006-9012-2.

Moraal, H., M. S. Potgieter, P. H. Stoker, and A. J. van der Walt (1989), Neutron monitor latitude survey of cosmic ray intensity during the 1986/1987 solar minimum, *Journal of Geophysical Research*, *94*, 1459–1464, doi: 10.1029/JA094iA02p01459.

Müller-Mellin, R., et al. (1995), COSTEP - Comprehensive Suprathermal and Energetic Particle Analyser, *Solar Physics*, *162*, 483–504.

Murdin, P. (Ed.) (2001a), *Encyclopedia of Astronomy and Astrophysics*, chap. Solar Flare Classification, IoP, ISBN 0333750888.

Murdin, P. (Ed.) (2001b), *Encyclopedia of Astronomy and Astrophysics*, chap. Magnetosphere of Earth, IoP, ISBN 0333750888.

Nara, Y., N. Otuka, A. Ohnishi, K. Niita, and S. Chiba (1999), Relativistic nuclear collisions at 1 AGeV energies from p+Be to Au+Au with the hadronic cascade model, *Phys. Rev. C*, *61*(2), 024,901, doi: 10.1103/PhysRevC.61.024901.

Nelson, W. R., H. Hirayama, and D. W. Rogers (1985), The egs4 code system, *SLAC-PUB 265*, Stanford Linear Accelerator Centre.

Niita, K., S. Chiba, T. Maruyama, T. Maruyama, H. Takada, T. Fukahori, Y. Nakahara, and A. Iwamoto (1995), Analysis of the (N,xN') reactions by quantum molecular dynamics plus statistical decay model, *Physical Review C*, *52*, 2620–2635, doi:10.1103/PhysRevC.52.2620.

Nymmik, R. A., M. I. Panasyuk, T. I. Pervaja, and A. A. Suslov (1992), A model of galactic cosmic ray fluxes, *International Journal of Radiation Applications and Instrumentation. Part D. Nuclear Tracks and Radiation Measurements*, *20*(3), 427 – 429, doi:DOI: 10.1016/1359-0189(92)90028-T.

O'Neill, P. M. (2006), Badhwar O'Neill galactic cosmic ray model update based on advanced composition explorer (ACE) energy spectra from 1997 to present, *Advances in Space Research*, *37*, 1727–1733, doi:10.1016/j.asr.2005.02.001.

Parker, E. N. (1958), Dynamics of the interplanetary gas and magnetic fields., *Astrophysical Journal*, *128*, 664.

Parker, E. N. (1963), *Interplanetary dynamical processes.*, New York, Interscience Publishers, ISBN 978-0470659168.

Parker, E. N. (1965), The passage of energetic charged particles through interplanetary space, *Planet. Space Sci.*, *13*, 9–49.

Picone, J. M., A. E. Hedin, D. P. Drob, and A. C. Aikin (2002), NRLMSISE-00 empirical model of the atmosphere: Statistical comparisons and scientific issues, *Journal of Geophysical Research (Space Physics)*, *107*, 1468, doi: 10.1029/2002JA009430.

Plainaki, C., A. Belov, E. Eroshenko, H. Mavromichalaki, and V. Yanke (2007), Modeling ground level enhancements: Event of 20 January 2005, *Journal of Geophysical Research (Space Physics)*, *112*(11), 4102, doi: 10.1029/2006JA011926.

Poirier, J., and C. D'Andrea (2002), Ground level muons in coincidence with the solar flare of 15 April 2001, *Journal of Geophysical Research (Space Physics)*, *107*, 1376, doi:10.1029/2001JA009187.

Potgieter, M. S. (1995), The Time-Dependent Transport of Cosmic Rays in the Heliosphere, *Astronomy & Astrophysics Supplements*, *230*, 393–403.

Raubenheimer, B. C., and P. H. Stoker (1974), Various aspects of the attenuation coefficient of a neutron monitor, *Journal of Geophysical Research*, *79*, 5069–5076, doi:10.1029/JA079i034p05069.

Reames, D. V. (1998), Solar energetic particles: Sampling coronal abundances, *Space Science Reviews*, *85*, 327–340, doi:10.1023/A:1005123121972.

Reitz, G. (1993), Radiation Environment in the Stratosphere, *Radiation Protection Dosimetry*, *48*(1), 5–20.

Sanuki, T., et al. (2000), Precise measurement of cosmic-ray proton and helium spectra with the BESS spectrometer, *Astrophysical Journal*, *545*, 1135–1142, doi:10.1086/317873.

Sanuki, T., et al. (2003), Measurement of cosmic-ray proton and antiproton spectra at mountain altitude, *Physics Letters B*, *577*, 10–17, doi:10.1016/S0370-2693(03)01569-7.

Sato, T., K. Niita, A. Endo, and L. Sihver (2008), Development of PARMA: PHITS-based analytical radiation model in the atmosphere, *Radiation Research*, *170*, 244–259.

Shea, M. A., and D. F. Smart (1982), Possible evidence for a rigidity-dependent release of relativistic protons from the solar corona, *Space Science Reviews*, *32*, 251–271, doi:10.1007/BF00225188.

Shea, M. A., and D. F. Smart (1990), A summary of major solar proton events, *Solar Physics*, *127*, 297–320.

Shea, M. A., D. F. Smart, and K. R. Pyle (1991), Direct solar neutrons detected by neutron monitors on 24 May 1990, *Geophysical Research Letters*, *18*, 1655–1658, doi:10.1029/91GL02001.

Shibata, K., T. Kawano, T. Nakagawa, O. Iwamoto, J. ichi Katkura, T. Fukahori, and S. Chiba (2002), Japanese evaluated nuclear data library version 3 revision-3: Jendl-3.3, *Journal of Nuclear Science and Technology*, *39*(11), 1125–1136.

Sihver, L., D. Matthiä, T. Koi, and D. Mancusi (2008), Dose calculations at high altitudes and in deep space with GEANT4 using BIC and JQMD models for nucleus-nucleus reactions, *New Journal of Physics*, *10*(10), 105,019, doi:10.1088/1367-2630/10/10/105019.

Simnett, G. M. (2006), The electron energy spectrum from large solar flares, *Solar Physics*, *237*, 383–395, doi:10.1007/s11207-006-0002-z.

Simpson, J. (1983), Elemental and isotopic composition of the galactic cosmic rays, *Annu. Rev. Nucl. Part. Sci.*, *33*, 323–381.

Simpson, J. A. (2000), The cosmic ray nucleonic component: The invention and scientific uses of the neutron monitor - (keynote lecture), *Space Science Reviews*, *93*, 11–32.

Sjöstrand, T., S. Mrenna, and P. Skands (2006), PYTHIA 6.4 physics and manual, *Journal of High Energy Physics*, *5*, 26, doi:10.1088/1126-6708/2006/05/026.

Smart, D. F., M. A. Shea, and P. J. Tanskanen (1971), A determination of the spectra, spatial anisotropy, and propagation characteristics of the relativistic solar cosmic-ray flux on november 18, 1968, in *International Cosmic Ray Conference*, *International Cosmic Ray Conference*, vol. 2, p. 483.

Smart, D. F., M. A. Shea, and E. O. Flückiger (2000), Magnetospheric models and trajectory computations, *Space Science Reviews*, *93*, 305–333.

Smart, D. F., M. A. Shea, A. J. Tylka, and P. R. Boberg (2006), A geomagnetic cutoff rigidity interpolation tool: Accuracy verification and application to space weather, *Advances in Space Research*, *37*, 1206–1217, doi:10.1016/j.asr.2006.02.011.

Smith, C. W., J. L'Heureux, N. F. Ness, M. H. Acuña, L. F. Burlaga, and J. Scheifele (1998), The ACE magnetic fields experiment, *Space Science Reviews*, *86*, 613–632, doi:10.1023/A:1005092216668.

Stone, E. C., et al. (1998), The Cosmic-Ray Isotope Spectrometer for the Advanced Composition Explorer, *Space Science Reviews*, *86*, 285–356, doi:10.1023/A:1005075813033.

Störmer, C. (1930), Periodische Elektronenbahnen im Felde eines Elementarmagneten und ihre Anwendung auf Brüches Modellversuche und auf Eschenhagens Elementarwellen des Erdmagnetismus. Mit 32 Abbildungen., *Zeitschrift fur Astrophysik*, *1*, 237.

Swinson, D. B., and M. A. Shea (1990), The September 29, 1989 ground-level event observed at high rigidity, *Geophysical Research Letters*, *17*, 1073–1075, doi:10.1029/GL017i008p01073.

Tsyganenko, N. A. (1989), A magnetospheric magnetic field model with a warped tail current sheet, *Planet. Space Sci.*, *37*, 5–20, doi:10.1016/0032-0633(89)90066-4.

Tsyganenko, N. A. (1995), Modeling the Earth's magnetospheric magnetic field confined within a realistic magnetopause, *Journal of Geophysical Research*, *100*, 5599–5612.

Tsyganenko, N. A. (2002), A model of the near magnetosphere with a dawn-dusk asymmetry 2. Parameterization and fitting to observations, *Journal of Geophysical Research (Space Physics)*, *107*(A8), 10–1, doi:10.1029/2001JA000220.

Tylka, A. J., et al. (1997), CREME96: A revision of the Cosmic Ray Effects on Micro-Electronics code, *IEEE Transactions on Nuclear Science*, *44*, 2150–2160, doi:10.1109/23.659030.

Usoskin, I. G., K. Alanko-Huotari, G. A. Kovaltsov, and K. Mursula (2005), Heliospheric modulation of cosmic rays: Monthly reconstruction for 1951-2004, *Journal of Geophysical Research (Space Physics)*, *110*, 12,108, doi: 10.1029/2005JA011250.

Vashenyuk, E. V., Y. V. Balabin, and P. H. Stoker (2007), Responses to solar cosmic rays of neutron monitors of a various design, *Advances in Space Research*, *40*, 331–337, doi:10.1016/j.asr.2007.05.018.

Villoresi, G., L. I. Dorman, N. Iucci, and N. G. Ptitsyna (2000), Cosmic ray survey to Antarctica and coupling functions for neutron component near solar minimum (1996-1997) 1. Methodology and data quality assurance, *Journal of Geophysical Research*, *105*, 21,025–21,034, doi:10.1029/2000JA900048.

Wiedenbeck, M. E., et al. (2001), The origin of primary cosmic rays: Constraints from ACE elemental and isotopic composition observations, *Space Science Reviews*, *99*, 15–26.

Zhizhin, M., E. Kihn, R. Redmon, D. Medvedev, and D. Mishin (2008), Space Physics Interactive Data Resource - SPIDR, *Earth Science Informatics*, *1*(2), 79–91.

# Appendix A

# List of Neutron Monitor Stations

A list of Neutron Monitor stations with corresponding geographic position, altitude $h$, standard pressure $p_0$, cut-off rigidity $R_c$ and detector type provided by IZMIRAN[1].

| | | Lat. | Long. | $h$ [m] | $p_0$ [mbar] | $R_c$ [GV] | Detector | Name |
|---|---|---|---|---|---|---|---|---|
| 1 | AATA | 43.25 | 76.92 | 806 | 938 | 6.66 | 6NM64 | ALMA-ATA A |
| 2 | AATB | 43.14 | 76.60 | 3340 | 675 | 6.69 | 18NM64 | ALMA-ATA B |
| 3 | AATC | 43.18 | 76.92 | 1670 | 920 | 6.67 | 6NM64 | ALMA-ATA C |
| 4 | AATH | 43.14 | 76.60 | 3340 | 675 | 6.69 | 6NM64H | ALMA-ATA Helios |
| 5 | AHMD | 23.01 | 72.61 | 50 | 1000 | 15.94 | 18NM64 | AHMEDABAD |
| 6 | ALGR | 27.90 | 78.10 | 300 | 1000 | 14.67 | 12IGY | ALIGARCH |
| 7 | ALRT | 82.50 | -62.33 | 57 | 1003 | 0.10 | 18NM64 | ALERT |
| 8 | ALBQ | 35.08 | -106.62 | 1567 | 910 | 4.47 | 12IGY | ALBUQUERQUE |
| 9 | APTY | 67.55 | 33.33 | 177 | 1000 | 0.65 | 18NM64 | APATITY |
| 10 | ATHN | 37.97 | 23.72 | 40 | 1000 | 8.72 | 3NM64 | ATHENS |
| 11 | BERK | 37.87 | -122.27 | 70 | 1024 | 4.54 | 12IGY | BERKELEY |
| 12 | BGNR | 43.00 | 0.00 | 550 | 1000 | 5.00 | 3NM64 | BAGNERES |
| 13 | BJNG | 40.04 | 116.19 | 48 | 1000 | 9.56 | 18NM64 | BEIJING |
| 14 | BRSB | -27.50 | 152.92 | 0 | 1010 | 7.21 | 12IGY | BRISBANE |
| 15 | BRUT | 33.90 | 35.47 | 15 | 1013 | 10.42 | 12IGY | BEIRUT |
| 16 | BUEN | -34.60 | -58.50 | 0 | 1000 | 10.63 | 18IGY | BUENOS AIRES |
| 17 | CALG | 51.08 | -114.13 | 1128 | 883 | 1.08 | 12NM64 | CALGARY |
| 18 | CAPS | 68.92 | -179.47 | 0 | 1016 | 0.45 | 12NM64 | CAPE SHMIDT |
| 19 | CASY | -66.28 | 110.53 | 0 | 1000 | 0.01 | 12IGY | CASEY |
| 20 | CDBA | -31.42 | -64.20 | 434 | 982 | 11.45 | 12IGY | CORDOBA |
| 21 | CHCL | -16.32 | -68.15 | 5200 | 552 | 13.10 | 12NM64 | CHACALTAYA |
| 22 | CHGO | 41.83 | -87.67 | 200 | 1000 | 1.72 | 12IGY | CHICAGO |
| 23 | CHUR | 58.75 | -94.08 | 39 | 1000 | 0.21 | 18NM64 | CHURCHILL |
| 24 | CLMX | 39.37 | -106.18 | 3400 | 685 | 3.03 | 12IGY | CLIMAX |
| 25 | COLL | 64.08 | -147.83 | 91 | 1013 | 0.54 | 12IGY | COLLEGE |
| 26 | DALS | 32.98 | -96.73 | 208 | 1017 | 4.35 | 18NM64 | DALLAS |
| 27 | DENV | 39.67 | -104.97 | 1600 | 850 | 2.91 | 12IGY | DENVER |
| 28 | DPRV | 46.10 | -77.50 | 145 | 996 | 1.02 | 48NM64 | DEEP RIVER |
| 29 | DRBS | 50.10 | 4.60 | 225 | 987 | 3.24 | 6NM64 | DOURBES |
| 30 | DRHM | 43.10 | -71.00 | 0 | 1000 | 1.41 | 18NM64 | DURHAM |
| 31 | DRWN | -12.43 | 130.87 | 0 | 1000 | 14.19 | 6NM64 | DARWIN |
| 32 | ELSW | -78.00 | -41.00 | 0 | 1000 | 0.79 | 12IGY | ELLSWORTH |
| 33 | ERVN | 40.50 | 44.17 | 2000 | 800 | 7.60 | 18NM64 | EREVAN |
| 34 | ERV3 | 40.50 | 44.17 | 3200 | 700 | 7.60 | 18NM64 | EREVAN3 |
| 35 | ESOI | 33.30 | 35.78 | 2025 | 800 | 10.00 | 6NM64 | TEL AVIV |
| 36 | FSMT | 60.00 | -112.00 | 0 | 1000 | 0.30 | 18NM64 | Fort SMITH |
| 37 | FRBG | 48.00 | 7.80 | 0 | 1000 | 3.41 | 12IGY | FREIBURG |
| 38 | FUSH | 37.68 | 140.45 | 66 | 1000 | 10.55 | 6NM64 | FUKUSHIMA |
| 39 | GFSY | 48.70 | 2.10 | 0 | 1000 | 3.50 | 6NM64 | GIV-SUR-IVETTE |
| 40 | GOTT | 51.52 | 9.93 | 273 | 1000 | 3.00 | 12IGY | GOTTINGEN |

[1] ftp://cr0.izmiran.rssi.ru/COSRAY!/

| | | | | | | | | |
|---|---|---|---|---|---|---|---|---|
| 41 | GSBY | 53.27 | -60.40 | 46 | 1011 | 0.52 | 18NM64 | GOOSE BAY |
| 42 | GLMG | 34.10 | 74.40 | 2743 | 800 | 11.58 | 12IGY | GOULMARG |
| 43 | HAIF | 38.80 | 35.00 | 2300 | 840 | 10.75 | 12IGY | HAIFA |
| 44 | HALL | 51.48 | 11.97 | 100 | 1000 | 3.07 | 12IGY | HALLE |
| 45 | HBRT | -42.92 | 147.24 | 0 | 1000 | 1.88 | 9NM64 | HOBART |
| 46 | HEIS | 80.60 | 58.00 | 20 | 1000 | 0.10 | 12IGY | HEISS ISLAND |
| 47 | HFLK | 47.31 | 11.38 | 2290 | 830 | 4.37 | 3NM64 | HAFELEKAR |
| 48 | HLE1 | 20.72 | -156.27 | 3052 | 724 | 13.30 | 12IGY | HALEAKALA1 |
| 49 | HLEA | 20.72 | -156.27 | 3052 | 724 | 13.30 | 6NM64 | HALEAKALA |
| 50 | HRMS | -34.42 | 19.22 | 26 | 1013 | 4.90 | 12NM64 | HERMANUS |
| 51 | HRST | 50.87 | 0.33 | 23 | 1000 | 2.93 | 12IGY | HERSTMONCEUX |
| 52 | HUAN | -12.03 | -75.33 | 3400 | 704 | 13.45 | 12IGY | HUANCAYO |
| 53 | INVK | 68.35 | -133.72 | 21 | 1011 | 0.18 | 18NM64 | INUVIK |
| 54 | INVC | -46.50 | 168.37 | 0 | 1000 | 1.86 | 12IGY | INVERCARGILL |
| 55 | IRK2 | 52.37 | 100.55 | 2000 | 800 | 3.66 | 12NM64 | IRKUTSK2 |
| 56 | IRK3 | 51.29 | 100.55 | 3000 | 715 | 3.66 | 6NM64 | IRKUTSK3 |
| 57 | IRKT | 52.47 | 104.03 | 433 | 965 | 3.66 | 18NM64 | IRKUTSK |
| 58 | JUN1 | 46.55 | 7.98 | 3550 | 643 | 4.48 | 12IGY | JUNGFRAUJOCH1 |
| 59 | JUNG | 46.55 | 7.98 | 3550 | 643 | 4.48 | 3NM64 | JUNGFRAUJOCH |
| 60 | KAMP | 0.33 | 32.55 | 1196 | 900 | 14.98 | 12IGY | KAMPALA |
| 61 | KERG | -49.35 | 70.25 | 0 | 1000 | 1.19 | 18NM64 | KERGUELEN |
| 62 | KHAB | 48.50 | 135.20 | 0 | 1003 | 5.54 | 18NM64 | KHABAROVSK |
| 63 | KIEL | 54.30 | 10.10 | 54 | 1007 | 2.29 | 18NM64 | KIEL |
| 64 | KIEV | 50.72 | 30.30 | 120 | 1000 | 3.62 | 18NM64 | KIEV |
| 65 | KLNG | 54.12 | 11.77 | 70 | 1000 | 2.43 | 12IGY | KUHLUNGSBORN |
| 66 | KODI | 10.23 | 77.48 | 2343 | 786 | 17.47 | 12IGY | KODAIKANAL |
| 67 | KRNA | 67.83 | 20.43 | 400 | 979 | 0.54 | 12NM64 | KIRUNA |
| 68 | KULA | 20.73 | -156.33 | 915 | 933 | 13.30 | 3NM64 | KULA |
| 69 | LAES | -6.73 | 147.00 | 0 | 1000 | 15.52 | 12IGY | LAE STATION |
| 70 | LARC | -62.20 | -58.96 | 40 | 980 | 3.00 | 6NM64 | LARC |
| 71 | LDVL | 40.00 | -105.00 | 3094 | 700 | 3.03 | 6NM64 | LEADVILLE |
| 72 | LEED | 53.80 | -1.50 | 72 | 1008 | 2.20 | 18NM64 | LEEDS |
| 73 | LINC | 40.82 | -96.68 | 350 | 994 | 2.22 | 12IGY | LINCOLN |
| 74 | LMKS | 49.11 | 20.13 | 2634 | 733 | 4.00 | 8NM64 | LOMNICKY STIT |
| 75 | LNDH | 51.60 | 10.10 | 140 | 1000 | 3.00 | 18NM64 | LINDAU |
| 76 | LNDN | 51.53 | -0.10 | 45 | 1000 | 2.73 | 12IGY | LONDON |
| 77 | LCRS | -33.45 | -70.60 | 540 | 990 | 11.00 | 6NM64 | LOS Cerrillos |
| 78 | MCMD | -77.95 | 166.60 | 48 | 992 | 0.01 | 18NM64 | MCMURDO |
| 79 | MGDN | 60.10 | 151.00 | 0 | 982 | 2.10 | 18NM64 | MAGADAN |
| 80 | MINA | -23.10 | -65.70 | 4000 | 646 | 12.51 | 12IGY | MINA AGUILA |
| 81 | MKPU | 21.30 | -157.65 | 100 | 1000 | 13.23 | 12IGY | MAKAPUU POINT |
| 82 | MNCH | 48.20 | 11.60 | 500 | 972 | 4.14 | 12IGY | MUNCHEN |
| 83 | MOSC | 55.47 | 37.32 | 200 | 1000 | 2.46 | 24NM64 | MOSCOW |
| 84 | MOS5 | 55.47 | 37.32 | 200 | 1000 | 2.46 | 6NM64 | MOSCOW 5th Sect |
| 85 | MRCH | 80.05 | 18.25 | 0 | 1000 | 0.06 | 12IGY | MURCHISON BAY |
| 86 | MRKA | 39.70 | 141.13 | 135 | 1000 | 10.16 | 20NM64 | MORIOKA |
| 87 | MRNY | -66.92 | 93.00 | 30 | 1013 | 0.04 | 12NM64 | MIRNY |
| 88 | MTNR | 36.12 | 137.55 | 2770 | 720 | 11.39 | 12NM64 | Mt. NORIKURA |
| 89 | MTWL | 42.92 | 147.23 | 725 | 946 | 1.89 | 6NM64 | Mt. WELLINGTON |
| 90 | MTWS | 44.28 | -71.30 | 1900 | 822 | 1.24 | 12IGY | Mt. WASHINGTON |
| 91 | MURM | 67.55 | 33.33 | 0 | 1000 | 0.65 | 12IGY | MURMANSK |
| 92 | MWSN | -67.60 | 62.88 | 0 | 1010 | 0.22 | 6NM64 | MAWSON |
| 93 | MXCO | 19.33 | -99.18 | 2274 | 794 | 9.53 | 6NM64 | MEXICO CITY |
| 94 | NAIN | 56.60 | -61.70 | 0 | 1000 | 0.40 | 18NM64 | NAIN |
| 95 | NDRH | 52.20 | 5.20 | 0 | 1000 | 2.76 | 12IGY | NEDERHORST |
| 96 | NLCH | 43.30 | 43.25 | 550 | 960 | 7.70 | 6NM64 | NALCHIK |
| 97 | NLC2 | 43.30 | 43.25 | 1850 | 820 | 7.70 | 6NM64 | NALCHIK2 |
| 98 | NLC3 | 43.30 | 43.25 | 3150 | 700 | 7.70 | 6NM64 | NALCHIK3 |
| 99 | NRLK | 69.26 | 88.05 | 0 | 1005 | 0.63 | 18NM64 | NORILSK |
| 100 | NTHF | 44.47 | -93.25 | 287 | 1013 | 1.43 | 12IGY | NORTHFIELD |
| 101 | NVBK | 54.80 | 83.00 | 163 | 1000 | 2.91 | 24NM64 | NOVOSIBIRSK |
| 102 | NWRK | 39.70 | -75.70 | 50 | 1013 | 1.97 | 9NM64 | NEWARK |
| 103 | OTWA | 45.40 | -75.60 | 101 | 1008 | 1.08 | 12IGY | OTTAWA |
| 104 | OULU | 65.02 | 25.50 | 0 | 1000 | 0.81 | 9NM64 | OULU |

| | | | | | | | | |
|---|---|---|---|---|---|---|---|---|
| 105 | PICD | 42.93 | 0.25 | 2860 | 734 | 5.36 | 9NM64 | PIC-DU-MIDI |
| 106 | PTFM | -26.68 | 27.92 | 1351 | 869 | 7.30 | 12IGY | POTCHEFSTROM |
| 107 | PWNK | 55.00 | -85.00 | 0 | 1000 | 0.50 | 18NM64 | PEAWANUCK |
| 108 | PRAG | 50.10 | 14.40 | 215 | 1000 | 3.53 | 12IGY | PRAGUE |
| 109 | PRED | 47.70 | 12.90 | 1614 | 900 | 4.29 | 3NM64 | PREDIGTSTUHL |
| 110 | REWA | 24.32 | 81.17 | 100 | 1013 | 15.89 | 12IGY | REWA |
| 111 | RIOD | -22.95 | -43.17 | 0 | 1013 | 11.73 | 12IGY | RIO DE JANEIRO |
| 112 | ROME | 41.90 | 12.50 | 60 | 1009 | 6.32 | 17NM64 | ROME |
| 113 | RSLT | 74.68 | -94.90 | 17 | 1000 | 0.10 | 6NM64 | RESOLUTE BAY |
| 114 | SACR | 32.70 | 105.70 | 3000 | 800 | 4.98 | 12IGY | SACRAMENTO PEAK |
| 115 | SDNY | -33.89 | 151.19 | 43 | 1013 | 4.69 | 12IGY | SYDNEY |
| 116 | SEOL | 37.53 | 126.93 | 45 | 1005 | 10.79 | 6NM64 | SEOUL |
| 117 | SLMA | 51.20 | -115.60 | 2283 | 781 | 1.14 | 6NM64 | SULPHUR MT. |
| 118 | SMRD | 39.38 | 66.56 | 750 | 940 | 7.65 | 24NM64 | SAMARCAND |
| 119 | SNAE | -70.30 | -2.35 | 52 | 987 | 1.06 | 6NM64 | SANAE |
| 120 | SNA8 | -70.30 | -2.35 | 52 | 987 | 1.06 | 4NM80 | SANAE8 |
| 121 | SMFR | 44.70 | 34.00 | 570 | 1000 | 5.51 | 12IGY | SIMFEROPOL |
| 122 | SOPO | -90.00 | 0.00 | 2820 | 680 | 0.11 | 3NM64 | SOUTH POLE |
| 123 | SPBN | 77.80 | 15.40 | 0 | 1013 | 0.20 | 6NM64 | SPITZBERGEN |
| 124 | SVER | 56.80 | 60.63 | 300 | 997 | 2.30 | 18NM64 | SVERDLOVSK |
| 125 | SWTH | 39.90 | -75.35 | 80 | 1013 | 1.92 | 9NM64 | SWARTHMORE |
| 126 | SYWA | -69.00 | 39.60 | 15 | 1000 | 0.42 | 12IGY | SYOWA BASE |
| 127 | TASH | 41.33 | 69.62 | 565 | 963 | 8.34 | 18NM64 | TASHKENT |
| 128 | TBLS | 41.72 | 44.80 | 510 | 950 | 6.91 | 18NM64 | TBILISI |
| 129 | TERA | -66.67 | 140.02 | 45 | 1000 | 0.01 | 9NM64 | TERRE ADELIE |
| 130 | THUL | 76.60 | -68.80 | 260 | 1005 | 0.10 | 9NM64 | THULE |
| 131 | TIBT | 30.11 | 90.53 | 4300 | 606 | 14.10 | 28NM64 | TIBET |
| 132 | TKYO | 35.75 | 139.72 | 40 | 1014 | 11.61 | 18NM64 | TOKYO |
| 133 | TSMB | -19.20 | 17.60 | 1240 | 880 | 9.29 | 18NM64 | TSUMEB |
| 134 | TURK | 60.40 | 22.60 | 32 | 1000 | 1.36 | 6NM64 | TURKU |
| 135 | TXBY | 71.60 | 128.90 | 0 | 1000 | 0.53 | 18NM64 | TIXIE BAY |
| 136 | UPPS | 59.85 | 17.55 | 0 | 1013 | 1.43 | 12IGY | UPPSALA |
| 137 | USHU | -54.80 | -68.30 | 0 | 1020 | 5.68 | 12IGY | USHUAIA |
| 138 | UTRT | 52.10 | 5.12 | 0 | 1013 | 2.76 | 18NM64 | UTRECHT |
| 139 | VICT | 48.42 | -123.32 | 71 | 1000 | 1.86 | 18NM64 | VICTORIA |
| 140 | VSTK | -78.45 | 106.87 | 3488 | 632 | 0.10 | 6NM64 | VOSTOK |
| 141 | WEIS | 47.80 | 9.50 | 427 | 965 | 4.16 | 12IGY | WEISSENAU |
| 142 | WELL | 41.22 | 174.92 | 0 | 1013 | 3.42 | 12IGY | WELLINGTON |
| 143 | WLKS | -66.42 | 110.45 | 0 | 1010 | 0.01 | 12IGY | WILKES |
| 144 | YKTK | 62.02 | 129.72 | 105 | 1000 | 1.70 | 18NM64 | YAKUTSK |
| 145 | ZUGS | 47.42 | 10.98 | 2960 | 707 | 4.24 | 12IGY | ZUGSPITZE |

# Appendix B

# Exemplary PLANETOCOSMICS macro file

A macro file as it was used for the calculation of particle fluences in the atmosphere. The example shown here is for primary protons in the lowest energy interval from 100 MeV to 108 MeV:

```
/control/verbose 1

#
#Atmosphere definition
#

/PLANETOCOS/GEOMETRY/SetType Flat
/PLANETOCOS/GEOMETRY/SetConsiderAtmosphere true
/PLANETOCOS/GEOMETRY/SetPlanetCoreThickness 10 km
/PLANETOCOS/GEOMETRY/SetLayerLength 10000 km
/PLANETOCOS/GEOMETRY/SetAp 10
/PLANETOCOS/GEOMETRY/SetF107 100
/PLANETOCOS/GEOMETRY/SetF107A 100
/PLANETOCOS/GEOMETRY/SetMaxLayerThickness 5. km
/PLANETOCOS/GEOMETRY/SetMinLayerThickness .01 km
/PLANETOCOS/GEOMETRY/SetHeigthOfWorldAboveAtmosphere 10 km
/PLANETOCOS/GEOMETRY/SetAtmosphereTop 200 km
/PLANETOCOS/GEOMETRY/SetAtmosphereModel NRLMSISE00

/PLANETOCOS/GEOMETRY/SetGroundAltitude 0 km
/PLANETOCOS/GEOMETRY/verbose 1

#
#Physics
#

/PLANETOCOS/PHYSICS/SelectTypeOfHadronicPhysics QGSP_BERT_HP
/PLANETOCOS/PHYSICS/SelectTypeOfEMPhysics STANDARD
#Using the interface to JQMD/JAM implemented in PHITS
/PLANETOCOS/PHYSICS/SelectTypeOfIonHadronicPhysics PHITS


#
#Soil definition
#

/PLANETOCOS/SOIL/ResetLayers
/PLANETOCOS/SOIL/AddLayer 2 1 g/cm3 10 m
/PLANETOCOS/SOIL/AddElementToLayer Hydrogen 0.111894
/PLANETOCOS/SOIL/AddElementToLayer Oxygen 0.888106

#
#Detection levels definition
#

/PLANETOCOS/GEOMETRY/DetectorAtAltitude 0.001 km
/PLANETOCOS/GEOMETRY/DetectorAtAltitude 0.01 km
/PLANETOCOS/GEOMETRY/DetectorAtAltitude 0.05 km
/PLANETOCOS/GEOMETRY/DetectorAtAltitude 0.1 km
/PLANETOCOS/GEOMETRY/DetectorAtAltitude 0.3 km
/PLANETOCOS/GEOMETRY/DetectorAtAltitude 0.6 km
/PLANETOCOS/GEOMETRY/DetectorAtAltitude 1 km
/PLANETOCOS/GEOMETRY/DetectorAtAltitude 2 km
/PLANETOCOS/GEOMETRY/DetectorAtAltitude 3 km
/PLANETOCOS/GEOMETRY/DetectorAtAltitude 4 km
/PLANETOCOS/GEOMETRY/DetectorAtAltitude 5 km
/PLANETOCOS/GEOMETRY/DetectorAtAltitude 6 km
/PLANETOCOS/GEOMETRY/DetectorAtAltitude 7 km
/PLANETOCOS/GEOMETRY/DetectorAtAltitude 8 km
```

```
/PLANETOCOS/GEOMETRY/DetectorAtAltitude  9 km
/PLANETOCOS/GEOMETRY/DetectorAtAltitude  10 km
/PLANETOCOS/GEOMETRY/DetectorAtAltitude  11 km
/PLANETOCOS/GEOMETRY/DetectorAtAltitude  12 km
/PLANETOCOS/GEOMETRY/DetectorAtAltitude  13 km
/PLANETOCOS/GEOMETRY/DetectorAtAltitude  14 km
/PLANETOCOS/GEOMETRY/DetectorAtAltitude  15 km
/PLANETOCOS/GEOMETRY/DetectorAtAltitude  16 km
/PLANETOCOS/GEOMETRY/DetectorAtAltitude  17 km
/PLANETOCOS/GEOMETRY/DetectorAtAltitude  18 km
/PLANETOCOS/GEOMETRY/DetectorAtAltitude  19 km
/PLANETOCOS/GEOMETRY/DetectorAtAltitude  20 km
/PLANETOCOS/GEOMETRY/DetectorAtAltitude  30 km
/PLANETOCOS/GEOMETRY/DetectorAtAltitude  50 km
/PLANETOCOS/GEOMETRY/DetectorAtAltitude  70 km
/PLANETOCOS/GEOMETRY/DetectorAtAltitude  90 km
/PLANETOCOS/GEOMETRY/DetectorAtAltitude  99 km

#
#Initialisation
#

/PLANETOCOS/Initialise

#
#GEOMAGNETIC DIPOLE
#

/PLANETOCOS/BFIELD/SwitchOff

#
#Histograms definition
#

#
#Primaries
#

/PLANETOCOS/ANALYSIS/PRIMARY/FluxHisto proton  1  100 10 4000000 MeV log
/PLANETOCOS/ANALYSIS/PRIMARY/CosZenithHisto proton 2 100 0. 1.
/PLANETOCOS/ANALYSIS/PRIMARY/CosZenVsEnergyHisto proton 3 200 .0001 200 GeV log 100 0. 1.

#
#Downward and upward flux of particles
#

/PLANETOCOS/ANALYSIS/SECONDARY/SelectAllDetectors
/PLANETOCOS/ANALYSIS/SECONDARY/SetTypeOfWeight INVERSE_COSTH


/PLANETOCOS/ANALYSIS/SECONDARY/DownwardFluxHisto proton   1 200  1e-08 1000000 MeV log
/PLANETOCOS/ANALYSIS/SECONDARY/DownwardFluxHisto e-       1 200  1e-08 1000000 MeV log
/PLANETOCOS/ANALYSIS/SECONDARY/DownwardFluxHisto gamma    1 200  1e-08 1000000 MeV log
/PLANETOCOS/ANALYSIS/SECONDARY/DownwardFluxHisto neutron 1 200  1e-08 1000000 MeV log

/PLANETOCOS/ANALYSIS/SECONDARY/UpwardFluxHisto proton   2 200  1e-08 1000000 MeV log
/PLANETOCOS/ANALYSIS/SECONDARY/UpwardFluxHisto e-       2 200  1e-08 1000000 MeV log
/PLANETOCOS/ANALYSIS/SECONDARY/UpwardFluxHisto gamma    2 200  1e-08 1000000 MeV log
/PLANETOCOS/ANALYSIS/SECONDARY/UpwardFluxHisto neutron 2 200  1e-08 1000000 MeV log

/PLANETOCOS/ANALYSIS/SECONDARY/CosZenithHisto proton   3 200 -1. 1.
/PLANETOCOS/ANALYSIS/SECONDARY/CosZenithHisto e-       3 200 -1. 1.
/PLANETOCOS/ANALYSIS/SECONDARY/CosZenithHisto gamma    3 200 -1. 1.
/PLANETOCOS/ANALYSIS/SECONDARY/CosZenithHisto neutron 3 200 -1. 1.

/PLANETOCOS/ANALYSIS/SECONDARY/CosZenithVsEkinHisto proton   4 200  1e-08 1000000 MeV log  200 -1. 1.
/PLANETOCOS/ANALYSIS/SECONDARY/CosZenithVsEkinHisto alpha    4 200  1e-08 1000000 MeV log  200 -1. 1.
/PLANETOCOS/ANALYSIS/SECONDARY/CosZenithVsEkinHisto e-       4 200  1e-08 1000000 MeV log  200 -1. 1.
/PLANETOCOS/ANALYSIS/SECONDARY/CosZenithVsEkinHisto e+       4 200  1e-08 1000000 MeV log  200 -1. 1.
/PLANETOCOS/ANALYSIS/SECONDARY/CosZenithVsEkinHisto mu-      4 200  1e-08 1000000 MeV log  200 -1. 1.
/PLANETOCOS/ANALYSIS/SECONDARY/CosZenithVsEkinHisto mu+      4 200  1e-08 1000000 MeV log  200 -1. 1.
/PLANETOCOS/ANALYSIS/SECONDARY/CosZenithVsEkinHisto pi-      4 200  1e-08 1000000 MeV log  200 -1. 1.
/PLANETOCOS/ANALYSIS/SECONDARY/CosZenithVsEkinHisto pi+      4 200  1e-08 1000000 MeV log  200 -1. 1.
/PLANETOCOS/ANALYSIS/SECONDARY/CosZenithVsEkinHisto kaon-    4 200  1e-08 1000000 MeV log  200 -1. 1.
/PLANETOCOS/ANALYSIS/SECONDARY/CosZenithVsEkinHisto kaon+    4 200  1e-08 1000000 MeV log  200 -1. 1.
/PLANETOCOS/ANALYSIS/SECONDARY/CosZenithVsEkinHisto gamma    4 200  1e-08 1000000 MeV log  200 -1. 1.
/PLANETOCOS/ANALYSIS/SECONDARY/CosZenithVsEkinHisto neutron 4 200  1e-08 1000000 MeV log  200 -1. 1.


#
#Energy deposited
#

/PLANETOCOS/ANALYSIS/EDEP/AtmoEdepVsDepthHisto 1 200
/PLANETOCOS/ANALYSIS/EDEP/AtmoEdepVsAltitudeHisto 1 200

#
#cut in range definition
#

/PLANETOCOS/CUT/SetCutInDepthForAllAtmosphericLayers 2. g/cm2
```

```
/run/setCut 1. cm
/run/particle/applyCuts true e-
/run/particle/applyCuts true gamma
/run/particle/applyCuts true e+
/run/particle/dumpCutValues

#
#Stopping energy
#

/PLANETOCOS/STOPCONDITION/SetStoppingEnergy e-          1e-08   MeV
/PLANETOCOS/STOPCONDITION/SetStoppingEnergy gamma       1e-08    MeV
/PLANETOCOS/STOPCONDITION/SetStoppingEnergy proton      1e-08    MeV
/PLANETOCOS/STOPCONDITION/SetStoppingEnergy alpha       1e-08    MeV
/PLANETOCOS/STOPCONDITION/SetStoppingEnergy neutron     1e-08   MeV


/PLANETOCOS/DURATION/SetMaxTotalDuration 12. hour

#
#No  visualisation
#

/vis/enable false
/tracking/storeTrajectory 0
/PLANETOCOS/DRAW/DrawTrajectory false

#
#Select Solar maximum galactic flux
#
/PLANETOCOS/RANDOM/SetRandomSeedAtRunStart true
/PLANETOCOS/ANALYSIS/ResetHistograms

/PLANETOCOS/SOURCE/ConsiderCutoff false
/gps/particle proton
/gps/pos/centre 0 0 180 km
/gps/direction 0 0 -1
/gps/ang/rot1 1 0 0
/gps/ang/rot2 0 1 0
/gps/ang/type cos
/gps/ang/mintheta 0 deg
/gps/ang/maxtheta 90 deg
/gps/ene/min 100.01 MeV
/gps/ene/max 107.896152167881 MeV
/gps/ene/type Pow
/gps/ene/alpha 0.
/tracking/verbose 0
/run/beamOn  1000000

#
#Save histograms with normalisation per primary flux
#

/PLANETOCOS/ANALYSIS/SaveTree template.root root
```

# Appendix C

# Neutron Monitor Count Rates

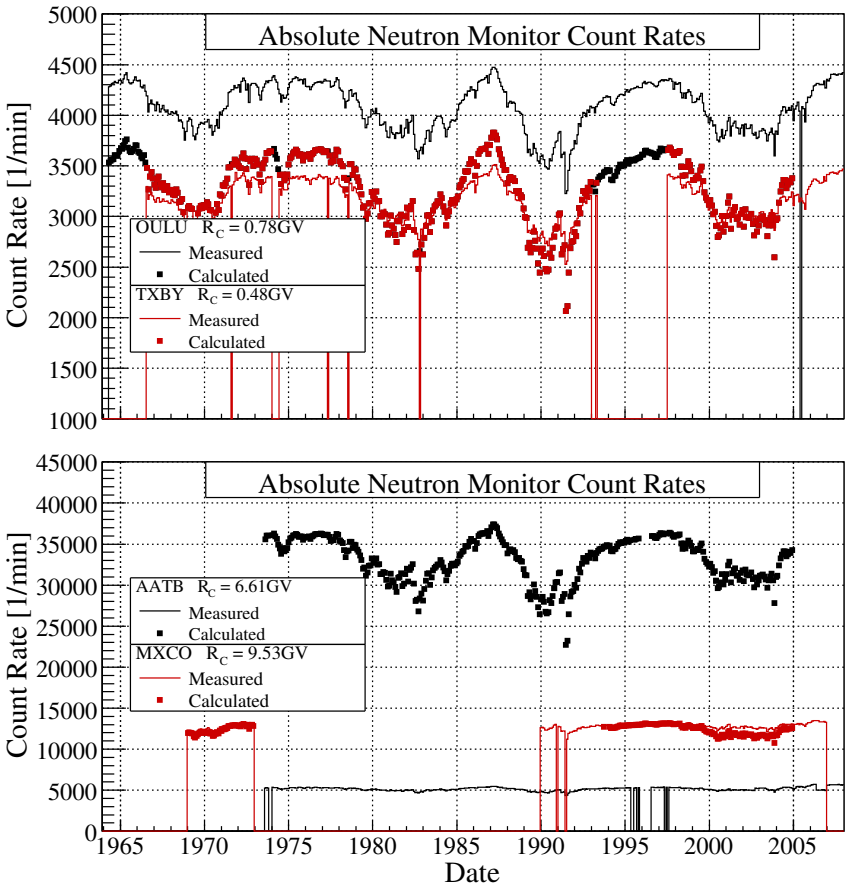


Figure C.1: Calculated and measured Neutron Monitor count rates for Oulu (OULU, 9-NM64, $R_C = 0.78$ GV, altitude 0 m, $p = 1000$ mb), Tixie Bay (TXBY, 18-NM64, $R_C = 0.48$ GV, altitude 0 m, $p = 1000$ mb), Alma-Ata B (AATB, 18-NM64, $R_C = 6.61$ GV, altitude 3340 m, $p = 675$ mb) and Mexico (MXCO, 6-NM64, $R_C = 9.53$ GV, altitude 2274 m, $p = 779$ mb). All normalized to a 6-NM64 detector.

# Appendix D

# Dose Rates

## D.1 Galactic Cosmic Rays

Table D.1: Effective dose rates $\dot{E}$ and ambient dose equivalent rates $\dot{H}^*(10)$ for solar minimum conditions ($\phi = 400$ MV) at altitude $a$, atmospheric depth $d$ and a geomagnetic cut-off $R_C = 0$ GV.

| | | neutrons | | protons | | photons | | $e^{-,+}$ | | $\mu^{-,+}$ | | All | |
|---|---|---|---|---|---|---|---|---|---|---|---|---|---|
| | | [$\mu$Sv/h] | | | | | | | | | | | |
| $a$ [m] | $d$ [g/cm$^2$] | $\dot{E}$ | $\dot{H}^*(10)$ | $\dot{E}$ | $\dot{H}^*(10)$ | $\dot{E}$ | $\dot{H}^*(10)$ | $\dot{E}$ | $\dot{H}^*(10)$ | $\dot{E}$ | $\dot{H}^*(10)$ | $\dot{E}$ | $\dot{H}^*(10)$ |
| 1.99e+04 | 57.2 | 7.4 | 9.5 | 16 | 6.4 | 1.2 | 0.6 | 1.9 | 3.9 | 0.37 | 0.35 | 26 | 19 |
| 1.78e+04 | 79.9 | 7.2 | 9.4 | 12 | 5.2 | 1.2 | 0.62 | 1.8 | 3.8 | 0.42 | 0.4 | 22 | 17 |
| 1.56e+04 | 112 | 6.6 | 8.5 | 8.7 | 3.8 | 1.1 | 0.6 | 1.6 | 3.5 | 0.43 | 0.41 | 18 | 15 |
| 1.34e+04 | 158 | 5.4 | 7 | 5.5 | 2.5 | 0.94 | 0.52 | 1.3 | 2.9 | 0.4 | 0.37 | 13 | 12 |
| 1.14e+04 | 218 | 3.9 | 5.1 | 3.1 | 1.5 | 0.69 | 0.39 | 0.89 | 2 | 0.32 | 0.3 | 8.5 | 8.5 |
| 9.47e+03 | 293 | 2.5 | 3.3 | 1.6 | 0.77 | 0.43 | 0.25 | 0.53 | 1.2 | 0.24 | 0.22 | 5 | 5.3 |
| 7.59e+03 | 385 | 1.4 | 1.8 | 0.69 | 0.35 | 0.23 | 0.13 | 0.26 | 0.64 | 0.16 | 0.15 | 2.6 | 2.9 |
| 5.74e+03 | 499 | 0.62 | 0.83 | 0.26 | 0.14 | 0.097 | 0.058 | 0.11 | 0.27 | 0.1 | 0.098 | 1.1 | 1.3 |
| 3.87e+03 | 640 | 0.22 | 0.3 | 0.078 | 0.043 | 0.034 | 0.021 | 0.04 | 0.099 | 0.067 | 0.063 | 0.4 | 0.48 |
| 1.97e+03 | 813 | 0.059 | 0.08 | 0.018 | 0.01 | 0.011 | 0.0066 | 0.014 | 0.036 | 0.043 | 0.041 | 0.13 | 0.15 |
| 116 | 1.02e+03 | 0.01 | 0.012 | 0.0031 | 0.0018 | 0.0041 | 0.0024 | 0.0065 | 0.016 | 0.029 | 0.027 | 0.041 | 0.045 |

Table D.2: Effective dose rates $\dot{E}$ and ambient dose equivalent rates $\dot{H}^*(10)$ for solar maximum conditions ($\phi = 1200$ MV) at altitude $a$, atmospheric depth $d$ and a geomagnetic cut-off $R_C = 0$ GV.

| | | neutrons | | protons | | photons | | $e^{-,+}$ | | $\mu^{-,+}$ | | All | |
|---|---|---|---|---|---|---|---|---|---|---|---|---|---|
| | | [$\mu$Sv/h] | | | | | | | | | | | |
| $a$ [m] | $d$ [g/cm$^2$] | $\dot{E}$ | $\dot{H}^*(10)$ | $\dot{E}$ | $\dot{H}^*(10)$ | $\dot{E}$ | $\dot{H}^*(10)$ | $\dot{E}$ | $\dot{H}^*(10)$ | $\dot{E}$ | $\dot{H}^*(10)$ | $\dot{E}$ | $\dot{H}^*(10)$ |
| 1.99e+04 | 57.2 | 3.3 | 4.1 | 6.4 | 2.7 | 0.73 | 0.37 | 1.3 | 2.4 | 0.24 | 0.23 | 11 | 8.5 |
| 1.78e+04 | 79.9 | 3.3 | 4.2 | 5.3 | 2.4 | 0.76 | 0.39 | 1.2 | 2.5 | 0.28 | 0.26 | 10 | 8.3 |
| 1.56e+04 | 112 | 3.1 | 3.9 | 4.1 | 1.9 | 0.75 | 0.39 | 1.1 | 2.4 | 0.29 | 0.28 | 8.9 | 7.7 |
| 1.34e+04 | 158 | 2.7 | 3.4 | 2.8 | 1.3 | 0.66 | 0.35 | 0.94 | 2 | 0.28 | 0.26 | 6.9 | 6.4 |
| 1.14e+04 | 218 | 2 | 2.6 | 1.7 | 0.85 | 0.5 | 0.28 | 0.67 | 1.5 | 0.24 | 0.22 | 4.8 | 4.8 |
| 9.47e+03 | 293 | 1.4 | 1.8 | 0.93 | 0.47 | 0.32 | 0.18 | 0.41 | 0.93 | 0.18 | 0.17 | 3 | 3.1 |
| 7.59e+03 | 385 | 0.78 | 1 | 0.44 | 0.23 | 0.17 | 0.1 | 0.21 | 0.49 | 0.13 | 0.12 | 1.6 | 1.8 |
| 5.74e+03 | 499 | 0.37 | 0.49 | 0.17 | 0.094 | 0.077 | 0.045 | 0.089 | 0.22 | 0.086 | 0.081 | 0.74 | 0.84 |
| 3.87e+03 | 640 | 0.14 | 0.19 | 0.056 | 0.031 | 0.028 | 0.017 | 0.033 | 0.081 | 0.057 | 0.053 | 0.28 | 0.33 |
| 1.97e+03 | 813 | 0.04 | 0.053 | 0.014 | 0.0078 | 0.0092 | 0.0055 | 0.012 | 0.03 | 0.038 | 0.035 | 0.095 | 0.11 |
| 116 | 1.02e+03 | 0.0071 | 0.0086 | 0.0024 | 0.0014 | 0.0036 | 0.0021 | 0.0058 | 0.014 | 0.026 | 0.025 | 0.034 | 0.037 |

## D.2 Solar Energetic Particle Events

Table D.3: Effective doses $E_D$ for different flight routes and locations at different atmospheric depths $d$ during GLE 42 from solar energetic particles (SEP) compared to the galactic cosmic ray (GCR) background.

| Route/Loc. | $d$ [g/cm$^2$] | | $E_D^{\text{GCR}}$ [$\mu$Sv] | $E_D^{\text{GCR+SEP}}$ [$\mu$Sv] | $E_D^{\text{GCR+SEP}}/E_D^{\text{GCR}}$ |
|---|---|---|---|---|---|
| **North Pole** | **200** | **Total** | **55** | **4.5e+02** | **8.1** |
| | | neutron | 23 (42%) | 3.2e+02 (71%) | 14 |
| | | photon | 5.6 (10%) | 18 (4%) | 3.2 |
| | | proton | 20 (36%) | 99 (22%) | 5.1 |
| | | $e^{+,-}$ | 4.8 (8.8%) | 8.7 (1.9%) | 4.3 |
| | | $\mu^{+,-}$ | 1.6 (2.9%) | 2.5 (0.57%) | 3.3 |
| **North Pole** | **300** | **Total** | **29** | **1.8e+02** | **6** |
| | | neutron | 14 (46%) | 1.3e+02 (75%) | 9.7 |
| | | photon | 3.1 (11%) | 7.4 (4.2%) | 2.4 |
| | | proton | 8.9 (30%) | 32 (18%) | 3.6 |
| | | $e^{+,-}$ | 2.5 (8.4%) | 3.8 (2.1%) | 3.6 |
| | | $\mu^{+,-}$ | 1.2 (4%) | 1.7 (0.94%) | 3 |
| **South Pole** | **200** | **Total** | **55** | **4.1e+02** | **7.6** |
| | | neutron | 23 (42%) | 3e+02 (72%) | 13 |
| | | photon | 5.6 (10%) | 17 (4.1%) | 3 |
| | | proton | 20 (36%) | 88 (21%) | 4.5 |
| | | $e^{+,-}$ | 4.8 (8.8%) | 8.3 (2%) | 4.1 |
| | | $\mu^{+,-}$ | 1.6 (2.9%) | 2.3 (0.56%) | 3 |
| **South Pole** | **300** | **Total** | **29** | **1.6e+02** | **5.6** |
| | | neutron | 14 (46%) | 1.2e+02 (75%) | 9 |
| | | photon | 3.1 (11%) | 7.2 (4.4%) | 2.3 |
| | | proton | 8.9 (30%) | 28 (17%) | 3.2 |
| | | $e^{+,-}$ | 2.5 (8.4%) | 3.7 (2.3%) | 3.6 |
| | | $\mu^{+,-}$ | 1.2 (4%) | 1.6 (0.95%) | 2.8 |
| **FRA-LAX** | **200** | **Total** | **53** | **3e+02** | **5.6** |
| | | neutron | 22 (42%) | 2e+02 (66%) | 8.9 |
| | | photon | 5.5 (10%) | 14 (4.6%) | 2.5 |
| | | proton | 19 (36%) | 79 (26%) | 4.1 |
| | | $e^{+,-}$ | 4.8 (9%) | 7.8 (2.6%) | 3.8 |
| | | $\mu^{+,-}$ | 1.6 (3%) | 2.3 (0.77%) | 3 |
| **FRA-LAX** | **300** | **Total** | **29** | **1.2e+02** | **4.3** |
| | | neutron | 13 (46%) | 87 (70%) | 6.6 |
| | | photon | 3.1 (11%) | 6.1 (4.9%) | 2 |
| | | proton | 8.7 (31%) | 27 (21%) | 3 |
| | | $e^{+,-}$ | 2.5 (8.6%) | 3.6 (2.9%) | 3.4 |
| | | $\mu^{+,-}$ | 1.2 (4%) | 1.5 (1.2%) | 2.8 |
| **JKF-PEK** | **200** | **Total** | **60** | **4.3e+02** | **7.2** |
| | | neutron | 25 (41%) | 3e+02 (69%) | 12 |
| | | photon | 6.4 (11%) | 18 (4.2%) | 2.9 |
| | | proton | 21 (36%) | 1e+02 (24%) | 4.7 |
| | | $e^{+,-}$ | 5.5 (9.2%) | 9.4 (2.2%) | 4 |
| | | $\mu^{+,-}$ | 1.9 (3.1%) | 2.8 (0.65%) | 3.2 |
| **JFK-PEK** | **300** | **Total** | **33** | **1.7e+02** | **5.3** |
| | | neutron | 15 (46%) | 1.3e+02 (73%) | 8.5 |
| | | photon | 3.6 (11%) | 7.8 (4.5%) | 2.2 |
| | | proton | 9.9 (30%) | 34 (19%) | 3.4 |
| | | $e^{+,-}$ | 2.9 (8.8%) | 4.2 (2.4%) | 3.5 |
| | | $\mu^{+,-}$ | 1.3 (4.1%) | 1.9 (1.1%) | 2.9 |

Table D.4: Average effective dose rates $\dot{E}_D$ for different flight routes and locations at different atmospheric depths $d$ during GLE 42 from solar energetic particles (SEP) compared to the galactic cosmic ray (GCR) background.

| Route/Loc. | $d$ [g/cm$^2$] | | $\dot{E}_D^{\text{GCR}}$ [$\mu$Sv/h] | $\dot{E}_D^{\text{GCR+SEP}}$ [$\mu$Sv/h] | $\dot{E}_D^{\text{GCR+SEP}}/\dot{E}_D^{\text{GCR}}$ |
|---|---|---|---|---|---|
| **North Pole** | **200** | **Total** | **5.3** | **43** | **8.1** |
| | | neutron | 2.2 (42%) | 31 (71%) | 14 |
| | | photon | 0.54 (10%) | 1.7 (4%) | 3.2 |
| | | proton | 1.9 (36%) | 9.5 (22%) | 5.1 |
| | | $e^{+,-}$ | 0.46 (8.8%) | 0.84 (1.9%) | 4.3 |
| | | $\mu^{+,-}$ | 0.15 (2.9%) | 0.24 (0.57%) | 3.3 |
| **North Pole** | **300** | **Total** | **2.8** | **17** | **6** |
| | | neutron | 1.3 (46%) | 13 (75%) | 9.7 |
| | | photon | 0.3 (11%) | 0.71 (4.2%) | 2.4 |
| | | proton | 0.86 (30%) | 3.1 (18%) | 3.6 |
| | | $e^{+,-}$ | 0.24 (8.4%) | 0.36 (2.1%) | 3.6 |
| | | $\mu^{+,-}$ | 0.11 (4%) | 0.16 (0.94%) | 3 |
| **South Pole** | **200** | **Total** | **5.3** | **40** | **7.6** |
| | | neutron | 2.2 (42%) | 29 (72%) | 13 |
| | | photon | 0.54 (10%) | 1.6 (4.1%) | 3 |
| | | proton | 1.9 (36%) | 8.5 (21%) | 4.5 |
| | | $e^{+,-}$ | 0.46 (8.8%) | 0.8 (2%) | 4.1 |
| | | $\mu^{+,-}$ | 0.15 (2.9%) | 0.22 (0.56%) | 3 |
| **South Pole** | **300** | **Total** | **2.8** | **16** | **5.6** |
| | | neutron | 1.3 (46%) | 12 (75%) | 9 |
| | | photon | 0.3 (11%) | 0.69 (4.4%) | 2.3 |
| | | proton | 0.86 (30%) | 2.7 (17%) | 3.2 |
| | | $e^{+,-}$ | 0.24 (8.4%) | 0.36 (2.3%) | 3.6 |
| | | $\mu^{+,-}$ | 0.11 (4%) | 0.15 (0.95%) | 2.8 |
| **FRA-LAX** | **200** | **Total** | **5.1** | **29** | **5.6** |
| | | neutron | 2.1 (42%) | 19 (66%) | 8.9 |
| | | photon | 0.53 (10%) | 1.3 (4.6%) | 2.5 |
| | | proton | 1.8 (36%) | 7.6 (26%) | 4.1 |
| | | $e^{+,-}$ | 0.46 (9%) | 0.75 (2.6%) | 3.8 |
| | | $\mu^{+,-}$ | 0.15 (3%) | 0.22 (0.77%) | 3 |
| **FRA-LAX** | **300** | **Total** | **2.8** | **12** | **4.3** |
| | | neutron | 1.3 (46%) | 8.3 (70%) | 6.6 |
| | | photon | 0.3 (11%) | 0.59 (4.9%) | 2 |
| | | proton | 0.84 (31%) | 2.6 (21%) | 3 |
| | | $e^{+,-}$ | 0.24 (8.6%) | 0.34 (2.9%) | 3.4 |
| | | $\mu^{+,-}$ | 0.11 (4%) | 0.15 (1.2%) | 2.8 |
| **JKF-PEK** | **200** | **Total** | **4.9** | **35** | **7.2** |
| | | neutron | 2 (41%) | 24 (69%) | 12 |
| | | photon | 0.52 (11%) | 1.5 (4.2%) | 2.9 |
| | | proton | 1.8 (36%) | 8.3 (24%) | 4.7 |
| | | $e^{+,-}$ | 0.45 (9.2%) | 0.77 (2.2%) | 4 |
| | | $\mu^{+,-}$ | 0.15 (3.1%) | 0.23 (0.65%) | 3.2 |
| **JFK-PEK** | **300** | **Total** | **2.7** | **14** | **5.3** |
| | | neutron | 1.2 (46%) | 10 (73%) | 8.5 |
| | | photon | 0.3 (11%) | 0.64 (4.5%) | 2.2 |
| | | proton | 0.81 (30%) | 2.8 (19%) | 3.4 |
| | | $e^{+,-}$ | 0.23 (8.8%) | 0.35 (2.4%) | 3.5 |
| | | $\mu^{+,-}$ | 0.11 (4.1%) | 0.15 (1.1%) | 2.9 |

Table D.5: Effective doses $E_D$ for different flight routes and locations at different atmospheric depths $d$ during GLE 60 from solar energetic particles (SEP) compared to the galactic cosmic ray (GCR) background.

| Route/Loc. | $d$ [g/cm$^2$] | | $E_D^{\text{GCR}}$ [$\mu$Sv] | $E_D^{\text{GCR+SEP}}$ [$\mu$Sv] | $E_D^{\text{GCR+SEP}}/E_D^{\text{GCR}}$ |
|---|---|---|---|---|---|
| **North Pole** | **200** | **Total** | **62** | **1.2e+02** | **1.9** |
| | | neutron | 27 (43%) | 73 (61%) | 2.7 |
| | | photon | 6 (9.7%) | 7.7 (6.4%) | 1.3 |
| | | proton | 22 (36%) | 31 (26%) | 1.4 |
| | | $e^{+,-}$ | 5.1 (8.3%) | 5.5 (4.6%) | 2.5 |
| | | $\mu^{+,-}$ | 1.7 (2.8%) | 1.8 (1.5%) | 2.2 |
| **North Pole** | **300** | **Total** | **33** | **54** | **1.6** |
| | | neutron | 16 (48%) | 33 (62%) | 2.1 |
| | | photon | 3.4 (10%) | 3.9 (7.3%) | 1.2 |
| | | proton | 9.9 (30%) | 12 (23%) | 1.2 |
| | | $e^{+,-}$ | 2.6 (8%) | 2.8 (5.2%) | 2.5 |
| | | $\mu^{+,-}$ | 1.2 (3.8%) | 1.3 (2.4%) | 2.1 |
| **South Pole** | **200** | **Total** | **62** | **1.7e+02** | **2.8** |
| | | neutron | 27 (43%) | 1.2e+02 (68%) | 4.4 |
| | | photon | 6 (9.7%) | 9.2 (5.3%) | 1.5 |
| | | proton | 22 (36%) | 39 (23%) | 1.8 |
| | | $e^{+,-}$ | 5.1 (8.3%) | 5.9 (3.4%) | 2.7 |
| | | $\mu^{+,-}$ | 1.7 (2.8%) | 1.8 (1.1%) | 2.2 |
| **South Pole** | **300** | **Total** | **33** | **73** | **2.2** |
| | | neutron | 16 (48%) | 50 (69%) | 3.2 |
| | | photon | 3.4 (10%) | 4.5 (6.1%) | 1.3 |
| | | proton | 9.9 (30%) | 14 (20%) | 1.4 |
| | | $e^{+,-}$ | 2.6 (8%) | 2.9 (4%) | 2.6 |
| | | $\mu^{+,-}$ | 1.2 (3.8%) | 1.3 (1.8%) | 2.2 |
| **FRA-LAX** | **200** | **Total** | **60** | **1.1e+02** | **1.9** |
| | | neutron | 25 (43%) | 66 (58%) | 2.6 |
| | | photon | 5.9 (10%) | 7.7 (6.7%) | 1.3 |
| | | proton | 21 (36%) | 33 (29%) | 1.5 |
| | | $e^{+,-}$ | 5.1 (8.5%) | 5.6 (4.9%) | 2.6 |
| | | $\mu^{+,-}$ | 1.7 (2.9%) | 1.8 (1.6%) | 2.2 |
| **FRA-LAX** | **300** | **Total** | **32** | **52** | **1.6** |
| | | neutron | 15 (47%) | 31 (60%) | 2.1 |
| | | photon | 3.3 (10%) | 4 (7.6%) | 1.2 |
| | | proton | 9.7 (31%) | 13 (25%) | 1.3 |
| | | $e^{+,-}$ | 2.6 (8.2%) | 2.8 (5.3%) | 2.6 |
| | | $\mu^{+,-}$ | 1.2 (3.9%) | 1.3 (2.4%) | 2.2 |
| **JKF-PEK** | **200** | **Total** | **67** | **1.5e+02** | **2.3** |
| | | neutron | 28 (42%) | 97 (63%) | 3.4 |
| | | photon | 6.8 (10%) | 9.5 (6.1%) | 1.4 |
| | | proton | 24 (36%) | 39 (25%) | 1.6 |
| | | $e^{+,-}$ | 5.9 (8.7%) | 6.5 (4.2%) | 2.6 |
| | | $\mu^{+,-}$ | 2 (2.9%) | 2.1 (1.3%) | 2.2 |
| **JFK-PEK** | **300** | **Total** | **36** | **68** | **1.9** |
| | | neutron | 17 (47%) | 44 (64%) | 2.6 |
| | | photon | 3.8 (11%) | 4.8 (7%) | 1.2 |
| | | proton | 11 (31%) | 15 (22%) | 1.4 |
| | | $e^{+,-}$ | 3 (8.4%) | 3.3 (4.8%) | 2.6 |
| | | $\mu^{+,-}$ | 1.4 (3.9%) | 1.5 (2.2%) | 2.2 |

Table D.6: Average effective dose rates $\dot{E}_D$ for different flight routes and locations at different atmospheric depths $d$ during GLE 60 from solar energetic particles (SEP) compared to the galactic cosmic ray (GCR) background.

| Route/Loc. | $d$ [g/cm$^2$] | | $\dot{E}_D^{\text{GCR}}$ [$\mu$Sv/h] | $\dot{E}_D^{\text{GCR+SEP}}$ [$\mu$Sv/h] | $\dot{E}_D^{\text{GCR+SEP}}/\dot{E}_D^{\text{GCR}}$ |
|---|---|---|---|---|---|
| **North Pole** | **200** | **Total** | **5.9** | **11** | **1.9** |
| | | neutron | 2.6 (43%) | 7.1 (61%) | 2.7 |
| | | photon | 0.58 (9.7%) | 0.74 (6.4%) | 1.3 |
| | | proton | 2.1 (36%) | 3 (26%) | 1.4 |
| | | $e^{+,-}$ | 0.49 (8.3%) | 0.53 (4.6%) | 2.5 |
| | | $\mu^{+,-}$ | 0.17 (2.8%) | 0.17 (1.5%) | 2.2 |
| **North Pole** | **300** | **Total** | **3.2** | **5.2** | **1.6** |
| | | neutron | 1.5 (48%) | 3.2 (62%) | 2.1 |
| | | photon | 0.32 (10%) | 0.38 (7.3%) | 1.2 |
| | | proton | 0.96 (30%) | 1.2 (23%) | 1.2 |
| | | $e^{+,-}$ | 0.25 (8%) | 0.27 (5.2%) | 2.5 |
| | | $\mu^{+,-}$ | 0.12 (3.8%) | 0.12 (2.4%) | 2.1 |
| **South Pole** | **200** | **Total** | **5.9** | **17** | **2.8** |
| | | neutron | 2.6 (43%) | 11 (68%) | 4.4 |
| | | photon | 0.58 (9.7%) | 0.89 (5.3%) | 1.5 |
| | | proton | 2.1 (36%) | 3.8 (23%) | 1.8 |
| | | $e^{+,-}$ | 0.49 (8.3%) | 0.57 (3.4%) | 2.7 |
| | | $\mu^{+,-}$ | 0.17 (2.8%) | 0.18 (1.1%) | 2.2 |
| **South Pole** | **300** | **Total** | **3.2** | **7** | **2.2** |
| | | neutron | 1.5 (48%) | 4.8 (69%) | 3.2 |
| | | photon | 0.32 (10%) | 0.43 (6.1%) | 1.3 |
| | | proton | 0.96 (30%) | 1.4 (20%) | 1.4 |
| | | $e^{+,-}$ | 0.25 (8%) | 0.28 (4%) | 2.6 |
| | | $\mu^{+,-}$ | 0.12 (3.8%) | 0.12 (1.8%) | 2.2 |
| **FRA-LAX** | **200** | **Total** | **5.7** | **11** | **1.9** |
| | | neutron | 2.4 (43%) | 6.4 (58%) | 2.6 |
| | | photon | 0.57 (10%) | 0.74 (6.7%) | 1.3 |
| | | proton | 2.1 (36%) | 3.2 (29%) | 1.5 |
| | | $e^{+,-}$ | 0.49 (8.5%) | 0.54 (4.9%) | 2.6 |
| | | $\mu^{+,-}$ | 0.16 (2.9%) | 0.17 (1.6%) | 2.2 |
| **FRA-LAX** | **300** | **Total** | **3.1** | **5.1** | **1.6** |
| | | neutron | 1.4 (47%) | 3 (60%) | 2.1 |
| | | photon | 0.32 (10%) | 0.38 (7.6%) | 1.2 |
| | | proton | 0.94 (31%) | 1.2 (25%) | 1.3 |
| | | $e^{+,-}$ | 0.25 (8.2%) | 0.27 (5.3%) | 2.6 |
| | | $\mu^{+,-}$ | 0.12 (3.9%) | 0.12 (2.4%) | 2.2 |
| **JKF-PEK** | **200** | **Total** | **5.5** | **13** | **2.3** |
| | | neutron | 2.3 (42%) | 8 (63%) | 3.4 |
| | | photon | 0.56 (10%) | 0.78 (6.1%) | 1.4 |
| | | proton | 2 (36%) | 3.2 (25%) | 1.6 |
| | | $e^{+,-}$ | 0.48 (8.7%) | 0.54 (4.2%) | 2.6 |
| | | $\mu^{+,-}$ | 0.16 (2.9%) | 0.17 (1.3%) | 2.2 |
| **JFK-PEK** | **300** | **Total** | **3** | **5.6** | **1.9** |
| | | neutron | 1.4 (47%) | 3.6 (64%) | 2.6 |
| | | photon | 0.31 (11%) | 0.39 (7%) | 1.2 |
| | | proton | 0.9 (31%) | 1.2 (22%) | 1.4 |
| | | $e^{+,-}$ | 0.25 (8.4%) | 0.27 (4.8%) | 2.6 |
| | | $\mu^{+,-}$ | 0.12 (3.9%) | 0.12 (2.2%) | 2.2 |

Table D.7: Effective doses $E_D$ for different flight routes and locations at different atmospheric depths $d$ during GLE 69 from solar energetic particles (SEP) compared to the galactic cosmic ray (GCR) background.

| Route/Loc. | $d$ [g/cm$^2$] | | $E_D^{\text{GCR}}$ [$\mu$Sv] | $E_D^{\text{GCR+SEP}}$ [$\mu$Sv] | $E_D^{\text{GCR+SEP}}/E_D^{\text{GCR}}$ |
|---|---|---|---|---|---|
| **North Pole** | **200** | **Total** | **81** | **2.1e+02** | **2.6** |
| | | neutron | 37 (46%) | 1.5e+02 (69%) | 4 |
| | | photon | 7.1 (8.8%) | 11 (5%) | 1.5 |
| | | proton | 29 (36%) | 46 (21%) | 1.6 |
| | | $e^{+,-}$ | 5.9 (7.2%) | 6.6 (3.1%) | 2.7 |
| | | $\mu^{+,-}$ | 2 (2.4%) | 2 (0.96%) | 2.2 |
| **North Pole** | **300** | **Total** | **42** | **89** | **2.1** |
| | | neutron | 21 (50%) | 62 (70%) | 3 |
| | | photon | 3.9 (9.3%) | 5.1 (5.7%) | 1.3 |
| | | proton | 13 (30%) | 17 (19%) | 1.3 |
| | | $e^{+,-}$ | 3 (7.1%) | 3.2 (3.6%) | 2.6 |
| | | $\mu^{+,-}$ | 1.4 (3.3%) | 1.4 (1.6%) | 2.2 |
| **South Pole** | **200** | **Total** | **81** | **4.5e+02** | **5.5** |
| | | neutron | 37 (46%) | 3.5e+02 (79%) | 9.5 |
| | | photon | 7.1 (8.8%) | 17 (3.7%) | 2.4 |
| | | proton | 29 (36%) | 69 (15%) | 2.4 |
| | | $e^{+,-}$ | 5.9 (7.2%) | 7.5 (1.7%) | 3 |
| | | $\mu^{+,-}$ | 2 (2.4%) | 2.1 (0.47%) | 2.3 |
| **South Pole** | **300** | **Total** | **42** | **1.7e+02** | **4.1** |
| | | neutron | 21 (50%) | 1.4e+02 (80%) | 6.5 |
| | | photon | 3.9 (9.3%) | 7 (4.1%) | 1.8 |
| | | proton | 13 (30%) | 22 (13%) | 1.7 |
| | | $e^{+,-}$ | 3 (7.1%) | 3.5 (2%) | 2.8 |
| | | $\mu^{+,-}$ | 1.4 (3.3%) | 1.5 (0.86%) | 2.2 |
| **FRA-LAX** | **200** | **Total** | **77** | **1.7e+02** | **2.1** |
| | | neutron | 34 (45%) | 1e+02 (60%) | 2.9 |
| | | photon | 7 (9%) | 9.8 (5.9%) | 1.4 |
| | | proton | 28 (36%) | 47 (28%) | 1.7 |
| | | $e^{+,-}$ | 5.8 (7.5%) | 6.7 (4%) | 2.7 |
| | | $\mu^{+,-}$ | 2 (2.5%) | 2.1 (1.2%) | 2.2 |
| **FRA-LAX** | **300** | **Total** | **40** | **73** | **1.8** |
| | | neutron | 20 (49%) | 46 (63%) | 2.4 |
| | | photon | 3.8 (9.5%) | 4.8 (6.6%) | 1.3 |
| | | proton | 12 (31%) | 17 (24%) | 1.4 |
| | | $e^{+,-}$ | 2.9 (7.3%) | 3.2 (4.4%) | 2.6 |
| | | $\mu^{+,-}$ | 1.4 (3.5%) | 1.4 (2%) | 2.2 |
| **JKF-PEK** | **200** | **Total** | **87** | **2e+02** | **2.3** |
| | | neutron | 39 (44%) | 1.2e+02 (63%) | 3.2 |
| | | photon | 8 (9.2%) | 11 (5.7%) | 1.4 |
| | | proton | 31 (36%) | 52 (26%) | 1.7 |
| | | $e^{+,-}$ | 6.7 (7.7%) | 7.6 (3.9%) | 2.7 |
| | | $\mu^{+,-}$ | 2.3 (2.6%) | 2.4 (1.2%) | 2.2 |
| **JFK-PEK** | **300** | **Total** | **45** | **86** | **1.9** |
| | | neutron | 22 (49%) | 56 (65%) | 2.5 |
| | | photon | 4.4 (9.7%) | 5.6 (6.5%) | 1.3 |
| | | proton | 14 (30%) | 19 (23%) | 1.4 |
| | | $e^{+,-}$ | 3.4 (7.5%) | 3.7 (4.3%) | 2.6 |
| | | $\mu^{+,-}$ | 1.6 (3.5%) | 1.7 (1.9%) | 2.2 |

Table D.8: Average effective dose rates $\dot{E}_D$ for different flight routes and locations at different atmospheric depths $d$ during GLE 69 from solar energetic particles (SEP) compared to the galactic cosmic ray (GCR) background.

| Route/Loc. | $d$ [g/cm$^2$] | | $\dot{E}_D^{\text{GCR}}$ [$\mu$Sv/h] | $\dot{E}_D^{\text{GCR+SEP}}$ [$\mu$Sv/h] | $\dot{E}_D^{\text{GCR+SEP}}/\dot{E}_D^{\text{GCR}}$ |
|---|---|---|---|---|---|
| **North Pole** | **200** | **Total** | **7.8** | **21** | **2.6** |
| | | neutron | 3.6 (46%) | 14 (69%) | 4 |
| | | photon | 0.68 (8.8%) | 1 (5%) | 1.5 |
| | | proton | 2.8 (36%) | 4.4 (21%) | 1.6 |
| | | $e^{+,-}$ | 0.57 (7.2%) | 0.63 (3.1%) | 2.7 |
| | | $\mu^{+,-}$ | 0.19 (2.4%) | 0.2 (0.96%) | 2.2 |
| **North Pole** | **300** | **Total** | **4** | **8.5** | **2.1** |
| | | neutron | 2 (50%) | 6 (70%) | 3 |
| | | photon | 0.37 (9.3%) | 0.49 (5.7%) | 1.3 |
| | | proton | 1.2 (30%) | 1.6 (19%) | 1.3 |
| | | $e^{+,-}$ | 0.29 (7.1%) | 0.31 (3.6%) | 2.6 |
| | | $\mu^{+,-}$ | 0.13 (3.3%) | 0.14 (1.6%) | 2.2 |
| **South Pole** | **200** | **Total** | **7.8** | **43** | **5.5** |
| | | neutron | 3.6 (46%) | 34 (79%) | 9.5 |
| | | photon | 0.68 (8.8%) | 1.6 (3.7%) | 2.4 |
| | | proton | 2.8 (36%) | 6.6 (15%) | 2.4 |
| | | $e^{+,-}$ | 0.57 (7.2%) | 0.72 (1.7%) | 3 |
| | | $\mu^{+,-}$ | 0.19 (2.4%) | 0.2 (0.47%) | 2.3 |
| **South Pole** | **300** | **Total** | **4** | **16** | **4.1** |
| | | neutron | 2 (50%) | 13 (80%) | 6.5 |
| | | photon | 0.37 (9.3%) | 0.68 (4.1%) | 1.8 |
| | | proton | 1.2 (30%) | 2.1 (13%) | 1.7 |
| | | $e^{+,-}$ | 0.29 (7.1%) | 0.34 (2%) | 2.8 |
| | | $\mu^{+,-}$ | 0.13 (3.3%) | 0.14 (0.86%) | 2.2 |
| **FRA-LAX** | **200** | **Total** | **7.4** | **16** | **2.1** |
| | | neutron | 3.3 (45%) | 9.6 (60%) | 2.9 |
| | | photon | 0.67 (9%) | 0.94 (5.9%) | 1.4 |
| | | proton | 2.7 (36%) | 4.5 (28%) | 1.7 |
| | | $e^{+,-}$ | 0.56 (7.5%) | 0.64 (4%) | 2.7 |
| | | $\mu^{+,-}$ | 0.19 (2.5%) | 0.2 (1.2%) | 2.2 |
| **FRA-LAX** | **300** | **Total** | **3.9** | **7.1** | **1.8** |
| | | neutron | 1.9 (49%) | 4.5 (63%) | 2.4 |
| | | photon | 0.37 (9.5%) | 0.47 (6.6%) | 1.3 |
| | | proton | 1.2 (31%) | 1.7 (24%) | 1.4 |
| | | $e^{+,-}$ | 0.28 (7.3%) | 0.31 (4.4%) | 2.6 |
| | | $\mu^{+,-}$ | 0.13 (3.5%) | 0.14 (2%) | 2.2 |
| **JKF-PEK** | **200** | **Total** | **7.1** | **16** | **2.3** |
| | | neutron | 3.2 (44%) | 10 (63%) | 3.2 |
| | | photon | 0.65 (9.2%) | 0.93 (5.7%) | 1.4 |
| | | proton | 2.6 (36%) | 4.3 (26%) | 1.7 |
| | | $e^{+,-}$ | 0.55 (7.7%) | 0.62 (3.9%) | 2.7 |
| | | $\mu^{+,-}$ | 0.18 (2.6%) | 0.19 (1.2%) | 2.2 |
| **JFK-PEK** | **300** | **Total** | **3.7** | **7.1** | **1.9** |
| | | neutron | 1.8 (49%) | 4.6 (65%) | 2.5 |
| | | photon | 0.36 (9.7%) | 0.46 (6.5%) | 1.3 |
| | | proton | 1.1 (30%) | 1.6 (23%) | 1.4 |
| | | $e^{+,-}$ | 0.28 (7.5%) | 0.3 (4.3%) | 2.6 |
| | | $\mu^{+,-}$ | 0.13 (3.5%) | 0.14 (1.9%) | 2.2 |

Ich erkläre hiermit,

- dass die vorliegende Arbeit—abgesehen von der Beratung durch den Betreuer—nach Inhalt und Form die eigene Arbeit ist.
- dass die Arbeit noch nicht an anderer Stelle im Rahmen eines Prüfungsverfahrens vorgelegen hat.
- dass die vorliegende Arbeit unter Einhaltung der Regeln guter wissenschaftlicher Praxis entstanden und selbständig verfasst worden ist und keine anderen als die angegebenen Quellen und Hilfsmittel verwendet wurden.

Teile der Arbeit wurden wie im Text angegeben in wissenschaftlichen Zeitschriften veröffentlicht.

Daniel Matthiä, Kiel, den